Multiscale, Multiphysics, and Data-Driven Modelling of the Laser Powder Bed Fusion Processing of Nitinol Shape Memory Alloy

By

Sampreet Rangaswamy, B.Tech., M.Sc.

A thesis submitted in fulfilment of the requirements for the degree of
Doctor of Philosophy (PhD)
from
Dublin City University
School of Mechanical and Manufacturing Engineering

Supervisor: Prof. Dermot Brabazon
Co-supervisor: Dr. Inam Ul Ahad

August 2026

Declaration

I hereby certify that this material, which I now submit for assessment on the programme of study leading to the award of Doctor of Philosophy (PhD) is entirely my own work, and that I have exercised reasonable care to ensure that the work is original and have conformed to the regulations on the use and declaration of Generative AI, and does not to the best of my knowledge breach any law of copyright, and has not been taken from the work of others save and to the extent that such work has been cited and acknowledged within the text of my work. I hereby certify that no Generative Artificial Intelligence (Gen AI) tools have been used in the creation of the thesis.

Signed: ____Sampreet Rangaswamy____ ID No.: 22269710 Date: 01-Aug-2026

Acknowledgements

Firstly, my sincere and heartfelt gratitude to my exceptional supervisor, **Prof. Dermot Brabazon**, for his kindness, invaluable guidance, unwavering support, and constant belief in me throughout this journey.

My deepest appreciation is extended to my co-supervisor, **Dr. Inam Ul Ahad**, for generously sharing his exceptional technical expertise, insightful feedback, counsel and guidance. I am also grateful to my advisors, **Dr. Merve Nur Doğu** and **Dr. Medad C.C. Monu** for the consistent support, guidance, and encouragement.

I would also like to thank **Dr. Hengfeng Gu**, **Mr. Abdul Khader Khan**, **Dr. Chong Teng**, and ANSYS Inc. for their support and technical guidance as industrial sponsors. I want to acknowledge **Mr. Declan Bourke** and Fort Wayne Metals for their support with the materials and resources.

I would also like to express gratitude to my guide and mentor, **Dr. Deepan Bharathi Kannan**, whose motivation and belief in my abilities inspired me to pursue a PhD, and his insights and mentorship have been instrumental in shaping my research and professional growth.

I would like to sincerely acknowledge **Ms. Joan Kelly** and all the staff at the School of Mechanical and Manufacturing Engineering and the Nano Research Facility for their assistance and support. I also gratefully acknowledge the financial and institutional support provided by Advanced Metallic Systems Centre for Doctoral Training, Science Foundation Ireland, I-Form, and Dublin City University.

Finally, I would like to extend my deepest thanks to my father **Dr. Rangaswamy K.B**, my mother **Ms. Manjula K.H**, family and friends, whose unwavering support, encouragement, and belief in me throughout my life gave me the strength and motivation to successfully complete this PhD.

Table of Contents

Multiscale, Multiphysics, and Data-Driven Modelling of the Laser Powder Bed Fusion Processing of Nitinol Shape Memory Alloy 1
Declaration 2
Acknowledgements 3
Table of Contents 4
List of Publications 8
List of Presentations 10
List of Awards 10
List of Figures 11
List of Tables 15
List of Abbreviations 16
Abstract 19
1. Chapter: Introduction 20
1.1 Background and Motivation 20
1.2 Thesis Aim and Objectives 23
1.3 Thesis Structure 23
1.4 Research Workflow and Thesis Framework 26
1.5 Scope and Limitations of the Research 28
2. Chapter: Review of the Laser Powder Bed Fusion of Nitinol - Defect Formation and Prediction 29
Abstract 29
2.1 Literature Search and Selection Methodology 30
2.2 Functional properties of NiTi 33
2.3 Applications of NiTi 34
2.3.1 Biomedical Applications: From Shape Memory to Superelastic Dominance 35
2.3.2 Aerospace, Automotive, and High-Performance Engineering 37
2.3.3 Elastocaloric Cooling 39
2.3.4 Industrial and Consumer Applications 42
2.4 Manufacturing of NiTi 43
2.4.1 Challenges in manufacturing NiTi 43
2.4.2 Manufacturing of NiTi by Laser Powder Bed Fusion (PBF-LB) 44
2.5 Defects in PBF-LB of NiTi 46
2.5.1 Porosity (balling, keyholing and lack-of-fusion) 49
2.5.2 Residual stress 55

2.5.3 Delamination and cracks 57
2.5.4 Surface roughness 60
2.5.5 Oxidation 62
2.6 Modelling the PBF-LB process of NiTi 65
2.6.1 Thermal modelling 66
2.6.2 Melt pool modelling 76
2.6.3 Residual Stress Modelling 78
2.6.4 Microstructure modelling 81
2.6.5 Derived predictions 83
2.7 Summary of the literature review 85
3. Chapter: Investigating Melt Pool Dimensions in Laser Powder Bed Fusion of Nitinol - An Analytical Approach 88
Abstract 88
3.1 Introduction 89
3.2 Materials and Methods 89
3.2.1 Experimental Details 89
3.2.2 Modelling Details 91
3.3 Results and Discussion 95
3.3.1 Qualitative NiTi Melt Pool Width and Depth Analysis 95
3.3.2 Quantitative NiTi Melt Pool Width and Depth Analysis 97
3.3.3 Model Predictions of NiTi Melt Pool Width and Depth 99
3.3.4 Model Prediction Accuracy 100
3.3.5 Power – Scan Speed (P-V) Process Maps 104
3.4 Conclusion 106
4. Chapter: Physics-Guided Digital Twin Framework for Melt Pool Prediction and Process Stability in Laser Powder Bed Fusion of Nitinol 108
Abstract 108
4.1 Introduction 109
4.2 Materials and Methods 110
4.2.1 Experimental Details 110
4.2.2 Pyrometric Infrared (IR) Data 114
4.2.3 CALPHAD 114
4.2.4 Thermal Modelling 115
4.2.5 Machine Learning 117
4.3 Results and Discussion 124
4.3.1 IR Data Analysis 124
4.3.2 Experimental Melt Pool Trend Analysis 125

4.3.3 Thermal Model Performance 126
4.3.4 Surrogate Model Performance 130
4.3.5 Physics-Based Melt Pool Regime Classification 131
4.3.6 Physics-Guided Decision Engine and Input Constraints 132
4.3.7 Physics-Constrained Process Parameter Search 132
4.3.8 Digital Twin Interpretation and Implications 133
4.3.9 Limitations and Future Outlook 135
4.4 Conclusion 135
5. Chapter: Evaluating Residual Stress in Additively Manufactured Nitinol Shape Memory Alloy 137
Abstract 137
5.1 Introduction 138
5.2 Materials and Methods 139
5.2.1 Experimental Details 139
5.3 Results and Discussion 142
5.3.1 RS analysis based on the XRD and ESPI-HD results 142
5.3.2 Effect of increasing VED by reduced scanning speed and hatch spacing on RS 144
5.3.3 Thermal data analysis for the correlation between the RS, VED and thermal gradient 147
5.4 Conclusion 150
6. Chapter: Residual Stress Estimation in Laser Powder Bed Fusion of Nitinol Shape Memory Alloy 151
Abstract 151
6.1 Introduction 152
6.2 Materials and Methods 153
6.2.1 Sample fabrication 153
6.2.2 Infrared Melt-Pool Monitoring 155
6.2.3 Beam Deflection Measurements 155
6.2.4 X-ray Diffraction (XRD) 156
6.2.5 Vick Hardness Measurements 156
6.2.6 Modelling Details 157
6.3 Results and Discussion 159
6.3.1 Thermal Response of NiTi Cantilever Samples during PBF-LB 159
6.3.2 Experimental Beam Deflection Analysis as an Indicator of Residual Stress 162
6.3.3 Processing Parameter Influence on Beam Deflection 164
6.3.4 Phase Constitution Influence on Beam Deflection 168
6.3.5 Vickers Hardness Analysis 171

6.3.6 Thermo-mechanical finite element modelling results....173
6.4 Conclusion....180
7. Chapter: Conclusion and Future Work....183
References....186
Declaration of Authorship for PhD by Publication....209
Section 1: Candidate's Details....209
Section 2: Paper Details....209
Section 3: Candidate's Contribution to the Paper....209
Section 4: Signature and Validation....210
Section 1: Candidate's Details....211
Section 2: Paper Details....211
Section 3: Candidate's Contribution to the Paper....211
Section 4: Signature and Validation....212
Section 1: Candidate's Details....213
Section 2: Paper Details....213
Section 3: Candidate's Contribution to the Paper....213
Section 4: Signature and Validation....214
Section 1: Candidate's Details....215
Section 2: Paper Details....215
Section 3: Candidate's Contribution to the Paper....215
Section 4: Signature and Validation....216
Section 1: Candidate's Details....217
Section 2: Paper Details....217
Section 3: Candidate's Contribution to the Paper....217
Section 4: Signature and Validation....218

List of Publications

1. **Sampreet Rangaswamy**, Declan Bourke, Medad C. C. Monu, Paul Healy, Hengfeng Gu, Inam Ul Ahad, and Dermot Brabazon, **Investigating Melt Pool Dimensions in Laser Powder Bed Fusion of Nitinol: An Analytical Approach**, Advanced Engineering Materials 26 (2024). https://doi.org/10.1002/adem.202401636
2. **Sampreet Rangaswamy**, Thomas Gillick, Medad CC Monu, Inam Ul Ahad, Dermot Brabazon, **Estimation of Residual Stress in Additive-Manufactured NiTi Alloy through Beam Mechanics and Finite Element Analysis**, Shape Memory Proceedings (2024). https://doi.org/10.31399/asm.cp.smst2024p0009
3. **Sampreet Rangaswamy**, Josiah Cherian Chekotu, Thomas Gillick, Cian Hughes, Jayne Nicholl, David Easton, Caner Şimşir, Dermot Brabazon, **Evaluating Residual Stress in Additively Manufactured Nitinol Shape Memory Alloy**, npj Advanced Manufacturing 2 (2025). https://doi.org/10.1038/s44334-025-00027-y
4. **Sampreet Rangaswamy**, Camille Rubio, Merve Nur Doğu, Medad C.C. Monu, Dermot Brabazon, **Review of the Laser Powder Bed Fusion of Nitinol: Defect Formation and Prediction**, Materials Today Advances (2026). https://doi.org/10.1016/j.mtadv.2026.100771
5. **Sampreet Rangaswamy**, Merve Nur Doğu, Camille Rubio, Hengfeng Gu, Abdul Khader Khan, Chong Teng, Inam Ul Ahad, Dermot Brabazon, **Physics-Guided Digital Twin Framework for Melt Pool Prediction and Process Stability in Laser Powder Bed Fusion of Nitinol**.
6. Thomas Gillick, **Sampreet Rangaswamy**, Medad C.C. Monu, Hengfeng Gu, Dermot Brabazon, **Residual Stress Estimation in Laser Powder Bed Fusion of Nitinol Shape Memory Alloy**.
7. Merve Nur Doğu, Meris Meric Ikiz, Gavin Chapman, **Sampreet Rangaswamy**, Merve Yesim Yalcin, Seren Ozer, Kemal Davut, Dermot Brabazon, **Effect of Hatch Distance and Scanning Speed Combinations at Constant Volumetric Energy Density on the Material Properties of IN939 Fabricated by Laser Powder Bed Fusion**, Key Engineering Materials (2026). https://doi.org/10.4028/p-C5YVCs
8. **Sampreet Rangaswamy**, Merve Nur Doğu, Dermot Brabazon, **Analytical Modelling of Track Formation in Laser Powder Bed Fusion of IN939**, DeepTech Connect Proceedings (2026).

9. Srinath S, **Sampreet Rangaswamy**, Shanmugapriya B, Nivetha I, Jasmine Farhana M, Deepan Bharathi Kannan T, **Effects of Shielding Gas in Joining SS304H Sheets through Laser Welding Process**, Welding International, (2026). https://doi.org/10.1080/09507116.2026.2624520
10. P Ajay Amirtharaj, **Sampreet Rangaswamy**, Deepan Bharathi Kannan T, Baksha Arivazhagan**, The Effect of Novel Double Pulse Metal Inert Gas Welding on Microstructure and Mechanical Properties of P91 Steel**, Steel Research International (2025). https://doi.org/10.1002/srin.202500879
11. P Ajay Amirtharaj, Arivarasan J, **Sampreet Rangaswamy**, Deepan Bharathi Kannan T, Kamatchi R, Jeya Suriya Nagarajan, **Mechanical and Microstructural Stability of P91 Steel Walls Fabricated by CMT-Based Wire Arc Additive Manufacturing**, Progress in Additive Manufacturing (2026). https://doi.org/10.1007/s40964-026-01785-7
12. Deepan Bharathi Kannan T, J. Prasanna, Amitesh Anand, Kasinath P R, **Sampreet Rangaswamy**, G. Rajeshkannan, **Single pulse MIG welding of inconel 625 with ER90S-B9 filler: Optimization and Characterization**, Welding International (2026). https://doi.org/10.1080/09507116.2026.2708919
13. Mithunraj S, Pirija N R, Ajay Amirtharaj P, **Sampreet Rangaswamy**, Deepan Bharathi Kannan T, **Comparative Study of TIG, A-TIG, Single-Pulse A-TIG, and Double-Pulse A-TIG Welding of P91 Steel Plates**.
14. Meris Meric Ikiz, Merve Nur Doğu, **Sampreet Rangaswamy**, Muhannad Ahmed Obeidi, Dermot Brabazon, **Optimization of Electropolishing Parameters for Enhancing the Surface Roughness of Powder Bed Fusion-Laser Beam NiTi Using Response Surface Methodology**.
15. Saeid Heidarinassab, Owen Benson, **Sampreet Rangaswamy** Inam Ul Ahad, Dermot Brabazon, **Thermal Conductivity Enhancement of Epoxy Abrasive Composites Using Hybrid SiC–Al_2O_3 Fillers via Experimental, Analytical, and FEA Approaches**, Journal of Materials Research and Technology (2026). https://doi.org/10.1016/j.jmrt.2026.07.262

List of Presentations

1. **Laser Powder Bed Fusion Process of Nitinol**, Advanced Metallic Systems Centre for Doctoral Training 14th Annual Postgraduate Research Conference 2023, University of Sheffield, UK.
2. **Investigation of Melt Pool Characteristics During Single Track Laser Powder Bed Fusion of Nitinol**, International Conference on Advances in Materials and Processing Technologies 2023, Universiti Putra Malaysia, Malaysia.
3. **Estimation of Residual Stress in Additive-Manufactured NiTi Alloy through Beam Mechanics and Finite Element Analysis**, Shape Memory and Superelastic Technologies Conference and Exposition 2024, Cascais, Portugal.
4. **Advancements in Shape Memory Alloys Utilizing 3D Printing: Shaping the Future of Material Engineering**, Pint of Science Festival 2024, Maynooth, Ireland.
5. **Development of Predictive Model for Laser Powder Bed Fusion of Nitinol**, Advanced Metallic Systems Centre for Doctoral Training 15th Annual Postgraduate Research Conference 2024, University of Manchester, UK.
6. **Laser Powder Bed Fusion of Nitinol: A Modelling Perspective**, 4th International Conference on Key Enabling Technologies (KEYTECH) 2024, Dublin City University, Ireland.
7. **Modelling the Laser Powder Bed Fusion of Nitinol**, I-Form Gathering 2024, Athlone, Ireland.

List of Awards

1. **Best Poster Presentation Award**, Advanced Metallic Systems for Doctoral Training Conference 2023.
2. **Best Photo Award for My Life in I-Form**, I-Form Gathering 2024.
3. **Dublin City University Faculty of Engineering and Computing Post Graduate Accommodation Scholarship Award** 2025-2026.

List of Figures

Figure 1.1 Conceptual overview of the research framework and connectivity between the different components of this thesis. 27
Figure 2.1 Literature search and screening process used for this review. 31
Figure 2.2 Crystal structures of martensite (B19') and austenite (B2) phases of NiTi and the effect of stress and temperature changes on phase transformations, adapted from [29]. 33
Figure 2.3 Schematics of the effect of nickel content on (a) NiTi martensite start temperature and (b) NiTi austenite finish temperature, adapted from [31,32]. 34
Figure 2.4 Applications of NiTi SMAs in various fields [40]. 35
Figure 2.5 NiTi self-expanding stent (a) deployment method [44] and (b) working principle showing unclogging and expanding of the arteries [45]. Superelastic staples (c) deployment method [46] and (d) intra-operative radiograph demonstrating the fusion of tarsometatarsal joints [47]. 36
Figure 2.6 (a) Variable geometry chevron of Boeing aircraft [67], (b) CAD model showing the cross-section of the wing along with the aerofoil at 35º inclination using NiTi springs [66]. 39
Figure 2.7 (a) Schematic of an elastocaloric process [54], (b-d) examples of PBF-LB processed lattice structures for elastocaloric studies, adapted from Kordizadeh et al. [59], and (e, f) adapted from Nyabadza et al. [60]. 41
Figure 2.8 A schematic of the PBF-LB process of NiTi [81]. 46
Figure 2.9 (a-b) Schematic illustration of defect evolution via conduction and keyhole melting mode during the PBF-LB processing if NiTi [97]; (c-f) cross-sectional optical micrographs of single-track, showing good and defective tracks (keyholing, lack of fusion, balling) consequent of melt pool regimes in PBF-LB. Reproduced from Xue et al. [98]; and (g) schematic depiction of the geometric feature space governing single-track melt bead morphology in PBF-LB, adapted from the *ANSYS Additive User's Guide* (2020). 47
Figure 2.10 Examples of porosity-type defects; (a) keyhole pores, (b) balling, and (c) lack of fusion defects. Adapted from [102,103]. 50
Figure 2.11 Processing maps showing the relationship between laser power (P) and scan speed (V) for three Ni-rich NiTi powder compositions: (a) Ni50.1Ti49.9, (b) Ni50.8iTi49.2, and (c) Ni51.2Ti48.8. Adapted from [98,122]. The maps delineate composition-specific good (i.e., stable) conduction-mode processing windows from regimes prone to lack-of-fusion at low P/V energy input and keyhole-induced porosity at excessive P/V energy density. The superimposed contour lines indicate the maximum hatch spacing permissible for each parameter combination, beyond which lack-of-fusion (LOF) defects are anticipated. 54
Figure 2.12 Failures caused by residual stress in PBF-LB produced parts, (a) cracks [134] (b) distortion and delamination [135], (c) Distortion caused by residual stress on PBF-LB produced components [136]. 56
Figure 2.13 Scanning strategies: (a) total fill, (d) meander (90° raster scanning) and (g) island. The final appearance of respective surfaces of the produced parts is shown in (b, e, h). The optical micrographs of the total fill and meander are shown respectively in (c, f) [134,141]. 57
Figure 2.14 SEM micrographs of liquation cracks in PBF-LB processed equi-atomic NiTi at (a) volumetric energy density (VED) of 80 J/mm^3 (hatch spacing of 63 μm) (b) VED of 120 J/mm^3 at hatch spacing of 42 μm (c) high-magnification image showing transverse cracks (approximately perpendicular to the fusion boundaries/scan direction) and

longitudinal cracks along fusion boundaries; and (d) high-magnification image highlighting the intergranular nature of the liquation cracks. Reproduced from [115]. ..59
Figure 2.15 Schematic representation of PBF-LB melt pool morphology: (a) regular laser tracks, and (b) remelted laser tracks [152]. ..61
Figure 2.16 Formation of oxide layers in NiTi [163]. ..63
Figure 2.17 Volumetric heat flux distributions with different heat source models (a) conical, (b) linearly decaying, (c) exponentially decaying, and (d) double ellipsoidal; (e) Model for the finite element thermal analysis, and (f) simulated temperature field [195]. ..70
Figure 2.18 A computation flowchart for thermal and microstructural simulation of PBF-LB NiTi [187]. ..76
Figure 2.19 A comparison between predicted and experimental observations of melt pool of NiTi (a) cross-sectional view, (b) top-view, and (c) longitudinal cross-section [200]. ...78
Figure 2.20 (a) PBF-LB printed NiTi (b) The model developed for residual stress evaluation. The contour method results for residual stress distribution for samples heat-treated at temperatures (c) 25, (d) 350, and (e) 450 [139]. ..81
Figure 2.21 Ansys Additive suite microstructure simulation depicting grain orientation and boundary [229]. ..83
Figure 2.22 Beam deflection after removing the supports showing the (a) numerical modelling and (b) a picture of the corresponding experimental measurement result [233]. ..85
Figure 3.1 Measurement of (a) track width from plan view; and (b) melt pool dimensions from transverse cross-sectional view. ..90
Figure 3.2 Top view micrographs of NiTi single tracks for different laser power and scan speed combinations. ..95
Figure 3.3 Cross-sectional view of melt pools formed by NiTi single tracks manufactured with various laser power and scanning speed combinations. ..96
Figure 3.4 Experimentally measured effects of (a) laser power on NiTi melt pool width, (b) scanning speed on NiTi melt pool width, (c) laser power on NiTi melt pool depth, and (d) scanning speed on NiTi melt pool depth. Error bars on the melt pool widths are based on the standard deviation calculated from a minimum of 10 measurements. ..98
Figure 3.5 Effects of (a) laser power on melt pool width, (b) scanning speed on melt pool width, (c) laser power on melt pool depth, and (d) scanning speed on melt pool depth, collated from the Rosenthal Equation (RE), Eagar-Tsai (ET) and Gladush-Smurov (GS) model predictions. ..100
Figure 3.6 Relative error between experimental and predicted results for: (a) melt pool width using the Rosenthal Equation (RE) model and Eagar-Tsai (ET) model at varying laser powers with constant scanning speed, (b) melt pool width using the RE model and ET model at varying scanning speeds with constant laser power, (c) melt pool depth using the RE model and Gladush-Smurov (GS) model at varying laser powers with constant scanning speed and (d) melt pool depth using the RE model and GS model at varying scanning speeds with constant laser power. ..103
Figure 3.7 P-V process maps highlighting regions of LOF (Lack of Fusion) and GC (Good Conduction) from (a), (b) the Rosenthal Equation (RE), (c), (d) Eagar-Tsai (ET) – Gladush-Smurov (GS) models' predictions. The maps are generated for a hatch spacing of 100 μm, a solidified layer thickness of 30 μm, and an actual powder layer thickness of 60 μm. ..105
Figure 4.1 (a) Top-view image of the single-track, (b) cross-section image of the single-track showing melt pool width and depth measurements (Sample 32), (c) measurement of the solidified powder layer thickness from the multi-bead experiments. ..111
Figure 4.2 Top-view of the single-tracks produced along with the parameter combinations. ..112

Figure 4.3 Cross-sectional of the single-tracks produced along with the parameter combinations. 113
Figure 4.4 Micrograph of a multi-bead (a) top-view (b) cross-sectional view. 113
Figure 4.5 CALPHAD (a) Thermal conductivity (b) thermal diffusivity, (c) specific heat (d) density of NiTi with respect to temperature. 115
Figure 4.6 Illustration of the baseplate, the single-bead and their dimensions in the model, adapted from the ANSYS Additive User's Guide (2020). 117
Figure 4.7 Schematic of the workflow of the physics-informed digital twin and decision engine. 122
Figure 4.8 GUI showing melt pool prediction. 123
Figure 4.9 GUI showing process optimization. 123
Figure 4.10 The effect of laser power on (a) maximum temperature, (b) average temperature, the effect of scan speed on (c) maximum temperature, (d) average temperature, and (e) the thermogram visualization of the single-tracks and multi-beads printed along with the corresponding temperature recorded from the pyromertic IR data monitoring. 124
Figure 4.11 (a) Effect of laser power on melt pool width (b) effect of laser power on melt pool depth, (c) effect of scan speed on melt pool width and (d) effect of scan speed on melt pool depth from the experimental measurements along with the corresponding R^2 values. 125
Figure 4.12 Simulation of the melt pool from the model (a) top-view (b) side view. 126
Figure 4.13 Thermal model predicted melt pool dimensions for 30 µm layer thickness - (a) melt pool width, (b) melt pool depth (c) melt pool length for 40 µm beam diameter, (a) melt pool width, (b) melt pool depth (c) melt pool length for 80 µm beam diameter, (a) melt pool width, (b) melt pool depth (c) melt pool length for 120 µm beam diameter. Dashed lines represent the overall trend. 128
Figure 4.14 Thermal model predicted melt pool dimensions for 30 µm layer thickness - (a) melt pool width, (b) melt pool depth (c) melt pool length for 40 µm beam diameter, (a) melt pool width, (b) melt pool depth (c) melt pool length for 80 µm beam diameter, (a) melt pool width, (b) melt pool depth (c) melt pool length for 120 µm beam diameter. Dashed lines represent the overall trend. 129
Figure 4.15 Thermal model predicted melt pool dimensions for 30 µm layer thickness - (a) melt pool width, (b) melt pool depth (c) melt pool length for 40 µm beam diameter, (a) melt pool width, (b) melt pool depth (c) melt pool length for 80 µm beam diameter, (a) melt pool width, (b) melt pool depth (c) melt pool length for 120 µm beam diameter. Dashed lines represent the overall trend. 130
Figure 4.16 Random Forest feature importance plots for melt pool (a) width, (b) depth, (c) length, and partial dependence showing the influence of laser power on melt pool (d) width, (e) depth, (f) length, and scan speed on melt pool melt pool (g) width, (h) depth, ... 134
Figure 5.1 (a) XRD measurement setup and (b) ESPI-hole drilling measurement setup, with the three axes of the sample (x, y, z), where the z-axis represents the build direction. . 142
Figure 5.2 XRD patterns observed for samples (a) S1, (b) S2 and (c) S3. 143
Figure 5.3 (a) Stress response to increasing VED, illustrating trends in normal stresses, shear stress, principal stresses and von-Mises stress, and (b) effect of increasing VED on the FWHM from XRD measurements. 146
Figure 5.4 (a) Thermal profiles showing temperature variations with build height for samples S1, S2, and S3, (b) correlation between VED and the thermal gradient, and (c) correlation between the thermal gradient and residual stress components. 148
Figure 6.1 (a) Dimensions of the printed cantilever beam sample, (b) as-built samples attached to the build substrate. 154

Figure 6.2 The variation of (a) maximum sample temperature and (b) average sample temperature with respect to increasing VED. (c) 2D Thermogram of melt pool thermal signatures of samples during printing of a single layer. 160
Figure 6.3 Surface response plots for the effect of DOE processing parameters on the average sample temperature. 161
Figure 6.4 (a) As-built NiTi cantilever beam deflection following the separation of support structures from build substrate. (b) deflection profile of the top surface of a sample at the maximum beam deflection point, obtained from Keyence 3D microscope. The deflection was measured by measuring the height difference (build (z)-direction) between the fixed portion and the free edge of the beam. The red colouration indicates areas of high deflection, while the transition to blue indicates lower deflection. 162
Figure 6.5 Maximum recorded deflection of each NiTi beam sample correlated with the corresponding number of support rows that are removed at the maximum deflection point. 163
Figure 6.6 Surface response curves for the effect of DOE processing parameters on the maximum beam deflection.....166
Figure 6.7 Maximum beam deflections with respect to VED. The processing parameters of each sample are shown in order of hatch spacing, laser power, scanning speed, as well as maximum sample deflection (δ). 167
Figure 6.8 XRD pattern for sample 2 and sample 5 (highlighting $NiTi_2$). This includes data for the full two-theta range for (a) sample 2 and (b) sample 5, as well as a zoomed-in region of the region where the key phase peaks were identified in sample 2 (c) and sample 5 (d). 168
Figure 6.9 Percentage of identified phases in analysed samples. This includes (a) Martensitic NiTi, (b) Austenitic NiTi, (c) Ni_4Ti_3 precipitates, and (d) total precipitate formation, which is the total combined percentage of Ni_4Ti_3, Ni_3Ti_3O, and $NiTi_2$ (data shown in this figure is for Sample 5 only).....169
Figure 6.10 Influence of austenitic NiTi phase fraction (a) and Ni_4Ti_3 phase fraction (b) on maximum deflection in NiTi cantilever beams.....170
Figure 6.11 Hardness maps of 2.4mm × 2.4mm area of (a) Sample 3, (b) Sample 10, and (c) Sample 12. Relationship of (d) mean, (e) median, and (f) maximum hardness values with respect to increasing retained austenite content recorded from XRD. The error bars in (a) represent 95% confidence intervals. 172
Figure 6.12 Model calibration results: (a) effect of varying Young's modulus between 30 and 50 GPa on predicted deflection and required effective thermomechanical flow stress, σfloweff, relative to the experimentally measured average maximum deflection, $\delta mean$=0.61 mm; and (b) comparison of true versus predicted deflection for all samples at the calibrated Young's modulus of 50 GPa. 175
Figure 6.13 (a) Model-deflection following support structure removal and (b) model-predicted stress distribution within beam sample. 177
Figure 6.14 Correlation heatmap showing relation between various entities of the model and experiments. 180

List of Tables

Table 1.1 Chapter wise publication details and the candidate contributions. 24
Table 2.1 Literature searching criteria used for this review. 32
Table 2.2 Relationship between melting regimes, defect types, key drivers, and mitigation strategies in PBF-LB NiTi. 48
Table 2.3 Comparison of heat source models for thermal modelling of PBF-LB NiTi. 69
Table 3.1 Parameter levels used for the production of the NiTi single tracks. 91
Table 3.2 Thermo-physical properties of NiTi used in the analytical models for calculating the melt pool dimensions. 92
Table 3.3 Comparison between experimental and predicted melt pool widths. 101
Table 3.4 Comparison between experimental and predicted melt pool depths. 102
Table 4.1 Comparison of AMPP thermal FE model predicted melt pool dimensions with experimental measurements and corresponding errors. 127
Table 5.1 Parameter levels used and respective volumetric energy densities. 140
Table 5.2 Stress components in the XY plane for samples S1, S2, and S3. 144
Table 6.1 Box-Behnken design of experiment printing parameters. 154
Table 6.2 CALPHAD temperature-dependent thermo-physical properties of NiTi. 157
Table 6.3 Modelling parameters. 158
Table 6.4 Model calibration results from fixed Young's modulus the and varying flow stress. 176
Table 6.5 Model calibration results from fixed flow stress and varying Young's modulus. 177

List of Abbreviations

A_f	: Austenite Finish Temperature
AM	: Additive Manufacturing
AMPP	: Additive Manufacturing Process Parameters
ANN	: Artificial Neural Network
ANOVA	: Analysis of Variance
A_s	: Austenite Start Temperature
CA	: Cellular Automata
CAD	: Computer-Aided Design
CALPHAD	: Calculation of Phase Diagrams
CNN	: Convolutional Neural Network
DOE	: Design of Experiments
EBSD	: Electron Backscatter Diffraction
EDM	: Exponentially Decaying Model
EDM	: Electrical Discharge Machining
ESPI	: Electronic Speckle Pattern Interference
ET	: Eagar-Tsai
FE	: Finite Element
FEA	: Finite Element Analysis
FEM	: Finite Element Modelling
GC	: Good Conduction

GS : Gladush-Smurov

GUI : Graphical User Interface

HAZ : Heat Affected Zone

HD : Hole Drilling

HIP : Hot Isostatic Pressing

ISM : Inherent Strain Method

KH : Keyhole

LDM : Linearly Decaying Model

LED : Linear Energy Density

LOF : Lack-of-Fusion

LPBF : Laser Powder Bed Fusion

L-PBF : Laser Powder Bed Fusion

MAE : Mean Absolute Error

MC : Monte Carlo

M_f : Martensite Finish Temperature

ML : Machine Learning

M_s : Martensite Start Temperature

Ni : Nickel

NiTi : Nickel-Titanium

Nitinol : Nickel-Titanium Naval Ordnance Laboratory

OL : Overlap

OM : Optical Microscopy

PBF-LB : Powder Bed Fusion-Laser Beam

PF : Phase Field

PM : Powder Metallurgy

RE : Rosenthal Equation

RMSE : Root Mean Square Error

RS : Residual Stress

SE : Super Elasticity

SEM : Scanning Electron Microscopy

SLM : Selective Laser Melting

SLRM : Selective Laser Remelting

SMA : Shape Memory Alloys

SME : Shape Memory Effect

TG : Thermal Gradient

Ti : Titanium

UTS : Ultimate Tensile Strength

VED : Volumetric Energy Density

VIM : Vacuum Induction Melting

VIR : Vacuum Arc Remelting

XRD : X-ray Diffraction

YS : Yield Strength

Abstract

Sampreet Rangaswamy

Multiscale, Multiphysics, and Data-Driven Modelling of the Laser Powder Bed Fusion Processing of Nitinol Shape Memory Alloy

This thesis investigates multi-scale modelling approaches for Powder Bed Fusion using a Laser Beam (PBF-LB) of nickel–titanium (NiTi), a shape memory alloy whose functional performance is highly sensitive to thermal history and composition. The objective was to improve melt pool predictability, process optimisation, and residual stress control through an integrated experimental and modelling framework. Single-track experiments were performed to investigate melt pool behaviour under varying laser power and scanning speed. Three analytical melt pool models were evaluated, with the Eagar–Tsai model predicting melt pool width with a mean absolute error below 10% and the Gladush–Smurov model predicting melt pool depth with errors below 20%. These findings highlight the limitations of single-model approaches and motivate hybrid predictive strategies for NiTi melt pool characterisation. Building on these findings, a high-fidelity thermal finite element model (FEM) incorporating CALPHAD-derived temperature-dependent material properties was developed and validated against experimental measurements, achieving prediction errors below 10% for melt pool dimensions. A multi-output machine learning surrogate model trained on the simulation data achieved coefficients of determination (R^2) greater than 0.95, enabling rapid melt pool prediction across a broad process window. A comprehensive multi-modal residual stress experimental characterisation was performed using hole-drilling, X-ray diffraction (XRD), and in-situ pyrometric measurements. A previously unreported non-monotonic relationship between volumetric energy density (VED) and residual stress was identified, revealing stress saturation and relaxation regimes governed by process parameters. A part scale thermo-mechanical finite element model was subsequently developed to predict residual stress from thermal history, phase evolution, and cantilever beam deflection, predicting von Mises residual stresses in the range of 35–120 MPa. Collectively, this work established an integrated framework linking process parameters, melt pool behaviour, thermal history, phase evolution, and residual stress development, providing practical tools for improving the reliability of additively manufactured NiTi components.

1. Chapter: Introduction

1.1 Background and Motivation

Additive manufacturing (AM) technologies have emerged as transformative manufacturing methods capable of producing complex, high-value components directly from digital models. Among the various AM technologies, Powder Bed Fusion using a Laser Beam (PBF-LB or LPBF or L-PBF) has gained widespread attention for the fabrication of metallic components due to its ability to produce intricate geometries with high dimensional accuracy and minimal material waste [1,2]. In this process, a focused laser selectively melts thin layers of metal powder, enabling the layer-by-layer construction of fully dense components. The flexibility offered by PBF-LB has driven its adoption across several sectors, including aerospace, biomedical engineering, energy, and advanced manufacturing [3,4].

Nickel–titanium (NiTi), commonly referred to as nitinol, is a shape memory alloy that exhibits unique functional properties including the shape memory effect and superelasticity [5]. These properties arise from reversible martensitic phase transformations and make NiTi particularly attractive for applications such as biomedical implants, aerospace actuators, robotics, and energy systems. In the biomedical sector, NiTi is widely used for devices such as stents, orthodontic wires, and minimally invasive surgical tools due to its excellent biocompatibility and fatigue resistance [6,7]. However, conventional manufacturing of NiTi components using casting, machining, or forming processes is often challenging due to the alloy's work hardening behaviour, tool wear issues, and difficulties associated with machining complex geometries [8,9].

The PBF-LB process offers significant potential for overcoming many of these manufacturing challenges by enabling the production of complex NiTi components with tailored geometries and potentially tunable functional properties. Despite these advantages, the additive manufacturing of NiTi remains particularly challenging due to the alloy's strong sensitivity to thermal history and composition. During the PBF-LB process, rapid heating and cooling cycles produce highly localized thermal gradients and complex melt pool dynamics, which strongly influence microstructure formation, phase transformation behaviour, and defect generation [10–12].

Several process-induced defects can arise during PBF-LB fabrication of NiTi, including porosity, cracking, oxidation, residual stresses, and poor surface quality. These defects can significantly affect both the structural integrity and functional performance of the material. In particular, residual stresses generated during rapid solidification can lead to distortion, cracking, and reduced fatigue life. Furthermore, the thermal conditions experienced during processing can alter the local nickel-to-titanium ratio through evaporation or segregation effects, thereby shifting phase transformation temperatures and degrading the alloy's shape memory and superelastic properties [13,14].

Understanding and controlling the complex interactions between process parameters, thermal history, microstructure evolution, and functional behaviour is therefore essential for achieving reliable and high-quality NiTi components using PBF-LB. However, experimental trial-and-error approaches alone are often costly, time-consuming, and limited in their ability to explore the vast parameter space associated with additive manufacturing processes.

As a result, modelling and simulation approaches have become increasingly important tools for predicting process outcomes and guiding parameter optimization. Physics-based modelling techniques, including analytical models and finite element simulations, have been widely used to study melt pool dynamics, heat transfer, and residual stress development. These models provide valuable mechanistic insight into the underlying physical phenomena governing the process. However, such approaches are often computationally expensive and require accurate temperature-dependent material property data, which is limited for NiTi alloys [15–17].

In parallel, data-driven approaches such as machine learning and surrogate modelling have gained increasing attention due to their ability to rapidly predict process outcomes and enable efficient exploration of large parameter spaces. Nevertheless, purely data-driven models often lack physical interpretability and struggle to generalize beyond the training dataset [18,19].

Recently, hybrid approaches that combine physics-based modelling with machine learning techniques have shown considerable promise. Physics-informed machine learning and digital twin frameworks allow the integration of high-fidelity simulations with fast surrogate models, enabling accurate and computationally efficient prediction of process behaviour [20–23]. These approaches offer a pathway toward intelligent additive manufacturing systems capable of real-time process monitoring, optimization, and control.

A digital twin can be broadly defined as a virtual representation of a physical system that is continuously updated using data from experiments, sensors, simulations, or operational processes to replicate the behaviour of its physical counterpart throughout its lifecycle. Unlike traditional simulation models, which are typically used as standalone predictive tools, digital

twins integrate multiple sources of information and can support bidirectional communication between the physical and virtual environments. This enables not only prediction of system behaviour but also process optimisation, decision support, and, ultimately, real-time control [22,24].

The implementation of digital twins in PBF-LB generally involves a combination of process modelling, sensing, data analytics, and decision-making algorithms. Physics-based models, such as thermal or thermo-mechanical finite element simulations, provide mechanistic insight into the process, while machine learning and surrogate models enable rapid prediction across large process parameter spaces. The integration of these approaches allows digital twins to balance computational efficiency with physical fidelity [25,26]. Recent developments have also demonstrated the potential for incorporating in-situ monitoring data into digital twin frameworks, enabling adaptive process control and real-time correction of process deviations [23,27].

For NiTi manufactured via PBF-LB, digital twin technologies are particularly attractive because of the strong coupling between process parameters, thermal history, phase transformation behaviour, and final component performance. Small variations in thermal conditions can significantly alter microstructure, phase constitution, residual stress development, and transformation temperatures. Consequently, a digital twin capable of predicting and controlling these interconnected phenomena offers a pathway towards more reliable production of NiTi components and supports the broader vision of intelligent additive manufacturing. The development and application of such a framework therefore forms a central theme of this thesis.

Despite recent progress in modelling additive manufacturing processes, several critical knowledge gaps remain for NiTi processed by PBF-LB. In particular, improved understanding is required in the following areas:

- Prediction of melt pool geometry and stability under varying process parameters
- Quantification of thermal history and its influence on phase transformation behaviour
- Understanding the mechanisms governing residual stress formation and distortion
- Integration of modelling approaches to support efficient process optimization

Addressing these challenges is essential for enabling reliable production of high-performance NiTi components and for unlocking the full potential of additive manufacturing technologies in advanced engineering applications.

1.2 Thesis Aim and Objectives

The overall aim of this thesis is to improve the predictability and process control of nickel–titanium components fabricated using PBF-LB by developing an integrated experimental and modelling framework that links process parameters, melt pool behaviour, thermal history, and residual stress development.

To achieve this aim, the research focuses on both experimental investigations and physics-informed modelling approaches for understanding key process phenomena in PBF-LB NiTi.

The specific objectives of this thesis are:

- To investigate the influence of PBF-LB process parameters on melt pool geometry in NiTi through single-track experimental studies and evaluate the predictive capability of commonly used analytical melt pool models for NiTi and identify their limitations when applied to this material system.
- To develop a physics-informed digital twin framework combining high-fidelity thermal finite element modelling and machine learning-based surrogate models for melt pool prediction and process optimization.
- To experimentally characterize residual stress distributions in PBF-LB manufactured NiTi using multi-modal measurement techniques and correlate these stresses with process conditions and thermal history.
- To develop a thermo-mechanical modelling framework for predicting residual stress and distortion in PBF-LB fabricated NiTi components.

Through these objectives, the thesis aims to advance the understanding of process–structure–property relationships in additively manufactured NiTi and provide practical tools for improving process optimization and component reliability.

1.3 Thesis Structure

This thesis is structured into seven chapters, each addressing a specific aspect of modelling and characterization of NiTi fabricated using PBF-LB.

The thesis is presented as a compilation of published research papers and submitted manuscripts containing original contributions. The contribution of the candidate to the publications are as following **Table 1.1**:

Table 1.1 Chapter wise publication details and the candidate contributions.

Chapter	Publication Title	Status	Candidate contribution
2	**Review of the Laser Powder Bed Fusion of Nitinol - Defect Formation and Prediction**	Published, Materials Today Advances, 2026	First author, Corresponding author, Conceptualization, Visualization, Methodology, Investigation, Writing – original draft, Formal analysis, Writing – review & editing.
3	**Investigating Melt Pool Dimensions in Laser Powder Bed Fusion of Nitinol - An Analytical Approach**	Published, Advanced Engineering Materials, 2024	First author, Corresponding author, Conceptualization, Methodology, Software, Data curation, Writing – original draft, Visualization, Investigation, Formal analysis, Writing – review & editing.
4	**Physics-Guided Digital Twin Framework for Melt Pool Prediction and Process Stability in Laser Powder Bed Fusion of Nitinol**	Review Completed, Materials, 2026	First author, Corresponding author, Conceptualization, Methodology, Software, Data curation, Writing –

			original draft, Visualization, Investigation, Formal analysis, Writing – review & editing.
5	**Evaluating Residual Stress in Additively Manufactured Nitinol Shape Memory Alloy**	Published, Npj Advanced Manufacturing, 2025	First author, Corresponding author, Conceptualization, Methodology, Data curation, Writing – original draft, Visualization, Investigation, Formal analysis, Writing – review & editing.
6	**Residual Stress Estimation in Laser Powder Bed Fusion of Nickel-Titanium Shape Memory Alloy**	Review Completed, Journal of Materials Research and Technology, 2026	First author, Conceptualization, Methodology, Software, Writing – original draft, Visualization, Investigation, Formal analysis, Writing – review & editing.

Chapter 1 introduces the background and motivation for the research, outlines the key challenges associated with PBF-LB of NiTi, and defines the aims and objectives of the thesis. **Chapter 2** presents a comprehensive literature review of the PBF-LB process of NiTi and current modelling approaches used to study PBF-LB processes. The chapter examines existing work on melt pool modelling, thermal simulations, microstructure prediction, defect formation, residual stress development, and emerging machine learning techniques used for process optimization.

Chapter 3 investigates the predictive capability of analytical melt pool models for NiTi fabricated using PBF-LB. Experimental single-track studies are performed to quantify the effects of laser power and scanning speed on melt pool geometry. The performance of commonly used analytical models, including the Rosenthal, Eagar–Tsai, and Gladush–Smurov models, is evaluated and compared with experimental results.

Chapter 4 presents the development of a physics-informed digital twin framework for melt pool prediction and process optimization in PBF-LB NiTi. A high-fidelity thermal finite element model calibrated using experimental measurements and CALPHAD-derived material properties is used to generate simulation data. A machine learning-based surrogate model is then trained to rapidly predict melt pool geometry and identify stable processing regimes.

Chapter 5 presents a comprehensive experimental investigation of residual stress in PBF-LB produced NiTi using a multi-modal characterization approach combining Electronic Speckle Pattern Interferometry–Hole Drilling and X-ray Diffraction. The results are correlated with in-situ thermal measurements and process parameters to provide new insights into residual stress evolution.

Chapter 6 focuses on residual stress estimation in PBF-LB fabricated NiTi components. A thermo-mechanical finite element modelling framework coupled with CALPHAD-based material data is developed to estimate residual stresses and distortion based on experimentally measured cantilever beam deflections.

Chapter 7 summarizes the key findings of the thesis and outlines recommendations for future research directions aimed at improving predictive modelling and process control in additive manufacturing of NiTi.

1.4 Research Workflow and Thesis Framework

The overall structure of the research conducted in this thesis is illustrated in **Figure 1.1**. The work progresses from fundamental understanding of melt pool physics to the development of predictive modelling tools and experimental validation of residual stress behaviour.

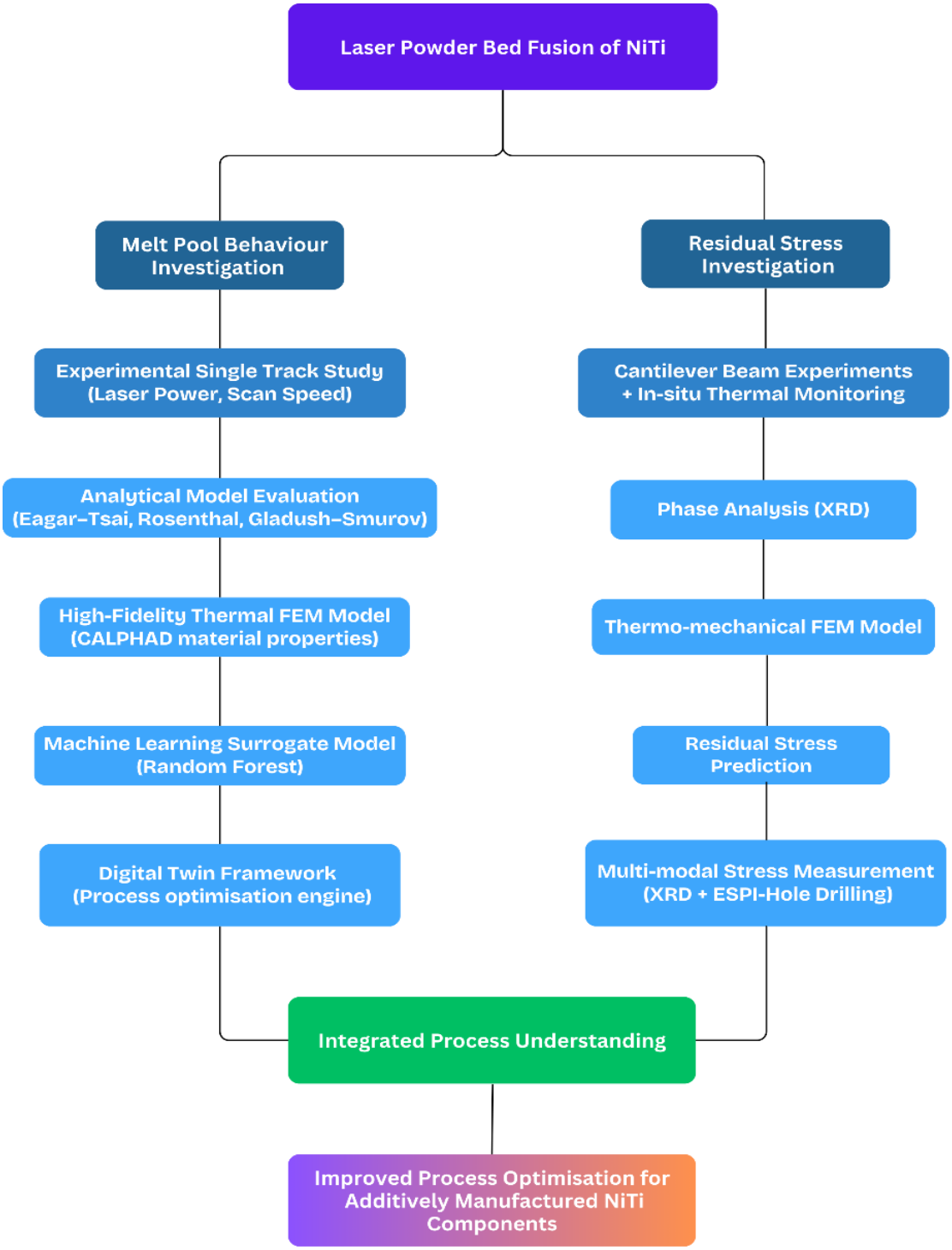


Figure 1.1 Conceptual overview of the research framework and connectivity between the different components of this thesis.

The workflow highlights how experimental investigation, physics-based modelling, and data-driven methods are integrated to develop improved predictive capability for PBF-LB NiTi processing. Melt pool modelling provides the foundation for understanding thermal behaviour, while residual stress modelling and experimental validation extend the analysis to component-level performance.

1.5 Scope and Limitations of the Research

The research presented in this thesis focuses on improving the understanding and predictive capability of PBF-LB processing of NiTi alloys through an integrated modelling and experimental approach. The scope of the work is centred on investigating key process phenomena that influence part quality and structural integrity, specifically melt pool behaviour and residual stress development. While the research provides important insights into melt pool behaviour and residual stress evolution in PBF-LB NiTi, several limitations should be acknowledged.

First, the melt pool investigations were primarily conducted using single-track experiments rather than full multilayer builds. Although single-track studies provide valuable fundamental understanding, additional complexities may arise during multi-layer fabrication due to heat accumulation and evolving thermal boundary conditions. Second, the digital twin framework developed in this thesis focuses on predicting melt pool geometry and identifying stable process regimes. Although the framework is designed to be extensible, predictions of additional process outcomes such as porosity distribution, surface roughness, and microstructural evolution were not fully implemented within the scope of this work. Third, although multi-modal experimental techniques were employed to characterize residual stress distributions, practical constraints associated with the time-intensive nature of these measurements limited the size of the experimental dataset. Expanding the dataset and exploring a wider parameter space would further improve statistical confidence in the observed trends. Finally, the thermo-mechanical modelling framework estimates effective residual stresses using calibrated material properties due to the limited availability of reliable temperature-dependent mechanical property data for additively manufactured NiTi. Future work incorporating more comprehensive material property datasets may further improve predictive accuracy.

Despite these limitations, the research presented in this thesis provides significant advances in the predictive modelling and experimental understanding of PBF-LB NiTi processing. The methodologies developed form a strong foundation for future work aimed at achieving fully predictive, intelligent additive manufacturing systems for shape memory alloys.

2. Chapter: Review of the Laser Powder Bed Fusion of Nitinol - Defect Formation and Prediction

---

Publication Status: Published

Sampreet Rangaswamy, Camille Rubio, Merve Nur Doğu, Medad C.C. Monu, Dermot Brabazon, **Review of the Laser Powder Bed Fusion of Nitinol: Defect Formation and Prediction**, Materials Today Advances (2026).

https://doi.org/10.1016/j.mtadv.2026.100771

Abstract

This review synthesizes current modelling efforts aimed at predicting key process–structure–property relationships in PBF-LB NiTi, including melt pool geometry and stability, thermal history, microstructural evolution, defect formation, residual stress development, and functional outcomes such as phase transformation temperatures. Both physics-based and data-driven modelling approaches are examined. Thermal and melt pool simulations, multi-physics finite element models, and microstructural prediction frameworks provide mechanistic insight into process–material interactions, while machine learning, surrogate, and hybrid models enable rapid parameter optimization and defect prediction. A central NiTi-specific insight emerging from the literature is that accurate prediction of local thermal history and composition evolution is critical for controlling phase transformation behaviour and thus functional performance. Physics-informed machine learning frameworks are highlighted as promising strategies to combine mechanistic fidelity with computational efficiency, supporting more reliable process optimization and functional property control in PBF-LB NiTi.

2.1 Literature Search and Selection Methodology

To ensure a comprehensive and representative overview of modelling, defect formation, and prediction strategies for NiTi fabricated via laser powder bed fusion (PBF-LB), a structured literature survey was conducted. Peer-reviewed publications were identified primarily through the Scopus, Web of Science, and Google Scholar databases. The search focused on articles published between 2000 and 2025, corresponding to the period in which research on additive manufacturing of NiTi and modelling of powder bed fusion processes has significantly expanded.

Search queries were constructed using combinations of relevant keywords, including “NiTi”, “Nitinol”, “shape memory alloy”, “laser powder bed fusion”, “LPBF”, “selective laser melting”, “microstructure modelling”, “process simulation”, “defect prediction”, “residual stress modelling”, and “machine learning in additive manufacturing”. Boolean operators were used to refine the search (e.g., “NiTi AND LPBF AND modelling”).

The initial database search produced a large set of candidate publications, which were screened based on title and abstract relevance. Studies focusing on PBF-LB processing of NiTi, modelling of process–structure–property relationships, defect formation mechanisms, and predictive computational approaches were retained. Publications unrelated to additive manufacturing, or focusing exclusively on conventional NiTi processing routes without relevance to modelling or LPBF, were excluded unless they provided fundamental modelling frameworks transferable to additive manufacturing. Additional relevant sources were identified through backward citation tracking of key review and experimental papers.

The overall literature screening and selection process is summarized in **Figure 2.1**, while **Table 2.1** provides a concise overview of the literature search strategy and inclusion criteria applied in this review.

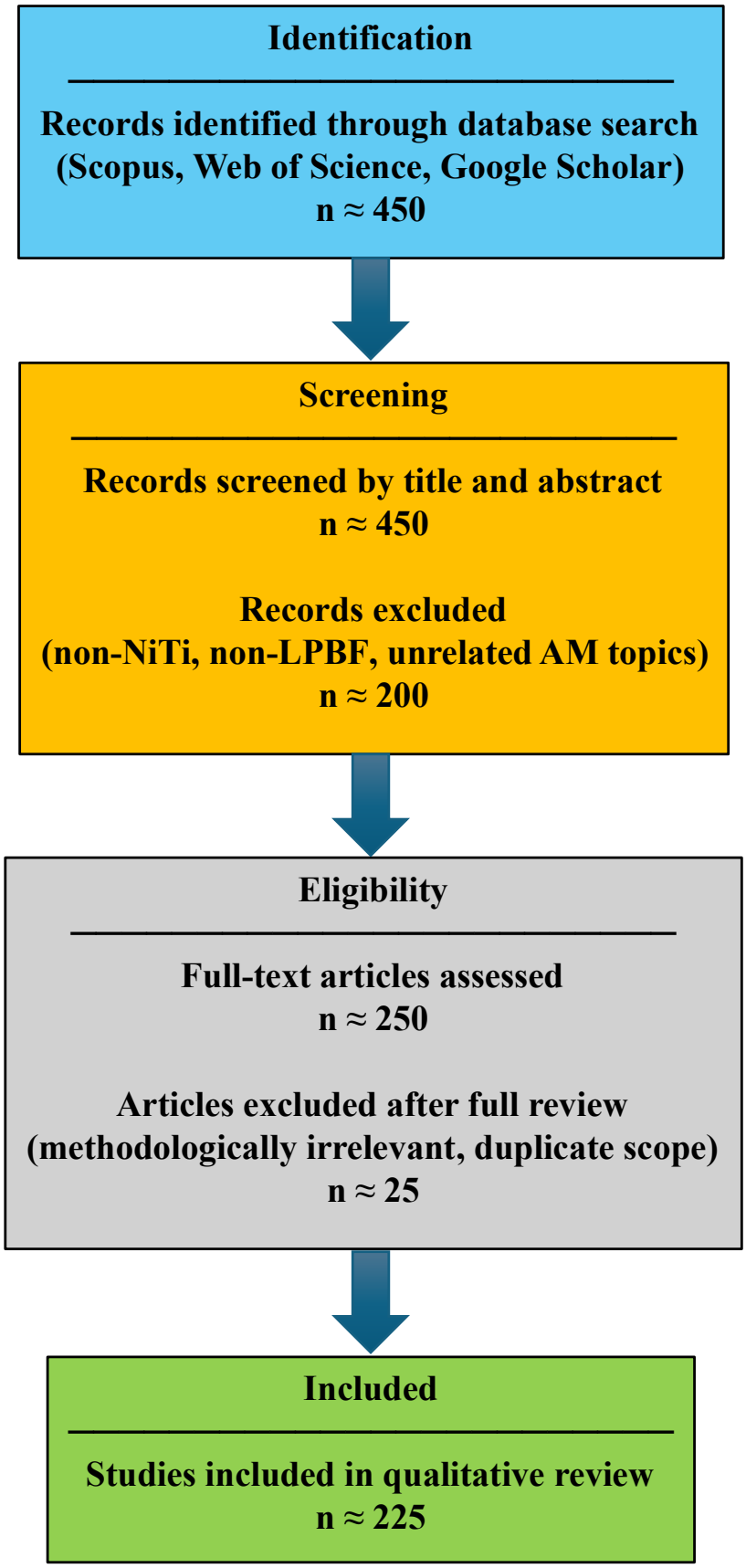


Figure 2.1 Literature search and screening process used for this review.

Table 2.1 Literature searching criteria used for this review.

LITERATURE SEARCHING CRITERIA	RELATED SPECIFICATION
LANGUAGE	English
PUBLICATION PERIOD	2000–2025 (primary focus on 2010–2025 PBF-LB-related studies)
DATE OF SEARCH	January 2026
BIBLIOGRAPHY SOURCES	Scopus, Web of Science, Google Scholar. Major publishers included Elsevier, Springer Nature, Wiley, Taylor & Francis, MDPI, IOP Publishing, Nature, and ASM International.
SEARCH KEYWORDS	"NiTi", "Nitinol", "shape memory alloy", "laser powder bed fusion", "PBF-LB", "LPBF", "selective laser melting", "additive manufacturing", "microstructure modelling", "defect prediction", "residual stress modelling", "machine learning in additive manufacturing".
INCLUSION CRITERIA	Studies focusing on NiTi or shape memory alloys processed by PBF-LB or related additive manufacturing methods; modelling approaches (thermal, microstructural, residual stress, or defect prediction); experimental validation of modelling results; and machine learning or data-driven predictive approaches relevant to PBF-LB processes.
EXCLUSION CRITERIA	Articles unrelated to additive manufacturing or not addressing modelling/prediction aspects; non-English publications; studies lacking full text access; and publications after January 2026.
PUBLICATION TYPE	Peer-reviewed journal articles, review papers, conference proceedings, and selected book chapters relevant to additive manufacturing of shape memory alloys.
SCOPE	Additive manufacturing of NiTi shape memory alloys, PBF-LB processing parameters, defect formation mechanisms, modelling of thermal and microstructural evolution, residual stress prediction, and emerging machine learning approaches for process optimization and defect prediction.

2.2 Functional properties of NiTi

NiTi shape memory alloys exhibit functional behaviour governed by reversible martensitic phase transformation between the high-temperature cubic B2 austenite phase and the low-temperature monoclinic B19′ martensite phase. This transformation can be thermally or stress induced and is characterized by four transformation temperatures: martensite start (Ms), martensite finish (Mf), austenite start (As), and austenite finish (Af), shown in **Figure 2.2**. These temperatures define the operational windows for shape memory and superelastic behaviour, and are highly sensitive to composition, thermal history, and microstructure [13,28].

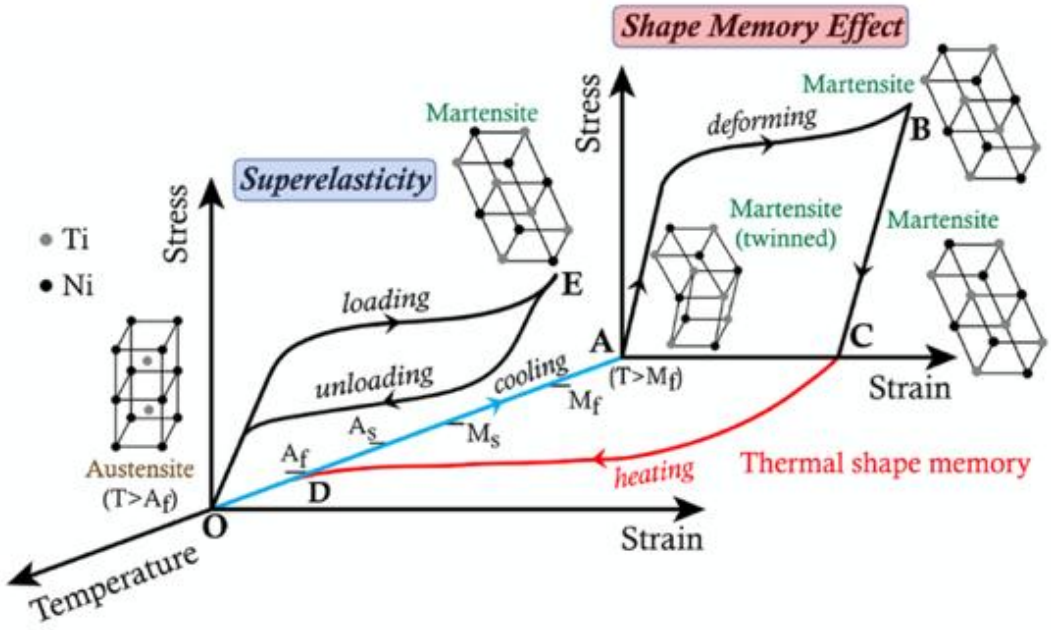


Figure 2.2 Crystal structures of martensite (B19') and austenite (B2) phases of NiTi and the effect of stress and temperature changes on phase transformations, adapted from [29].

For PBF-LB NiTi, this sensitivity is particularly important because small variations in processing conditions can alter local composition and cooling rates, leading to spatial variability in transformation temperatures and functional response. Nickel content plays a dominant role [30]; even minor Ni loss during laser processing can significantly increase transformation temperatures and shift the balance between superelastic and shape memory behaviour as shown in **Figure 2.3** (a-b).

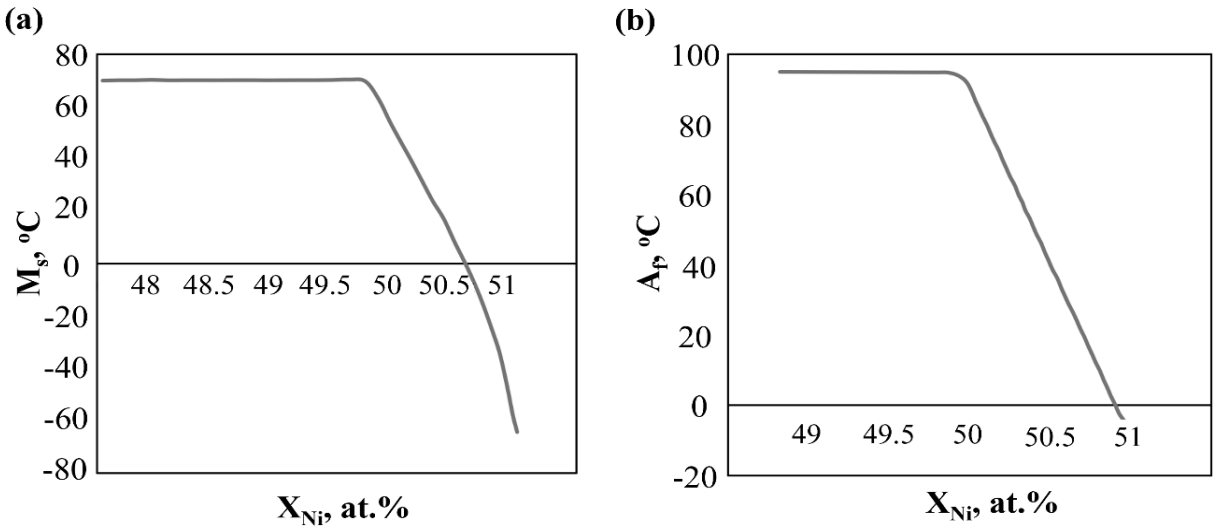


Figure 2.3 Schematics of the effect of nickel content on (a) NiTi martensite start temperature and (b) NiTi austenite finish temperature, adapted from [31,32].

Microstructural features generated during PBF-LB, including grain size, texture, porosity, and dislocation density, further influence transformation kinetics and functional stability [33,34]. Fine microstructures and heterogeneous phase distributions can promote localized transformation behaviour, while high defect densities and residual stresses may increase hysteresis and degrade cyclic performance [35–38]. Consequently, predictive modelling of thermal history, composition evolution, and defect formation is essential for understanding and controlling functional performance in additively manufactured NiTi.

2.3 Applications of NiTi

The exceptional functional properties of NiTi have driven its adoption in high-performance fields, including aerospace, biomedical engineering, and a range of general engineering applications. Its excellent biocompatibility and corrosion resistance make it particularly suitable for long-term implantation in the human body, while its low toxicity and favourable osseointegration enable safe use in medical devices without eliciting adverse biological responses. Compared with commonly used biomedical alloys such as nickel–chromium, cobalt–chromium, and α–β titanium alloys, NiTi exhibits superior mechanical performance, including enhanced durability, malleability, and flexibility [39]. However, fully exploiting these properties often exceeds the capabilities of conventional manufacturing routes such as machining and casting. Advanced biomedical devices require complex, miniaturized, and patient-specific geometries; aerospace applications demand lightweight and functionally

integrated structures; and emerging technologies, such as elastocaloric cooling, benefit from high–surface-area architectures. **Figure 2.4** presents an overview of a number of these applications of NiTi. These requirements present significant manufacturing challenges. In this context, PBF-LB has emerged as a transformative technology, enabling the direct fabrication of intricate and customized NiTi components with tailored microstructures. This section reviews the principal application areas of NiTi, emphasizing the design requirements and manufacturing limitations that motivate the adoption of PBF-LB and impose stringent quality demands on the process.

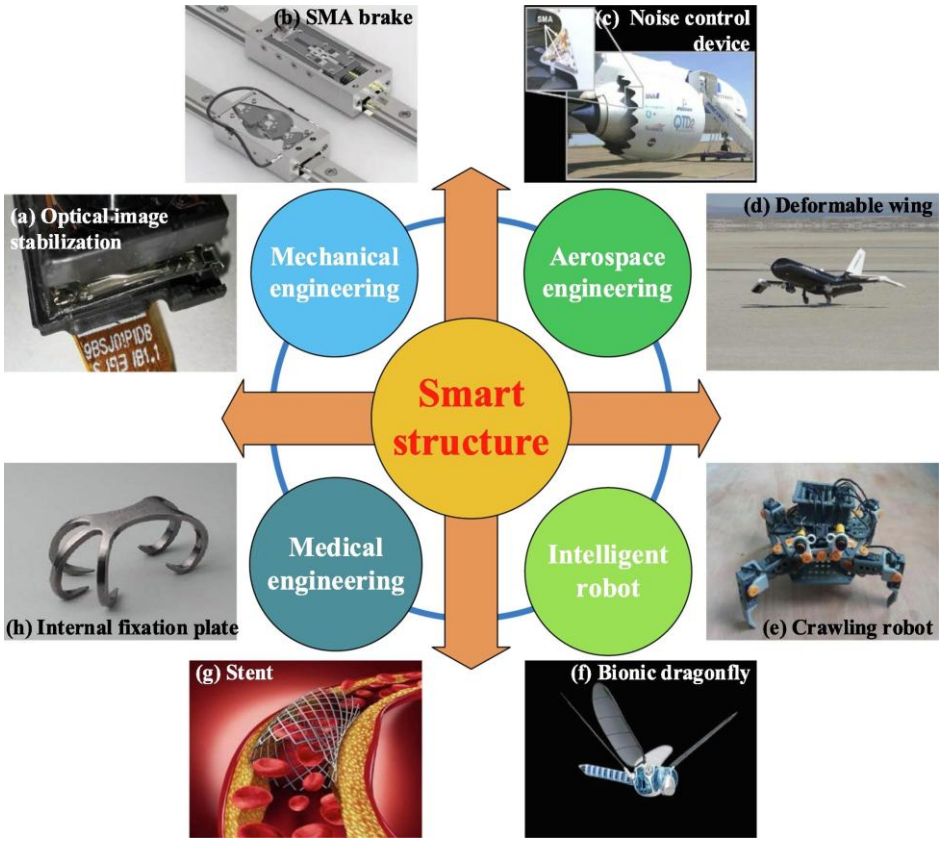


Figure 2.4 Applications of NiTi SMAs in various fields [40].

2.3.1 Biomedical Applications: From Shape Memory to Superelastic Dominance

NiTi's widespread use as a biomaterial is rooted in its outstanding biocompatibility, corrosion resistance, and low toxicity. Its two hallmark functional properties; the shape memory effect (SME) and superelasticity (SE) as discussed earlier, have been exploited, driving an evolution in medical device design. Early biomedical implants primarily relied on the one-way SME, in which a device plastically deformed in the martensitic state recovers a predefined shape upon

heating to body temperature as it transforms to austenite. This mechanism underpinned first-generation devices such as the Simon vena cava filter, used to prevent pulmonary embolism in patients unable to tolerate anticoagulants, and early self-expanding stents designed to maintain arterial patency [41,42].

Contemporary implant designs increasingly favour superelasticity, wherein the alloy is fully austenitic at body temperature and undergoes stress-induced martensitic transformation to accommodate large, fully reversible strains. A representative example is the deployment of superelastic NiTi stents, which are radially compressed into a catheter for minimally invasive delivery to the target site. Upon release, the stent recovers its original geometry through superelastic unloading, exerting a sustained outward force to reopen obstructed blood vessels, as illustrated in **Figure 2.5**. This transition from SME-dominated to SE-dominated designs offers substantial advantages, including simplified deployment, improved reliability, and continuous physiological loading. Moreover, superelastic NiTi implants can flex with natural body movements without accumulating permanent deformation, thereby maintaining long-term functional and structural integrity [43,44].

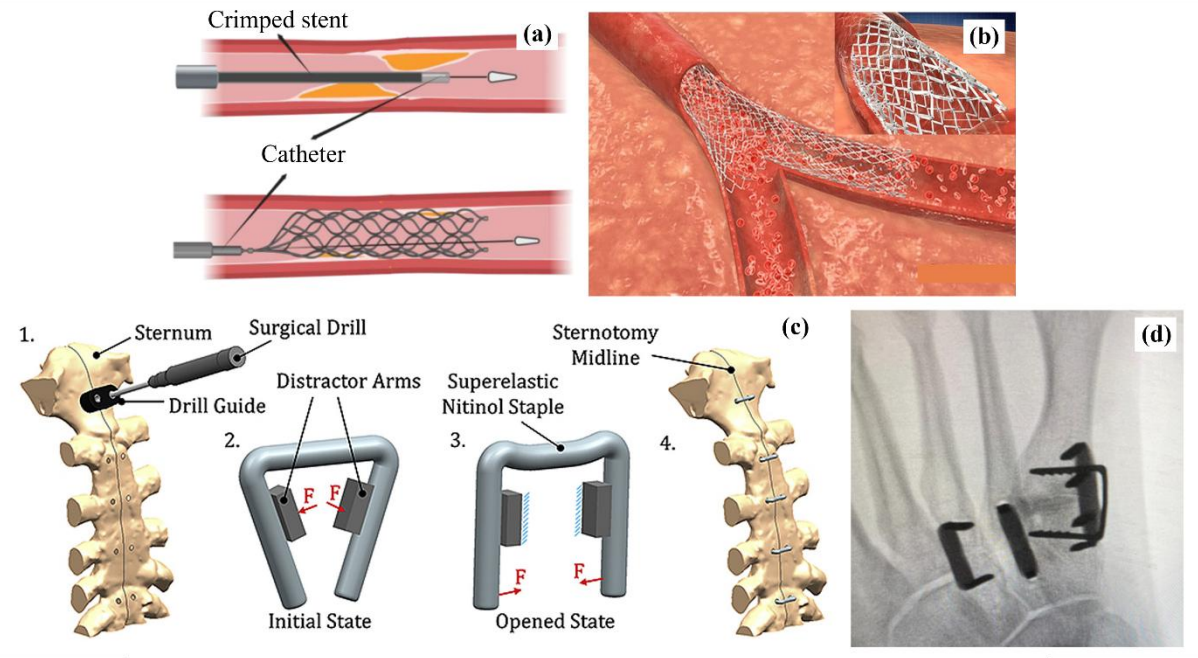


Figure 2.5 NiTi self-expanding stent (a) deployment method [44] and (b) working principle showing unclogging and expanding of the arteries [45]. Superelastic staples (c) deployment method [46] and (d) intra-operative radiograph demonstrating the fusion of tarsometatarsal joints [47].

Beyond vascular applications, NiTi is widely used in orthopaedic implants. Devices such as compression staples (**Figure 2.5**) are employed to stabilise fractured bones. Shape memory

NiTi staples are implanted in an open configuration and subsequently close to apply compressive forces across the fracture site upon heating, either by body temperature or an external heat source [48]. However, pseudoelastic (superelastic) staples are now generally preferred. Shape memory staples activated by external heating require additional equipment, while body-temperature-activated designs exhibit relatively low stiffness. In contrast, superelastic staples are fully austenitic at room temperature and require no activation; they are inserted in an expanded state and generate sustained compressive forces upon release through superelastic recovery [47,49]. In parallel, NiTi is increasingly favoured over stainless steel in magnetic resonance imaging (MRI) environments due to its lower magnetic susceptibility, which reduces imaging artefacts [50]. It is also widely used in orthodontics for dental wires and braces, where its superelastic response enables continuous, gentle force delivery for tooth alignment. Additional biomedical applications include artificial organs, birth control devices, and treatments for erectile dysfunction [51–53].

Consequently, additive manufacturing, particularly PBF-LB, has emerged as a key enabling technology for NiTi biomedical devices by enabling the fabrication of patient-specific implants, porous architectures that promote osseointegration, and geometrically complex devices that cannot be produced using conventional manufacturing routes. However, realizing these benefits requires precise control of PBF-LB process parameters and defect formation, as porosity, compositional variation, and surface roughness can significantly influence the transformation behaviour and long-term reliability of NiTi implants.

2.3.2 Aerospace, Automotive, and High-Performance Engineering

NiTi's unique functional properties make it particularly attractive for demanding aerospace, automotive, and high-performance engineering applications, where components are subjected to dynamic loading, stringent weight constraints, and limited installation space. NiTi-based shape memory alloys (SMAs) are used in a wide range of functions, including actuators, manipulators, vibration dampers, release mechanisms, and structural connectors. Compared with conventional electromagnetic actuators, SMA-based systems offer several advantages, such as reduced weight and volume, mechanical simplicity, and lower system-level cost [64]. A well-established example in the automotive sector is the SMA-driven anti-glare rear-view mirror (EAGLE mirror), which adapts to changing light conditions [65]. In aerospace systems, NiTi actuators have been implemented in landing gear components, door mechanisms, and

adaptive structures, while SMA-based sensors are employed to monitor temperature and pressure variations during flight.

One of the most prominent aerospace demonstrations of SMA technology is Boeing's Variable Geometry Chevron, shown in **Figure 2.6** (a). This system was developed to reduce jet engine noise without compromising performance at cruise altitude. SMA beams embedded within the chevrons along the exhaust nozzle trailing edge were thermally activated to induce controlled bending, resulting in effective noise reduction during take-off and landing [66,67]. The success of this application validated the reliability of SMAs in harsh aerospaace environments and stimulated further research into adaptive and morphing structures. In particular, the use of NiTi in aircraft wing morphing has attracted significant attention due to its potential to reduce power consumption, improve aerodynamic efficiency, and increase flight speed. Notable research initiatives include the Smart Aircraft and Marine Propulsion System Demonstration (SAMPSON) and DARPA's Smart Wing Program [67,68].

Airfoil flaps represent a critical element of wing morphing systems and have traditionally relied on hydraulic or pneumatic actuation, which is complex, heavy, and maintenance intensive. NiTi-based actuators provide a promising alternative, enabling lighter, simpler, and more reliable mechanisms with precise control over flap motion. Chellangi et al. [66] demonstrated the use of thermally actuated NiTi springs for aerofoil control, as illustrated in **Figure 2.6** (b). By connecting multiple springs with different transformation temperatures in series, a progressive and finely controlled change in aerofoil angle was achieved. This approach highlights the versatility of NiTi actuators across aerospace and automotive domains.

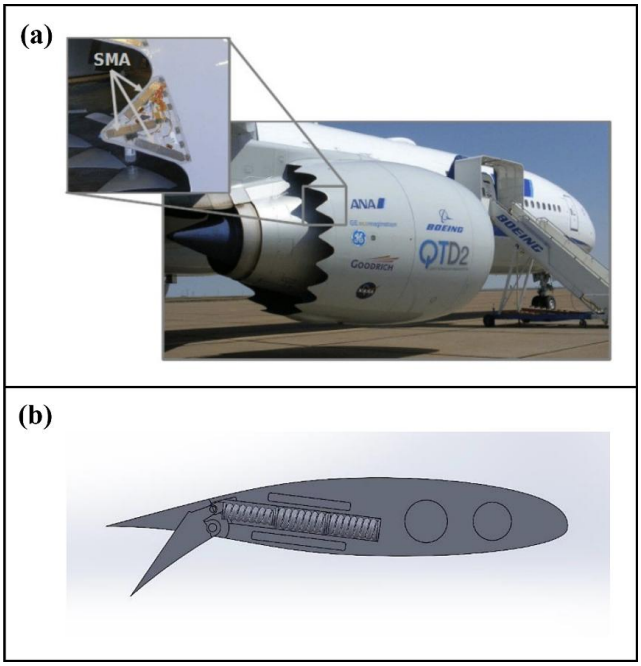


Figure 2.6 (a) Variable geometry chevron of Boeing aircraft [67], (b) CAD model showing the cross-section of the wing along with the aerofoil at 35º inclination using NiTi springs [66].

In this context, PBF-LB processing presents a promising manufacturing route for NiTi components in aerospace and automotive systems, enabling the fabrication of lightweight, monolithic structures with integrated actuation or adaptive functionality. The ability to produce topologically optimized lattices and compliant mechanisms offers significant advantages for morphing structures and compact actuation systems, although achieving reliable performance requires careful control of PBF-LB-induced defects and thermal history.

2.3.3 Elastocaloric Cooling

Beyond mechanical actuation, NiTi exhibits a pronounced elastocaloric effect arising from its stress-induced thermoelastic martensitic transformation (**Figure 2.7** a) [54]. At the initial temperature T_0, the unstressed alloy is fully austenitic. Under adiabatic loading beyond the critical transformation stress, martensite forms and releases latent heat, resulting in an adiabatic temperature increase ΔT_{ad} (**State I**). Maintaining the applied stress allows heat to be rejected to the surroundings, returning the material to T_0 (**State II**). Subsequent adiabatic unloading destabilizes martensite and drives the reverse transformation to austenite, absorbing latent heat and producing a temperature decrease of ΔT_{ad} (**State III**). Finally, heat absorption from the environment restores the alloy to T_0, completing the cooling cycle (**State IV**) [55,56]. This

reversible solid-state process positions NiTi as a leading candidate for elastocaloric cooling systems, offering a potentially more energy-efficient and environmentally sustainable alternative to vapor-compression refrigeration technologies [56,57].

The cooling performance of elastocaloric NiTi is governed primarily by two factors: (i) fatigue life, which is strongly limited by defect populations that act as crack initiation sites under cyclic superelastic loading [58], and (ii) heat-transfer efficiency, which scales with the effective surface area available for thermal exchange [59]. PBF-LB processing directly addresses the latter by enabling the fabrication of complex, high-surface-area geometries including porous lattices, finned architectures, and integrated micro-channel heat exchangers; that maximize surface-to-volume ratio and promote rapid heat transfer (**Figure 2.7** b-f). Reported elastocaloric responses in PBF-LB NiTi lattice structures include ΔT_{ad} = 5.31°C at 10 kN for a $Ni_{50.8}Ti_{49.2}$ diamond-cell lattice (surpassing gyroid and primitive designs) [59], ΔT_{ad} = 11.2°C at 40 kN for an as-built Ni_{51}Ti lattice (outperforming a bulk NiTi counterpart that required 80 kN to reach 12.9°C) [60], and ΔT_{ad} = 23.2°C for $Ni_{51.4}$Ti aged at 723 K for 5 h [61].

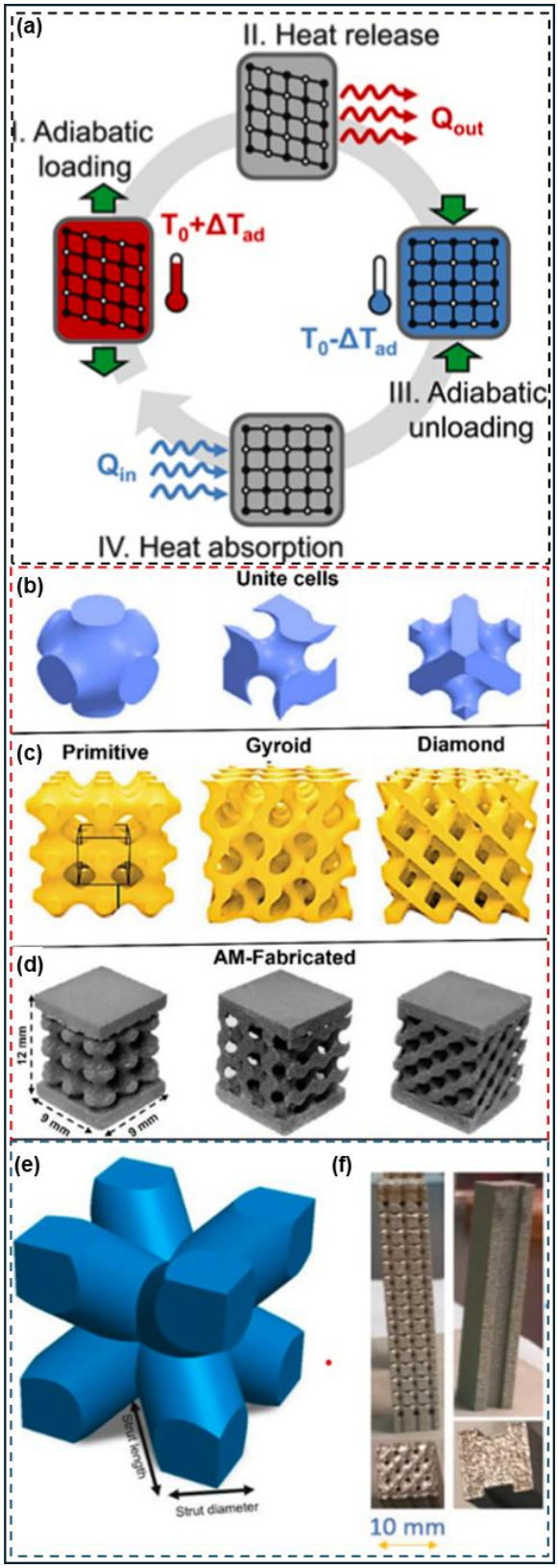


Figure 2.7 (a) Schematic of an elastocaloric process [54], (b-d) examples of PBF-LB processed lattice structures for elastocaloric studies, adapted from Kordizadeh et al. [59], and (e, f) adapted from Nyabadza et al. [60].

Recent frontier research has further advanced the understanding of thermoelastic effects in NiTi alloys and their 4D printing applications, particularly in overcoming traditional performance trade-offs. Additive manufacturing enables precise control of microstructure and transformation behaviour, allowing the thermoelastic response of NiTi to be engineered at multiple scales. For example, recent studies have demonstrated that encoded microstructures in 4D-printed NiTi alloys can overcome the conventional trade-off between cooling capacity and energy efficiency in elastocaloric refrigeration, highlighting the potential of architected materials for advanced thermal management systems. In addition, laser beam manipulation in PBF-LB processing has been shown to enable fine tailoring of elastocaloric properties by controlling local thermal histories and microstructural evolution, offering new strategies for optimizing functional performance in NiTi-based smart materials [62,63].

However, elastocaloric cooling also imposes some of the most stringent durability requirements of any NiTi application, demanding millions of reversible superelastic cycles without functional degradation. Here, a persistent challenge arises: PBF-LB commonly introduces process-induced defects such as sub-surface porosity, micro-cracks, and surface asperities, each of which can serve as preferential stress concentrators that severely compromise fatigue resistance. As a result, the feasibility of PBF-LB NiTi for elastocaloric systems hinges on advancing defect prediction, mitigation, and process-stability strategies to reliably satisfy the required service lifetimes.

Consequently, while PBF-LB enables the fabrication of complex heat-transfer architectures that significantly enhance elastocaloric performance, the process simultaneously introduces defects such as porosity and surface irregularities that can degrade fatigue life under cyclic superelastic loading. Addressing these challenges requires predictive modelling and defect mitigation strategies to ensure reliable long-term performance of PBF-LB fabricated NiTi cooling systems.

2.3.4 Industrial and Consumer Applications

In heating and ventilation, SMAs are employed in actuators and valves for precise control of airflow and temperature. In automation and control, SMA actuators provide compact and reliable solutions for various systems. The corrosion resistance and mechanical properties of NiTi make it ideal for use in harsh chemical processing environments. Safety devices, such as fire sprinkler systems, utilize SMAs to operate based on temperature changes, enhancing security. In the field of electronics, particularly microelectromechanical systems (MEMS),

NiTi's properties are harnessed for precise movements and controls [69–71]. Additionally, SMAs are utilized in household appliances, robotic systems, mobile antennas, eyewear, and smartwatches due to their reliable actuation and adaptability. This demonstrates their versatility and efficiency across multiple domains, making them a valuable group of material in various industries [72,73]. Even in consumer and industrial applications, the drive for miniaturization, part consolidation, and on-demand manufacturing of niche components makes PBF-LB an increasingly relevant technology for NiTi.

2.4 Manufacturing of NiTi

Given the relevance of NiTi in multiple application areas, it is therefore essential to understand how fabrication processes influence its properties. Specifically, the limitations and challenges associated with conventional processing routes, and how these challenges motivate the adoption of additive manufacturing techniques.

2.4.1 Challenges in manufacturing NiTi

Several factors influence the performance of NiTi alloys, with composition being the most critical. Variations in nickel content can significantly affect the transformation temperatures between martensite and austenite phases. It is also crucial to avoid contaminants such as oxygen, nitrogen, and carbon, as they impact transformation temperatures, hysteresis loops, strength, and ductility of the material [74,75].

In addition to composition, the manufacturing process strongly influences NiTi's microstructure, affecting lattice defects, grain structure, texture, precipitate formation, and surface quality. Combined with the alloy's high reactivity, these sensitivities make machining and shaping NiTi particularly challenging, which has limited its wider industrial use [76–79]. Conventional methods like casting, metal forming (cold/hot rolling), and powder metallurgy are often prone to oxidation, cracking, or dimensional inaccuracies. Vacuum Induction Melting (VIM) and Vacuum Arc Remelting (VAR), although commonly employed, also present challenges such as extreme reactivity, segregation due to density differences in reacting melts, and rapid grain growth at high temperatures, which negatively impact fatigue performance [79,80]. Even with a vacuum atmosphere, impurity pickup, particularly of oxygen and carbon, remains an issue due to multiple remelting steps required to obtain homogeneous alloys

[79,81]. Despite their differences, VIM and VAR processes yield similar mechanical and fatigue properties [80,82].

As-cast NiTi products typically require further processing to improve microstructure, surface quality, and dimensional accuracy. Post-processing operations include hot and cold working, machining, surface treatment, joining, and heat treatment. Machining NiTi is particularly difficult due to its high ductility and tendency to work-harden, making complex geometries challenging to achieve through conventional methods [83]. Powder metallurgy (PM) can reduce some issues such as segregation and grain growth by offering more precise control over chemical composition and limiting the need for extensive machining [84,85]. However, powder-based methods are still susceptible to impurity pickup during atomization and part fabrication [78,86], and PM parts often require additional post-processing to achieve full density (e.g., hot isostatic pressing (HIP)) and satisfactory surface quality.

Beyond composition control, machining difficulty, and impurity sensitivity, conventional NiTi processing faces other limitations: producing complex geometries generally requires extensive secondary operations, high-temperature processing causes rapid grain growth that reduces fatigue performance, and joining or assembling components can locally alter functional properties. Uncontrolled porosity and residual defects from casting or PM also compromise mechanical integrity, and traditional approaches provide limited ability to create functionally graded or engineered microstructures [83].

These cumulative challenges have increasingly motivated the adoption of additive manufacturing (AM). AM enables layer-by-layer fabrication, allowing near-net-shape geometries with reduced machining, precise microstructural control, engineered porosity, and the potential for functionally graded properties. Such capabilities directly address many of the limitations inherent to conventional NiTi processing.

2.4.2 Manufacturing of NiTi by Laser Powder Bed Fusion (PBF-LB)

AM method can produce fine, homogenous microstructures, which are beneficial for mechanical performance and consistent shape-memory effects. AM also produces less material waste compared to subtractive manufacturing methods making it a material-efficient manufacturing process [87].

PBF-LB is the most widely used AM technique for creating near-net-shaped NiTi components [79]. It involves selectively melting a thin layer of powdered material spread on a build

platform using a laser, guided by a computer-aided design (CAD) model. The process uses a high-purity inert gas such as Argon or Nitrogen atmosphere to minimize oxidation and contamination from impurities, crucial for maintaining the desired properties of NiTi [88]. The PBF-LB process is governed by several parameters that have significant impact on the properties and potential defects of the printed part and therefore require careful control. These parameters are interrelated through the volumetric energy density (VED), defined as **Equation 2.1**:

$$VED = \frac{P}{Vth} \quad \textbf{(Eq. 2.1)}$$

where P is the laser power, V is the scanning velocity, t is the layer thickness and h is the hatch spacing [89]. This term is often used to characterize and analyse the effect of printing parameters on the final part. However, this approach is noted to be overly simplistic, as each parameter has a distinct impact which cannot be fully captured by energy density alone [79]. For instance, in the work of Shi et al. [90], it was seen that different laser power and scan speed combinations with the same energy density resulted in parts with different functional and mechanical properties.

Despite its advantages, PBF-LB faces several challenges that must be addressed to optimize component quality and performance. Surface roughness and porosity can be problematic, often requiring post-processing treatments such as polishing or heat treatment to improve surface finish and mechanical integrity. Maintaining the correct composition is also challenging due to potential evaporation of elements like nickel during the high-temperature process, which can alter transformation temperatures and functional properties [91,92]. Even under highly controlled atmospheres (e.g., high-purity argon or nitrogen), some oxygen and carbon contamination is inevitable [93,94]. In addition to these compositional challenges, the rapid localized heating and cooling inherent to PBF-LB generates steep thermal gradients, which induce residual stresses that can lead to cracking and further compromise dimensional stability and mechanical performance. **Figure 2.8** shows the PBF-LB process schematic.

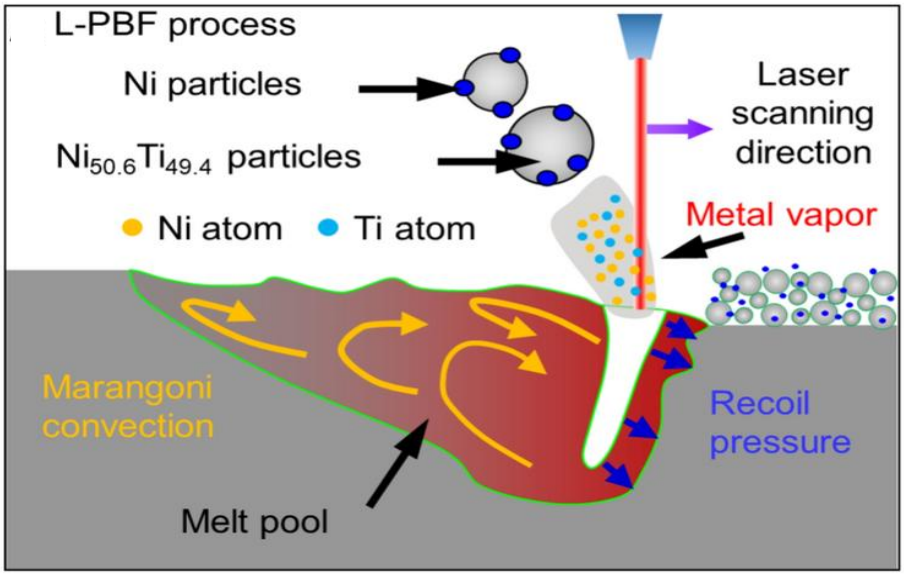


Figure 2.8 A schematic of the PBF-LB process of NiTi [81].

2.5 Defects in PBF-LB of NiTi

Despite its advantages, PBF-LB has several challenges that can affect the quality and functionality of the final NiTi product. Defect formation is strongly influenced by the laser–material interaction, which determines the thermal profile and melt pool behaviour during fabrication. The commonly observed defects in PBF-LB NiTi such as porosity, balling, keyhole and lack-of-fusion pores, residual stress, delamination, cracks, surface roughness, and oxidation [95,96], are all closely related to how energy is delivered to the powder bed and how the molten material solidifies. Two main melting regimes, **conduction mode** and **keyhole mode,** play a central role in the formation of these defects and schematically illustrated in **Figure 2.9** (a-b) [97]. In conduction mode, heat is primarily transferred through the powder and solid material, creating a shallow and stable melt pool. While this reduces the risk of keyhole-induced porosity and excessive evaporation, insufficient energy can lead to **lack-of-fusion defects** and incomplete layer bonding, which are linked to residual porosity, delamination, and surface roughness. In contrast, keyhole mode occurs at higher energy densities, forming a deep vapor cavity in the melt pool. This can improve interlayer fusion and reduce lack-of-fusion defects but may induce **keyhole porosity**, localize compositional changes, and increase residual stress, all of which can contribute to cracks and distortion. The transition between these regimes and the resultant defects are directly observable in the cross-sectional morphologies of single tracks, as shown in **Figure 2.9** (c-f), which depict good and defective tracks.

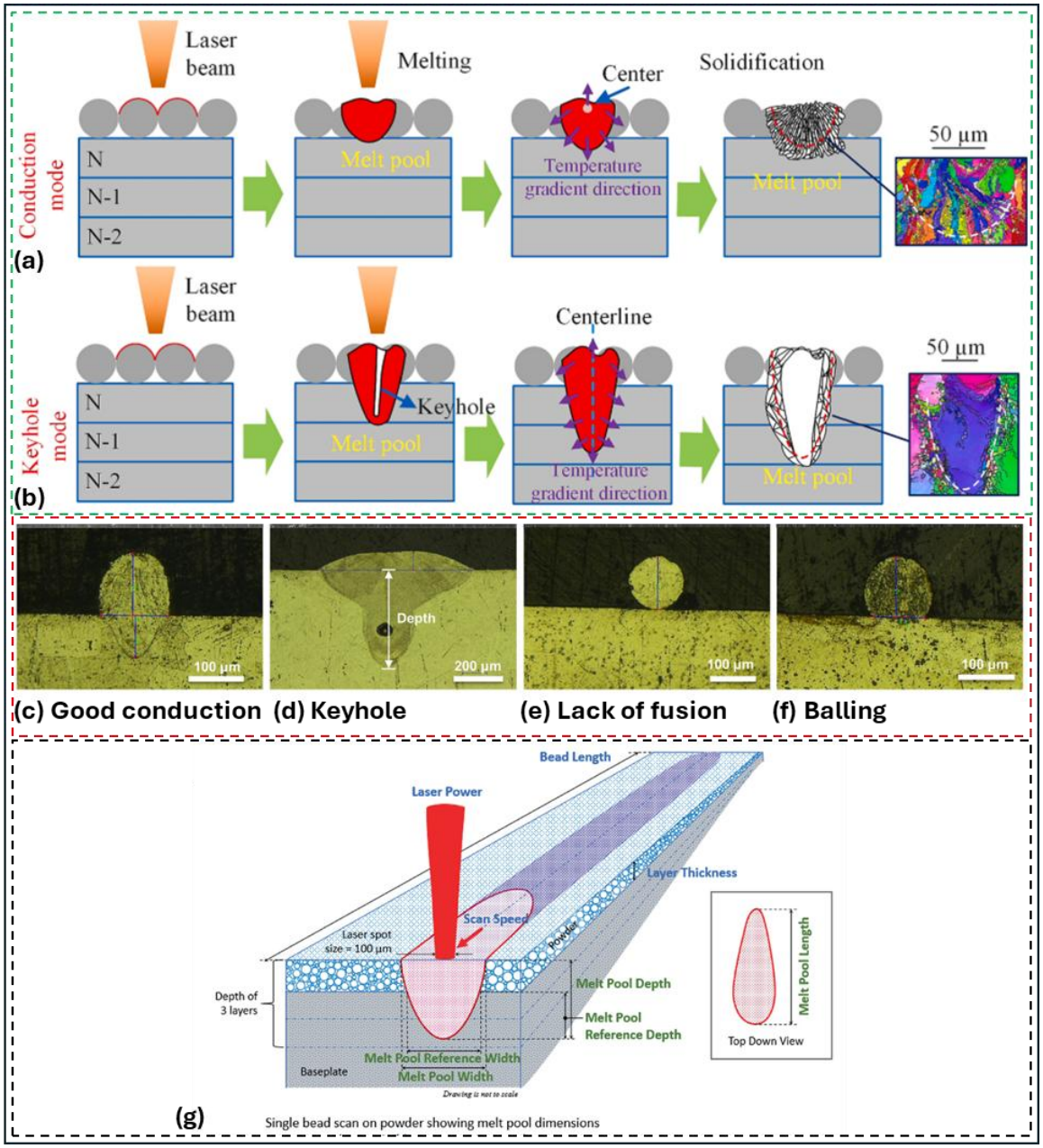


Figure 2.9 (a-b) Schematic illustration of defect evolution via conduction and keyhole melting mode during the PBF-LB processing if NiTi [97]; (c-f) cross-sectional optical micrographs of single-track, showing good and defective tracks (keyholing, lack of fusion, balling) consequent of melt pool regimes in PBF-LB. Reproduced from Xue et al. [98]; and (g) schematic depiction of the geometric feature space governing single-track melt bead morphology in PBF-LB, adapted from the *ANSYS Additive User's Guide* (2020).

These single-track features are not isolated phenomena but are intrinsically linked to the formation of bulk, multi-layer defects. The geometric feature space governing single-track melt bead morphology, schematically depicted in **Figure 2.9** (g), defines the foundational quality of each deposited layer. Inadequate track geometry, propagates through subsequent layers,

manifesting as volumetric defects and high surface roughness in the final part. Therefore, the melt pool behaviour captured in single-track analyses provides a critical predictive link to the defect states observed in consolidated bulk material.

Because each defect type emerges from specific thermal and fluid-flow conditions tied to these melting regimes, their occurrence cannot be understood in isolation from the process physics. Understanding the interplay between conduction and keyhole modes is therefore essential for controlling defect formation in PBF-LB NiTi. Subsequent sections discuss each defect type in detail, illustrating the influence of process parameters and melt pool behaviour. To summarize the relationship between melting regimes, defect formation mechanisms, and potential mitigation strategies in PBF-LB NiTi, **Table 2.2** provides a consolidated overview linking melt pool behaviour with the most commonly observed pore types and their primary process drivers.

Table 2.2 Relationship between melting regimes, defect types, key drivers, and mitigation strategies in PBF-LB NiTi.

Melting Regime	Typical Defect / Pore Type	Primary Process Drivers	Mitigation Strategies
Conduction Mode (Low–Moderate Energy Density)	Lack-of-fusion pores, irregular porosity, poor interlayer bonding	Insufficient laser power, excessive scan speed, large hatch spacing, inadequate overlap between tracks	Increase energy density, optimize hatch spacing and layer thickness, adjust scan speed, ensure sufficient track overlap
Transition Regime	Balling, unstable melt tracks, surface roughness	High scan speed, poor wetting behaviour, melt pool instability, improper powder spreading	Adjust scan speed and laser power balance, optimize powder layer uniformity, improve scan strategy
Keyhole Mode (High Energy Density)	Keyhole porosity (spherical pores), gas entrapment, compositional change (Ni evaporation)	Excessive laser power, low scan speed, deep vapor cavity formation, recoil pressure effects	Reduce energy density, optimize laser power–scan speed combination, improve shielding gas flow
Multi-Layer Accumulation	Residual stress, cracking, distortion, delamination	Steep thermal gradients, repeated thermal cycling, poor melt pool stability	Preheating, optimized scan strategies, controlled cooling, parameter optimization

2.5.1 Porosity (balling, keyholing and lack-of-fusion)

Porosity is a critical defect in additively manufactured NiTi, as it accelerates crack initiation and propagation and significantly degrades fatigue performance [89]. Depending on morphology and origin, porosity in PBF-LB–processed NiTi can be broadly classified into spherical gas-related pores, irregular lack-of-fusion (LOF) pores, and balling-induced porosity (**Figure 2.10**). The prevalence of each porosity type reflects the stability of melt-pool formation, powder consolidation behaviour, and local thermophysical conditions during processing.

Gas porosity and keyhole-related pores: Gas pores in PBF-LB–processing primarily originates from the entrapment of ambient gas within the powder bed, where the molten pool solidifies before gas bubbles can escape. Gas pores are also described as spherical porosity, given that the aspect ratio is approximately equal to 1 (**Figure 2.10** a), It is observed in both pre-alloyed and in-situ alloyed NiTi feedstocks. In the latter case, its formation is further exacerbated by elemental powder segregation between Ni and Ti particles, which promotes local compositional inhomogeneities, incomplete melting, and gas retention, as demonstrated by Bourke et al. [99].

Mitigation of spherical porosity therefore depends on the careful selection of processing parameters that promote stable melt-pool behaviour, epitaxial solidification, and continuous inter-track bonding. For *in-situ* alloyed NiTi, additional process-specific considerations include the positioning of samples relative to the re-coater sweep direction and matching the particle size distributions of elemental Ni and Ti powders to minimise segregation [99]. Stable porosity-minimising conditions are generally achieved under conduction-dominated melting, where melt pools remain shallow and thermally driven. This regime is characterised by a melt-pool depth-to-width ratio not exceeding 0.5 in PBF-LB processed NiTi, as illustrated in **Figure 2.9** (a) and expressed as [95,96,100,101]:

$$\frac{meltpool\ depth}{meltpool\ width} \leq 0.5 \qquad \textbf{(Eq. 2.2)}$$

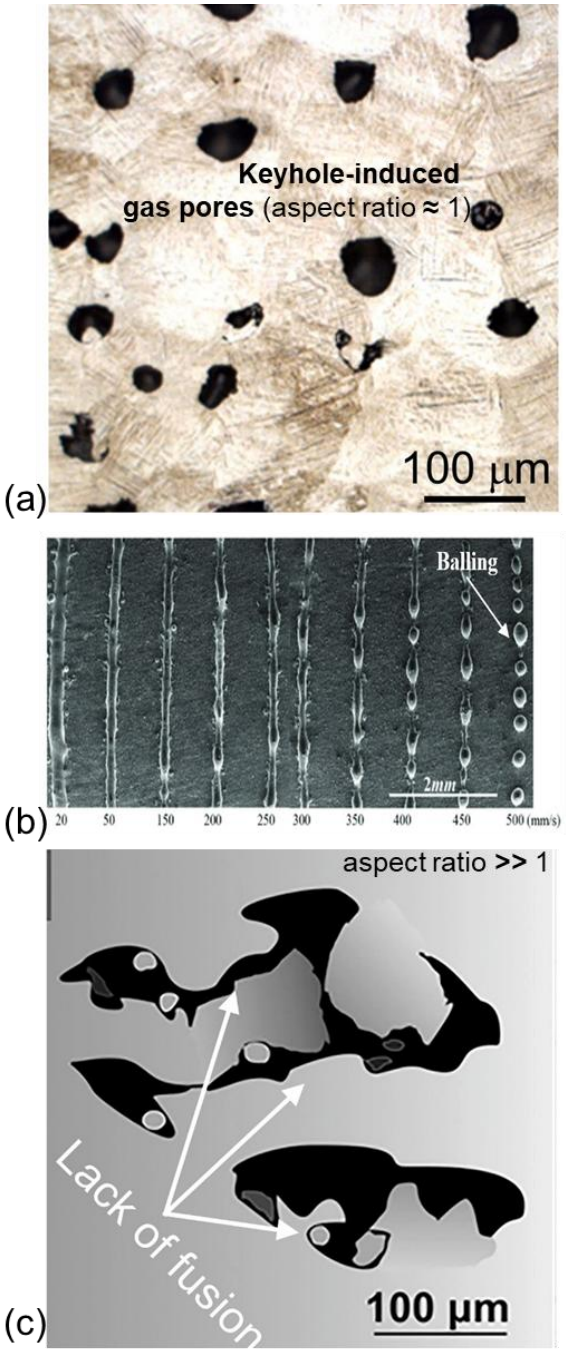


Figure 2.10 Examples of porosity-type defects; (a) keyhole pores, (b) balling, and (c) lack of fusion defects. Adapted from [102,103].

Although a depth-to-width ratio of 0.5 is widely accepted for NiTi, alternative thresholds have been reported for other alloys (e.g. 0.8 for IN718), highlighting that conduction-mode criteria are material dependent [104]. Within this stable regime, Yang et al. [105] showed that increasing laser power while reducing scan speed enhances interlayer bonding by increasing melt-pool size and energy input. In contrast, Li et al. [96] reported that hatch spacing has a limited influence on pore formation provided sufficient track overlap is maintained. Note that

geometrically, the keyhole regime is associated with melt pools exhibiting depth-to-width ratios greater than 0.5 and expressed as:

$$\frac{meltpool\ depth}{meltpool\ width} > 0.5 \qquad \textbf{(Eq. 2.3)}$$

At higher energy inputs, spherical porosity becomes increasingly associated with keyhole instability. Haberland et al. [94] reported that volumetric energy densities exceeding approximately 74 J/mm³ during PBF-LB processing of NiTi promote pore formation due to the onset of keyholing. In this regime, excessive energy input generates a deep, vapor-driven cavity that is susceptible to collapse, leading to the entrapment of gas bubbles or metal vapour within the solidifying melt pool [106,107]. These keyhole-induced pores are therefore mechanistically distinct from gas pores formed under conduction-mode conditions and are characteristic of unstable vapor–cavity dynamics.

Additional sources of spherical porosity include excessive laser power or scan velocity, which can induce metal vaporisation, recoil pressure, and the ejection of vapor jets and hot spatters [108]. Process interventions such as laser re-melting can reduce balling and improve microstructural uniformity, albeit at the cost of increased build time. Base-plate preheating can also improve melt flowability and reduce balling, although excessive preheating may promote droplet spatter formation and clusters of partially melted particles [109,110]. Atmospheric control is likewise critical: oxygen trapped between deposited layers can expand under laser heating and form large pores, with Li et al. [96] showing that oxygen levels below 0.1% are necessary to effectively mitigate balling and gas-related porosity in PBF-LB of NiTi.

Balling: Balling is a prominent defect in PBF-LB processing that produces irregular pore morphologies and severely degrades surface quality in NiTi components (**Figure 2.10** b). It arises primarily from Plateau–Rayleigh capillary instability, whereby an elongated liquid filament breaks into droplets to minimise surface energy [111]. This instability is strongly influenced by thermal gradients and Marangoni convection, which drive liquid metal from regions of lower surface tension (hotter zones) toward regions of higher surface tension, particularly near the melt-pool boundary with surrounding unmelted powder [112]. The combined action of capillary breakup and thermocapillary flow destabilises melt tracks, leading to droplet formation, poor track continuity, and, in severe cases, re-coater interference (scraping) and build failure [113].

Geometrically, balling is associated with an excessive melt-pool length-to-width ratio. Xue et al. [98] identified a critical value of 2 beyond which the PBF-LB processed single-tracks becomes unstable:

$$\frac{meltpool\ length}{meltpool\ width} \geq 2 \qquad \textbf{(Eq. 2.4)}$$

Although often linked to high laser power and high scan speed, balling can also occur under insufficient energy input, where poor wetting and reduced melt-pool cohesion lead to discontinuous, bead-like tracks [103]. Surface contamination of either the powder or substrate may further aggravate balling by inhibiting wetting at the melt–solid interface [114]. Within the conduction–keyhole framework, balling reflects melt-pool instability predominantly within the low-to-moderate energy-density regime, where melt pools are elongated or under-driven rather than vapor-dominated.

Lack-of-fusion porosity: Lack-of-fusion porosity (**Figure 10** c) is another defect mechanism associated primarily with insufficient energy input, where the supplied laser energy is inadequate to fully melt and consolidate the powder bed. LOF pores are typically irregular in shape, sharp-edged, and form at inter-track or inter-layer boundaries due to incomplete overlap and insufficient remelting of underlying layers [115]. The aspect ratio of LOF is typically far greater than 1. Xue et al. [98] defined the LOF regime of single-tracks geometrically using the melt-pool depth-to-layer-thickness ratio:

$$\frac{meltpool\ depth}{layer\ thickness} < 1 \qquad \textbf{(Eq. 2.5)}$$

Prevention of LOF in the bulk, multi-layer component requires the melt-pool width to exceed the hatch spacing and the melt-pool depth to surpass the layer thickness, ensuring adequate inter-track bonding and partial remelting of one to two underlying layers. Overlap (OL) defines the ratio of melt-pool width to hatch spacing, and Walker et al. [116], recommended of OL greater than 36% resulted in PBF-LB processed NiTi (Ni-50.09 at. %). Laser power and scan speed exert strong control over these conditions: higher power and lower scan speed enlarge melt-pool dimensions, whereas low power or excessively high scan speeds reduce penetration depth and promote discontinuous tracks.

While insufficient energy input primarily promotes LOF porosity by limiting melt-pool penetration and overlap, variations in scan speed also influence track morphology and microstructural evolution by modifying melt-pool size, thermal gradients, and cooling rates. These changes can produce unimodal, bimodal, or multimodal grain structures in PBF-LB–processed NiTi [117]. At very low scan speeds (high energy input), the melt pool becomes larger and more persistent (keyhole mode molten pool), which can increase porosity and

elemental evaporation, whereas intermediate scan speeds often yield more stable columnar or cellular microstructures with lower defect content in PBF-LB processed NiTi [118]. As energy density increases and conduction-mode melting becomes more stable, the frequency of LOF defects generally diminishes.

Process window considerations and porosity mitigation strategies: Across both pre-alloyed and in-situ alloyed NiTi feedstocks, achieving high relative density generally requires intermediate energy-input regimes [99,119]. Energy densities that are too low promote lack-of-fusion and balling-related porosity, whereas excessive energy input destabilises the melt pool and favours keyhole-induced pore formation. Despite this qualitative consensus, the literature reports no single optimal energy density for NiTi, owing to the strong dependence of laser–powder interaction, absorptivity, and melting behaviour on alloy composition.

This composition sensitivity is evident in predictive process maps for NiTi alloys constructed as functions of laser power and scan speed (i.e., linear energy density, P/V), as shown in **Figure 2.11** (a-c). Pronounced shifts in the stable processing window are observed, particularly within the 50–100 W laser power range at low scan speeds (< 500 mm s^{-1} i.e., 0.5 m s^{-1}), alongside a systematic narrowing of the defect-free window with increasing Ni content. This trend is attributed to the higher susceptibility of Ni-rich compositions to brittleness and residual stress accumulation [120–122]. While such maps are effective for identifying composition-specific parameter windows that yield dense parts within a given hatch-spacing range, they also reveal a fundamental limitation: neither linear nor volumetric energy density alone reliably predicts printability. Identical nominal energy densities achieved through different parameter combinations often produce substantially different melt-pool geometries, defect populations, and final part densities. Comparable shortcomings of energy-density-based metrics have been widely reported for other PBF-LB-processed metallic alloys [9,123–126], underscoring the need for physically grounded, multi-parameter descriptors of process stability.

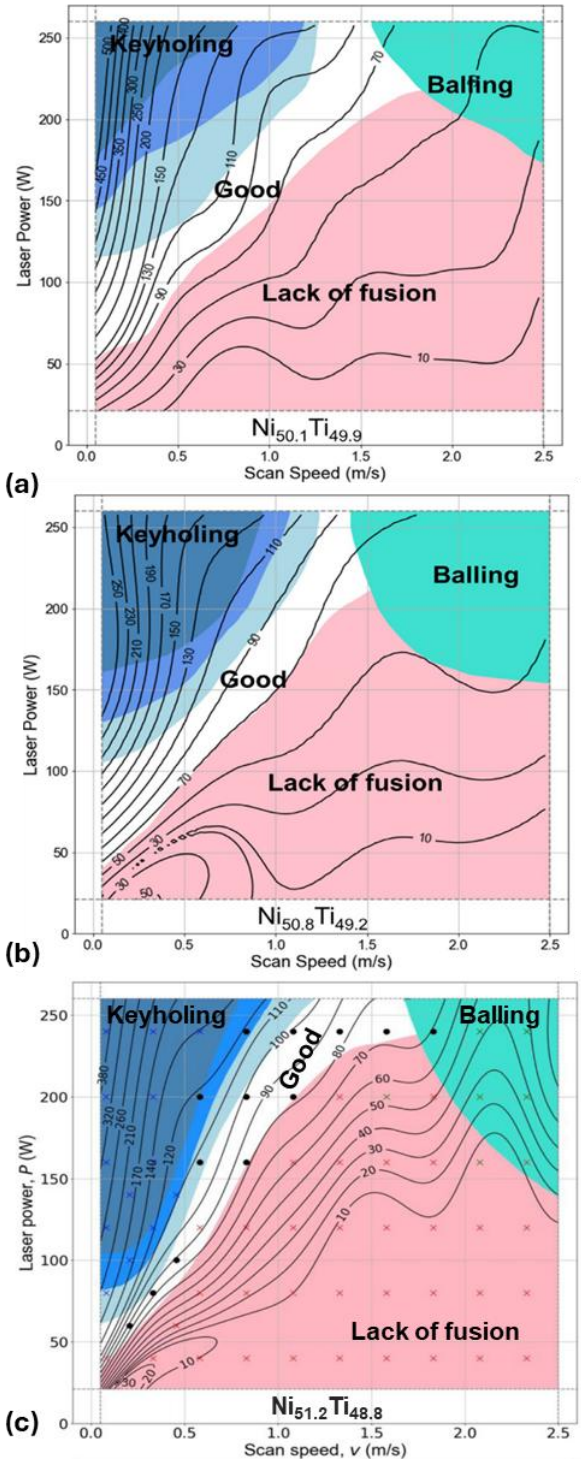


Figure 2.11 Processing maps showing the relationship between laser power (P) and scan speed (V) for three Ni-rich NiTi powder compositions: (a) $Ni_{50.1}Ti_{49.9}$, (b) $Ni_{50.8}iTi_{49.2}$, and (c) $Ni_{51.2}Ti_{48.8}$. Adapted from [98,122]. The maps delineate composition-specific good (i.e., stable) conduction-mode processing windows from regimes prone to lack-of-fusion at low P/V energy input and keyhole-induced porosity at excessive P/V energy density. The superimposed contour lines indicate the maximum hatch spacing permissible for each parameter combination, beyond which lack-of-fusion (LOF) defects are anticipated.

While porosity is often treated as a defect that reduces mechanical performance, recent studies suggest that the distribution, morphology, and size of pores can significantly influence the phase transformation mechanisms governing superelasticity. In particular, pores can introduce localized stress concentrations that alter the stress-induced martensitic transformation pathway. For example, atomistic and experimental studies have shown that the presence of pores can modify the transformation sequence from the conventional B2 → B19′ transition to a two-step transformation (B2 → B19 → B19′) near pore surfaces, which may affect the stress–strain response and recovery behaviour of NiTi alloys [127].

Furthermore, controlled pore architectures have been reported to influence the evolution of martensite variants and transformation kinetics, potentially enhancing energy dissipation and strain recovery under cyclic loading. This indicates that the mechanical functionality of NiTi alloys is not solely governed by overall porosity but also by pore distribution and internal surface characteristics, which can interact with the transformation-induced deformation mechanisms [128,129]. Consequently, relying solely on porosity or relative density as the primary metric for process optimization in additive manufacturing may be insufficient. A more comprehensive evaluation that considers the coupled effects of pore architecture, local stress fields, and phase transformation behaviour is necessary to better understand and optimize the superelastic performance of additively manufactured NiTi components.

2.5.2 Residual stress

Residual stress is a significant characteristic in thermal manufacturing processes, particularly affecting parts produced by the PBF-LB process by leading to various defects and failures [130]. The high temperature gradients and densification ratio inherent to PBF-LB contribute to elevated residual stresses. These thermal stresses commonly manifest around the melt pool, causing surface defects, porosity, and, in severe cases, distortion, shrinkage, cracking, warping, and delamination from support structures. Consequently, these factors compromise mechanical properties, fatigue life, part density, and dimensional accuracy of PBF-LB parts [131]. This issue is particularly critical for NiTi shape memory alloys, as their functional performance strongly depends on stress-induced martensitic transformations and precise thermo-mechanical behaviour. Residual stresses introduced during PBF-LB can significantly alter transformation temperatures, stabilize martensite phases, and modify the superelastic response, thereby affecting the functional reliability of the material. Furthermore, the repeated rapid heating and

cooling cycles during layer-by-layer fabrication generate complex residual stress distributions along the build direction, which may interact with the phase transformation mechanisms of NiTi and lead to microcracking or distortion of thin structures. Due to the strong coupling between thermal history, phase transformation, and mechanical behaviour in NiTi alloys, controlling residual stress is therefore a key challenge in achieving both structural integrity and functional performance in PBF-LB fabricated NiTi components, motivating ongoing research on scan strategies, preheating, and process optimization to mitigate stress accumulation [118,132,133]. Various failures observed in metal additive manufacturing due to residual stress are depicted in **Figure 2.12**.

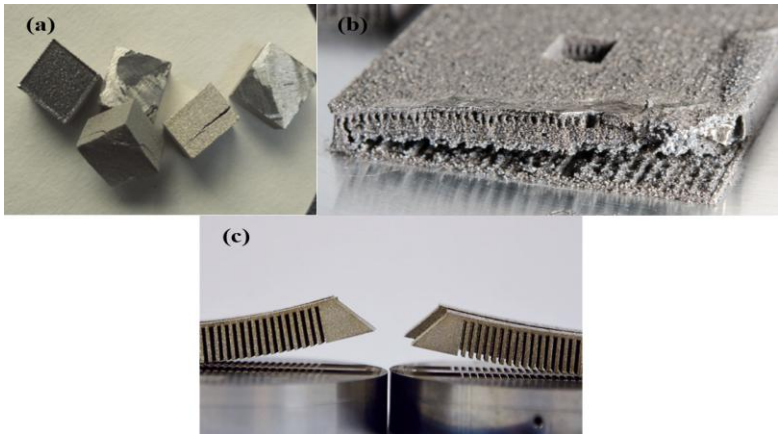


Figure 2.12 Failures caused by residual stress in PBF-LB produced parts, (a) cracks [134] (b) distortion and delamination [135], (c) Distortion caused by residual stress on PBF-LB produced components [136].

Mitigation strategies involve adjusting process parameters to minimize thermal gradients, controlling cooling rates, and using proper design and optimization of support structures, to minimize distortion and warping during printing of NiTi. In addition, post-processing techniques such as heat treatment and HIP can also be applied in order to relieve these thermal residual stresses. Finite element (FE) simulation methods are commonly employed to predict the distribution and evolution of residual stresses in PBF-LB due to the complexity and challenges of experimental measurement. Some of the experimental techniques used for measuring residual stresses are X-ray diffraction (XRD), hole drilling method, contour method, neutron diffraction, ultrasonic method, and thermoelastic method [137,138]. Rangaswamy et al. [138] established a non-monotonic relationship between VED, thermal gradient and residual stresses in PBF-LB printed NiTi, with stresses measured using XRD and the hole drilling method and in-situ melt pool temperature monitored via infrared pyrometry. Ma et al. [139] evaluated the residual stresses in PBF-LB NiTi through contour method, prior to and post heat

treatment and found that the heat treatment reduced the residual stress levels and enhanced the superelasticity of NiTi.

2.5.3 Delamination and cracks

Stresses generated during the PBF-LB process can lead to defects, such as cracking which occurs when these stresses surpass the material's ultimate yield strength. The elongated, nonsymmetric shape of the melt pool also induces uneven thermal gradients and shrinkage along the melt track, creating local residual stresses. Strategies like reducing the scanned area per layer through part orientation and shorter scan vectors, such as implementing an island scanning strategy, have shown promise in reducing these stresses and minimizing cracking as shown in **Figure 2.13** [140]. In typical PBF-LB scan strategies, the outer border or contour scans define the part boundary and improve surface quality, while hatching refers to the internal infill scanning used to consolidate the bulk material. Adjusting the energy input between these zones is commonly used to manage residual stresses and mitigate cracking.

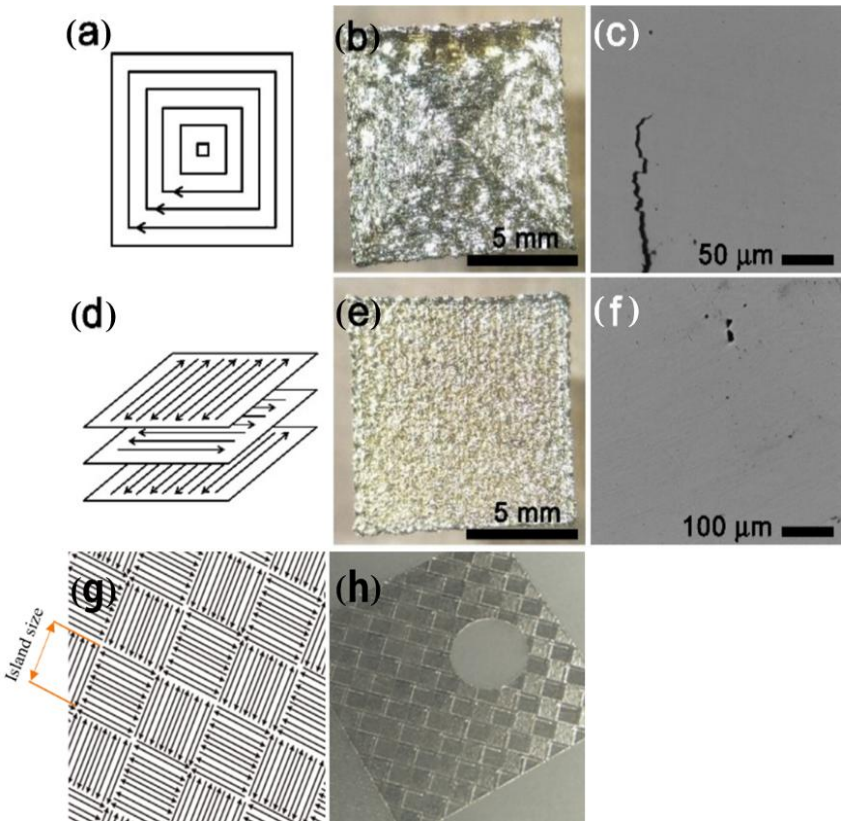


Figure 2.13 Scanning strategies: (a) total fill, (d) meander (90° raster scanning) and (g) island. The final appearance of respective surfaces of the produced parts is shown in (b, e, h). The optical micrographs of the total fill and meander are shown respectively in (c, f) [134,141].

The linear energy density (E_L), defined as the ratio of power to scan speed, is a design parameter that can be used for assessing parameter selection leading to defect-free manufacturing of NiTi parts via PBF-LB [142]. Cracks are especially problematic when producing superelastic NiTi. Achieving superelasticity itself with PBF-LB is also challenging, which according to Dadbakhsh et al. [143] is partly due to the formation of martensite caused by thermal stresses. Additionally, Lu et al. [144] noted that nickel vaporization during production can increase the austenite finish temperature, thereby diminishing the superelastic behaviour of the material. As a result, identifying process parameters that simultaneously enable superelasticity and prevent cracking is challenging. However, Li et al. [121] reported a narrow processing window involving high scanning speeds and laser power that successfully produced crack-free, superelastic parts. Monu et al., [115,145] reported increased susceptibility to liquation cracking in equiatomic NiTi processed by PBF-LB at high VED (**Figure 2.14** a–d). Specifically, samples fabricated at a VED of 80 J/mm exhibited an average liquation crack length of $61.32 \pm 4.35\mu m$. Increasing the VED by 100% to 120 J/mm³ led to a marked increase in both liquation crack length and crack density, with an average crack length of $126.39 \pm 135.58\mu m$. The reported maximum longitudinal crack length observed (**Figure 2.14** b–c) reached approximately 515.56 µm.

Delamination defects in PBF-LB of NiTi alloys are strongly influenced by both alloy composition and processing parameters, which together govern melt pool behavior, microstructural evolution, and residual stress development. NiTi alloys are highly sensitive to small variations in composition, particularly the Ni content. During PBF-LB, the extremely high melt-pool temperatures can cause preferential evaporation of Ni, leading to local compositional shifts toward Ti-rich regions. This compositional deviation may promote the formation of brittle Ti-rich intermetallic phases (e.g., Ti_2Ni) and alter transformation behavior, thereby reducing ductility and increasing susceptibility to cracking or interlayer separation. Because the phase transformation temperature of NiTi can shift significantly with very small changes in Ni concentration, even minor compositional fluctuations introduced during processing can affect thermal stresses and the mechanical response of the material [146,147].

Processing parameters such as laser power, scan speed, hatch spacing, and scan strategy also play a critical role in the formation of delamination defects. These parameters control the energy input and thermal gradients during fabrication, which in turn influence melt-pool stability, solidification rate, and residual stress accumulation. Excessive energy input can intensify Ni evaporation and increase thermal gradients, while insufficient energy input may

lead to incomplete melting and weak interlayer bonding. The rapid heating and cooling cycles characteristic of PBF-LB generate steep thermal gradients and high residual stresses within the build, which may exceed the local fracture strength and result in cracking or delamination between layers. Furthermore, scanning strategies that promote uneven heat distribution can exacerbate residual stress development and distortion, increasing the likelihood of defect formation [118,132,145]. Therefore, controlling both composition stability and process parameters is essential for minimizing delamination and achieving dense, defect-free NiTi components.

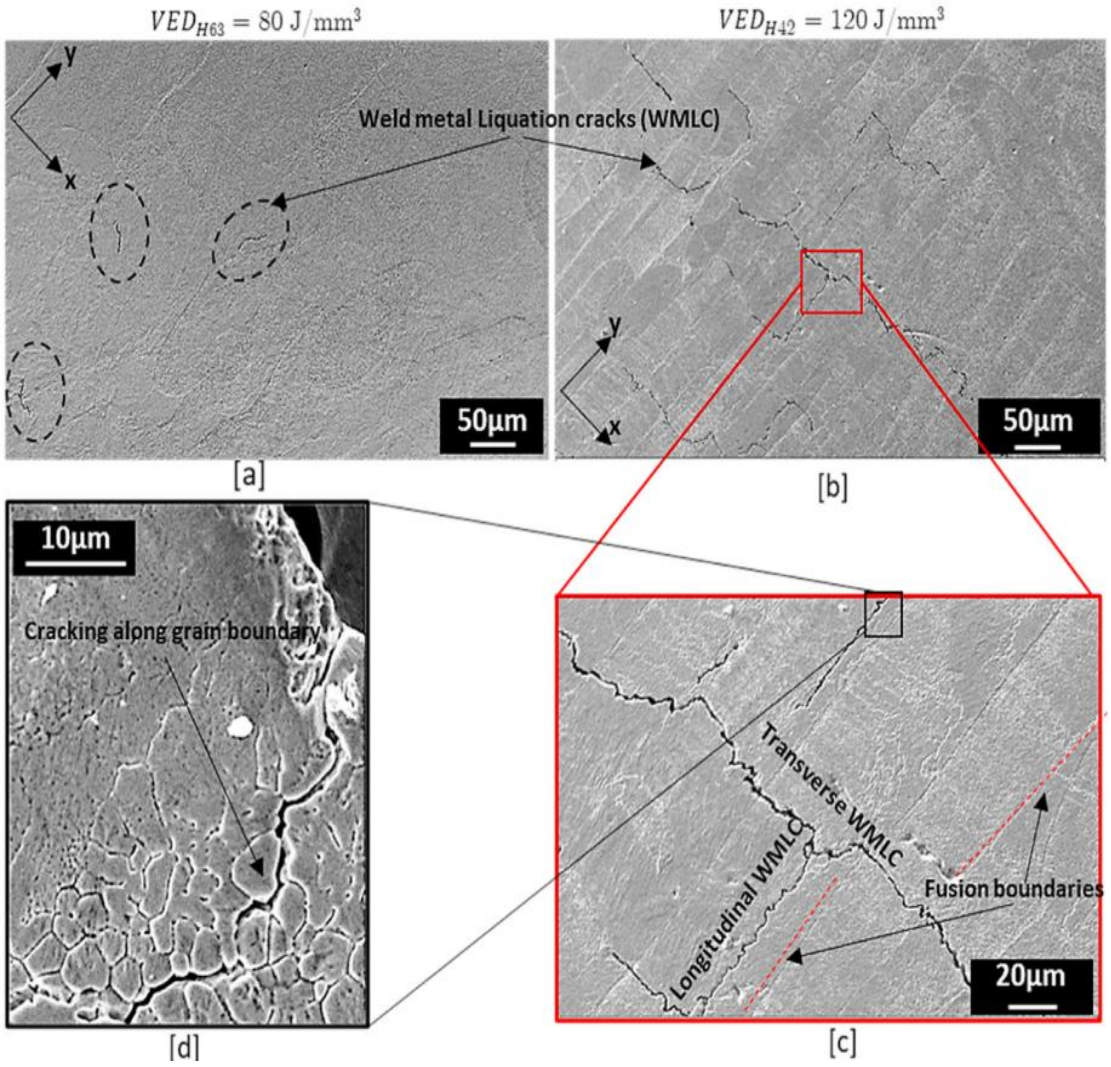


Figure 2.14 SEM micrographs of liquation cracks in PBF-LB processed equi-atomic NiTi at (a) volumetric energy density (VED) of 80 J/mm^3 (hatch spacing of 63 µm) (b) VED of 120 J/mm^3 at hatch spacing of 42 µm (c) high-magnification image showing transverse cracks (approximately perpendicular to the fusion boundaries/scan direction) and longitudinal cracks along fusion boundaries; and (d) high-magnification image highlighting the intergranular nature of the liquation cracks. Reproduced from [115].

2.5.4 Surface roughness

Surface roughness is intrinsic to additively manufactured components due to the layer-wise nature of the PBF-LB process and is strongly influenced by processing conditions. Although not typically classified as a defect, surface roughness is a critical quality attribute, particularly for NiTi, where surface condition directly affects biocompatibility via osteointegration and nickel ion release [148]. This is especially relevant for biomedical applications, as PBF-LB-fabricated NiTi generally exhibits poorer surface quality than conventionally processed material. Beyond the inherent stair-stepping effect, partially melted powder particles adhering to the surface can detach during service, posing biological risks. Surface roughness also governs corrosion behaviour and acts as a preferential site for crack initiation, thereby significantly influencing fatigue life [86,149].

Feedstock characteristics play a central role in determining surface finish. Fine powders with controlled morphology are preferred, as irregular particles and powder satellites increase surface roughness and degrade part quality. Powder satellites, in which small particles are attached to larger ones can increase surface roughness and negatively affect the part quality [89]. Process-related phenomena including partially melted particles, balling, spatter formation, and melt pool instability; further exacerbate surface irregularities. While post-processing techniques such as mechanical, chemical, and electrochemical treatments can improve surface quality, they increase manufacturing time and cost [150]. Consequently, optimisation of process and build parameters is often preferred. Processing maps (e.g., **Figure 2.11**) of NiTi [98], indicate that parameter sets approaching the keyholing boundary and avoiding balling are more likely to produce smoother surfaces, albeit with an increased risk of keyhole-induced defects. Layer thickness and laser beam diameter are also influential; Sow et al. [151] showed that a larger beam diameter combined with lower volumetric energy density yields smoother surfaces than a smaller beam operating at higher energy density.

The scanning strategy has a significant influence on surface roughness in PBF-LB. The use of a contour scan with optimized process parameters, together with appropriate part positioning and orientation relative to the gas flow direction, has been shown to improve surface quality [140,150]. The contour refers to the laser scan path that defines the outer boundary of each layer and plays a critical role in controlling edge definition and surface finish. Selective laser remelting (SLRM), illustrated in **Figure 2.15**, is an additional strategy employed to further reduce surface roughness.

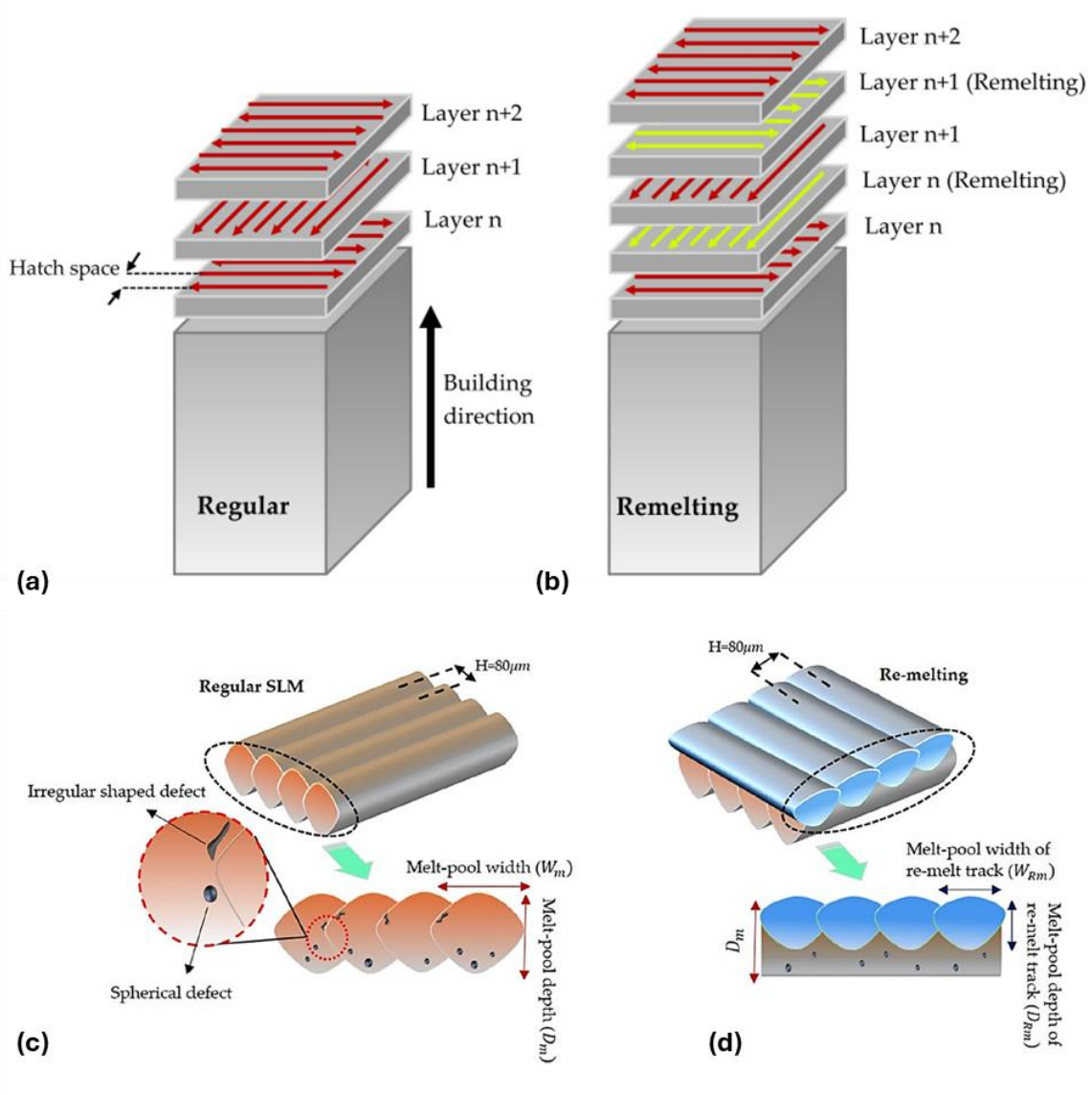


Figure 2.15 Schematic representation of PBF-LB melt pool morphology: (a) regular laser tracks, and (b) remelted laser tracks [152].

In SLRM, previously consolidated material is reprocessed to smooth surface irregularities and reduce near-surface porosity. When every layer is remelted, the build time approximately doubles relative to standard fabrication (**Figure 2.15** a and c). To reduce this time penalty, an alternative strategy involves remelting every second layer (**Figure 2.15** b and d), which increases the total processing time by only ~50% compared with the original build.

Remelting is typically performed using a lower volumetric energy density (VED) than that applied during initial layer fabrication. Using this alternate-layer SLRM approach, Bayati et al. [152] achieved an approximately 50% reduction in surface roughness in PBF-LB-processed

$Ni_{50.8}Ti_{49.2}$ components, together with improved density, by employing a remelting parameter set corresponding to at least 50% of the primary VED ($83\,\mathrm{J\,mm^{-3}}$). Importantly, these improvements were obtained without significant changes in transformation temperatures. The enhanced surface quality and densification were attributed to the elimination of irregular porosity in the upper region of previously deposited layers, thereby improving the overall quality of the fabricated parts [152,153].

Recent research has focused on several surface polishing techniques, which can be broadly categorized into mechanical, chemical/electrochemical, and energy-based methods. Mechanical polishing methods, including abrasive flow machining, vibratory finishing, and micro-grinding, are widely used to remove loosely bonded particles and reduce macro-scale roughness. However, these techniques may be limited when processing complex geometries typical of additively manufactured parts. Consequently, chemical and electrochemical polishing methods, such as acid etching and electropolishing, have attracted considerable attention because they can uniformly smooth complex surfaces while also improving corrosion resistance by forming a stable TiO_2-rich oxide layer on NiTi surfaces [154–156].

More recently, advanced polishing approaches such as laser polishing, plasma polishing, and hybrid finishing techniques have been investigated to further improve surface quality of additively manufactured NiTi components. Laser polishing utilizes controlled surface remelting to reduce surface irregularities and significantly decrease roughness without mechanical contact [157]. Similarly, electrochemical polishing has been widely optimized to achieve substantial reductions in surface roughness by selectively dissolving surface asperities under controlled voltage, temperature, and electrolyte conditions [158]. Hybrid processes that combine mechanical and electrochemical methods are also emerging as effective solutions for complex geometries and internal channels [159,160]. Overall, these recent advances in polishing technologies play a critical role in enhancing the surface integrity, functional performance, and biomedical applicability of NiTi components fabricated by additive manufacturing.

2.5.5 Oxidation

The atmosphere within the PBF-LB chamber is a critical determinant of oxygen uptake in NiTi components, as oxidation can occur both on the part surface and on every newly deposited powder layer. Impurities originate primarily from residual chamber gases, surface oxides or

carbonates formed during powder gas-atomization, and trace contaminants interacting with the molten alloy during laser exposure [161]. Given titanium's high oxygen affinity and the preferential evaporation of nickel at elevated temperatures, available oxygen or carbon species promote the formation of secondary phases such as $Ti_4Ni_2O_x$, $TiNiO_3$, TiO_2, $TiNi_3$, and TiC, which locally modify alloy composition and functional behaviour [140]. Studies by Xue et al. [98] and Haberland et al. [94] demonstrated that oxygen and carbon uptake in as-built NiTi increases with higher PBF-LB process energy densities, though levels in PBF-LB NiTi remain significantly lower than in as-cast material [162].

Residual oxygen enters the melt pool through two primary feedstock-related pathways: inter-particle gas entrapped between powder particles, and native surface oxide films on the powder. The extreme thermal gradients and vigorous melt-pool convection cannot fully expel this entrapped oxygen before reactive incorporation, making truly oxide-free processing challenging [12]. Consequently, most oxides formed are Ti-rich, leading to local Ti depletion and a reduction in phase-transformation temperatures [122,140]. The surface oxidation of near-equiatomic NiTi follows a sequential, diffusion-controlled mechanism, initiated by the preferential oxidation of titanium, which forms an outer TiO_2 layer and creates a Ti-depleted, Ni-enriched zone beneath. As oxidation continues, Ni enrichment eventually reaches the solubility limit in the B2 matrix, precipitating an inner $TiNi_3$ intermetallic layer. Once the $TiNi_3$ layer attains a critical thickness which hinders outward Ti diffusion, the oxidation pathway shifts to the decomposition of $TiNi_3$. This leads to the formation of an intermediate composite layer of TiO_2 and Ni (Ti) solid solution, as illustrated in **Figure 2.16**, establishing a dynamic equilibrium.

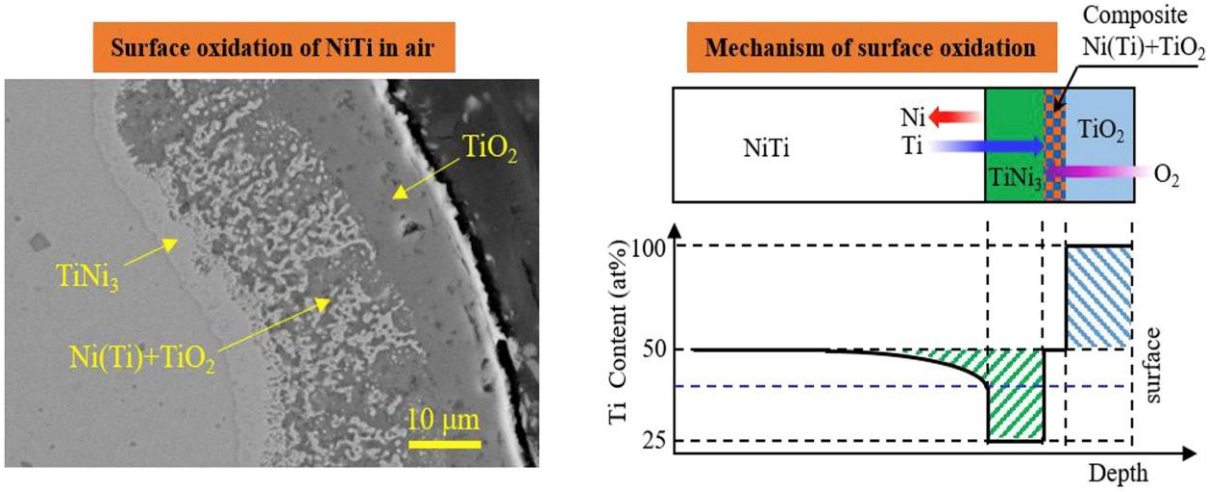


Figure 2.16 Formation of oxide layers in NiTi [163].

In this steady state, $TiNi_3$ concurrently forms at its inner interface and decomposes at its outer interface, maintaining a constant thickness while the composite layer expands inward and results in a distinct multilayer architecture. These surface oxides are brittle ceramic compounds that exhibit no martensitic transformation, thus acting as a mechanical constraint to shape memory deformation and recovery [163]. For example, Xue et al. [122] investigated the effect of chamber oxygen levels (100 ppm vs. 500 ppm) on $Ni_{51.2}Ti_{48.8}$ (at. %) and found that lowering the oxygen content noticeably enhances functional response. Samples processed at 100 ppm showed markedly better tensile superelastic behaviour than those fabricated at 500 ppm. At test temperatures of 25 °C and 35 °C (about 10 °C above the A_f temperature), the low-oxygen material was able to recover approximately 4 % and 6 % strain, respectively, whereas the higher-oxygen material exhibited substantially reduced recoverable strain.

The relationship between Ni loss and phase transformation temperature in NiTi alloys deserves further clarification. In conventional NiTi metallurgy, a decrease in Ni content typically shifts the alloy toward a Ti-rich composition, which generally leads to an increase in martensitic transformation temperatures (Ms, As, and Af). Nevertheless, several studies on additively manufactured NiTi have reported cases where the transformation temperature decreases despite a reduction in Ni content. This seemingly contradictory behaviour is often associated with the complex microstructural evolution occurring during rapid solidification processes such as PBF-LB. Factors including non-equilibrium solidification, suppression or redistribution of precipitates (e.g., Ni_4Ti_3), residual stress accumulation, and local compositional heterogeneity can significantly influence the effective matrix composition and transformation behaviour. In addition, oxidation and oxygen incorporation may alter local chemistry and defect structures, further affecting phase transformation characteristics [14,146,164]. Therefore, the transformation temperature of additively manufactured NiTi alloys cannot be explained solely by bulk Ni concentration, and a comprehensive analysis considering microstructure, precipitate evolution, residual stress level, and processing-induced defects is necessary to fully understand this phenomenon.

Oxidation behaviour is further influenced by the prevailing melt-pool regime. In conduction mode, the shallow melt pool incorporates oxygen primarily through surface reactions and the wetting of surface oxides, with limited transport to deeper zones. In keyhole mode, the deep vapor cavities, elevated temperatures, and intensified convection enhance the entrapment and transport of oxygen-bearing species into the melt, promoting oxide inclusion and local

compositional perturbations. Given these pathways, gettering strategies offer a complementary approach to reduce oxygen uptake. Getters are materials that preferentially react with oxygen, scavenging reactive species before they interact with the NiTi melt [165,166]. Relevant categories include [165] (a) Evaporable getters (e.g., Mg, Ca), which volatilize at high temperature and bind oxygen in gaseous or liquid phases. (b) Non-evaporable getters (e.g., Al, Ti, Zr, Y, Si), which react with dissolved or gaseous oxygen to form stable, high–melting point oxides. (c) Reactive gases (e.g., H_2), which remove impurities by forming volatile compounds with oxygen or other contaminants [167]. Examples from other systems, such as silane-doped argon in PBF-LB of Ti-6Al-4V [168] or ZrH_2 additions in tungsten PBF-LB processing by NASA [169], demonstrate how in-situ gettering mechanisms can be adapted for PBF-LB processing of NiTi, particularly under high-energy-density, keyhole-dominated conditions where oxidation risks are greatest.

2.6 Modelling the PBF-LB process of NiTi

The integration of multi-scale modelling and simulation techniques will enhance the reliability, efficiency, and performance of NiTi components produced through PBF-LB. Such computational modelling serves as a potent tool for investigating additive manufacturing processes. By simulating various design iterations, engineers can evaluate different geometries, support structures, and build orientations. This iterative process helps in minimizing material usage, reducing post-processing requirements, and enhances the overall efficiency of the manufacturing process [4,98,103,122,170]. As several physical phenomena are involved in additive manufacturing and in particular PBF-LB, various attempts have been made to develop models to predict different aspects of the process. However, modelling a multifaceted process like PBF-LB remains challenging, especially for specialized materials such as shape memory alloys. This is mainly due to the fact that it is made up of several independent sub-processes occurring at different scales and governed by diverse physical phenomena. A tailored modelling approach is required in order to capture the real interplay of thermodynamics, intricate geometries and material behaviour, especially considering the thermomechanical phase transformation characteristics [15–17,171].

Models play a key role in analysing and optimising the process as well as predicting the properties of the part. Numerous models in the literature are developed for laser welding and additive manufacturing. These models can predict important aspects of printed parts such as microstructure and phase transformations, thermal behaviour, mechanical properties, melt pool

dimensions, and defect formation [172–174]. These features are intertwined and often need to be investigated together to gain meaningful insights. There are two main approaches for modelling the PBF-LB process: physics-based models and data-driven models. Physics-based models rely on mathematical equations grounded in fundamental physical principles to illustrate material performance. Although they often require simplifying assumptions, these models can accurately predict outcomes based on process conditions and provide detailed insights into the physical mechanisms, upon proper calibration. This allows them to capture multiscale and multi-physics interactions crucial for materials like SMAs [175–177]. On the other hand, data-driven modelling relies on empirical data and machine learning (ML) algorithms for optimizing the process through pattern recognition. These models are increasingly integrated into PBF-LB workflows to achieve smart part design, automatic support generation, optimizing part location and build orientation. They can also be utilized for in-situ monitoring, allowing for adjustment of process parameters to counteract defects occurring during the processing by analysing historical data [178,179]. Their ability to adapt to the intricacy and nonlinearity of SMA printing, along with lower computational expenses, makes them highly favourable. However, the requirement of large and high-quality datasets and the produced machine learning algorithm can pose challenges in interpreting the underlying physical significance of their predictions, which is commonly referred to as the "black box" problem [180,181].

These limitations can be mitigated through hybrid approaches integrating physical knowledge into machine learning. This can be seen in the recently emerged techniques such as physics-informed machine learning and physics-informed Bayesian optimization [182–185]. These developments aid in reducing the data requirements, enhance prediction accuracy and shorten the trial-and-error cycle. While these techniques have been effective in predicting phase transformations and thermomechanical behaviour in SMAs and optimizing AM process parameters, they have yet to be fully applied to additively manufactured SMAs. The datasets used for these models range from empirical data, such as micrographs and in situ monitoring results to numerical modelling and simulation outputs, with finite element analysis (FEA) now also being a common and valuable source [140,171,186,187].

2.6.1 Thermal modelling

The inherent complexity of thermodynamics in PBF-LB, characterized by highly localized cooling rates and steep thermal gradients, plays an essential role in determining the final

properties of printed NiTi components. The interplay between thermal history and shape memory alloy behaviour makes thermal modelling particularly significant for understanding and optimizing the PBF-LB process for NiTi [171]. While PBF-LB excels at producing parts with complex geometries, such intricate designs present challenges as geometrical factors heavily influence heat distribution, dissipation, and fluid flow dynamics during processing [188]. For NiTi alloys, accurate thermal modelling is especially critical because the phase transformation temperatures (martensite-austenite transition), transformation hysteresis, and resulting shape memory effects are directly governed by the thermal history experienced during fabrication. Thermal modelling enables tracking of this history, prediction of melt pool dimensions, and estimation of residual stresses and microstructural evolution [171], all of which dictate the functional performance of printed NiTi parts.

Accurate thermal property data for NiTi is fundamental to any modelling approach. Specific properties including material's density (ρ), specific heat capacity (c), and thermal conductivity (k), are obtained either experimentally or, more commonly, via CALPHAD-based thermodynamic software such as Thermo-Calc, JMatPro, or PyCalphad. For NiTi, particular attention must be paid to the temperature dependence of these properties, as the alloy undergoes solid-state phase transformations that alter its thermal behaviour.

2.6.1.1 Physics-based Thermal Modelling for NiTi

Physics-based thermal modelling begins by solving heat transfer equations to simulate temperature distribution during and after laser exposure [171,187]. The transient heat conduction equation forms the foundation:

$$\rho c \frac{\partial T}{\partial t} = \frac{\partial}{\partial x}\left(k \frac{\partial T}{\partial x}\right) + \frac{\partial}{\partial y}\left(k \frac{\partial T}{\partial y}\right) + \frac{\partial}{\partial z}\left(k \frac{\partial T}{\partial z}\right) + Q \quad \textbf{(Eq. 2.6)}$$

The convection and radiation heat transfer equations are expressed respectively in **Eq. 2.7** and **Eq. 2.8** [186,189], where t represents the time, T represents the temperature, and Q is the heat source. Boundary conditions account for convective (Q_c) and radiative heat (Q_{rad}) losses:

$$Q_c = h(T - T_0) \quad \textbf{(Eq. 2.7)}$$

$$Q_{rad} = \varepsilon\sigma(T^4 - T_0^4) \quad \textbf{(Eq. 2.8)}$$

where h is the coefficient of thermal convection, T is the surface temperature and T_0 is the ambient temperature, ε is the material's emissivity, and σ is Stephen Boltzmann's constant. While many models simplify by considering only conduction, the accuracy of predictions for NiTi, particularly regarding melt pool geometry and cooling rates, depends strongly on the heat source formulation. This is typically modelled as a Gaussian volumetric heat source given in **Eq. 2.9**, which provides a spatially distributed energy input resembling the laser beam profile.

$$Q = \frac{2(AP)}{\pi w^2} exp\ \frac{-2r^2}{w^2} \quad \textbf{(Eq. 2.9)}$$

where A is the absorptivity, P is the laser power, w is the laser spot radius and r is the position of the laser beam. However, more sophisticated volumetric heat source models have been developed to better capture the energy distribution in PBF-LB. **Table 2.3** summarizes the key heat source models applicable to NiTi processing, their characteristics, and their relevance for predicting NiTi-specific features.

The Rosenthal equation offers a simplified analytical solution for a moving point heat source on a semi-infinite solid [190]:

$$T - T_0 = \frac{AP}{2\pi kr} e^{-\frac{v(j+r)}{2\alpha}} \quad \textbf{(Eq. 2.10)}$$

where T is the transient temperature in the material, T_0 indicates the initial temperature of the base plate, A is the absorptivity, P the laser power, k is thermal conductivity of the material, and v is the laser scanning speed. The thermal diffusivity, α defined as $\alpha = \frac{k}{\rho C_p}$. Consider a typical PBF-LB process in which the laser scanning is performed along the *x*-axis for a duration t. The distance from the laser beam along this axis will then be *x*-*Vt*, which is replaced by *j* in **Eq. 2.10**. The distance r of any point (x, y, z) on the base plate from the laser beam is defined as $r = \sqrt{j^2 + y^2 + z^2}$. x, y, z are the laser's spatial coordinates along the three Cartesian axes).

The Eagar-Tsai (ET) improves upon Rosenthal by incorporating a moving Gaussian heat source [191]:

$$T - T_0 = \int_0^t \frac{AP(t-t')^{-\frac{1}{2}} e^{\left(-\frac{x^2+y^2}{4\alpha(t-t')+2a^2} - \frac{z^2}{4\alpha(t-t')}\right)}}{\pi\rho C_p \sqrt{4\pi\alpha}(2\alpha(t-t')+a^2)} dt' \quad \textbf{(Eq. 2.11)}$$

where t is the total scanning time, t' represents the instantaneous time, and a is the radius of the laser beam. All the other variables retain their previous definitions. This time-dependent formulation better captures the thermal history experienced by NiTi during processing.

Recent advances have focused on volumetric heat sources that account for energy attenuation through the powder bed. These include the conical, linearly decaying, exponentially decaying, and double-ellipsoidal models as illustrated in **Figure 2.17**. While these volumetric heat source models describe the spatial distribution of laser power within the material volume, they differ in how heat intensity decays with depth and in the radial or axial directions. These differences influence their ability to approximate realistic melt pool geometries in PBF-LB processed NiTi [192].

Table 2.3 Comparison of heat source models for thermal modelling of PBF-LB NiTi.

Model	[Equation] *Key Inputs*	Key Outputs	Advantages	Limitations	NiTi-Specific Relevance
Rosenthal [190]	**[Eq. 2.10]** $P,\ v, A, k,\ \alpha$	Temperature distribution, cooling rates	Analytical, computationally efficient	Neglects convection/radiation, assumes steady state	Provides rapid estimation of cooling rates for predicting martensitic transformation, but underestimates melt pool width and overestimates melt pool depth in NiTi tracks [170]
Eagar-Tsai [193]	**[Eq. 2.11]** $P,\ v, A,\ \alpha, a,\ t$	Temperature field, melt pool geometry	Includes moving Gaussian source, time-dependent	Semi-infinite domain, constant properties	Improved melt pool width prediction with < 10% mean absolute error; but unreliable for estimating melt pool depth of NiTi tracks [170]
Conical [194,195] [196]	**[Eq. 2.12]** P, A, h, w	Volumetric heat distribution, melt pool depth	Captures depth-dependent energy attenuation	Requires calibration of cone height	Useful for predicting penetration depth in NiTi single tracks
Linearly Decaying (LDM) [192,197–199]	**[Eq. 2.14]** $P, w, h,\ \beta,\ v$	Heat flux distribution, maximum penetration depth	Simple analytical form, links to process parameters	β is not universally transferable, requires recalibration.	Applicable for conduction-mode NiTi processing where keyholing is avoided
Exponentially Decaying (EDM) [180–182]	**[Eq. 2.19]** $P, A, w,\ \delta, v$	Depth-dependent energy absorption, melt pool dimensions	Physically grounded (Beer-Lambert), computationally efficient	Assumes homogeneous powder optical properties	Most physically representative for NiTi powder systems; δ governs melt depth
Double-Ellipsoidal (Goldak) [176,177,183,184]	**[Eq. 2.20-2.21]** $P, A,\ v, a_f, a_r, b, c, f_f, f_r$	Asymmetric melt pool geometry, temperature gradients	Captures directional heat flow, experimentally validated for NiTi [200]	Neglects fluid convection, requires extensive calibration	Successfully applied to NiTi [200] with $f_f = 0.4;\ f_r = 1.6;\ b = 10^{-6}$ m and $c = 400 \times 10^{-6}$ m; captures melt pool asymmetry critical for track continuity
FEM (Ansys Additive, CALPHAD) [189,201] [202]	*Full thermal properties, geometry, scan strategy*	Melt pool dimensions, porosity, thermal history, residual stresses	High spatial/temporal resolution, multiphysics capability	Computationally expensive, requires temperature-dependent property calibration	Industry standard for NiTi process optimization; predicts transformation behaviour

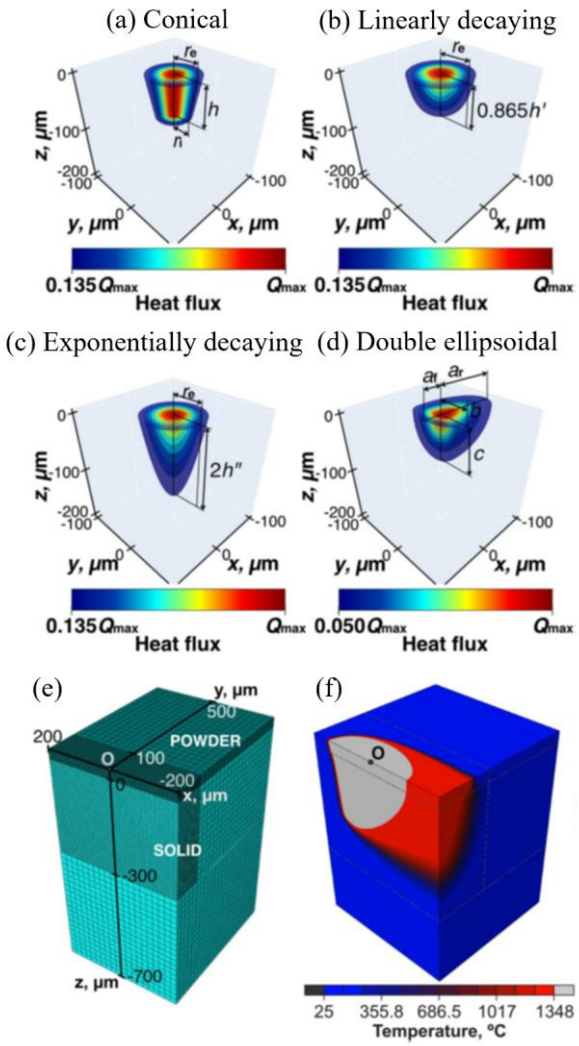


Figure 2.17 Volumetric heat flux distributions with different heat source models (a) conical, (b) linearly decaying, (c) exponentially decaying, and (d) double ellipsoidal; (e) Model for the finite element thermal analysis, and (f) simulated temperature field [195].

While the general heat conduction and analytical models are well-established, a consolidated description of the volumetric heat source models is lacking, particularly for NiTi, where the literature remains sparse. Therefore, the following paragraphs provide an extended overview of these models to establish a coherent foundation and its applicability to NiTi, where available.

The conical volumetric heat source model: The conical volumetric heat source model (**Figure 2.17** a) describes laser energy deposition within a three-dimensional conical volume whose base is located at or near the top surface of the workpiece and whose apex extends into the material [196]. This formulation explicitly captures the variation of heat input along the build direction z, while maintaining a Gaussian heat flux distribution in the radial (x–y) plane at each depth. In this model, the volumetric heat flux is maximal at the top surface $(z = 0)$ and

decreases toward the bottom of the cone ($z = h$). The radius of the energy deposition region decreases linearly with depth, while the peak heat flux along the cone axis is maintained constant. Consequently, the conical heat source can be interpreted as a superposition of Gaussian heat sources with depth-dependent radii and identical central intensities [196].

To satisfy energy conservation, the volumetric heat flux is normalized such that the integral of the heat source over the conical volume equals the absorbed laser power AP. The governing heat flux expression is given as [194,195]:

$$q_{(x,y,z)} = \frac{6AP}{\pi h w^2(z)} exp\left[-3\frac{(x^2+y^2)}{w^2(z)}\right],\ 0 \le z \le h \qquad \textbf{(Eq. 2.12)}$$

where P is the laser power, A is the effective laser absorptivity, h is the conical heat source height (maximum penetration depth), z is the depth measured along the build direction. Outside the domain $0 \le z \le h$, the volumetric heat flux is zero. w is the Gaussian beam radius at the top surface ($z = 0$) is defined as:

$$w(z) = w\left(1 - \frac{z}{h}\right) \qquad \textbf{(Eq. 2.13)}$$

Linearly Decaying Volumetric Heat Source Model (LDM): The LDM assumes that the laser energy input at the powder surface follows a Gaussian distribution in the radial (x–y) plane, and that the heat flux attenuates linearly with depth (z) within a prescribed penetration height. This approach provides a simplified representation of laser attenuation while retaining analytical tractability and is frequently applied in reduced-order melt pool models where shallow, smoothly tapered penetration is desired (**Figure 2.17** b) [192,197–199].

Zhou et al. [198] and Bayat et al. [199] employed this framework for modelling heat deposition in laser sintering and PBF-LB processes, respectively. In this formulation, the laser energy obeys Gaussian decay on the surface and decreases linearly to zero at the **maximum sintered/melting depth** (z_{max}). Consequently, the volumetric heat flux reaches a maximum at the surface ($z = 0$) and diminishes to zero at the prescribed penetration depth. The LDM volumetric heat flux distribution is given as [198]:

$$q_{(x,\ y,\ z)} = \frac{2P}{h\pi w^2} exp\left[-2\frac{(x^2+y^2)}{w^2}\right](1 - \beta z) \qquad \textbf{(Eq. 2.14)}$$

where P is the laser power, w is the Gaussian beam radius (approximated by the laser spot radius), and h is the height of the volumetric heat source taken as the maximum penetration depth ($z_{max} = h$). This yields a conical energy deposition field with $z \in [0, h]$ and $q_{(x,\ y,\ z)} = 0$ at $z = h$.

The linear attenuation coefficient β represents the rate at which energy decreases with depth and is defined as:

$$\beta = {}^{E_L}/_{z_{max}} \quad \textbf{(Eq. 2.15)}$$

where E_L is the incident laser energy at the powder surface. Thus, the available laser energy at any depth z within the powder bed can be expressed as:

$$E_{(x,y,z)} = -\beta z + E_L \quad \textbf{(Eq. 2.16)}$$

The maximum penetration depth $z_{\max}$ follows from a heat-balance criterion in the YOZ plane at $x = 0$, derived under a semi-infinite conduction assumption in which beam absorption is lumped into effective thermal parameters. It accounts for laser dwell time, material thermal properties, and scan velocity [198]:

$$z_{max} = \left\{4\alpha t \ln \frac{\sqrt{2}\alpha I_0 w}{\lambda v T_c (4\alpha t)^{3/2}} \frac{1}{\frac{2}{w^2}+\frac{1}{4\alpha t}}\right\}^{1/2} \quad \textbf{(Eq. 2.17)}$$

where T_c is the melting temperature of the powder, λ is the effective thermal conductivity, α is the effective thermal diffusivity, v is scanning velocity, t is the local dwell time of the laser traveling at v at each position, and I_0 is the beam centre intensity at the spot centre. This expression governs the geometric extent of the heat source and links the decay function directly to process parameters; however, it is not universally transferable to all alloys, scan strategies, or thermal boundary conditions without recalibration. The LDM model is appropriate under conduction-mode conditions where [192,197–199]; (a) phase explosion or evaporation is negligible, (b) keyholing does not occur (no deep vapor cavity formation), (c) melt pool depth remains comparable to the maximum penetration depth, and (d) powder optical properties can be treated as homogeneous.

Exponentially Decaying Volumetric Heat Source Model (EDM): EDM is derived from Beer–Lambert optical attenuation, which models exponentially decreasing absorption with depth:

$$q(z) = q_0 \exp(-\alpha z) \quad \textbf{(Eq. 2.18)}$$

where $\alpha = 1/\delta$ and δ is the optical penetration depth. The radial (x–y) heat flux distribution is modelled as Gaussian, producing a Gaussian–exponential hybrid source that reflects strong near-surface absorption with rapid decay at depth (**Figure 2.17** c) [199,203]. This behaviour is more physically representative of light–metal interaction in powder systems and is widely used in conduction-mode PBF-LB melt pool simulations [204]. Yin et al., [203] implemented this model for a laser moving along the +x direction at velocity v, with the volumetric heat flux expressed as:

$$q_{(x,\ y,\ z,\ t)} = \frac{2AP}{\pi w^2 \delta} exp\left[-2\frac{(x-vt)^2+y^2}{w^2}\right] exp\left[-\frac{|z|}{\delta}\right] \quad \textbf{(Eq. 2.19)}$$

where A denotes the effective laser absorptivity by the powder bed, P is the laser power, w is the Gaussian beam radius at the point where the peak intensity diminishes to $1/e^2$ of its maximum value, δ is the optical penetration depth (Beer–Lambert attenuation length), v is the scan velocity, and $x - vt$ defines the local coordinate in the moving laser frame.

This formulation yields a near-surface energy deposition with heat dissipating rapidly beyond approximately 3δ, naturally constraining heat input to the upper melt region. Relative to the linearly decaying model, δ is the physically grounded depth-governing parameter (versus the geometrically imposed $h = z_{\max}$ in the LDM). This model is valid under the same conduction-mode regime assumptions applied to the LDM framework, specifically, (a) melt pool depth remains comparable to optical penetration depth ($z \sim \delta$), and (b) powder optical response is approximated as homogeneous; multiple scattering is lumped into A and δ. Under these assumptions, the model provides a closed-form, computationally efficient representation of heat deposition and is generally more physically grounded than linear decay formulations for metallic powder systems [199,203].

Double-Ellipsoidal Volumetric Heat Source Model: The double-ellipsoidal heat source model (**Figure 2.17** d), originally proposed by Goldak, represents the moving laser as two three-dimensional ellipsoidal volumetric heat sources located ahead of and behind the beam centreline. The front and rear ellipsoids are assigned different characteristic dimensions and power fractions, allowing the model to capture the inherent asymmetry of experimentally observed melt pools during laser processing [205].

Within each ellipsoid, the volumetric heat flux follows a Gaussian distribution along the longitudinal (scan), transverse, and depth directions. This formulation enables independent control of melt pool length, width, and penetration depth. For a laser scanning along the positive x-direction at velocity v, the volumetric heat flux is expressed as [194,196,200,205]:

$$q(x,y,z,t) = \begin{cases} \frac{6\sqrt{3}\,APf_f}{\pi^{3/2}a_f bc}\exp\left[-3\left(\frac{(x-vt)^2}{a_f^2}+\frac{y^2}{b^2}+\frac{z^2}{c^2}\right)\right], & x \le vt, \\ \frac{6\sqrt{3}\,APf_r}{\pi^{3/2}a_r bc}\exp\left[-3\left(\frac{(x-vt)^2}{a_r^2}+\frac{y^2}{b^2}+\frac{z^2}{c^2}\right)\right], & x > vt, \end{cases} \quad \textbf{(Eq. 2.20)}, \textbf{(Eq. 2.21)}$$

where P is the laser power, v is the laser scan velocity, and A is the effective laser absorptivity. The parameters f_f and f_r denote the fractions of the absorbed laser power assigned to the front

and rear ellipsoids, respectively, with the constraint $f_f + f_r = 2$. The quantities $a_f$and $a_r$are the semi-axis coefficients in the scan direction (x-direction) for the front and rear ellipsoids, respectively, while $b$and $c$are the transverse (y-direction) and depth (z-direction) semi-axis coefficients.

These geometric and power-distribution parameters are not universal constants and must be determined experimentally or calibrated empirically for a given material system and process parameter window. For NiTi alloys, Chernyshikhin et al [200] reported values of $f_f = 0.4$ and $f_r = 1.6$. Using a Bound Optimization BY Quadratic Approximation (BOBYQA) algorithm, they further identified optimal shape coefficients of $b = 10^{-6}$ m and $c = 400 \times 10^{-6}$ m.

The double-ellipsoidal model effectively captures melt pool asymmetry arising from directional heat flow and laser motion [206]. However, it assumes a prescribed longitudinal energy distribution and does not explicitly resolve convective heat transport within the melt pool. As a result, longitudinal heat flow is indirectly represented through the asymmetric ellipsoidal geometry rather than through coupled fluid flow, which can reduce temperature gradients and smooth isotherms in planes normal to the scan direction [205]. In essence, heat conduction is isotropic and melt pool fluid dynamics is neglected. As with the other volumetric heat source models, the double-ellipsoidal models also assumes that powder bed is homogeneous, continuous, and flat; evaporation is neglected [200].

2.6.1.2 Data-Driven Approaches for NiTi Thermal Modelling

While physics-based models remain the predominant approach for thermal simulation of PBF-LB NiTi (**Table 2.3**), data-driven methods are emerging as computationally efficient alternatives. These approaches are particularly attractive for NiTi processing due to the wide parameter space that must be explored to achieve desired transformation temperatures and mechanical behaviour. However, their application to NiTi remains limited, with most studies focusing on other alloy systems.

In thermal simulations, boundary conditions are commonly simplified using convective heat transfer to approximate heat loss mechanisms, helping manage the high computational cost associated with FEM [187,195,207,208]. Data-driven models offer a pathway to further reduce these computational demands while enabling faster predictions, though they are less commonly used for thermal modelling of NiTi specifically. The potential of data-driven approaches for

NiTi lies specifically in their ability to rapidly map the relationship between process parameters and resulting thermal histories—relationships that directly govern the phase transformation behaviour unique to shape memory alloys. This rapid mapping capability is particularly valuable for NiTi because the thermal history determines not only microstructural evolution but also the characteristic transformation temperatures that define the alloy's functional performance.

However, the unique characteristics of NiTi present distinct challenges for purely data-driven approaches. The alloy's composition-dependent transformation temperatures and its pronounced sensitivity to thermal gradients mean that data-driven models must capture highly nonlinear relationships that are specific to NiTi metallurgy. Consequently, training data must adequately sample the parameter space where desirable shape memory properties are obtained, which itself requires careful experimental design. This creates a circular challenge: data-driven models need comprehensive training data from the very parameter space they aim to explore efficiently.

Figure 2.18 demonstrates the inherent interdependence of thermal and microstructural phenomena in NiTi processing, showing how Hosseinzadeh et al. [187] incorporated melt pool dimensions and thermal behaviour into a computational algorithm to model NiTi microstructural evolution. Addressing these coupled phenomena typically requires physics-based modelling, which captures the underlying physical interactions governing NiTi's unique behaviour. Data-driven and machine learning approaches offer alternative routes when thermal behaviour is not modelled explicitly, enabling property predictions based on empirical correlations rather than first principles.

For NiTi, such approaches could potentially predict transformation temperatures, recoverable strain, or superelastic response directly from process parameters, thereby bypassing detailed thermal simulation. This direct prediction capability is particularly appealing for NiTi because the functional properties are costly and time-consuming to characterize experimentally. However, the limited availability of high-quality NiTi processing data and the alloy's intrinsic sensitivity to both composition and thermal history currently constrain the generalizability of purely data-driven models.

These constraints suggest that for NiTi, the most effective approach may combine physics-based understanding with data-driven efficiency, leveraging the strengths of each while mitigating their individual limitations.

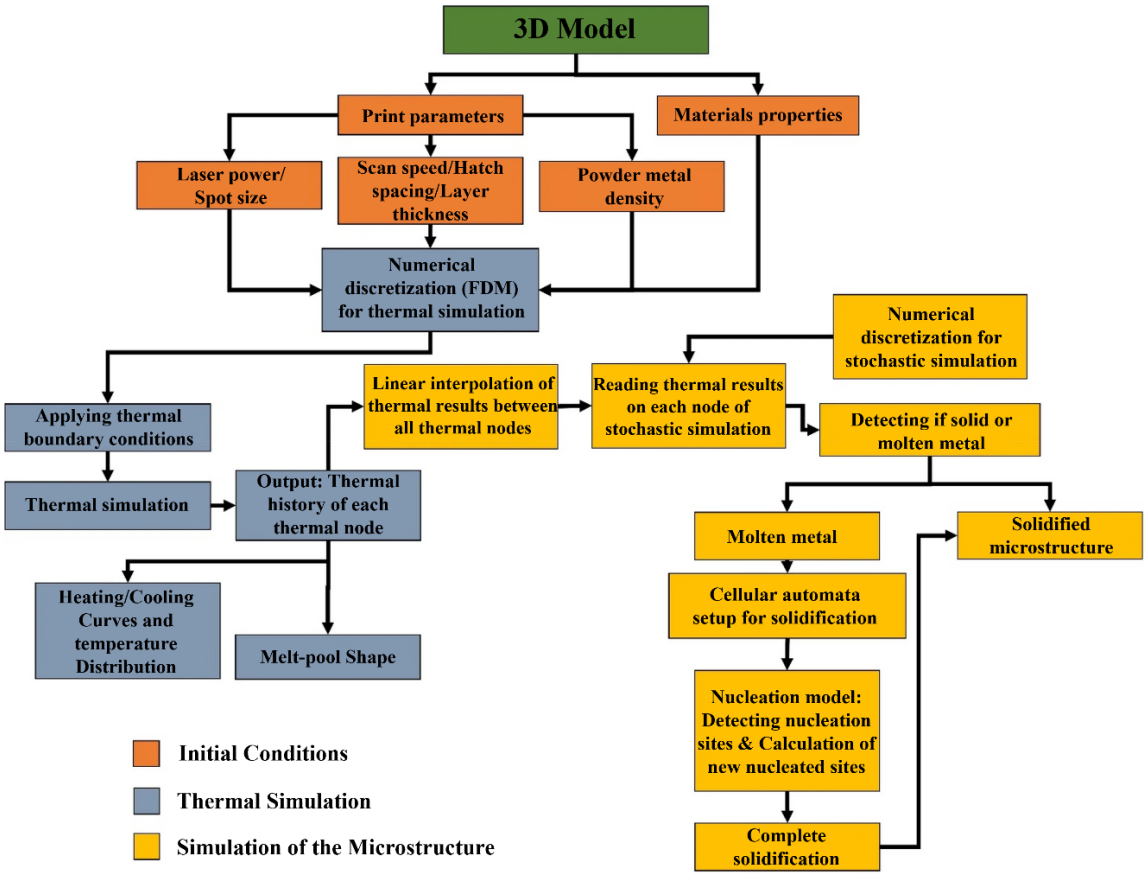


Figure 2.18 A computation flowchart for thermal and microstructural simulation of PBF-LB NiTi [187].

2.6.2 Melt pool modelling

Melt pool dimensions are fundamental because they directly influence the microstructure and defects of the solidified material, which affects the mechanical properties of the finished part. Using analytical models for thermal modelling is an advantageous alternative to FEM, offering a simpler, more efficient approach to predicting melt pool dimensions, notably width and depth. Rosenthal laid the basis and the theory for using a heat conduction model to predict melt pool formation, and the Rosenthal equation is still applied for this purpose. Nevertheless, Rangaswamy et al. [170] established that this model produced results with lower accuracy when it came to the melt pool dimensions of NiTi in PBF-LB. The Eagar-Tsai (ET) thermal

model is another widely employed approach to predict the geometry of the melt pool. Rangaswamy et al. [170] also observed that this model provided a more accurate prediction of the melt pool width for NiTi in PBF-LB compared to the Rosenthal model, but it fell short in reliably predicting the melt pool depth. The Gladush and Smurov [209] model is frequently utilized as a correction tool alongside other analytical models and was specifically developed to address melt pool depth, which is the most challenging aspect to predict. Chernyshikhin et al. [200] employed COMSOL Multiphysics software to develop a model that estimates the melt pool dimensions of NiTi during PBF-LB, shown in **Figure 2.19**. As mentioned previously, the finite element method plays an important part for modelling melt pool dimensions through thermal simulations, providing reliable predictions when employing volumetric heat sources. However, its predictive effectiveness is limited under conditions of high energy density, necessitating specific modifications to accurately depict the transition from conducting to keyhole melting mode [208,210]. Similar to other elements of PBF-LB, melt pool dimensions can also be predicted using data-driven modelling techniques. Commonly utilized machine learning methods, such as principal component analysis, support vector machines, and linear discriminant analysis, have demonstrated their effectiveness in predicting melt pool geometries. Among these, artificial neural networks (ANN) models are particularly valuable due to their robust integration of the multi-scale dimension, which is critical for analysing melt pools. Specifically, convolutional neural networks (CNNs) are frequently central to various modelling frameworks because they are tailored for tackling issues related to images and acoustic emissions [211,212]. Fang et al. [213] employed this model within their probabilistic data-driven framework, that incorporates for process noise and uncertainty. Similarly, Vaghefi et al. [188] combined it with a deep multilayer perceptron to accurately predict melt pool depth, achieving a commendable accuracy rate of 95% even for previously unseen part geometries post-training. Straying away from traditional techniques, Hang et al. [211] presented a dimensional analysis framework offering enhanced generality compared to earlier studies as it utilizes experimental data from a range of materials and additive manufacturing machines.

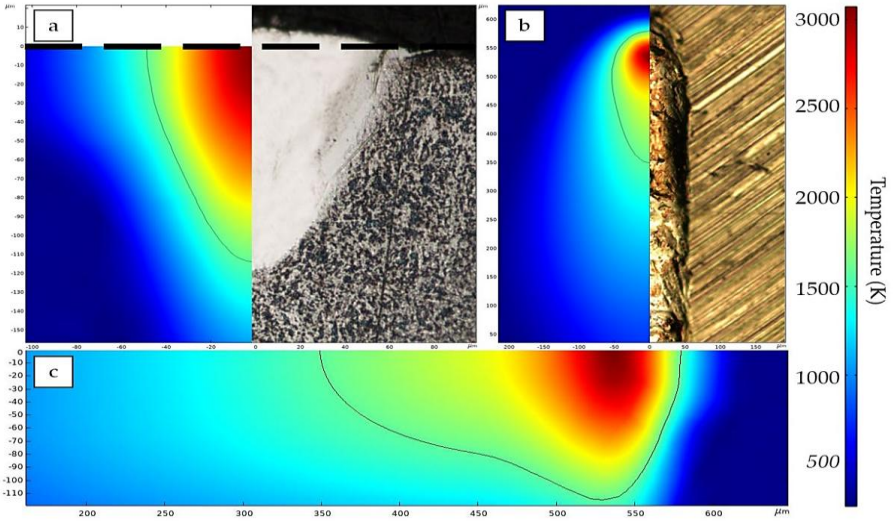


Figure 2.19 A comparison between predicted and experimental observations of melt pool of NiTi (a) cross-sectional view, (b) top-view, and (c) longitudinal cross-section [200].

2.6.3 Residual Stress Modelling

Residual stress modelling in PBF-LB is typically performed using thermo-mechanical frameworks that couple temperature evolution with elastic–plastic deformation. Because residual stresses originate from highly non-uniform heating and cooling cycles, modelling approaches usually begin with the prediction of the temperature field and subsequently determine the resulting thermoelastic stresses.

The resulting thermal gradients generate thermal strains that contribute to residual stress formation. The total strain in the material can be expressed as:

$$\varepsilon_{total} = \varepsilon_e + \varepsilon_p + \varepsilon_{th} \quad \textbf{(Eq. 2.22)}$$

where ε_e, ε_p, and ε_{th} represent elastic strain, plastic strain, and thermal strain, respectively. The thermal strain component is given by:

$$\varepsilon_{th} = \alpha(T - T_0) \quad \textbf{(Eq. 2.23)}$$

where α is the coefficient of thermal expansion and T_0 is the reference temperature. Residual stresses arise when thermal contraction during cooling is constrained by surrounding material or previously solidified layers.

Analytical modelling approaches have also been developed to relate residual stress directly to processing parameters. For example, simplified analytical formulations relate the residual stress magnitude to the thermal gradient and elastic modulus:

$$\sigma_{res} \approx E\alpha\Delta T \quad \textbf{(Eq. 2.24)}$$

where E is the Young's modulus and ΔT represents the temperature difference between the melt pool and the surrounding material. Such analytical models provide a rapid method for estimating residual stress trends and evaluating the influence of process parameters such as laser power, scan speed, and hatch spacing. However, high-fidelity thermo-mechanical finite element models remain necessary to accurately capture the complex interactions among heat transfer, mechanical constraints, and layer-wise deposition in PBF-LB processes [214,215].

In classical thermal stress mechanics, the thermoelastic potential function is commonly used to evaluate thermal stresses under plane strain conditions. To simplify the analysis of thermal stresses in the PBF-LB process, the thermoelastic potential function can be indirectly related to the temperature distribution field, which is obtained from thermal modelling of the process [216,217]. By replacing the thermoelastic potential function with the temperature distribution function $T(x, y, z)$, the stress components can be expressed in terms of the temperature gradients as:

$$\sigma_x^* = -2\mu \frac{\partial^2 T}{\partial y^2} \quad \textbf{(Eq. 2.25)}$$

$$\sigma_y^* = -2\mu \frac{\partial^2 T}{\partial x^2} \quad \textbf{(Eq. 2.26)}$$

$$\sigma_z^* = -2\mu \left(\frac{\partial^2 T}{\partial x^2} + \frac{\partial^2 T}{\partial y^2}\right) \quad \textbf{(Eq. 2.27)}$$

where σ_x^*, σ_y^*, and σ_z^* represent the indirectly calculated thermal stresses along the x, y, and $z$directions, respectively, T denotes the temperature field, and μ is the shear modulus. These relations enable the estimation of thermal stresses directly from the predicted temperature distribution, which is typically obtained using analytical or numerical heat transfer models of the PBF-LB process. This approach provides an efficient way to link temperature gradients to stress development during the layer-by-layer fabrication process.

More advanced analytical formulations predict thermal stresses by employing Green's functions associated with point body loads [218,219]. In this framework, the thermal stress field induced by non-uniform heating can be expressed as a superposition of stresses due to body forces, normal tractions, and hydrostatic stresses. For example, the stress component in the scanning direction can be expressed as:

$$\sigma_{xx}(x,z) = -\frac{\alpha(T)E(T)}{1-2\nu(T)} \int_0^\infty \int_{-\infty}^\infty \left(G_{xh}\frac{\partial T}{\partial x} + G_{xv}\frac{\partial T}{\partial z}\right) dx'dz' + \frac{2z}{\pi}\int_{-\infty}^\infty \frac{p(s)(s-x)^2}{((s-x)^2+z^2)^2} ds - \frac{\alpha(T)E(T)T(x,z)}{1-2\nu(T)} \quad \textbf{(Eq. 2.28)}$$

$$\sigma_{zz}(x,z) = -\frac{\alpha(T)E(T)}{1-2\nu(T)}\int_0^{\infty}\int_{-\infty}^{\infty}\left(G_{zh}\frac{\partial T}{\partial x} + G_{zv}\frac{\partial T}{\partial z}\right)dx'dz' + \frac{2z^3}{\pi}\int_{-\infty}^{\infty}\frac{p(s)}{((s-x)^2+z^2)^2}ds - \frac{\alpha(T)E(T)T(x,z)}{1-2\nu(T)} \quad \textbf{(Eq. 2.29)}$$

$$\sigma_{xz}(x,z) = -\frac{\alpha(T)E(T)}{1-2\nu(T)}\int_0^{\infty}\int_{-\infty}^{\infty}\left(G_{xzh}\frac{\partial T}{\partial x} + G_{xzv}\frac{\partial T}{\partial z}\right)dx'dz' + \frac{2z^2}{\pi}\int_{-\infty}^{\infty}\frac{p(s)(s-x)}{((s-x)^2+z^2)^2}ds \quad \textbf{(Eq. 2.30)}$$

$$\sigma_{yy}(x,z) = \nu(T)(\sigma_{xx}+\sigma_{zz}) - \alpha(T)E(T)T(x,z) \quad \textbf{(Eq. 2.31)}$$

where α is the thermal expansion coefficient, E is Young's modulus, and $G_{xh}, G_{xv}, G_{zh}, G_{zv}$ are plane-strain Green's functions describing the stress response to temperature gradients.

To predict the final residual stress state, the thermal stresses must be coupled with the material constitutive model, which describes plastic deformation at high temperature. One widely used model in additive manufacturing simulations is the Johnson–Cook flow stress model, which accounts for strain hardening, strain-rate sensitivity, and thermal softening [220,221]:

$$\sigma = (A + B\varepsilon_p^n)\left(1 + C\ln\frac{\dot{\varepsilon}_p}{\dot{\varepsilon}_0}\right)\left(1-\left(\frac{T-T_0}{T_m-T_0}\right)^m\right) \quad \textbf{(Eq. 2.32)}$$

where ε_p is the effective plastic strain, $\dot{\varepsilon}_p$ is the plastic strain rate, T is the material temperature, T_m is the melting temperature, and A, B, C, n, m are material constants.

Overall, these analytical and numerical formulations provide valuable insight into the formation of residual stresses in PBF-LB processes. However, most analytical models neglect geometric complexity and assume bulk temperature-dependent material properties. For NiTi alloys, residual stress modelling becomes more challenging due to the strong temperature dependence of material properties and the presence of stress-induced martensitic phase transformations, which can significantly influence stress evolution during cooling. Therefore, advanced modelling approaches increasingly integrate thermo-mechanical coupling with transformation kinetics and process parameter effects to better predict residual stress distributions in additively manufactured NiTi components. Consequently, high-fidelity finite element simulations are often required to capture the full thermo-mechanical behaviour, particularly for complex geometries and materials with temperature-dependent phase transformations such as NiTi alloys. The model employed by Ma et al. [139] for residual stress prediction in PBF-LB NiTi is shown in **Figure 2.20**.

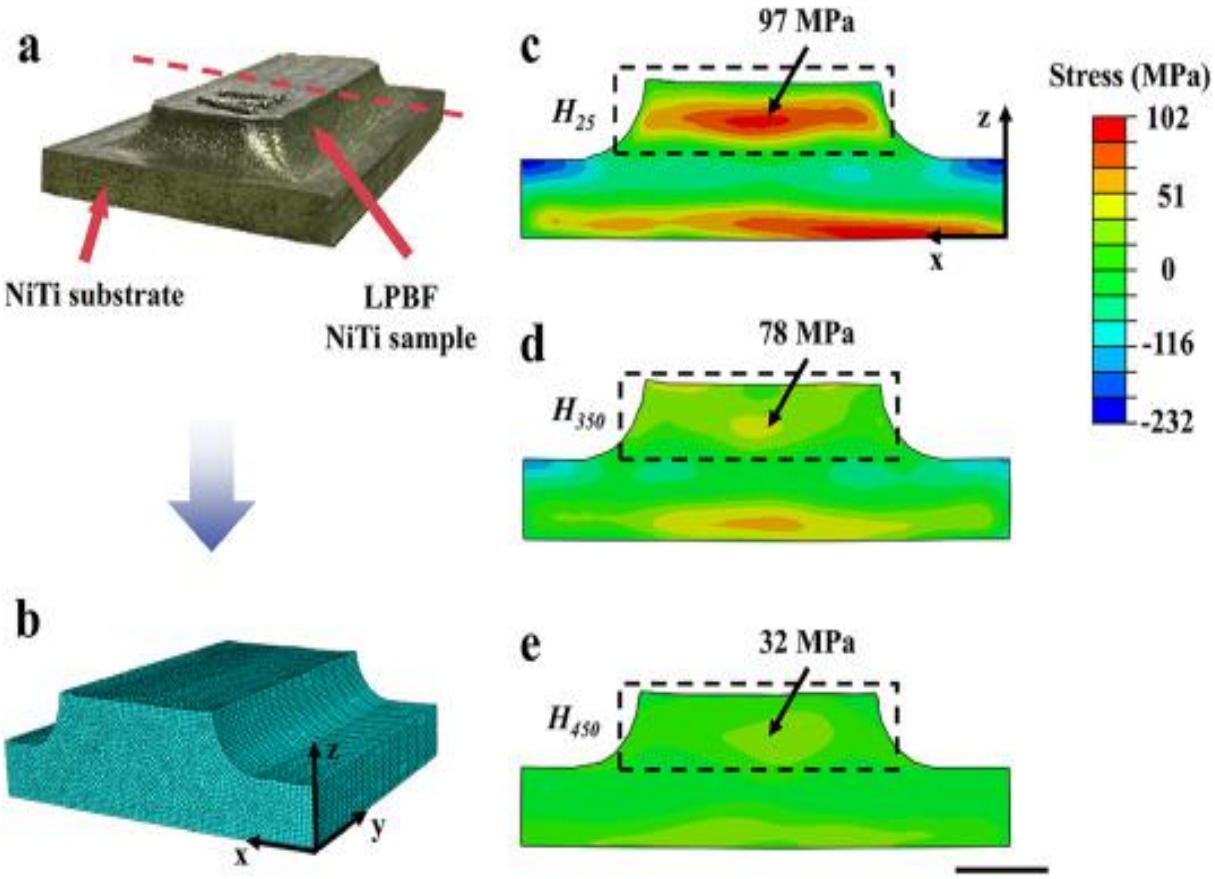


Figure 2.20 (a) PBF-LB printed NiTi (b) The model developed for residual stress evaluation. The contour method results for residual stress distribution for samples heat-treated at temperatures (c) 25, (d) 350, and (e) 450 [139].

2.6.4 Microstructure modelling

Microstructural modelling is crucial for simulating PBF-LB parts since microstructure directly influences mechanical properties, with grain orientation being significant in anisotropy, necessitating a good understanding of its features to ensure part reliability. Most models utilize multi-scale frameworks, enabling better comprehension of the various subprocesses involved in PBF-LB and facilitating precise predictions [222,223]. As previously mentioned, thermal history is a primary method for assessing solidification and microstructural changes such as grain growth, phase transformations, and texture development. The majority of microstructure modelling techniques are numerical and rely on this thermal history; for example, cellular automata (CA), Monte Carlo (MC), and phase field (PF) methods are commonly employed. The MC method is a meso-scale model that uses random samples to represent the system and is often linked to the Metropolis algorithm for alloys. It iteratively models microstructure evolution by computing energy changes resulting from random

modifications to the microstructure in order to accept or reject these changes until equilibrium is achieved [224,225]. CA is also a meso-scale technique, while PF is a micro-scale model; however, they share similarities as both employ an updating grid of cells, with their distinction lying in how they define the interface between solid and liquid regions [223,226]. In CA, the interface consists of a layer of cells, while PF relies on the progression of phase field variables. Since these variables spread over multiple grid nodes, the PF method requires finer grid spacing to accurately resolve the smallest components of the microstructure. Combined with CA's discrete nature, this leads to PF methods incurring higher computational expenses [171,187,227]. Although these techniques are frequently applied for microstructure simulations, their substantial computational demands often limit their application to small areas, a challenge that is evolving rapidly [228]. For instance, Zinovieva et al. [228] tackled this issue by integrating CA with finite differences to model a large-scale component and predict the grain structure, achieving definitive results for Inconel 718. Hosseinzadeh et al. [187] developed a computer simulation tool to estimate the microstructural evolution of NiTi alloys using a multiscale multi-physics model. Their simulation tool is rooted in a thermal finite-difference model linked to the CA method, enabling effective predictions of the 3D printed grain morphologies and thereby laying a foundation for future investigations. Other novel strategies are being formulated to model microstructure, including computational techniques that connect distinct models of the various subprocesses involved in PBF-LB, as illustrated by Cummins et al. [227], who strived to establish a unified and customizable modelling framework. Data-driven methodologies once again play a vital role in accurately predicting melt pool microstructure while being more efficient in terms of time and resources. Qadeer et al. [229] employed a data-driven model trained with microstructure predictions from Ansys physics-based numerical model as datasets (an example of these predictions can be found in **Figure 2.21**). They noted in their work enhanced predictive capabilities through their use of convolutional neural networks applied to the FEA datasets.

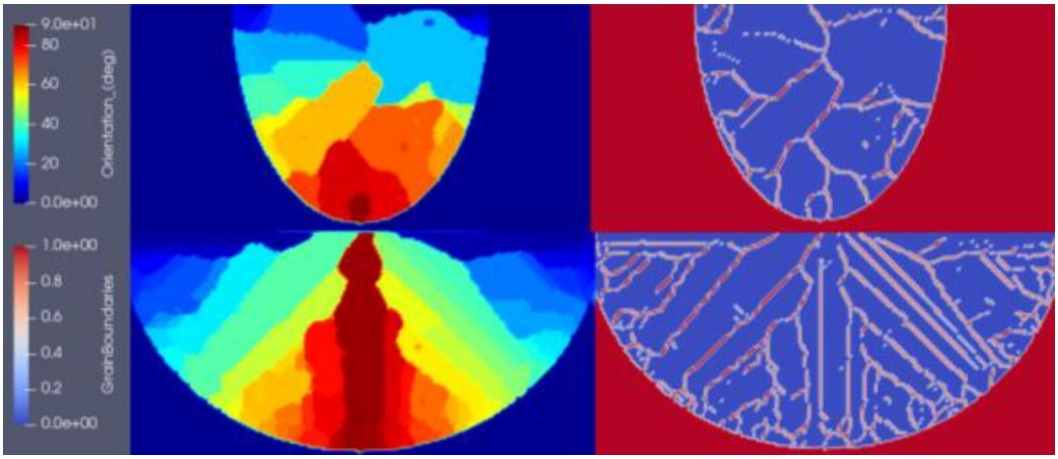


Figure 2.21 Ansys Additive suite microstructure simulation depicting grain orientation and boundary [229].

Validation of microstructure modelling frameworks for PBF-LB NiTi typically relies on comparison with experimentally characterized grain structures and phase distributions. Techniques such as electron backscatter diffraction (EBSD) and scanning electron microscopy (SEM) are commonly used to examine grain morphology, orientation, and texture predicted by numerical simulations. In addition, X-ray diffraction (XRD) and differential scanning calorimetry (DSC) measurements are often employed to validate predicted phase fractions and transformation temperatures, providing experimental benchmarks for assessing the accuracy of simulated microstructural evolution and its implications for functional behaviour. Despite advances in microstructure modelling, accurately predicting functional behaviour in PBF-LB NiTi remains challenging because small process-induced composition changes, particularly nickel evaporation, can shift transformation temperatures and alter the balance between shape memory and superelastic responses.

2.6.5 Derived predictions

Additionally, modelling of PBF-LB process enables the prediction of phase transformation, residual stress and distortion as well as other defects. In particular, multiscale modelling strategies are crucial in capturing these phenomena appropriately. For instance, physics-based defects prediction is often based on melt pool morphology modelling as most porosities are directed by the melting modes and process parameters. Parsazadeh et al. [230] developed an optimized mathematical model that can predict melt pool morphology and determine the area fraction of lack-of-fusion, yielding satisfactory predictions of the fraction, although it cannot precisely locate these defects. This model was trained based on experimental data obtained

from SS316L, though it is claimed to be independent from the thermophysical properties of the modelled material. Data-driven machine learning methods can facilitate the prediction of these defects by enabling the identification of patterns related to the process parameters and are especially useful for real time in situ detection which allows to adjust the process parameters to minimize defects [171]. Zhao et al. [231] presented a novel method employing deep learning on 3D point clouds rather than the conventional 2D image-based monitoring, thus overcoming some of the latter's limitations related to lighting and inadequate data capture, while accurately identifying three-dimensional defects. They observed that mechanical properties are influenced by the chemical composition, along with numerous other facets of the printing process. Microstructure and phase transformation are pivotal for achieving optimum mechanical properties highlighting the impact of the alloy's thermal behaviour, alongside defects, surface quality, and build direction as other important contributors [171].

Mehrpouya et al. [232] utilized an ANN trained on experimental data to predict how processing parameters affect the mechanical behaviour of NiTi, focusing on transformation temperatures and strain recovery ratios, achieving commendable accuracy in comparison with experimental findings. Residual stress and distortion are typically derived from thermal modelling such as melt pool behaviour and microstructure, although a few studies incorporate mechanical loads with the inherent strain method (ISM). This method offers the advantage of reducing computational effort but faces notable limitations in precision as a trade-off [207]. To simulate the addition of layers in PBF-LB, ISM requires the use of discrete layers characterised by a thickness that is a multiple of the actual powder layer thickness. They are called lumped layers, and they greatly influence the precision of this modelling method along with the mesh size employed. Monu et al. [145] used this approach to analyse the effect of bi-directional scan pattern on residual stress and distortion in NiTi parts produced via PBF-LB. The residual stress distribution was found to correlate well with the in situ melt pool temperature data collected during the process.

Although modelling efforts for PBF-LB NiTi are advancing, the prediction of residual stress, distortion, and their interaction with phase transformation behaviour remains relatively limited compared with other additively manufactured alloys. Extending modelling frameworks successfully applied to other materials may therefore provide valuable pathways for improving predictive capability in NiTi systems, where thermo-mechanical coupling and phase transformation effects are particularly important.

For example, Benchabane et al. [233] employed a mesoscale thermomechanical finite element model to investigate the influence of build plate preheating on residual stress and distortion in

Inconel 718 cantilever specimens. Their study demonstrated that such models can capture the characteristic deflection behaviour observed experimentally (**Figure 2.22**), highlighting their potential for predicting distortion in PBF-LB components. Similarly, Zhang et al. [234] developed a high-resolution ISM for Hastelloy X that incorporated actual layer thickness rather than the lumped layers commonly used in conventional ISM approaches. Comparison with experimentally measured residual strains showed improved predictive accuracy relative to traditional ISM models.

While these approaches have been validated for nickel-based superalloys, their application to NiTi remains relatively unexplored. Adapting such thermomechanical and inherent strain modelling frameworks to account for NiTi-specific phenomena, including phase transformation behaviour and composition-dependent material properties, could significantly improve the prediction of residual stress, distortion, and functional performance in additively manufactured NiTi components.

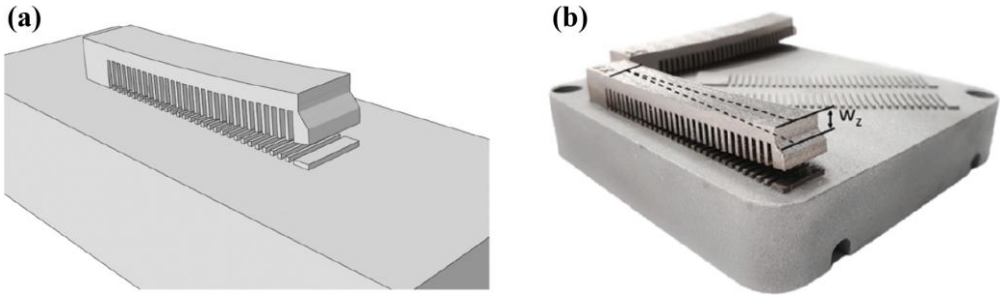


Figure 2.22 Beam deflection after removing the supports showing the (a) numerical modelling and (b) a picture of the corresponding experimental measurement result [233].

2.7 Summary of the literature review

This review has examined the state of modelling and process optimization strategies for the additive manufacturing of NiTi using PBF-LB, with a particular focus on understanding and predicting melt pool behaviour, microstructural evolution, defect formation, and functional performance. Achieving high-quality, defect-free NiTi components remains challenging due to the alloy's sensitivity to composition, its complex thermo-mechanical phase transformation behaviour, and the tightly coupled thermal and kinetic phenomena intrinsic to the PBF-LB process. From this literature review, it is evident that process parameter optimization and robust modelling are central to addressing these challenges.

Both physics-based and data-driven modelling approaches play complementary roles in advancing understanding and control of PBF-LB of NiTi. Finite element and analytical models

provide mechanistic insight into heat transfer, melt pool dynamics, residual stress development, and defect mechanisms, but their predictive capability is constrained by computational cost and the limited availability of reliable high-temperature thermophysical and mechanical property data for NiTi. Data-driven approaches, including machine learning and surrogate models, offer rapid prediction and optimization capabilities but often lack physical interpretability and generalizability beyond the datasets on which they are trained. Emerging hybrid strategies, most notably physics-informed machine learning, represent a promising pathway to bridge this gap by embedding physical constraints into data-driven frameworks, thereby improving robustness while reducing data requirements.

Within this context, several interconnected research directions emerge as critical for progressing PBF-LB of NiTi from laboratory-scale demonstrations toward reliable, industrial adoption. First, there is a clear need for integrated multi-physics and multi-scale modelling frameworks capable of simultaneously capturing thermal transport, microstructure evolution, phase transformation behaviour, and mechanical response. Such frameworks are particularly important for NiTi, where functional properties are highly sensitive to local thermal histories and compositional variations. Second, the predictive fidelity of all modelling approaches is fundamentally limited by the availability of accurate high-temperature material property data. Systematic experimental efforts to populate and validate thermophysical and mechanical property databases for NiTi across the relevant temperature ranges are therefore essential. Third, advances in in-situ monitoring and real-time closed-loop control offer a direct route to mitigating defects and process variability. When coupled with fast predictive models and artificial intelligence, real-time feedback control can enable adaptive parameter adjustment during fabrication, addressing melt pool instability, compositional fluctuations, and defect formation as they occur. Fourth, while physics-informed machine learning has shown promise in broader additive manufacturing contexts, its application to shape memory alloys remains underexplored. Targeted development of these methods for NiTi could substantially enhance predictive capability and accelerate process optimization while maintaining physical consistency. Finally, continued emphasis on experimental validation and standardization is required. Benchmark datasets, standardized testing protocols, and cross-comparison of modelling approaches are necessary to establish confidence in predictive tools and to facilitate meaningful comparison across studies.

Overall, further advances in modelling fidelity, data integration, and experimental validation are essential to fully realize the potential of PBF-LB for NiTi. Addressing these challenges will not only improve process reliability and component performance but also support the broader adoption of additively manufactured NiTi in high-precision, mission-critical applications where functional reliability is paramount.

3. Chapter: Investigating Melt Pool Dimensions in Laser Powder Bed Fusion of Nitinol - An Analytical Approach

---

Publication Status: Published

Sampreet Rangaswamy, Declan Bourke, Medad C.C. Monu, Paul Healy, Hengfeng Gu, Inam Ul Ahad, Dermot Brabazon, **Investigating Melt Pool Dimensions in Laser Powder Bed Fusion of Nitinol: An Analytical Approach**, Advanced Engineering Materials 26 (2024).

https://doi.org/10.1002/adem.202401636

Abstract

This study focuses on single-track nitinol samples fabricated via PBF-LB. Investigating the effects of laser power and scanning speed on melt pool dimensions revealed that melt pool width increases linearly with laser power and decreases logarithmically with scanning speed. However, melt pool depth exhibited outliers that deviated from these trends. Three analytical models were evaluated to predict melt pool dimensions, generally aligning with experimental trends. Notably, the Eagar-Tsai model delivered the most accurate predictions for melt pool width, with a mean absolute error of less than 10%, while the Gladush-Smurov model was more reliable for melt pool depth predictions, showing a mean absolute error under 20%. In contrast, the Rosenthal equation yielded less reliable results for both dimensions. This suggests that a combined approach utilizing the strengths of both the Eagar-Tsai and Gladush-Smurov models may provide the most accurate predictions for the melt pool profile of NiTi in PBF-LB.

3.1 Introduction

Analytical models serve as a favorable alternative to the intricate, time-consuming and computationally expensive finite-element modelling (FEM). Phenomenon that occur within metal AM include light absorption, solid to liquid and liquid to solid phase transformations, solid state phase transformations, Marangoni fluid flow, preferential elemental evaporation, convection, conduction, radiation, and spatter formation. Given that AM involves multiple physical phenomena, diverse models have been developed to examine distinct aspects of these processes; however, modelling the complex process of PBF-LB remains challenging [15–17]. Models help manufacturers predict the properties of the finished part before the process begins, saving time, energy, and resources. Numerous models in the literature are developed for laser welding and additive manufacturing. These models can predict various properties, but melt pool dimensions are fundamental because they directly influence the microstructure of the solidified material, which affects the mechanical properties of the finished part. There is limited literature on using and developing analytical models for additive manufacturing of NiTi, given the material's complexity, leaving a significant knowledge gap. This study investigates three commonly used analytical methods in laser-based additive manufacturing/welding—namely, the Rosenthal equation (RE), Eagar-Tsai (ET) model, and Gladush and Smurov (GS) model—to estimate the melt pool width and depth of nitinol during PBF-LB. The obtained results were then compared against experimental measurements of the melt pool dimensions to evaluate the prediction accuracy of these models. The findings of this research are anticipated to contribute to our understanding of the predictive capabilities of these analytical methods in modelling NiTi melt pool characteristics, thereby aiding in the optimization of laser-based additive manufacturing processes.

3.2 Materials and Methods

3.2.1 Experimental Details

The production of single tracks on a nitinol base plate using the Aconity MINI (GmbH) metal 3D printer was accomplished by applying a layer of gas-atomized, pre-alloyed nitinol powder. The printer utilized a laser with a wavelength of 1068 nm and a power capacity of 200 W. The pre-alloyed nitinol powder had an atomic composition of 50.3% nickel and 49.7% titanium,

with particle sizes ranging from 29-68 µm. To maintain a low oxygen level in the build chamber and minimize contamination, argon was used as a shielding gas.

The nitinol base plate had dimensions of 95mm x 95mm x 6mm, and a powder layer with a thickness of 60 µm was applied. For the design of experiments (DoE), a 5x5 matrix was employed, varying the laser power (P) from 100 W to 180 W and the scanning speed (V) from 0.2 m/s to 1 m/s. The laser spot size (beam radius) was kept constant at 35 µm. A total of 25 single-track samples were produced using different combinations of these parameters. **Table 3.1** outlines the parameter levels employed in this study, along with the corresponding calculation of linear energy density (E_L), defined as the ratio of power to speed.

A Keyence VHX2000 3D optical microscope was used to measure the melt pool widths and depths (see **Figure 3.1** a-b). To examine the melt pool cross sections, they were cut by Electrical Discharge Machining (EDM) at a distance of 2 mm from the end of the track. Following this, the samples were embedded in a cold resin mount. Subsequently, they underwent a grinding process using silicon carbide papers ranging from 80 to 4000 grit. This was followed by polishing with diamond suspension with particle sizes of 9, 6, 3, 1, and 0.6 µm, at a rotary speed ranging from 250 to 300 rpm. Additionally, a chemical solution consisting of 5 ml nitric acid (HNO_3), 4 ml hydrofluoric acid (HF), and 40 ml de-ionized (DI) water was employed for etching the samples.

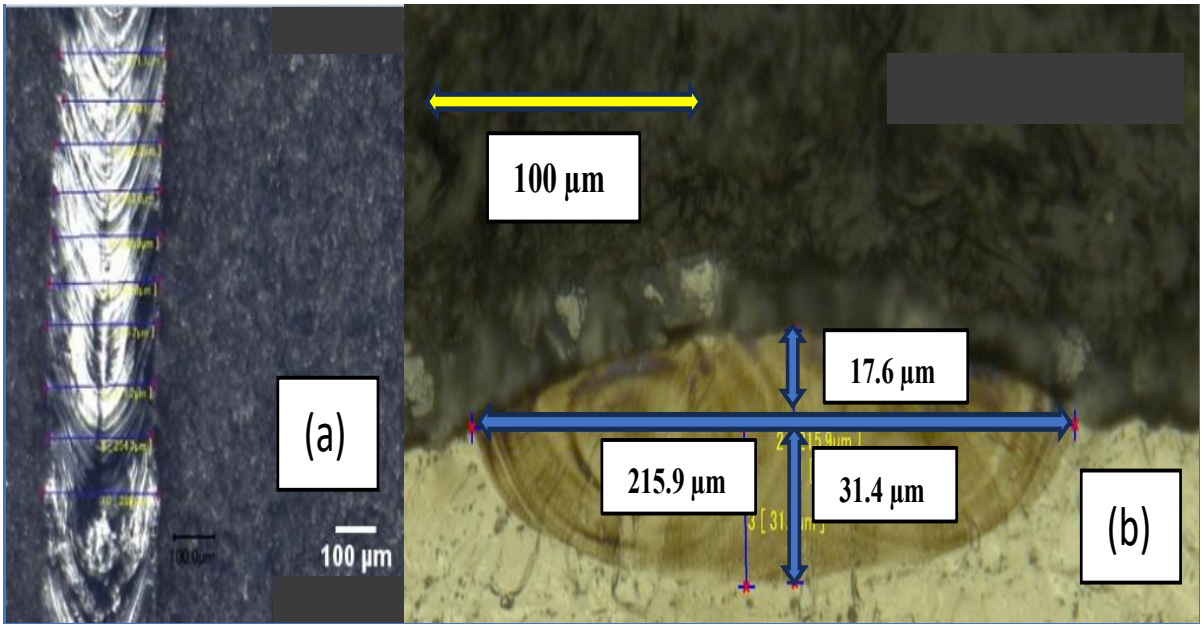


Figure 3.1 Measurement of (a) track width from plan view; and (b) melt pool dimensions from transverse cross-sectional view.

Table 3.1 Parameter levels used for the production of the NiTi single tracks.

P (W)	V (m/s)	E_L (P/V) (J/m)
	0.2	500
	0.4	250
100	0.6	170
	0.8	130
	1	100
	0.2	600
	0.4	300
120	0.6	200
	0.8	150
	1	120
	0.2	700
	0.4	350
140	0.6	230
	0.8	180
	1	140
	0.2	800
	0.4	400
160	0.6	270
	0.8	200
	1	160
	0.2	900
	0.4	450
180	0.6	300
	0.8	230
	1	180

3.2.2 Modelling Details

Rosenthal equation (RE), Eagar-Tsai (ET) model, and Gladush and Smurov (GS) models, the three commonly used analytical models for predicting melt pool dimensions in laser welding and additive manufacturing, are explored. An advantage of using these analytical models is that they can be easily implemented using available spreadsheet applications like MS Excel,

rather than requiring the use of sophisticated and proprietary software. These models assume temperature-independence of the properties of the material. The properties of NiTi needed for the models were sourced from literature or determined using the CALPHAD method through Thermo-Calc 2024a software, utilizing the TCNI11 database [103,200,235]. The properties were obtained with respect to the melting temperature of NiTi (1583 K), given that this temperature represents the point of maximum energy deposition [236]. The properties of NiTi used in this work are given in **Table 3.2**.

Table 3.2 Thermo-physical properties of NiTi used in the analytical models for calculating the melt pool dimensions.

Property (Unit)	**Value**	**Ref.**
Thermal conductivity, k (W/mK)	20	CALPHAD, [235]
Specific heat capacity, C_p (J/kgK)	700	CALPHAD
Density, ρ (kg/m^3)	6100	CALPHAD, [103]
Thermal Diffusivity, α (m^2/s)	4.8 x 10^{-6}	CALPHAD
Laser absorptivity, A	0.3 - 0.4	[103,200,235]
Melting temperature, T_m (K)	1583	[103,200]
Boiling Temperature, T_b (K)	3033	[103,200,235]

3.2.2.1 Rosenthal Equation (RE) model

The Rosenthal equation [190], as presented in **Eq. 3.1**, provides a simplified analytical solution to the heat conduction equation for a moving point heat source on a semi-infinite solid geometry. This model enables the prediction of several thermal phenomena, including temperature gradients, thermal histories, cooling rates, and solidification rates. However, it is subject to limitations due to inherent assumptions such as steady-state conditions, constant and uniform material properties, a point heat source, and the omission of factors like heat loss through convection and radiation, latent heat during phase transformation and fluid flow within the molten pool [237,238].

$$T - T_0 = \frac{AP}{2\pi kr} e^{-\frac{V(j+r)}{2\alpha}} \quad \textbf{(Eq. 3.1)}$$

where T is the transient temperature in the material, T_0 is the initial base plate temperature, A is absorptivity, P is the laser power, k is thermal conductivity of the material, V is scanning speed, α is thermal diffusivity given by $\alpha = {}^{k}/_{\rho C_p}$, ρ represents the material density, and C_p is the specific heat capacity. Consider a typical PBF-LB process where the laser scanning is performed along the x-axis for a duration of time t. The distance from the laser beam along the

axis will then be x-Vt, which is replaced by j in **Eq. 3.1** and r is the distance of any point (x, y, z) on the base plate from the laser beam defined as $\sqrt{j^2 + y^2 + z^2}$ (x, y, z are the laser beam scanning distances along the three axes of the Cartesian coordinate system).

Tang et al. [239] derived an equation for melt pool width given in **Eq. 3.2** based on the Rosenthal equation and tested it on aluminium, titanium and steel alloys. They assumed the melt pool to adopt a semi-elliptical shape, with the melt pool depth considered to be half of the width as shown in **Eq. 3.3**. Furthermore, they posited that the addition of powder has no effect on the melt pool dimensions. These analytical expressions are employed in this study to model the melt pool dimensions and assess their predictive accuracy for NiTi.

$$\text{Width} = \sqrt{\frac{8AP}{\pi e \rho C_p V(T_m - T_o)}} \quad \textbf{(Eq. 3.2)}$$

$$\text{Depth} = \sqrt{\frac{2AP}{\pi e \rho C_p V(T_m - T_o)}} \quad \textbf{(Eq. 3.3)}$$

where T_m is the melting temperature, and e is Euler's number. Other variables retain their meanings afore-described.

3.2.2.2 Eagar-Tsai (ET) model

The Eagar-Tsai (ET) [191] thermal model refines the Rosenthal equation (RE) by introducing a moving Gaussian heat source on a semi-infinite flat plate, providing a more accurate representation of temperature distribution. Although the ET model retains many assumptions similar to those in the RE model, it offers significantly improved prediction accuracy, particularly in regions near the heat source. As a result, the ET model has become widely adopted for predicting melt pool geometries in laser welding and PBF-LB processes. However, a key limitation of the ET model is its inability to account for keyhole-mode laser melting, restricting its applicability to conduction-mode melting. In PBF-LB processes, parameter combinations can lead to both conduction and keyhole-mode melting, and the ET model tends to underestimate melt pool depth in scenarios where keyhole-mode melting occurs [240,241]. The model that was originally designed for temperature distribution in welding, is based on **Eq. 3.4** [242]:

$$T - T_0 = \int_0^t \frac{AP(t-t')^{-\frac{1}{2}} e^{\left(-\frac{x^2+y^2}{4\alpha(t-t')+2a^2} - \frac{z^2}{4\alpha(t-t')}\right)}}{\pi \rho C_p \sqrt{4\pi\alpha}(2\alpha(t-t')+a^2)} dt' \quad \textbf{(Eq. 3.4)}$$

where t is the total scanning time, t' is instantaneous time and a is the laser beam radius. Other variables retain their meanings afore-described.

Rubenchik et al. [236] conducted a scaling law analysis on the original ET model using SS 316, Ti-6Al-4V and Inconel alloys to establish expressions for melt pool dimensions (see **Eq. 3.5** and **Eq. 3.6**). These models are utilized in this work to evaluate their predictive capability for NiTi. These are based on two dimensionless numbers p and B given in **Eq. 3.7** and **Eq. 3.8**, which define the melting process. The model involves several assumptions, including the absence of a powder layer, neglecting melt motion and the effects of evaporation and surface tension.

$$\text{Width} = \frac{a}{Bp^3}[0.0021 - 0.047p + 0.34p^2 - 1.9p^3 - 0.33p^4 + B(0.00066 - 0.007p - 0.00059p^2 + 2.8p^3 - 0.12p^4) + B^2(-0.0007 + 0.015p - 0.12p^2 + 0.59p^3 - 0.023p^4) + B^3(0.00001 - 0.00022p + 0.002p^2 - 0.0085p^3 + 0.0014p^4)] \quad \textbf{(Eq. 3.5)}$$

$$\text{Depth} = \frac{a}{\sqrt{p}}[0.008 - 0.0048B - 0.047p - 0.099Bp + plnp(0.32 + 0.015B) + lnB(0.0056 - 0.89p + 0.29plnp)] \quad \textbf{(Eq. 3.6)}$$

$$p = \frac{\alpha}{Va} \quad \textbf{(Eq. 3.7)}$$

$$B = \frac{AP}{\pi\rho C_p T_m \sqrt{\alpha V a^3}} \quad \textbf{(Eq. 3.8)}$$

3.2.2.3 Gladush and Smurov (GS) model

The model developed by Gladush and Smurov [209] is often used as an alternative correction model when other analytical models fail to accurately predict melt pool depth. This model is specifically designed to predict melt pool depth and does not provide predictions for melt pool width. The derivation of the GS model is extended to encompass keyhole-mode melting by assuming a cylindrical melt pool and solving the heat conduction equation for a semi-infinite flat plate, which gives a simple expression given in **Eq. 3.9** [243,244]:

$$\text{Depth} = \frac{AP}{2\pi k T_b} \ln\left(\frac{a + \frac{\alpha}{V}}{a}\right) \quad \textbf{(Eq. 3.9)}$$

where T_b is the boiling temperature, and other variables retain their meanings afore-described.

3.3 Results and Discussion

3.3.1 Qualitative NiTi Melt Pool Width and Depth Analysis

Figure 3.2 illustrates the NiTi single tracks fabricated using different combinations of laser power and scanning speed. A noticeable visual trend can be observed, indicating that the track width decreases when the scanning speed is increased while keeping the power level constant. Conversely, when the power level was increased while maintaining a constant speed level, the track width increased. This implies that wider tracks are formed when higher inputs of E_L are utilized, specifically at high power and low scanning speed levels. On the contrary, as the E_L decreased, the tracks became narrower. Furthermore, at lower levels of E_L, interruptions in the tracks were observed, indicating a lack of fusion. This suggests that the energy input (density) was insufficient to achieve a continuous bead formation. Additionally, discontinuities in the tracks, known as the balling phenomenon, can be observed at the highest levels of laser power and scanning speed (see **Figure 3.2**). It is also noteworthy that, for a given energy input (from **Table 3.1**), the track width increases with an increase in laser power.

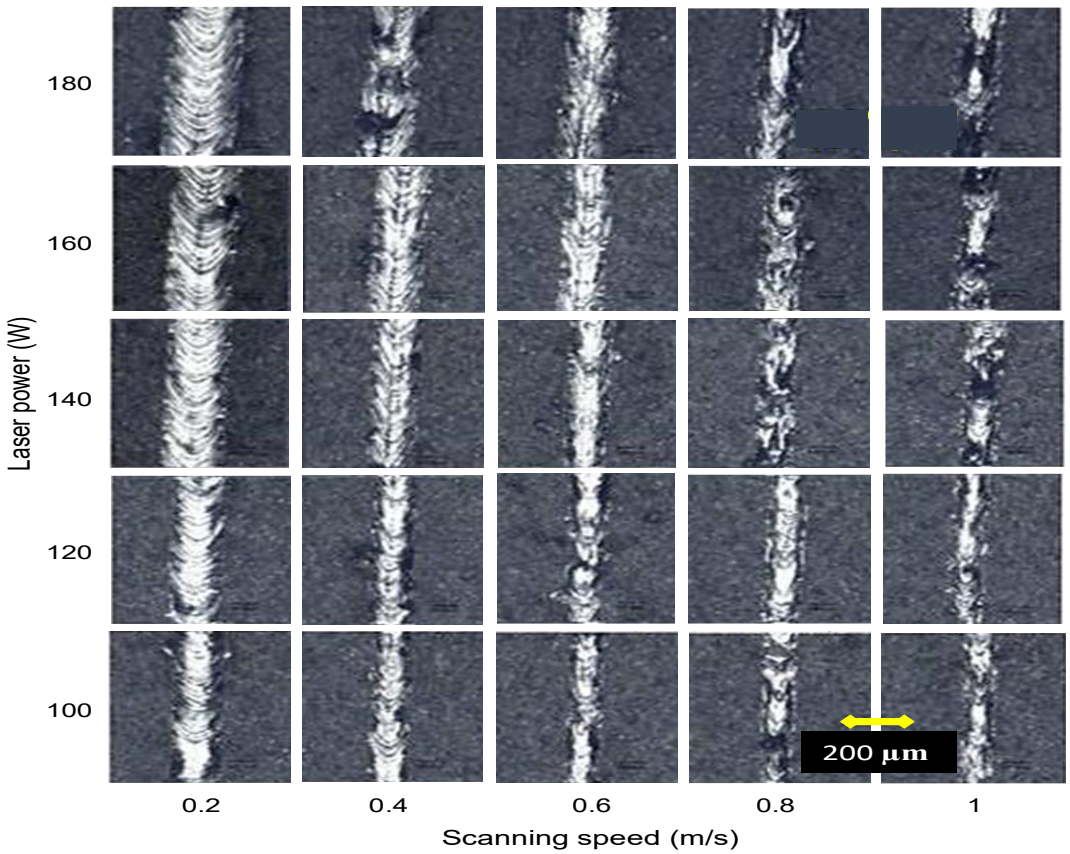


Figure 3.2 Top view micrographs of NiTi single tracks for different laser power and scan speed combinations.

A similar interpretation can be made for the melt pool depth, as depicted in **Figure 3.3**, which displays the cross-sectional views of the tracks. The melt pool depth is strongly influenced by the parameters, with an increase in laser power resulting in deeper melt pools and an increase in scanning speed leading to shallower melt pools. This indicates that higher E_L contributes to greater melt pool depth. Similar to the width, it is observed that melt pool depth varies for the same energy input depending on the levels of laser power and scanning speed suggesting that solely considering the linear energy density is not enough for optimizing the process parameters. Similar observations were found in a previous study by Lu et al [235]. Some micrographs are missing for certain combinations of laser power and scanning speed in **Figure 3.3**, because the melt pool became too small to measure accurately, suggesting a lack of fusion. The balling phenomenon can also be observed for combinations of high power and high speed. Interestingly, no keyholing phenomenon, a defect hole formed in the material at higher energy densities, was observed in any of the samples. These findings align with similar results reported by previous studies conducted [245–247]. However, in most of these previous studies, keyholing phenomenon and higher melt pool depths are reported. The melt pools obtained in this work were shallower than those found in previous studies. Keyhole porosity would be less likely to form in shallower melt pools.

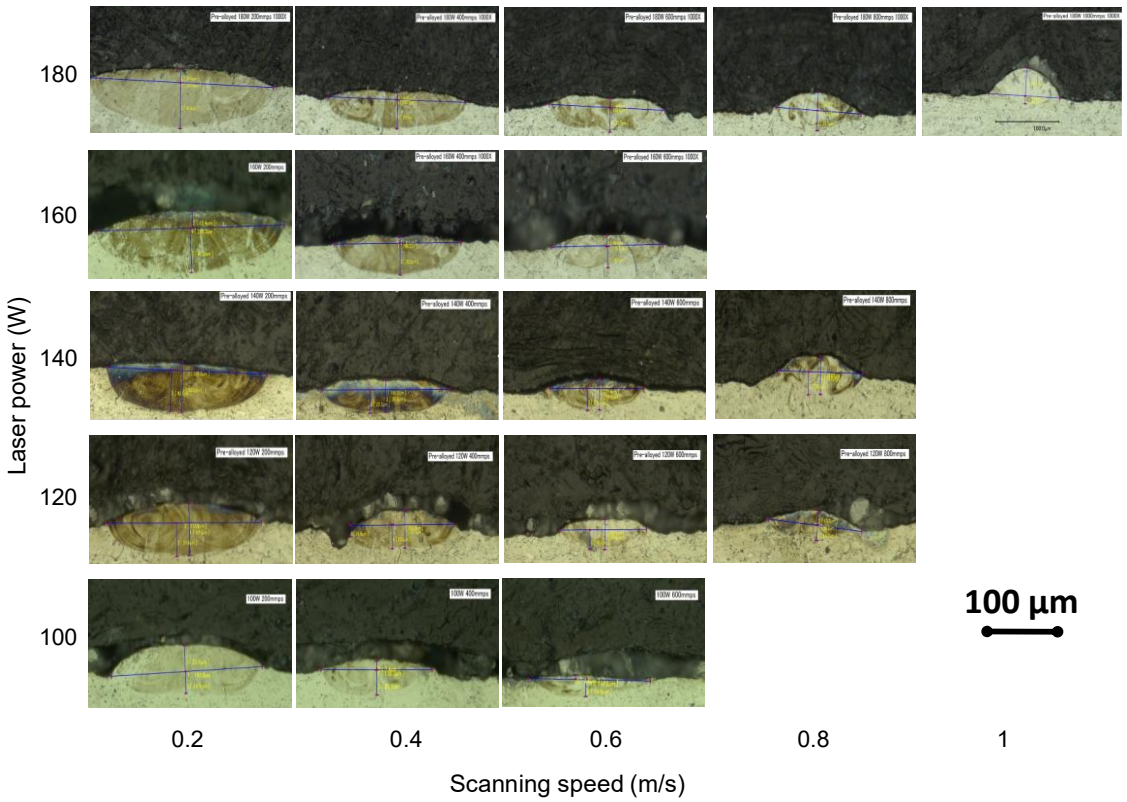


Figure 3.3 Cross-sectional view of melt pools formed by NiTi single tracks manufactured with various laser power and scanning speed combinations.

3.3.2 Quantitative NiTi Melt Pool Width and Depth Analysis

Figure 3.4 (a-b) depict the effect of laser power and scanning speed on the width of the NiTi melt pool, whereas **Figure 3.4** (c-d) illustrate the influence of these parameters on the depth of the NiTi melt pool. By statistical curve fitting analysis, it is evident from **Figure 3.4** (a), that the width increased with an increase in laser power, in a linear fashion. This suggests that higher laser power leads to greater energy deposition, resulting in a larger melt pool width [248]. The melt pool width decreased when the laser scanning speed was increased, but in a rather logarithmic trend as shown in **Figure 3.4** (b). As such, at lower scanning speeds (e.g., from 0.2 m/s to 0.4 m/s), a significant reduction in width was observed. However, at higher speeds (e.g., from 0.8 m/s to 1 m/s), the reduction in width became less pronounced. This logarithmic relationship with scanning speed reflects how changes in speed affect the width less drastically as speed increases due to the balance between energy input and the time available for heat dissipation affecting the width of the melt pool. The R^2 values for both the linear and logarithmic trends were between 0.98 – 0.99. Yadroitsev et al. [249] demonstrated that energy density directly affects the morphology of the melt pool, influencing both its width and depth. However, exceptions to this relationship, such as the non-linear correlation between melt pool morphology, laser power, and speed, have been documented in previous studies on nitinol and other nickel alloys [250–252]. Similar observation was made for melt pool depth in our work, as explained in the following paragraphs.

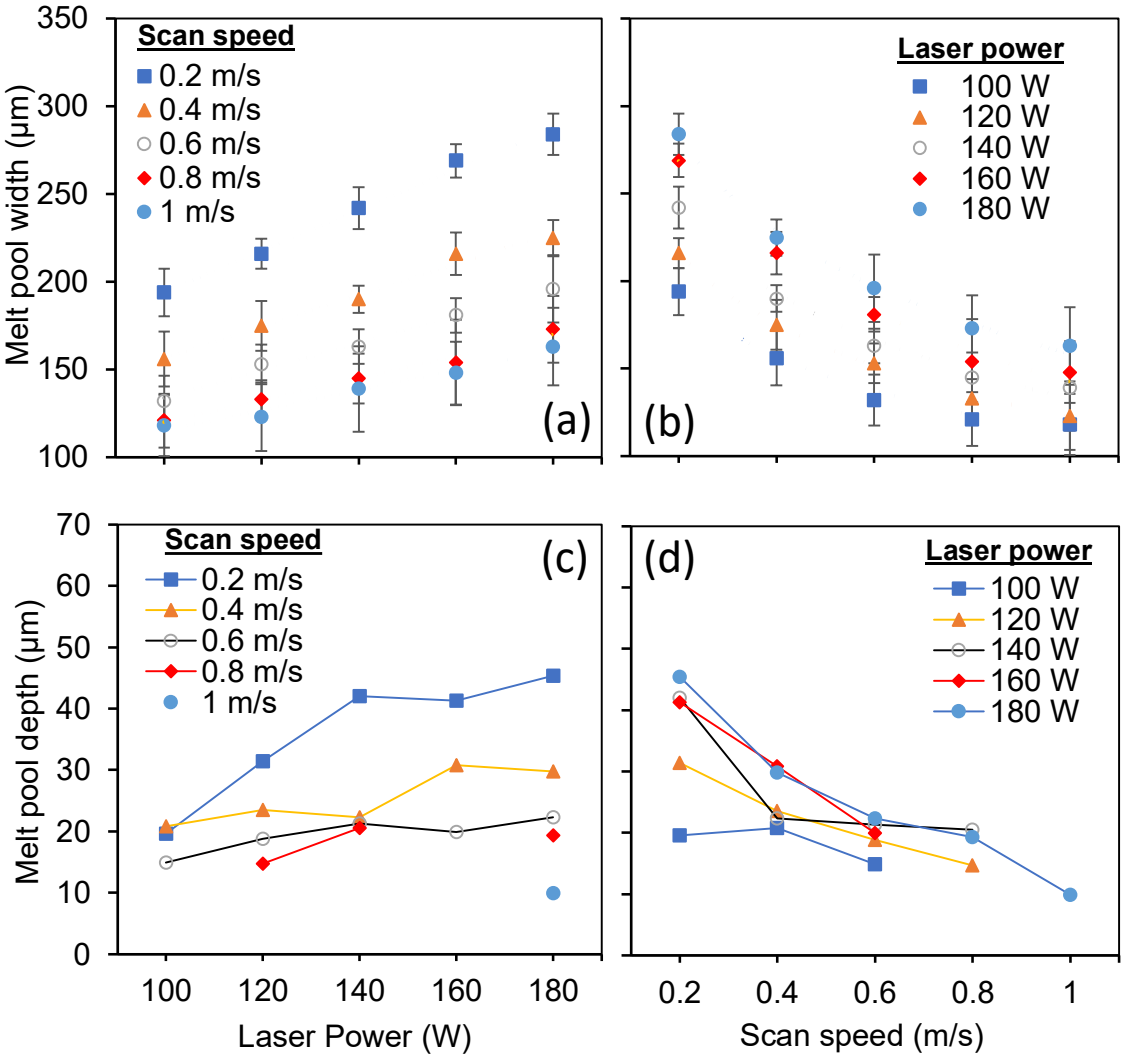


Figure 3.4 Experimentally measured effects of (a) laser power on NiTi melt pool width, (b) scanning speed on NiTi melt pool width, (c) laser power on NiTi melt pool depth, and (d) scanning speed on NiTi melt pool depth. Error bars on the melt pool widths are based on the standard deviation calculated from a minimum of 10 measurements.

Regarding melt pool depth, as shown in **Figure 3.4** (c-d), the relationship with laser power and scanning speed exhibited outliers that disrupted the expected linear or logarithmic trends. For instance, the calculated R^2 values for a linear correlation between laser power and the melt pool depth of NiTi single tracks ranged from 0.37 to 0.8, indicating a high degree of scatter. This variability makes it difficult to generalize the relationship between NiTi melt pool depth and the range of laser power and scanning speeds explored. As a result, simple solid lines were used to connect the data points in **Figure 3.4** (c-d). Whereas, the dashed lines in **Figure 3.4** (a-b) represent the respective linear and logarithmic curve-fitting trend lines. The scatter observed underscores the complexity of the relationship between linear energy density input (determined by laser power and scanning speed) and melt pool depth, particularly for NiTi.

Unlike melt pool width, which is a near-surface feature, melt pool depth is a volumetric feature influenced by multiple factors beyond just linear energy input and exposure time. For instance, Metelkova et al. [253] observed a consistent and generalizable linear relationship for single track widths in SS316L stainless steel, along with a logarithmic relationship for melt pool depths. In contrast, Lane et al. [254] reported linear relationships for both melt pool depth and width in single tracks of IN625. These differing trends, compared to the NiTi used in this study, suggest that material properties significantly influence melt pool solidification and morphology. Differences in thermal conductivity, absorptivity, temperature gradients, and heat dissipation mechanisms are likely contributors to this variability. Another factor affecting melt pool depth variability is the measurement methodology. Depth is typically measured from a single point along the track, whereas melt pool width is measured at multiple points (at least 10) along the track. In both conduction and keyhole melting modes, laser penetration depth can fluctuate along the scan direction, further contributing to the scatter in depth measurements [253,255].

3.3.3 Model Predictions of NiTi Melt Pool Width and Depth

Figure 3.5 shows the predictions of RE, ET, and GS analytical methods in modelling NiTi melt pool characteristics. The melt pool width predictions from both the RE and ET models exhibited a linear increase with increase in laser power as depicted in **Figure 3.5** (a). Conversely, the melt pool width demonstrated a logarithmic decrease with increasing scanning speeds (as illustrated in **Figure 3.5** b). The melt pool width trends strongly corroborate with the quantitative experimental observations discussed earlier providing consistency between the model predictions and the actual experimental interpretation for melt pool widths (refer to **Figure 3.5** a-b). However, it is important to note that for every instance of laser power at all scanning speeds shown in **Figure 3.5** (a-b), the ET model predictions were consistently higher than that of the RE model. Further details on the prediction accuracy will be discussed later.

Regarding the melt pool depth, the ET model exhibited significant underestimation. This discrepancy may be attributed to the model's sole consideration of conduction-mode melting and other associated assumptions. Similar findings have been documented in existing literature [103,241,244]. Consequently, the melt pool depths predicted by the ET model are not included in further analyses. The predictions from the other two models (RE and GS models) indicated that the melt pool depth would generally increase linearly with higher laser power and decrease logarithmically with increased scanning speed. However, unlike the experimental results,

outliers were not observed in the model predictions. This divergence can be attributed to the models' exclusive consideration of scanning parameters and material properties while neglecting other factors that could potentially influence melt pool depth during the experiments.

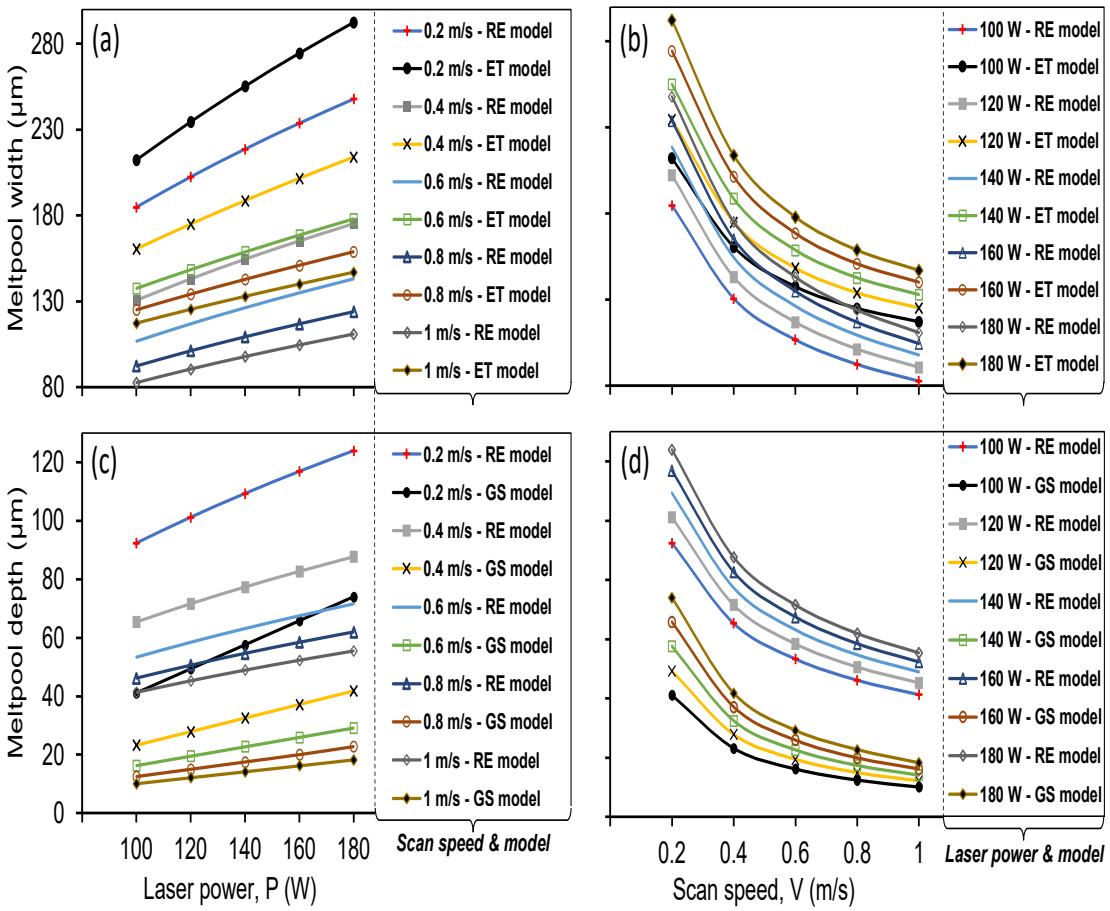


Figure 3.5 Effects of (a) laser power on melt pool width, (b) scanning speed on melt pool width, (c) laser power on melt pool depth, and (d) scanning speed on melt pool depth, collated from the Rosenthal Equation (RE), Eagar-Tsai (ET) and Gladush-Smurov (GS) model predictions.

3.3.4 Model Prediction Accuracy

To assess the accuracy of the prediction, the analytical model results were compared to experimental data by calculating the relative percentage error. **Table 3.3** and **Table 3.4** provide a detailed tabular summary of the error calculations. Note that the closer the percentage error is to zero, the more accurate the prediction.

Table 3.3 Comparison between experimental and predicted melt pool widths.

P (W)	V (m/s)	Exp. Melt Pool Width (µm)	RE Model Melt Pool Width (µm)	RE Model Melt Pool Width Error (%)	ET Model Melt Pool Width (µm)	ET Model Melt Pool Width Error (%)
100	0.2	194	185	-4	212	9
100	0.4	156	131	-16	161	2
100	0.6	132	107	-19	138	4
100	0.8	121	92	-23	125	3
100	1	118	83	-29	117	-0.4
120	0.2	216	202	-6	235	8
120	0.4	175	143	-18	175	-0
120	0.6	153	117	-23	148	-3
120	0.8	133	101	-24	134	0.8
120	1	123	91	-26	125	2
140	0.2	242	219	-9	255	5
140	0.4	190	155	-18	189	-0.6
140	0.6	163	126	-22	159	-2
140	0.8	145	109	-24	143	-1
140	1	139	98	-29	133	-4
160	0.2	269	234	-12	275	2
160	0.4	216	165	-23	202	-6
160	0.6	181	135	-25	169	-6
160	0.8	154	117	-24	151	-2
160	1	148	105	-29	140	-5
180	0.2	284	248	-12	292	2
180	0.4	225	175	-22	214	-4
180	0.6	196	143	-27	178	-9
180	0.8	173	124	-28	159	-8
180	1	163	111	-32	147	-9

Table 3.4 Comparison between experimental and predicted melt pool depths.

P (W)	V (m/s)	Exp. Melt Pool Depth (µm)	RE Model Melt Pool Depth (µm)	RE Model Melt Pool Depth Error (%)	GS Model Melt Pool Depth (µm)	GS Model Melt Pool Depth Error (%)
100	0.2	44	92	110	41	-6
100	0.4	28	65	133	23	-17
100	0.6	18	53	196	16	-10
100	0.8	-	46	-	12	-
100	1	-	41	-	10	-
120	0.2	49	101	106	49	0.6
120	0.4	37	72	93	28	-24
120	0.6	29	58	101	19	-33
120	0.8	28	51	80	15	-46
120	1	-	45	-	12	-
140	0.2	53	109	106	58	8
140	0.4	31	77	151	32	5
140	0.6	30	63	113	23	-23
140	0.8	34	55	62	17	-48
140	1	-	49	-	14	-
160	0.2	57	117	106	66	16
160	0.4	37	83	124	37	0.6
160	0.6	30	67	122	26	-14
160	0.8	-	58	-	20	-
160	1	-	52	-	16	-
180	0.2	60	124	107	74	23
180	0.4	38	88	130	42	9
180	0.6	31	72	129	29	-6
180	0.8	37	62	65	23	-39
180	1	46	55	21	18	-60

Figure 3.6 provides a graphical comparison of the predictive accuracy of different models for melt pool width and depth. The RE model consistently underestimates melt pool width, with the highest absolute percentage error reaching 32% and a mean absolute percentage error (MAPE) of around 20%. In contrast, the ET model demonstrates higher accuracy in predicting width, as shown in **Figure 3.6 (**a-b), with absolute errors below 10% across all P-V

combinations and a MAPE of less than 5%. For melt pool depth, the GS model outperforms the RE model, achieving a MAPE of around 20%, while the RE model shows overestimation errors exceeding 100% (**Figure 3.6** c-d).

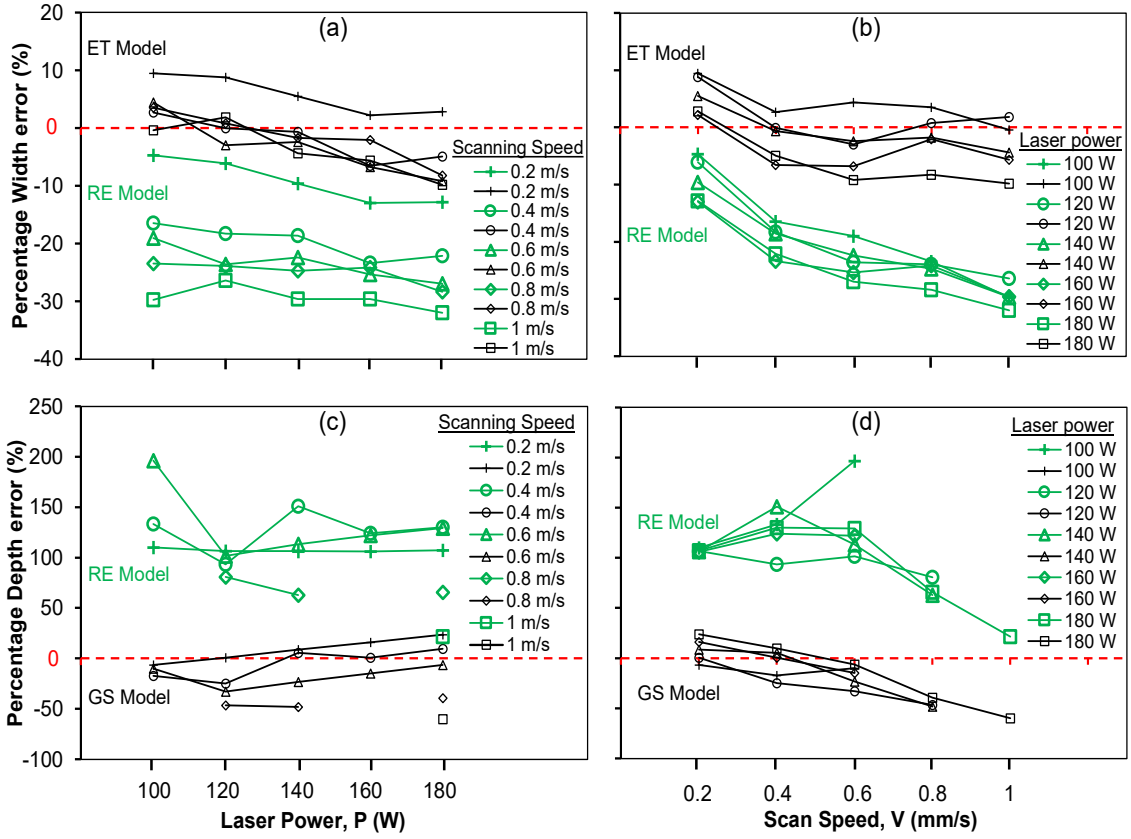


Figure 3.6 Relative error between experimental and predicted results for: (a) melt pool width using the Rosenthal Equation (RE) model and Eagar-Tsai (ET) model at varying laser powers with constant scanning speed, (b) melt pool width using the RE model and ET model at varying scanning speeds with constant laser power, (c) melt pool depth using the RE model and Gladush-Smurov (GS) model at varying laser powers with constant scanning speed and (d) melt pool depth using the RE model and GS model at varying scanning speeds with constant laser power.

Another key observation is how the prediction accuracy of the models changes with varying laser power and scanning speed. For melt pool width (**Figure 3.6** a-b), both the ET and RE models exhibit a near-linear downward trend in error as power and speed increase. However, this change is less pronounced in the ET model, where the absolute error remains within the 10% range. In contrast, for the RE model, the prediction error stays within 13% at the lowest scanning speed of 0.2 m/s, regardless of laser power. At higher scanning speeds (0.4 –1 m/s), however, the RE model significantly underestimates the width, with errors ranging from 15%

to 32%. Interestingly, the error in the RE model is more sensitive to changes in scanning speed than in laser power; for a given speed, the error does not change significantly with varying power, but it increases with higher speeds. For melt pool depth (**Figure 3.6** c-d), the RE model shows more scatter in prediction accuracy compared to the GS model, which follows a more linear trend. Notably, for the GS model, error decreases with increasing power but increases with rising speed. High error values are particularly evident at certain power-speed combinations, especially those involving high power and speed. This discrepancy may result from the GS model's assumption that the melt pool exhibits a keyhole-type morphology, while observations in **Figure 3.3** indicate the occurrence of balling for these P-V combinations, which contradicts the keyhole mode assumption.

We hypothesize that the decline in prediction accuracy of the models under varying process parameters arises from the simplifications and assumptions made during model development, as well as material and process-related factors discussed earlier. A key assumption in the models is that material properties remain constant and do not vary with temperature. However, in reality, properties such as thermal conductivity, specific heat capacity, density, and laser absorptivity are highly temperature-dependent. Additionally, there is a lack of data on temperature-dependent properties for additively manufactured materials, particularly at very high temperatures. These complexities make it challenging to pinpoint a single cause for the models' reduced accuracy. Further investigation is needed, and resolving these issues in the models will be a central focus of future research.

3.3.5 Power – Scan Speed (P-V) Process Maps

Process maps were constructed based on model predictions to indicate regions of lack of fusion and good conduction. Balling was excluded, as melt pool length was not predicted in the models used in this study. The criteria in **Eq. 3.10** and **Eq. 3.11** must be satisfied to avoid lack of fusion and keyholing, respectively [15,239].

$$\left(\frac{H}{w}\right)^2 + \left(\frac{L}{d}\right)^2 \leq 1 \qquad \textbf{(Eq. 3.10)}$$

$$\frac{w}{d} > 1.5 \qquad \textbf{(Eq. 3.11)}$$

where, H is hatch spacing, L is layer thickness, w is melt pool width and d is melt pool depth. These calculations were based on a hypothetical hatch spacing of 100 μm and a solidified layer thickness of 30 μm (assuming a 50% powder packing density, resulting in an actual powder layer thickness of 60 μm). **Figure 3.7** (a-b) show the calculation of process maps using the melt

pool width and depth values from the RE model. **Figure 3.7** (c-d), on the other hand, were produced using the predictions of melt pool width from the ET model and melt pool depth from the GS model. As can be seen in the process maps, no keyholing was predicted, aligning with the experimental observations shown in **Figure 3.3**. Moreover, a comparison of **Figure 3.7** with **Figure 3.3** also reveals that the combined ET and GS models predict lack of fusion more effectively than the RE model. However, it is essential to acknowledge that the process maps serve only as guidance and may not capture all the complexities of the process.

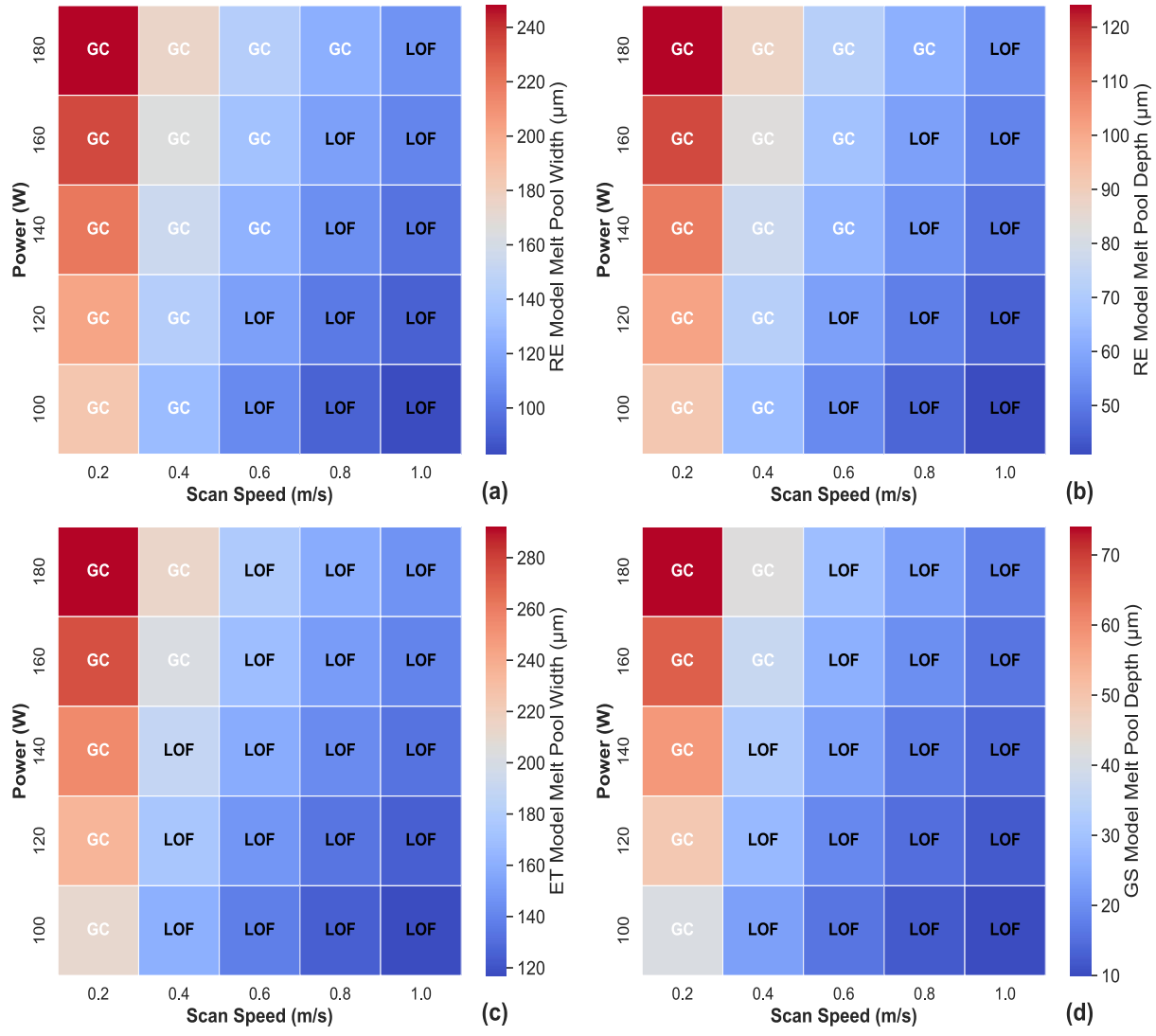


Figure 3.7 P-V process maps highlighting regions of LOF (Lack of Fusion) and GC (Good Conduction) from (a), (b) the Rosenthal Equation (RE), (c), (d) Eagar-Tsai (ET) – Gladush-Smurov (GS) models' predictions. The maps are generated for a hatch spacing of 100 µm, a solidified layer thickness of 30 µm, and an actual powder layer thickness of 60 µm.

The overall findings indicate that the Eagar-Tsai model provided the most accurate predictions for NiTi single tracks melt pool width, while the Gladush-Smurov model offered the best accuracy for NiTi single tracks melt pool depth. Therefore, it is evident that utilizing both models is beneficial for achieving the most accurate prediction of solidified melt pool dimensions in PBF-LB processed NiTi. Monitoring the melt pool dimensions in PBF-LB is crucial as they directly influence the microstructural and mechanical properties of the manufactured part [256]. A high energy input produces wide and deep melt pools, while low energy input leads to narrow and shallow ones. Excessive melt pool width may cause material spreading, overbuilding, and poor surface finish. On the other hand, narrow melt pools can result in incomplete fusion, leading to gaps or defects, and reduced part quality. A controlled melt pool width minimizes the stair-stepping effect, improving surface smoothness. In terms of depth, inadequate melt pool depth can cause poor bonding between layers, resulting in lack of fusion porosity. If the melt pool is too deep, keyhole porosity forms, weakening the structure. Both porosity types adversely affect the strength of the component [257–259]. Moreover, the melt pool dimensions significantly influence the local thermal gradients. Higher local thermal gradients lead to higher residual stresses which can in turn result in localized cracking [260]. Melt pool dimensions also inversely affect cooling rates, which in turn govern the resulting grain structure of the material. These effects ultimately define the part's mechanical properties, such as strength and toughness [261,262]. Predictive models can help estimate melt pool dimensions, reducing the need for costly and time-consuming experiments. However, these models may not always be accurate, as their predictions are sensitive to various factors, including process conditions and environmental variables [15,263,264].

3.4 Conclusion

The objective of this study was to evaluate the predictive capability of analytical models in estimating melt pool width and depth for NiTi single tracks based on PBF-LB process parameters. Experimental analysis revealed that laser power exhibited an almost linear correlation with melt pool width, while scanning speed showed a logarithmic relationship. However, melt pool depth did not follow a consistent pattern with respect to either laser power or scanning speed.

Among the models investigated, the Eagar-Tsai model provided the most accurate predictions for melt pool width, while the Gladush-Smurov model delivered reasonably accurate

predictions for melt pool depth. In contrast, the Rosenthal equation did not yield reliable results for either width or depth predictions. Thus, combining the Eagar-Tsai model for width and the Gladush-Smurov model for depth resulted in the most reliable overall predictions for the melt pool dimensions across the range of power and speed (P-V) combinations tested.

Process maps were generated from the model predictions, revealing regions of good conduction and lack of fusion, while indicating that no keyholing was predicted. These findings enhance the ability to predict melt pool dimensions for NiTi processed via PBF-LB. Incorporating these results into finite element models, with temperature-dependent material properties, would lead to a more comprehensive and robust framework for predicting NiTi melt pool morphology.

This work also emphasizes that the predictive capabilities of analytical models differ across alloy systems. A model that performs accurately for one material may not be suitable for another. Moreover, the models' accuracy varies depending on the specific PBF-LB parameters used. A major factor contributing to the accuracy of the models stems from the simplifications and assumptions, such as the idea that material properties remain constant with temperature. Furthermore, data on the temperature-dependent properties of additively manufactured materials is limited. Future research should aim to address these limitations and improve accuracy of the models.

Contribution towards the thesis: This chapter evaluates classical analytical melt pool models against experimental data to assess their applicability to NiTi, identifying the strengths and limitations of commonly used formulations. This work provided essential baseline understanding for subsequent high-fidelity modelling. The work demonstrated that analytical model performance is strongly alloy-dependent and parameter-regime dependent, challenging the widespread assumption of model transferability across materials.

4. Chapter: Physics-Guided Digital Twin Framework for Melt Pool Prediction and Process Stability in Laser Powder Bed Fusion of Nitinol

---

Publication Status: Review Completed

Sampreet Rangaswamy, Merve Nur Doğu, Camille Rubio, Hengfeng Gu, Abdul Khader Khan, Chong Teng, Inam Ul Ahad, Dermot Brabazon, **Physics-Informed Digital Twin for Melt Pool Prediction and Stability in Laser Powder Bed Fusion of Nitinol**.

Abstract

Powder bed fusion–laser beam (PBF-LB) of nickel–titanium (NiTi) has attracted increasing interest in aerospace, biomedical, and energy applications due to its shape memory and superelastic properties combined with the capability to fabricate complex geometries. However, the strong sensitivity of NiTi to thermal history and process variability makes predictive modeling and parameter selection challenging. In this work, a physics-guided digital twin framework integrated with a decision engine is developed for melt pool prediction and stability assessment in NiTi processed by PBF-LB. A high-fidelity thermal finite element model calibrated using experimental measurements and CALPHAD-derived temperature-dependent material properties was employed to simulate melt pool geometries. The thermal model showed prediction errors below 10% for melt pool width and depth. A multi-output surrogate model trained on the validated simulation dataset enabled rapid prediction of melt pool geometrical features, achieving test-set R^2 values exceeding 0.95 with low MAE and RMSE values. Five-fold cross-validation further confirmed robust predictive performance. The framework integrates surrogate predictions with physics-based melt pool stability criteria to enable rapid exploration of physically feasible processing conditions and provides a computationally efficient foundation for future supervisory process-control strategies.

4.1 Introduction

High-fidelity numerical simulations, particularly thermal models implemented in commercial software such as Ansys Additive Manufacturing Process Parameters (AMPP), provide valuable insight into melt pool evolution and underlying heat transfer mechanisms. These models capture the complex thermal interactions governing melt pool geometry and its influence on process–structure relationships. However, their high computational cost limits their applicability for rapid process exploration, optimization, and real-time decision-making [201,229]. As a result, there is growing interest in surrogate modeling approaches that can approximate simulation outputs at a fraction of the computational cost [265–267].

Recent studies have applied machine learning techniques to predict melt pool characteristics in laser-based additive manufacturing. While these approaches demonstrate promising predictive accuracy, many remain purely data-driven, offering limited physical interpretability and few safeguards against non-physical predictions [18,19,268]. In the context of manufacturing process control and optimization, this lack of embedded physical knowledge poses a significant challenge, as mathematically optimal solutions may correspond to physically unstable or unmanufacturable regimes, limiting their practical applicability in process design and control [269–271].

To address these limitations, physics-informed digital twins have emerged as a powerful paradigm for additive manufacturing. Rather than relying solely on black-box regression, such frameworks integrate data-driven surrogate models with explicit physical constraints, domain knowledge, and decision logic not only to predict process outcomes rapidly but also to assess process stability and guide parameter selection in a physically meaningful manner. This capability is particularly important for materials such as NiTi, where melt pool stability governs defect formation, thermal gradients, and ultimately microstructure-dependent functional properties [20–23].

In this work, an offline physics-guided digital twin is developed for melt pool prediction and stability assessment in PBF-LB of NiTi. A high-fidelity thermal finite element model on Ansys AMPP, calibrated using experimental measurements, is used to generate a comprehensive dataset of melt pool geometries. A multi-output surrogate model is then trained to predict melt pool width, depth, and length with high accuracy. Physics-based stability criteria, formulated using dimensionless geometric ratios, are embedded to classify processing regimes, including conduction, keyhole, balling, and lack of fusion.

The proposed framework further functions as a decision engine by enabling physics-constrained optimization of laser process parameters toward stable conduction-mode operation. By combining rapid surrogate evaluation with rule-based physical reasoning, the digital twin framework provides both quantitative predictions and qualitative insight into the solidified melt pool dimensions. The present implementation represents a process-level digital twin operating in an offline predictive mode. While the framework currently relies on surrogate predictions generated from experimentally calibrated thermal simulations, the architecture is designed to be extensible toward real-time implementation through future integration of in-situ sensing, feedback communication, adaptive model updating and closed-loop process control.

4.2 Materials and Methods

4.2.1 Experimental Details

Single-track experiments were conducted on a NiTi substrate using an Aconity MINI metal additive manufacturing system (Aconity GmbH). A layer of gas-atomized, prealloyed NiTi powder was deposited onto the base plate prior to laser exposure. The system was equipped with a laser operating at a wavelength of 1068 nm and a maximum output power of 200 W. The pre-alloyed powder composition consisted of 50.54 at.% nickel and 49.46 at.% titanium, with particle sizes in the range of 15-53 μm. Argon was supplied to the build chamber as a shielding gas to suppress oxidation and maintain a low-oxygen processing environment.

The NiTi base plate had dimensions of 95 × 95 × 6 mm. Throughout the experiments, a solidified powder layer thickness of approximately 30 μm, measured from the multi-beads formed alongside the single tracks, was maintained. To achieve this, an actual powder layer thickness of approximately 150 μm was applied, resulting in a solidified layer thickness of ~30 μm and indicating an effective powder packing density of about 20%. The multi-beads were fabricated with constant parameters of 200 W laser power, 1000 mm/s scan speed, and 120 μm hatch spacing. For the single-track experiments, a factorial design of experiments was implemented using a 6 × 6 parameter matrix, in which laser power was varied between 150 and 200 W and scan speed ranged from 500 to 1000 mm/s. The laser beam diameter (spot size at the focal plane) was held constant at 80 μm for all the experiments. In total, 36 single-track specimens were fabricated using distinct combinations of power and scan speed.

Melt pool widths and depths were quantified using a Keyence VHX-1 three-dimensional optical microscope. Related example captured images are shown in **Figure 4.1**. For cross-

sectional characterization, the tracks were sectioned using ATM Brilliant 250 cutting machine approximately at the center of the track. The extracted sections were mounted in a transparent hot mounting resin and prepared using standard metallographic procedures. Grinding was performed with silicon carbide papers of progressively finer grit sizes from 80 to 1200, followed by polishing with diamond suspensions of 9, 3, and 1 µm particle size at rotational speeds between 250 and 300 rpm. To reveal melt pool morphology, the polished samples were chemically etched using a solution containing 5 mL nitric acid (HNO_3), 4 mL hydrofluoric acid (HF), and 40 mL deionized (DI) water. More images of the top-view and cross-sectional view of the tracks fabricated are provided in **Figure 4.2**, **Figure 4.3** and **Figure 4.4**.

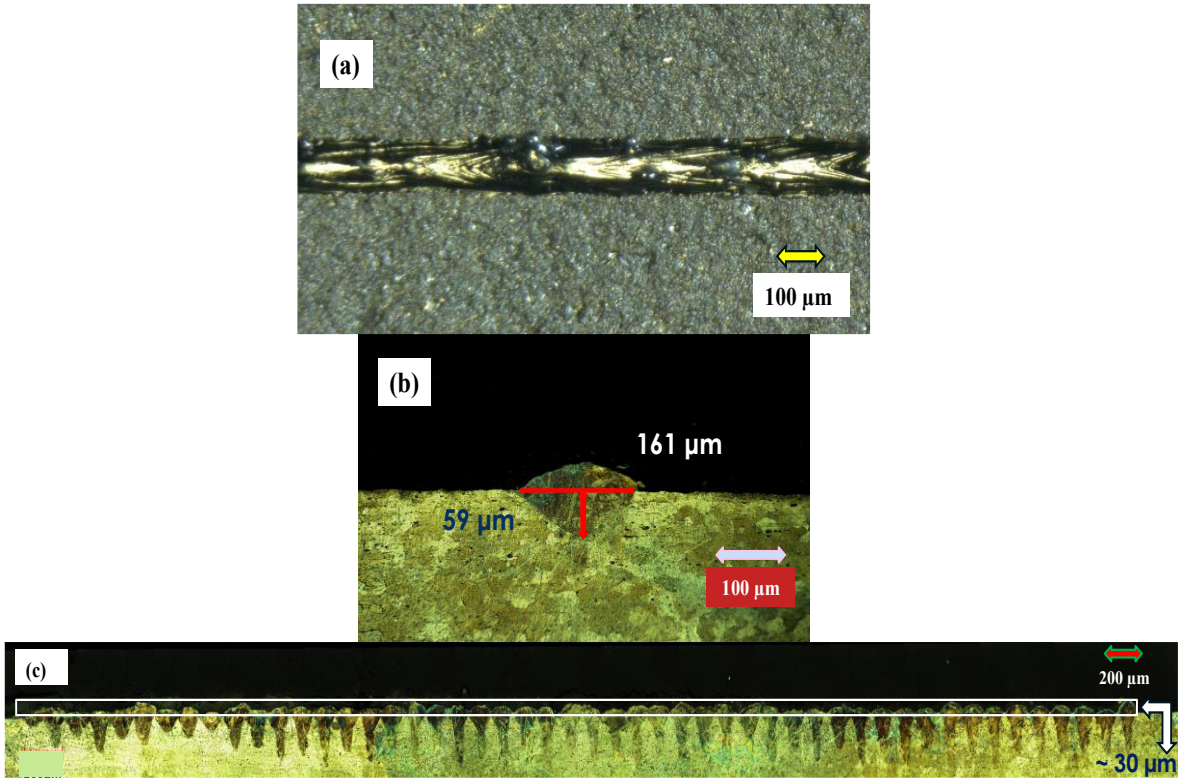


Figure 4.1 (a) Top-view image of the single-track, (b) cross-section image of the single-track showing melt pool width and depth measurements (Sample 32), (c) measurement of the solidified powder layer thickness from the multi-bead experiments.

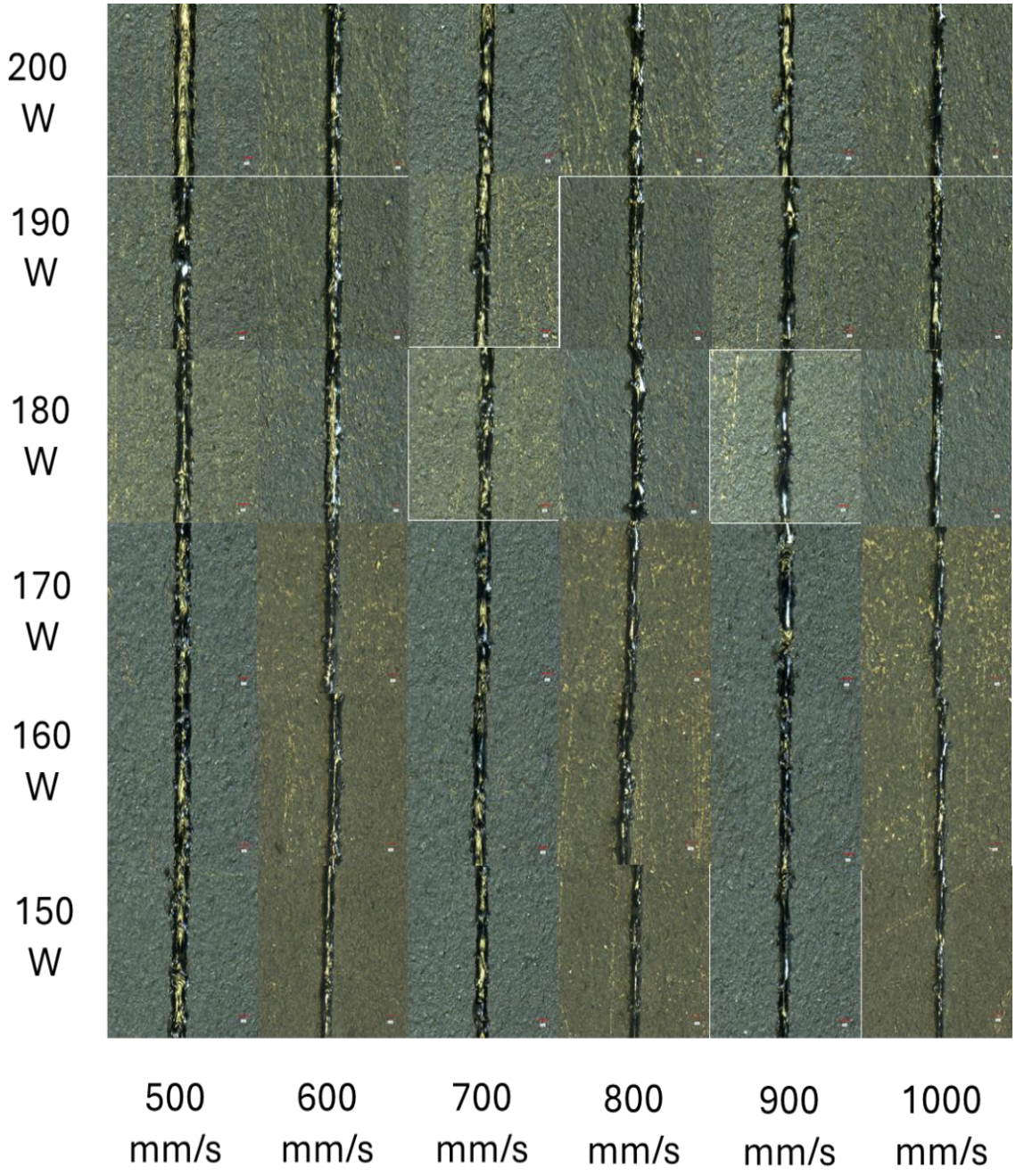


Figure 4.2 Top-view of the single-tracks produced along with the parameter combinations.

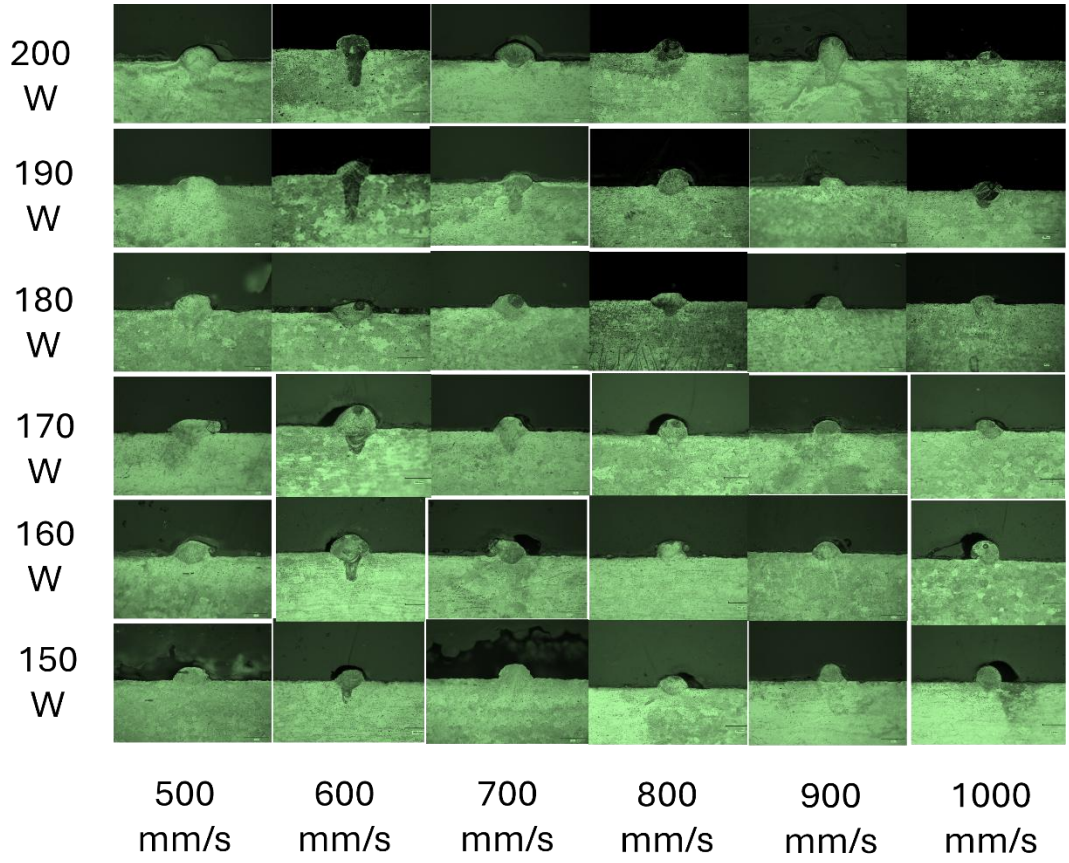


Figure 4.3 Cross-sectional of the single-tracks produced along with the parameter combinations.

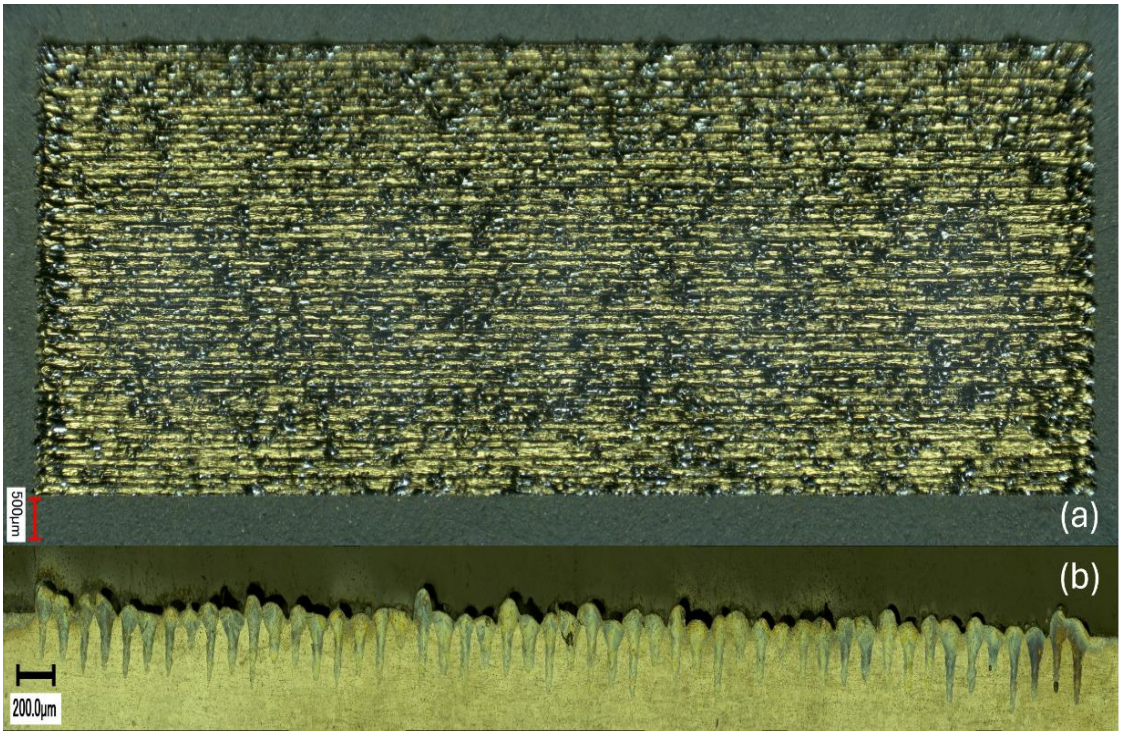


Figure 4.4 Micrograph of a multi-bead (a) top-view (b) cross-sectional view.

4.2.2 Pyrometric Infrared (IR) Data

Thermal measurements of the molten pool were obtained using two pyrometers manufactured by KLEIBER Infrared GmbH, integrated into the Aconity MINI PBF-LB system. These sensors capture the emitted radiation from the laser-material interaction zone within a wavelength range of 1500–1700 nm. The acquired infrared (IR) data are stored along with their corresponding spatial coordinates (x, y) on the build plate.

In this work, the recorded data were processed to generate graphical visualizations that illustrate temperature variations across the build layer. The data acquisition rate was 100,000 samples per second, resulting in about 1,065,000 data points for the single layer, each containing spatial and thermal information. To facilitate comparison and visualization of the thermal behaviour, the temperature values were normalized to a dimensionless scale between 0 and 1.

4.2.3 CALPHAD

The temperature-dependent NiTi material properties were obtained via CALPHAD method in Thermo-Calc 2025a software employing TCTI6 titanium alloys database using Equilibrium with Freeze-in Temperature model. This titanium alloys is the most updated database for shape memory alloys as it contains B2 austenite phase as well as B19′ martensite phase. These properties namely thermal conductivity, thermal diffusivity, specific heat capacity and density are shown in **Figure 4.5**.

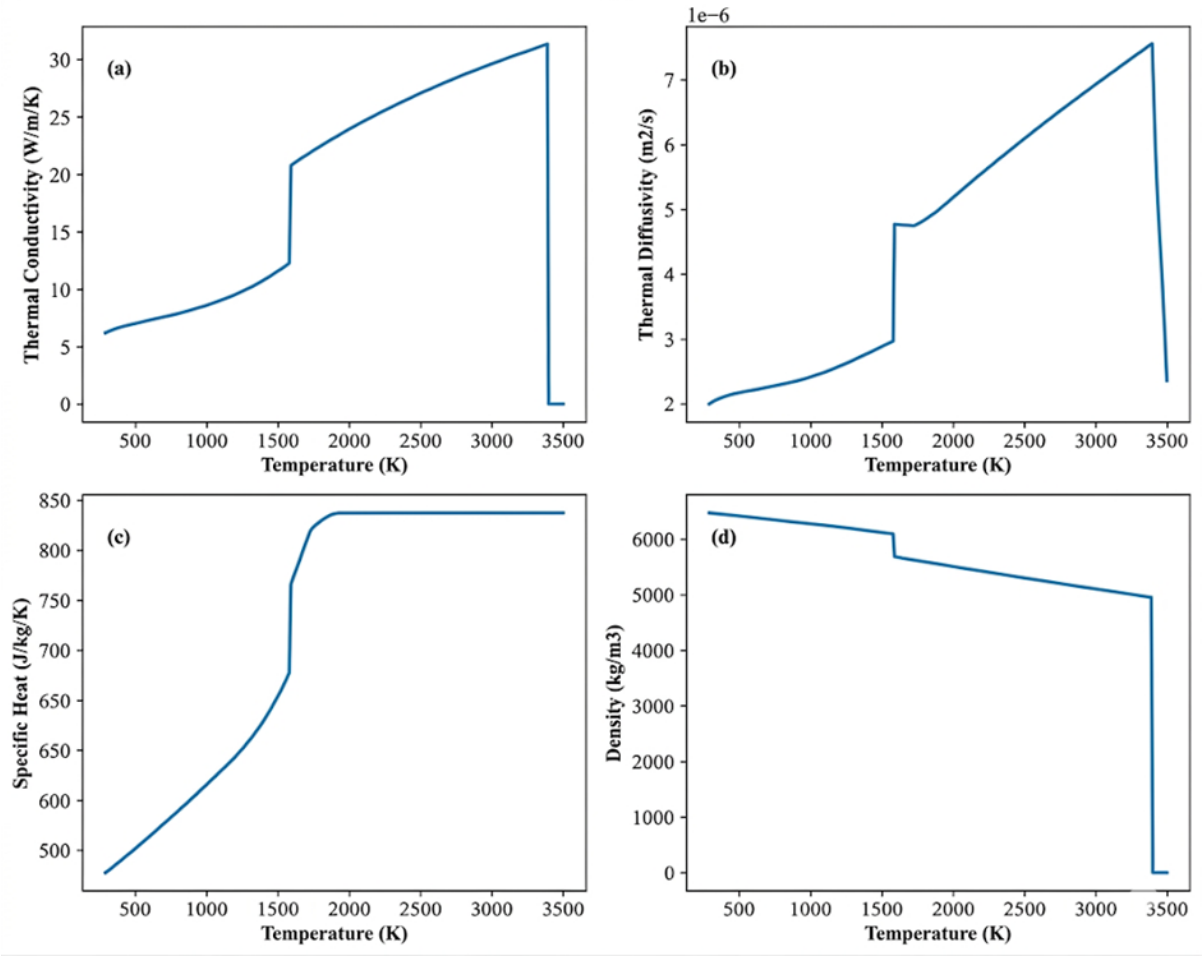


Figure 4.5 CALPHAD (a) Thermal conductivity (b) thermal diffusivity, (c) specific heat (d) density of NiTi with respect to temperature.

4.2.4 Thermal Modelling

A thermal finite element model on Ansys AMPP software version 2025R2 was used for simulating the single tracks as shown in **Figure 4.6**. A structured Cartesian mesh is adopted to maintain fixed coordinates and to enable more accurate identification of melt pool dimensions. A refined mesh resolution of 15 μm was applied, which is internally verified by Ansys Additive. NiTi was added to the software as n user-defined material with the thermo-physical properties and a quarter of the experimental dataset was used to tune the model. The governing equations of the thermal model are given in **Eq. 4.1**, **Eq. 4.2** and **Eq. 4.3** where **Eq. 4.1** represents the Fourier thermal conduction equation, **Eq. 4.2** represents the heat loss due to convection and **Eq. 4.3** represents the Gaussian heat source.

$$\rho c \frac{\partial T}{\partial t} = \frac{\partial}{\partial x}\left(k \frac{\partial T}{\partial x}\right) + \frac{\partial}{\partial y}\left(k \frac{\partial T}{\partial y}\right) + \frac{\partial}{\partial z}\left(k \frac{\partial T}{\partial z}\right) + Q \quad \textbf{(Eq. 4.1)}$$

where ρ is density, c is specific heat k thermal conductivity T is temperature, t is time, Q is heat source and x, y and z are directions.

$$Q_c = h(T - T_0) \quad \textbf{(Eq. 4.2)}$$

where Q_c is the heat loss due to convection, h is the coefficient of thermal convection, T is transient temperature and T_0 is the initial temperature.

$$Q = 2\frac{AP}{\pi w^2} \exp \frac{-2r^2}{w^2} \quad \textbf{(Eq. 4.3)}$$

where Q is the heat flux input, A is the absorptivity, P is the laser power, w is the laser beam diameter and r is the position of the laser beam.

In the thermal model, temperature-dependent ratios between solid and powder properties are applied to account for the lower effective conductivity and density of the powder. This approach allows the model to represent not only the room-temperature powder behavior but also the thermal properties at elevated temperatures prior to melting. Details regarding the ratio relating the powder property to the solid property are given below:

- **Thermal Conductivity Ratio** values:
    - Ratio = 0.01 from 2 Kelvin to [0.6 x the solidus temperature]
    - Ratio = 0.4 from [0.6 x the solidus temperature] to the liquidus temperature of the material
    - Ratio = 1 from the liquidus temperature to 15000 Kelvin.
- **Density Ratio** values:
    - Ratio = 0.2 from 2 Kelvin to the liquidus temperature of the material.

(0.2 is the value that corresponds to the powder packing density in the build chamber after the recoating process)

    - Ratio = 1 from the liquidus temperature to 15000 Kelvin.
- **Specific Heat Ratio** value is always 1.

Other boundary conditions in the model are:

- The top boundary of the build has a constant forced convection applied uniformly. Aside from the laser model, radiation effects are neglected.
- The lateral boundary conditions are adiabatic while using a buffer region of powder extending out from the part's bounding box to avoid any boundary effects.
- The user-specified Baseplate Temperature is used as a fixed-temperature boundary condition at the bottom of the build.

For further details about the model, the reader is referred to the work by Teng et al. [272].

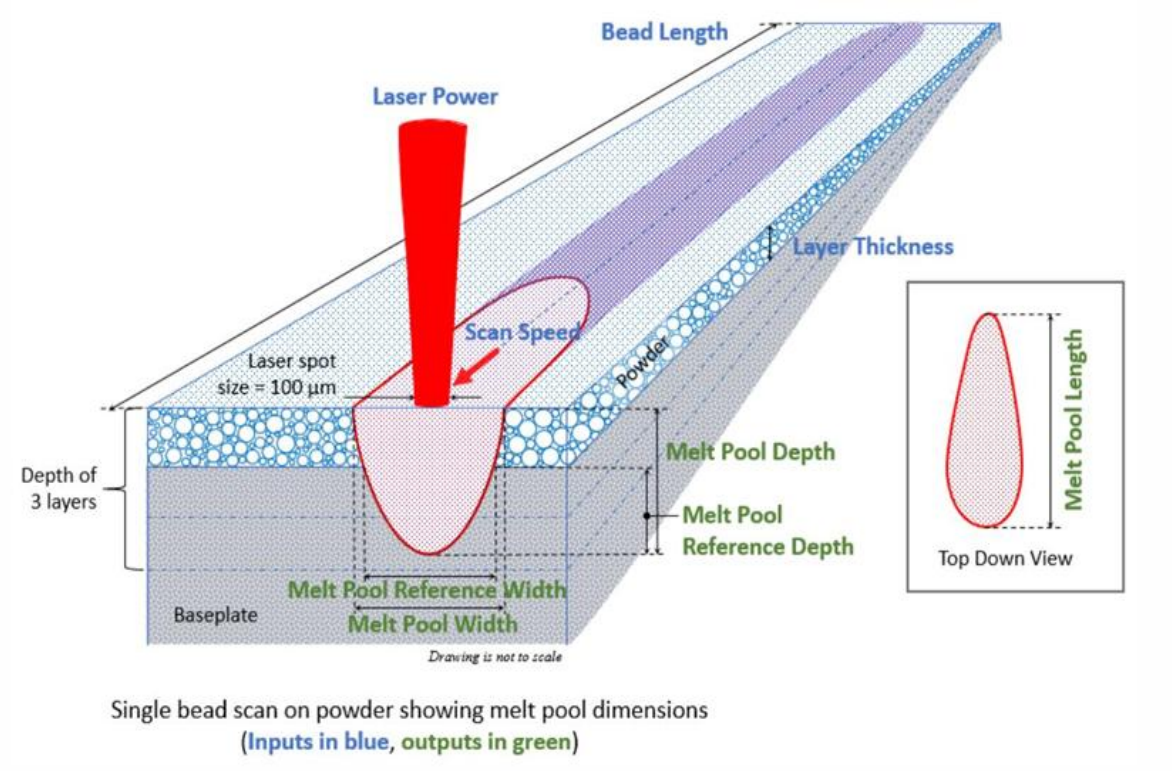


Figure 4.6 Illustration of the baseplate, the single-bead and their dimensions in the model, adapted from the ANSYS Additive User's Guide (2020).

4.2.5 Machine Learning

4.2.5.1 Data Generation and Pre-processing

Thermal simulation data were generated using the Ansys Additive thermal model for single-track laser melting. The dataset comprises process parameters and corresponding melt pool geometrical characteristics extracted from the simulated transient thermal fields. All data were assembled into a structured dataset and used directly without normalization, as tree-based models are invariant to monotonic feature scaling.

4.2.5.2 Surrogate Model Development

A data-driven surrogate model was developed to approximate the mapping between laser process parameters and melt pool geometry obtained from high-fidelity AMPP thermal simulations. A Random Forest regressor was selected due to its suitability for limited datasets, ability to capture nonlinear interactions between process parameters, and improved robustness through ensemble averaging. To mitigate overfitting, the model complexity was controlled using constrained tree depth and minimum leaf size parameters.

The final surrogate model employed 400 decision trees (n_estimators = 400), with a maximum tree depth of 18 and a minimum leaf size of 2. These parameters were selected empirically to

balance predictive accuracy and model generalization. To predict multiple geometrical outputs simultaneously, a multi-output regression framework was implemented using a MultiOutputRegressor wrapper.

The thermal simulations were performed on a workstation equipped with an Intel Xeon W-2275 CPU (3.30 GHz), 128 GB RAM and 14 cores. Each simulation required approximately 15 minutes to compute the melt pool geometry for a single set of process parameters. In contrast, the developed surrogate-based digital twin enables prediction of melt pool characteristics in less than one second. This represents a reduction in computational time by over three orders of magnitude, highlighting the potential of the proposed framework for rapid process exploration, optimization, and real-time decision support in PBF-LB of NiTi.

4.2.5.3 Physics-Guided Digital Twin Architecture

The trained surrogate model was integrated within a physics-guided digital twin framework for rapid prediction and assessment of melt pool behaviour in PBF-LB of NiTi. The framework combines data-driven surrogate predictions with explicit physics-based regime classification and constrained decision logic to support process exploration within physically meaningful operating conditions. Unlike conventional physics-informed machine learning approaches, physical constraints are not embedded directly into the surrogate model training objective. Instead, physically motivated melt pool stability criteria are incorporated at the decision-engine level to guide parameter selection and regime assessment rather than through direct embedding of governing equations within the surrogate model loss function.

The digital twin maps a vector of laser process parameters (**Eq. 4.4**):

$$\mathbf{x} = \{h, d_b, P, v\} \quad \textbf{(Eq. 4.4)}$$

where

- h= layer thickness (μm)
- d_b= beam diameter (μm)
- P= laser power (W)
- v= scan speed (mm/s)

to predicted melt pool geometrical features (**Eq. 4.5**):

$$\mathbf{y} = \{W, D, W_{ref}, D_{ref}, L\} \quad \textbf{(Eq. 4.5)}$$

Where

- W= melt pool width
- D= melt pool depth
- W_{ref}= melt pool reference width
- D_{ref}= melt pool reference depth
- L= melt pool length

Melt pool width corresponds to the width measured at the top surface of the deposited powder layer, while melt pool depth represents the combined depth of the remelted region and powder layer thickness. Reference melt pool width and reference melt pool depth are defined at the top of the remelted substrate beneath the deposited powder layer and therefore characterize only the remelted substrate geometry.

The surrogate model $\hat{f}(\cdot)$ was trained to approximate the Ansys Additive thermal simulation response (**Equation (4.6)**):

$$\hat{\mathbf{y}} = \hat{f}(\mathbf{x}) \quad \textbf{(Eq. 4.6)}$$

The surrogate model consists of a Random Forest regressor implemented in a multi-output framework (**Equation (4.7)**):

$$\hat{f}(\mathbf{x}) = \left[\widehat{W}(\mathbf{x}), \widehat{D}(\mathbf{x}), \widehat{W}_{ref}(\mathbf{x}), \widehat{D}_{ref}(\mathbf{x}), \hat{L}(\mathbf{x})\right] \quad \textbf{(Eq. 4.7)}$$

To improve generalization assessment, the surrogate model was evaluated using an 80/20 train-test split together with five-fold cross-validation. The final deployed surrogate was subsequently retrained using the full dataset to maximize predictive fidelity within the calibrated process space.

The digital twin was implemented as a modular Python framework consisting of dedicated prediction, regime-classification, and decision-engine components. This architecture enables reproducible deployment across graphical user interfaces, parameter-search routines, and future supervisory control extensions.

4.2.5.4 Decision Engine and Physics-Constrained Parameter Search

The digital twin framework was coupled with a physics-constrained decision engine to identify process parameter combinations associated with stable conduction-mode melting. Rather than performing gradient-based optimization, the framework employs a surrogate-assisted discrete parameter search constrained to the validated design-of-experiments (DOE) parameter space.

The search space was defined using laser power and scan speed as optimization variables while maintaining fixed layer thickness and beam diameter (**Eq. 4.8**).

$$\mathbf{z} = \{\mathrm{P}, \mathrm{v}\} \quad \textbf{(Eq. 4.8)}$$

For fixed layer thickness and beam diameter, the decision engine performs a discrete parameter search over predefined laser power and scan speed combinations corresponding to the validated DOE space used for surrogate model training. Restricting the search to DOE-consistent parameter combinations prevents extrapolation beyond the calibrated surrogate domain and improves physical reliability of the predictions. Candidate parameter combinations were evaluated using the surrogate model together with physics-based regime classification criteria. A candidate parameter set was considered feasible only if it satisfied conduction-regime conditions (**Eq. 4.9**). Among feasible candidates, a scalarized objective function was used to quantify melt pool stability, penalizing deviations from target geometric ratios:

- Reference depth-to-width ratio near 0.5
- Length-to-width ratio near 2–3

$$\mathcal{F} = \{\mathbf{z} \mid \mathrm{Regime}(\mathbf{z}) = \mathrm{Conduction}\} \quad \textbf{(Eq. 4.9)}$$

A scalarized stability objective was minimized (**Equation (4.10)**):

$$\mathrm{J}(\mathbf{z}) = \mid \mathrm{R_{DW}}(\mathbf{z}) - 0.5 \mid + \mid \mathrm{R_{LW}}(\mathbf{z}) - 2.5 \mid \quad \textbf{(Eq. 4.10)}$$

Regime classification was determined using dimensionless geometric ratios derived from predicted melt pool dimensions (**Eq. 4.11 and Eq. 4.12**):

$$R_{DW} = \frac{D_{ref}}{W_{ref}} \quad \textbf{(Eq. 4.11)}$$

$$R_{LW} = \frac{L}{\mathrm{W}} \quad \textbf{(Eq. 4.12)}$$

where R_{DW} represents the reference depth-to-width ratio and R_{LW} denotes the melt pool length-to-width ratio. The target values of 0.5 and 2.5 correspond to characteristic geometric ratios associated with stable conduction-mode melting reported in the literature. Minimization of $J(z)$ therefore selects parameter combinations closest to the desired stable melt pool morphology while remaining within the feasible conduction regime. The first term penalizes deviation from characteristic conduction-mode penetration behavior, while the second term penalizes excessive melt pool elongation associated with balling instability. The candidate minimizing this stability metric was selected as the optimal solution (**Eq. 4.13**). The optimal parameters were selected as:

$$\mathbf{z}^{*} = \arg\min_{\mathbf{z}\in\mathcal{F}} J(\mathbf{z}) \quad \textbf{(Eq. 4.13)}$$

The proposed framework employs a surrogate-assisted parameter exploration strategy rather than a formal gradient-based optimization algorithm. Candidate process parameters are sampled within predefined physically valid ranges and evaluated using the surrogate model. Predicted melt pool geometries are subsequently filtered using physics-based regime classification criteria to identify feasible conduction-mode conditions.

A scalarized stability objective function is then evaluated for all feasible candidates, and the parameter combination minimizing deviation from target geometric stability ratios is selected as the preferred operating condition.

4.2.5.5 Graphical User Interface Integration

A graphical user interface (GUI) was developed using the Tkinter framework to enable interactive use of the digital twin. The GUI allows users to:

- Enter PBF-LB process parameters,
- Predict melt pool geometry and processing regime,
- Perform physics-constrained parameter search for conduction-mode operation.

The interface displays predicted melt pool dimensions, geometric stability ratios, and the corresponding melt pool regime classification in real time, thereby enabling rapid engineering assessment without direct interaction with computationally intensive thermal simulations. **Figure 4.7** illustrates the overall workflow of the proposed framework and the GUI is shown in **Figure 4.8** and **Figure 4.9**.

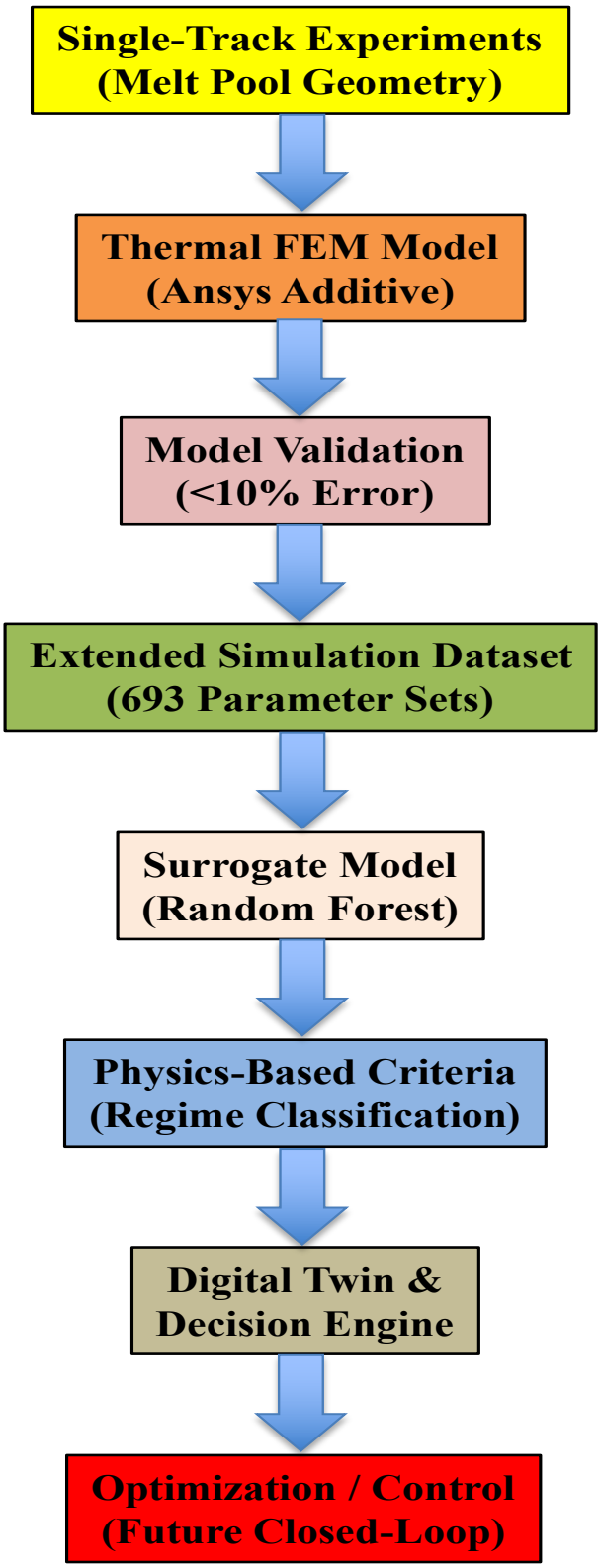


Figure 4.7 Schematic of the workflow of the physics-informed digital twin and decision engine.

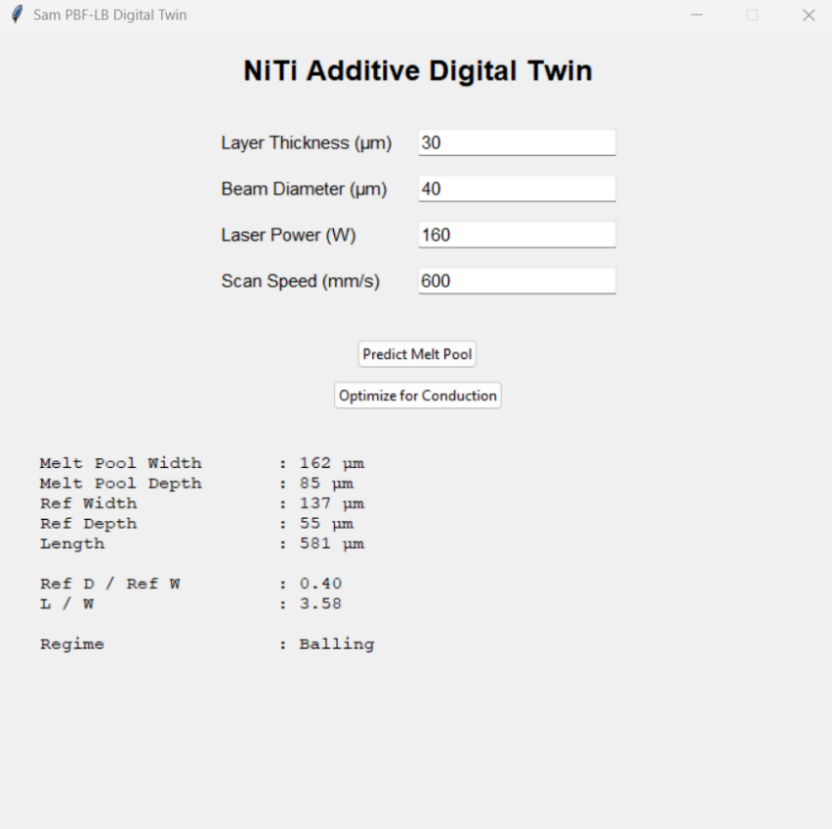


Figure 4.8 GUI showing melt pool prediction.

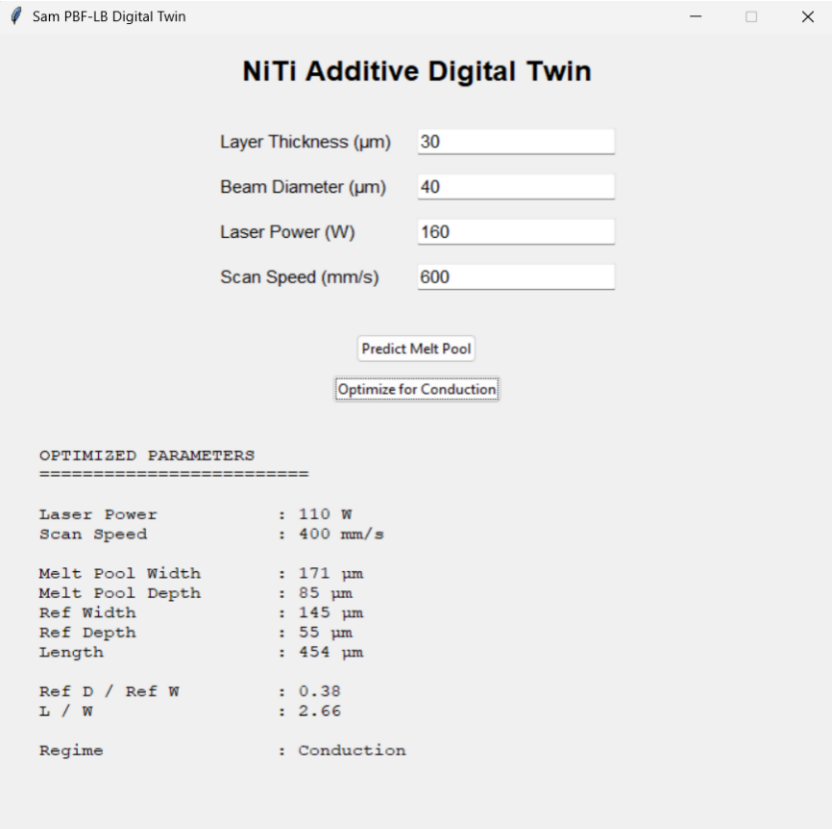


Figure 4.9 GUI showing process optimization.

4.3 Results and Discussion

4.3.1 IR Data Analysis

Figure 4.10 shows the relationship between laser power, scan speed and temperature recorded by the pyrometers as well as the thermogram layout of the printed single-tracks and multi-beads. It can be observed that the temperature increases with increasing power and decreases wirh increasing speed. This reflects the effect of energy density on melt pool temperature and thus the melt pool dimensions, where increase in energy density causes an increase in these attributes and vice-versa [257].

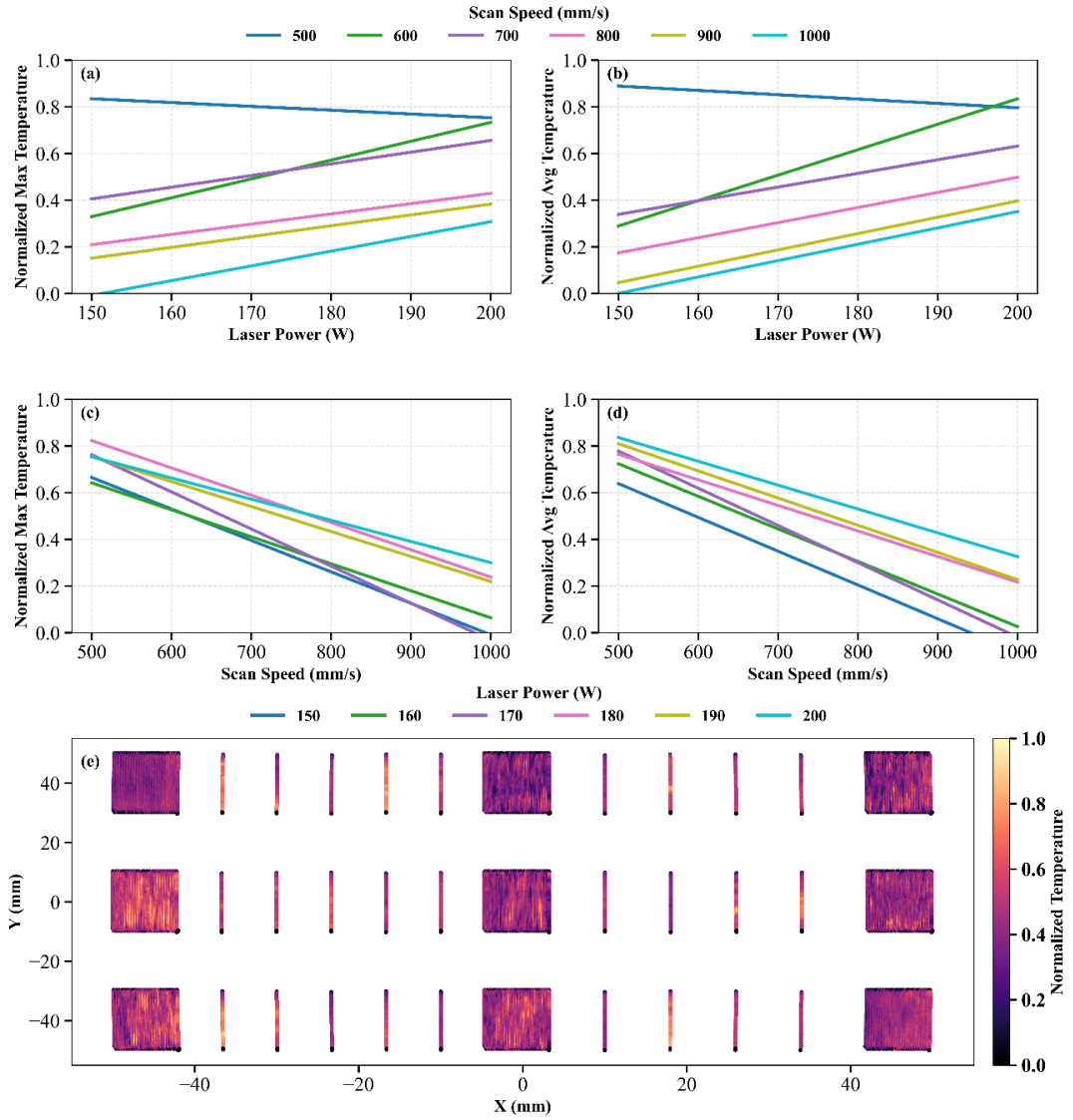


Figure 4.10 The effect of laser power on (a) maximum temperature, (b) average temperature, the effect of scan speed on (c) maximum temperature, (d) average temperature, and (e) the thermogram visualization of the single-tracks and multi-beads printed along with the corresponding temperature recorded from the pyromertic IR data monitoring.

4.3.2 Experimental Melt Pool Trend Analysis

Figure 4.11 presents the experimentally measured variation of melt pool width and depth as functions of laser power and scan speed for different processing conditions. The experimental results reveal clear and physically consistent trends where melt pool width and depth increase systematically with increasing laser power, whereas both quantities decrease with increasing scan speed, supporting the trends in IR melt pool temperature data **(Figure 4.10)**. At higher laser powers, the increased thermal energy input promotes greater heat accumulation and enhanced melting, resulting in wider and deeper melt pools. Conversely, increasing scan speed reduces the interaction time between the laser and material, thereby decreasing the absorbed energy per unit length and limiting melt pool growth. The observed behavior agrees well with established thermophysical interpretations reported in the literature for laser-based additive manufacturing processes [170,186,211].

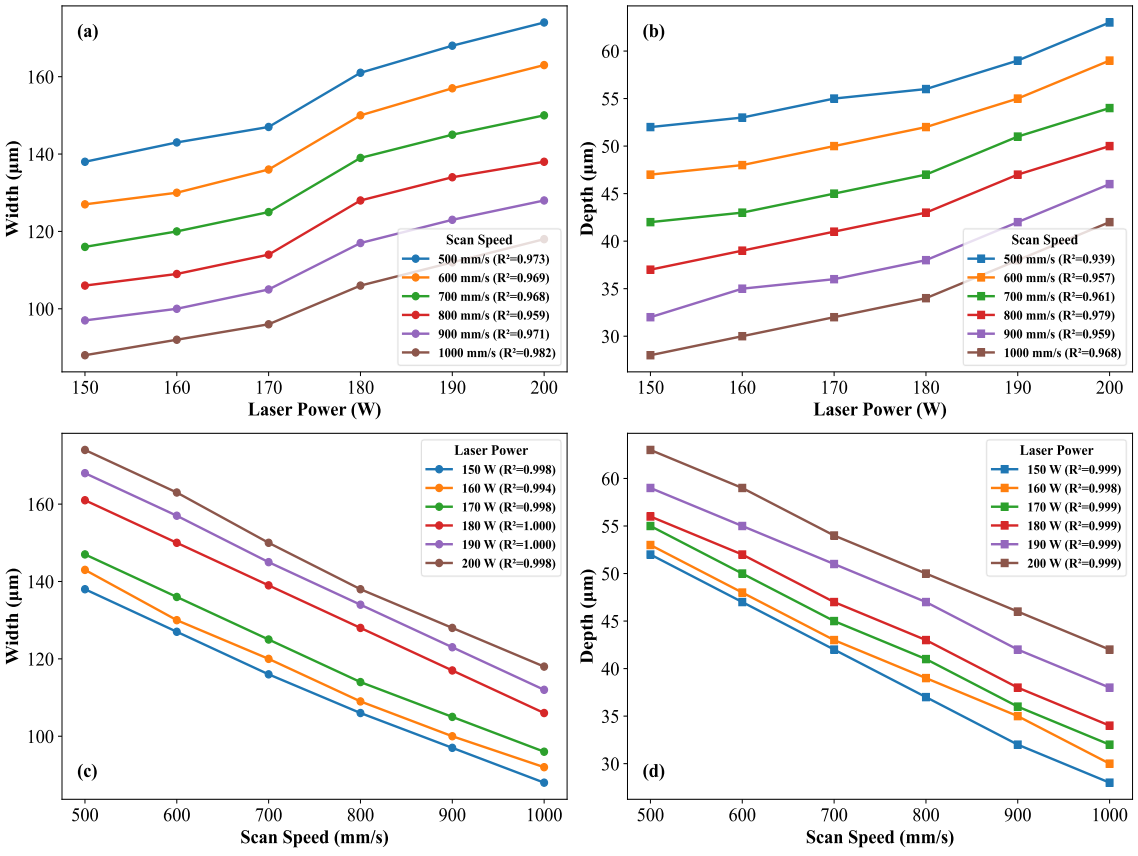


Figure 4.11 (a) Effect of laser power on melt pool width (b) effect of laser power on melt pool depth, (c) effect of scan speed on melt pool width and (d) effect of scan speed on melt pool depth from the experimental measurements along with the corresponding R^2 values.

4.3.3 Thermal Model Performance

The developed FE thermal model was employed to simulate melt pool behavior for the 36 process parameter combinations used in the single-track experiments. The model demonstrated good agreement with experimental measurements, achieving prediction accuracies exceeding 90% for melt pool width and depth across most parameter sets. A detailed comparison between simulated melt pool dimensions, along with the corresponding prediction errors, is provided in **Table 4.1**. In addition to width and depth, the thermal model was used to estimate melt pool length, which is difficult to measure reliably in the experimental setup. Percentage error was calculated as:

$$\text{Error (\%)} = \frac{\text{Predicted} - \text{Experimental}}{\text{Experimental}} \times 100 \qquad \textbf{(Eq. 4.14)}$$

where positive values indicate overprediction and negative values indicate underprediction relative to experimental measurements. A representative example of a simulated melt pool is shown in **Figure 4.12**.

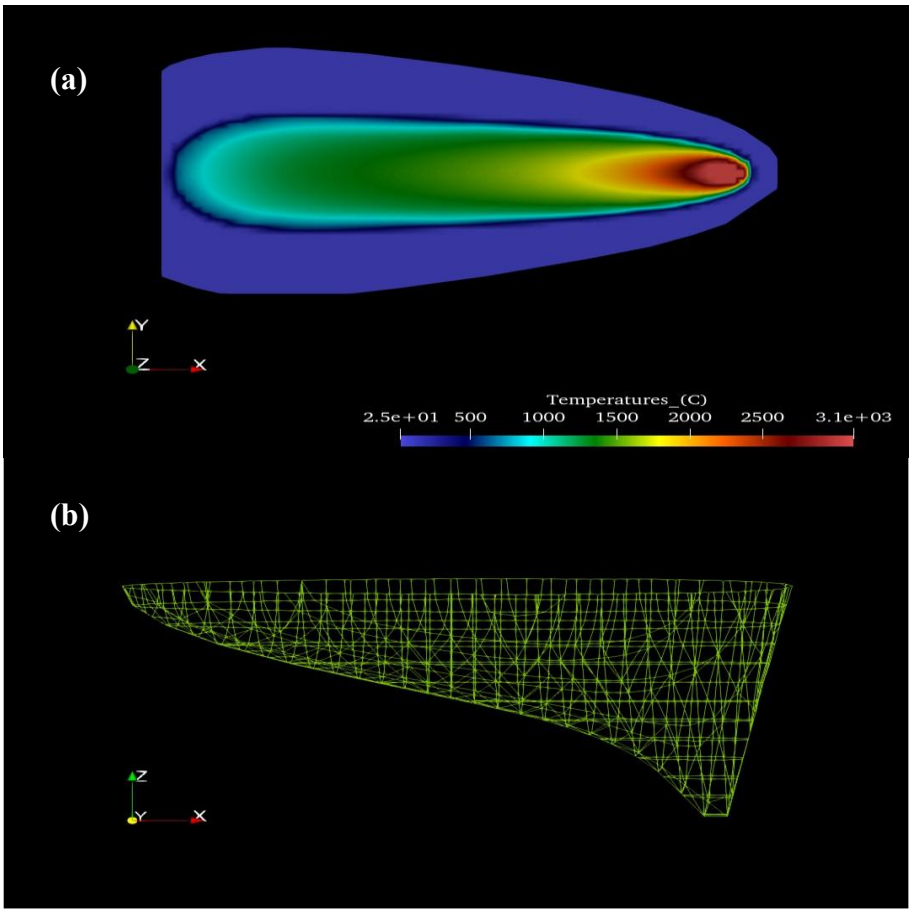


Figure 4.12 Simulation of the melt pool from the model (a) top-view (b) side view.

Table 4.1 Comparison of AMPP thermal FE model predicted melt pool dimensions with experimental measurements and corresponding errors.

Sample No.	Laser Power (W)	Scan Speed (mm/s)	Exp. Melt Pool Width (µm)	Model Melt Pool Ref Width (µm)	Width Error (%)	Exp. Melt Pool Depth (µm)	Model Melt Pool Ref Depth (µm)	Depth Error (%)	Melt Pool Width (µm)	Melt Pool Depth (µm)	Melt Pool Length (µm)
1	150	500	138	152	10.1	52	57	9.4	173	87	567
2	150	600	127	139	9.7	47	51	7.9	163	81	578
3	150	700	116	126	9.0	42	45	7.3	151	75	578
4	150	800	106	115	8.0	37	40	7.5	140	70	570
5	150	900	97	105	8.5	32	34	7.2	133	64	559
6	150	1000	88	95	7.5	28	29	4.7	125	59	544
7	160	500	143	156	9.1	53	59	11.1	178	89	588
8	160	600	130	143	9.9	48	53	9.4	166	83	601
9	160	700	120	131	8.9	43	47	10.3	156	77	603
10	160	800	109	119	9.3	39	42	7.5	142	72	598
11	160	900	100	110	10.0	35	37	6.0	137	67	593
12	160	1000	92	100	8.6	30	32	6.0	129	62	577
13	170	500	147	160	8.7	55	60	9.6	183	90	606
14	170	600	136	146	7.6	50	54	8.6	169	85	623
15	170	700	125	135	7.8	45	50	10.2	159	80	629
16	170	800	114	123	8.3	41	44	7.9	147	74	628
17	170	900	105	114	8.4	36	40	10.2	139	70	626
18	170	1000	96	105	8.9	32	34	7.6	132	64	610
19	180	500	161	163	1.2	56	61	9.4	186	91	622
20	180	600	150	150	-0.2	52	56	7.6	171	86	642
21	180	700	139	139	-0.3	47	51	8.6	163	81	654
22	180	800	128	128	-0.1	43	46	7.8	152	76	655
23	180	900	117	117	0.3	38	42	9.3	141	72	652
24	180	1000	106	109	2.9	34	37	8.7	136	67	644
25	190	500	168	166	-1.2	59	62	5.4	189	92	636
26	190	600	157	153	-2.8	55	57	4.5	173	88	661
27	190	700	145	141	-2.5	51	53	3.4	165	83	676
28	190	800	134	131	-1.9	47	48	2.8	157	78	681
29	190	900	123	121	-1.5	42	44	3.9	145	74	681
30	190	1000	112	112	0.4	38	39	3.5	138	69	675
31	200	500	174	169	-3.0	63	63	-0.1	191	93	650
32	200	600	163	156	-4.5	59	58	-0.9	177	89	678
33	200	700	150	144	-4.0	54	54	0.5	167	84	697
34	200	800	138	135	-2.2	50	50	0.1	159	80	706
35	200	900	128	125	-2.7	46	46	-0.9	149	76	708
36	200	1000	118	115	-2.1	42	41	-2.2	140	71	701

Following validation of the thermal model against experimental observations, the dataset was systematically expanded to cover 693 process parameter combinations. This extended dataset comprised three layer thicknesses, three beam diameters, eleven laser power levels, and seven scan speeds. The resulting melt pool dimensions predicted for this expanded parameter space are presented in **Figure 4.13**, **Figure 4.14**, and **Figure 4.15**. For most of the parameter combinations, melt pool dimensions exhibit an approximately linear dependence on laser power and scan speed. However, in certain cases, a logarithmic relationship with scan speed is observed. Similar trends were reported in our previous study, where both experimental measurements and predictions from various analytical models demonstrated comparable scan speed–dependent behaviour [170]. The comprehensive dataset generated through this approach was subsequently used to train the surrogate model described in the following sections.

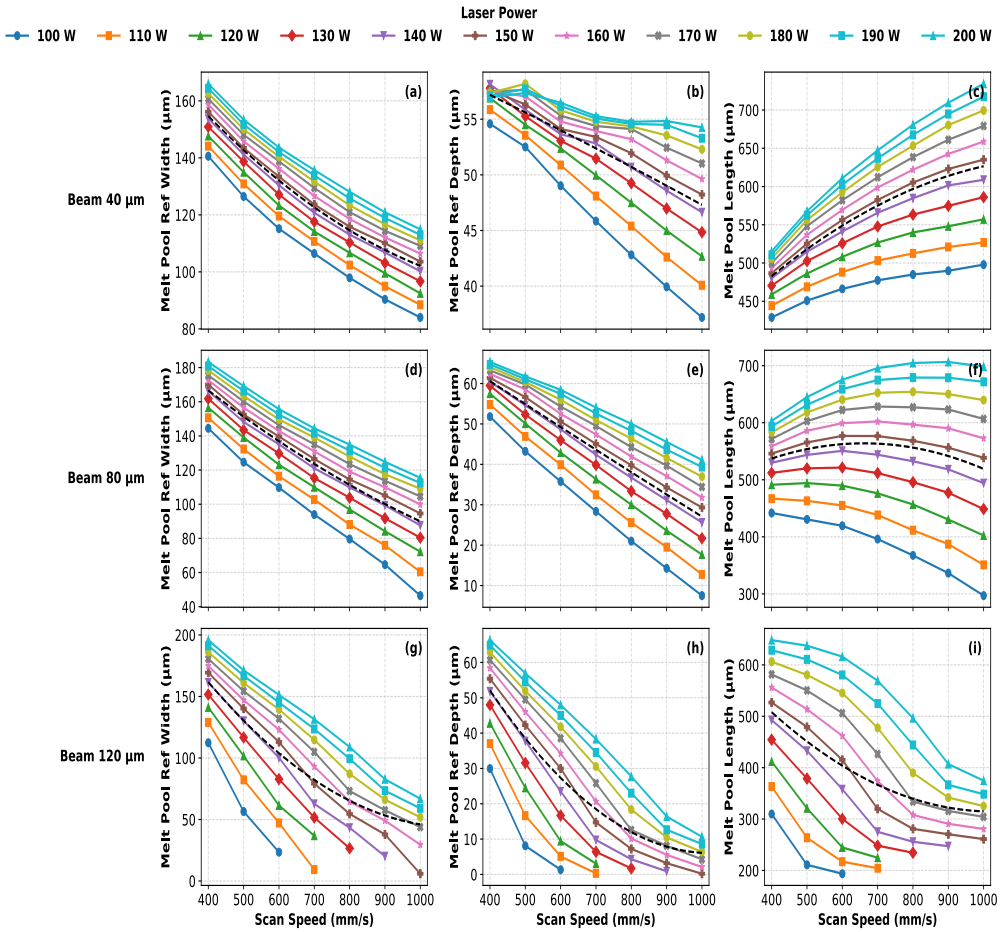


Figure 4.13 Thermal model predicted melt pool dimensions for 30 µm layer thickness - (a) melt pool width, (b) melt pool depth (c) melt pool length for 40 µm beam diameter, (a) melt pool width, (b) melt pool depth (c) melt pool length for 80 µm beam diameter, (a) melt pool width, (b) melt pool depth (c) melt pool length for 120 µm beam diameter. Dashed lines represent the overall trend.

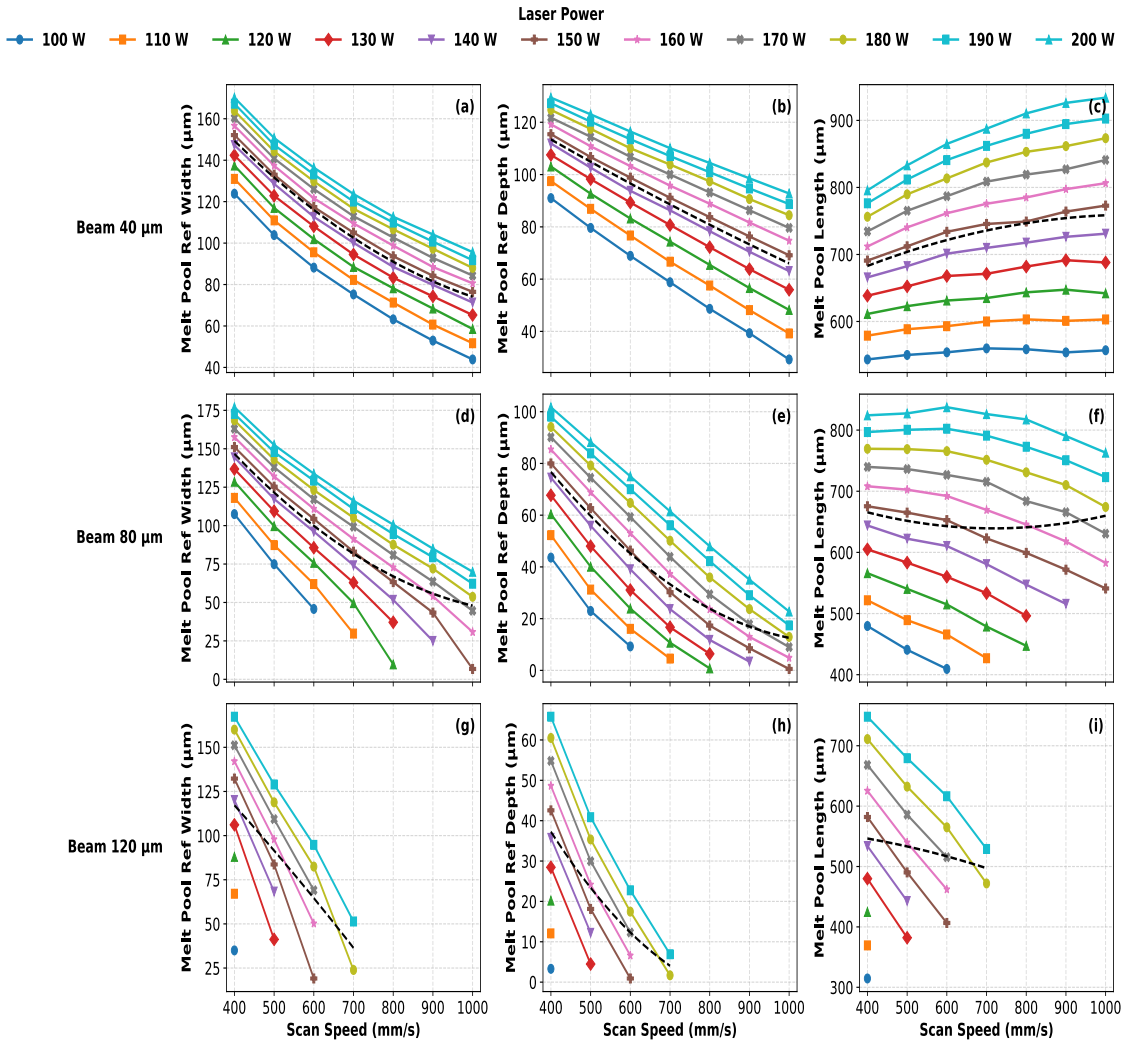


Figure 4.14 Thermal model predicted melt pool dimensions for 30 µm layer thickness - (a) melt pool width, (b) melt pool depth (c) melt pool length for 40 µm beam diameter, (a) melt pool width, (b) melt pool depth (c) melt pool length for 80 µm beam diameter, (a) melt pool width, (b) melt pool depth (c) melt pool length for 120 µm beam diameter. Dashed lines represent the overall trend.

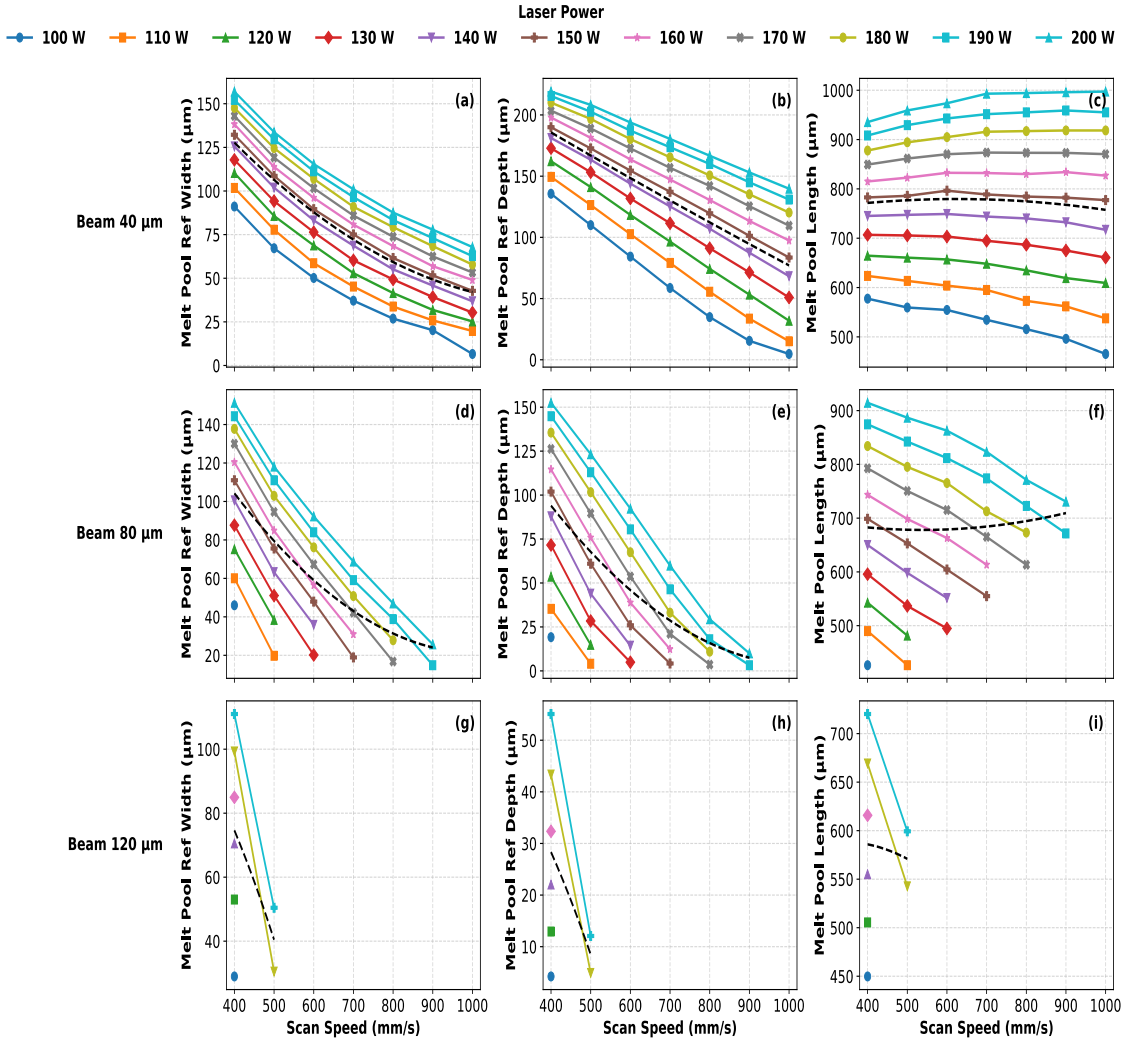


Figure 4.15 Thermal model predicted melt pool dimensions for 30 µm layer thickness - (a) melt pool width, (b) melt pool depth (c) melt pool length for 40 µm beam diameter, (a) melt pool width, (b) melt pool depth (c) melt pool length for 80 µm beam diameter, (a) melt pool width, (b) melt pool depth (c) melt pool length for 120 µm beam diameter. Dashed lines represent the overall trend.

4.3.4 Surrogate Model Performance

The surrogate model performance was evaluated using the coefficient of determination (R^2), mean absolute error (MAE), and root mean square error (RMSE) on an independent test dataset obtained using an 80/20 train-test split. In addition, five-fold cross-validation was performed to assess model robustness and generalization within the calibrated process parameter space. The multi-output Random Forest surrogate demonstrated consistently high predictive accuracy across all melt pool geometrical descriptors:

- Melt pool width: $R^2 = 0.959$, MAE = 6.19 μm, RMSE = 8.17 μm
- Melt pool depth: $R^2 = 0.991$, MAE = 3.57 μm, RMSE = 5.72 μm
- Reference width: $R^2 = 0.964$, MAE = 6.90 μm, RMSE = 10.42 μm
- Reference depth: $R^2 = 0.982$, MAE = 4.01 μm, RMSE = 6.00 μm
- Melt pool length: $R^2 = 0.983$, MAE = 20.70 μm, RMSE = 28.16 μm

The corresponding five-fold cross-validation results further confirmed model stability, with mean R^2 values of 0.964, 0.988, 0.962, 0.980, and 0.982 for melt pool width, depth, reference width, reference depth, and melt pool length, respectively. The low standard deviations across folds (<0.01) indicate consistent predictive performance and limited sensitivity to data partitioning.

The high R^2 values demonstrate that the surrogate effectively captures the nonlinear relationships between laser process parameters and melt pool geometry within the simulated process space. The relatively low MAE and RMSE values indicate strong agreement between surrogate predictions and the underlying AMPP thermal simulation outputs in absolute dimensional terms. Among the predicted quantities, melt pool length exhibited comparatively larger errors, which is attributed to its stronger sensitivity to trailing thermal gradients, heat accumulation, and solidification dynamics compared with width- and depth-related features. Overall, the surrogate model provides an accurate and computationally efficient approximation of the calibrated thermal simulations, enabling rapid melt pool prediction suitable for digital twin deployment and physics-constrained parameter exploration.

4.3.5 Physics-Based Melt Pool Regime Classification

Beyond numerical prediction accuracy, the digital twin incorporates explicit physics-based criteria to classify melt pool regimes. Regime classification is based on dimensionless geometric ratios derived from predicted melt pool features, specifically the reference depth-to-width ratio and the melt pool length-to-width ratio. These criteria reflect well-established physical interpretations of melt pool stability in laser powder bed fusion processes.

The following regimes are identified within the framework:

- **Lack of fusion**, corresponding to insufficient penetration when the melt pool reference depth is smaller than the layer thickness [239]
- **Conduction mode**, characterized by stable melting within the range $0.3 \leq D_{\text{ref}}/W_{\text{ref}} \leq 0.6$ [215]

- **Keyhole mode**, associated with excessive penetration when $D_{\text{ref}}/W_{\text{ref}} > 0.6$ [101]
- **Balling**, identified when the melt pool length-to-width ratio exceeds a critical threshold of 3 [108]

This rule-based classification incorporates metallurgical and fluid-mechanical knowledge into the regime assessment process, ensuring that melt pool regime identification is governed by physically motivated criteria rather than purely data-driven classification. As a result, the framework provides not only quantitative melt pool geometry predictions but also qualitative insight into process stability and manufacturability.

4.3.6 Physics-Guided Decision Engine and Input Constraints

A key contribution of this work is the integration of physics-guided constraints within the decision-engine framework. Input parameters are restricted to discrete values corresponding to the experimentally and numerically validated DOE space used for surrogate model development, thereby preventing extrapolation beyond the surrogate's reliable operating domain. This constraint-based strategy ensures that all predictions and parameter-search results remain physically meaningful and manufacturable.

By enforcing both numerical validity and discrete parameter constraints, the digital twin operates as a controlled decision-support tool rather than a purely predictive model. This design choice is particularly important for additive manufacturing applications, where small deviations in process parameters can lead to unstable melt pool behaviour or defect formation [262].

4.3.7 Physics-Constrained Process Parameter Search

The developed framework enables automated process parameter exploration through a physics-constrained parameter-search routine aimed at identifying conduction-mode operating conditions. The decision engine leverages the surrogate model to rapidly evaluate candidate parameter combinations while rejecting solutions that violate melt pool stability criteria.

Unlike unconstrained parameter-selection approaches, the proposed decision engine prioritizes physical feasibility over purely mathematical optimality. As a result, optimized solutions consistently satisfy conduction-mode conditions while maintaining realistic laser power and scan speed combinations. This demonstrates the suitability of the digital twin for use as a supervisory decision-support tool in additive manufacturing process planning.

4.3.8 Digital Twin Interpretation and Implications

The integration of surrogate modelling, physics-based regime classification, and constrained optimization constitutes a process-level physics-guided digital twin framework for laser powder bed fusion of NiTi. The developed framework enables rapid prediction of melt pool geometry and stability, allowing rapid exploration of process parameter effects without repeated high-fidelity simulations. This capability represents a significant reduction in computational cost and provides a practical pathway for accelerated process development and optimization.

Figure 4.16 shows the feature importance and partial dependence plots to evaluate the effects of various PBF-LB process parameters on melt pool geometry. The feature importance analysis reveals that different melt pool dimensions are governed by distinct process parameters, highlighting the multi-physics nature of laser-matter interaction in PBF-LB [273]. Melt pool width is primarily controlled by scan speed and laser power, reflecting the role of energy input per unit length and lateral heat diffusion [108,190]. In contrast, melt pool depth is dominated by beam diameter and layer thickness, indicating the importance of power density and penetration efficiency [101,274]. Melt pool length is most sensitive to beam diameter and laser power, consistent with thermal trailing and solidification dynamics [262,275].

Partial dependence plots further demonstrate monotonic and physically consistent trends, with increasing laser power enhancing all melt pool dimensions, while increasing scan speed systematically reduces width, depth, and length [92,276]. The trends corroborate well with the parameter-temperature relationship from the IR data analysis illustrated in **Figure 4.10**. These results validate the surrogate model's physical fidelity and provide a mechanistic basis for regime-based process optimization.

From a materials perspective, the predicted melt pool geometries are directly linked to solidification conditions, thermal gradients, and cooling rates, which govern microstructure evolution, defect formation, and phase transformation behaviour in NiTi. In particular, the transition between conduction, keyhole, balling, and lack-of-fusion regimes provides a physically meaningful basis for identifying process windows that minimize defects and ensure stable processing conditions [132,133,257]. The incorporation of such physics-based criteria within the digital twin enables not only prediction but also informed decision-making aligned with materials performance requirements.

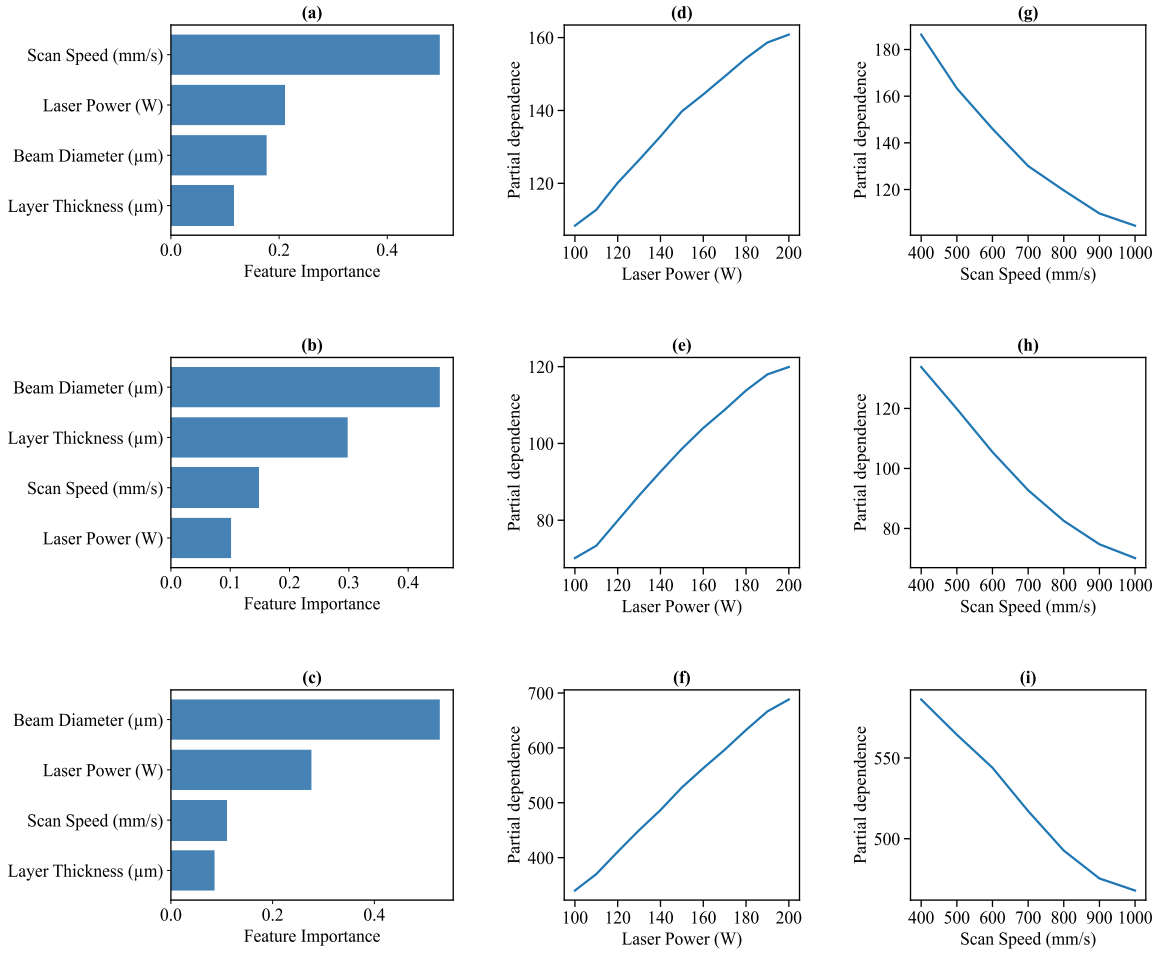


Figure 4.16 Random Forest feature importance plots for melt pool (a) width, (b) depth, (c) length, and partial dependence showing the influence of laser power on melt pool (d) width, (e) depth, (f) length, and scan speed on melt pool melt pool (g) width, (h) depth,

Importantly, the framework is inherently extensible. While the present study focuses on offline prediction and optimization, the architecture is readily adaptable to closed-loop or supervisory control by incorporating in-situ sensing and feedback. In this context, the surrogate model serves as the predictive core, while the physics-based decision logic ensures safe and stable operation.

Overall, the results demonstrate that embedding physical knowledge into data-driven surrogate models yields a robust, interpretable, and computationally efficient digital twin. The proposed approach not only enhances process understanding but also provides a scalable foundation for linking process parameters to microstructure and functional performance in NiTi-based additive manufacturing.

4.3.9 Limitations and Future Outlook

Several limitations of the present study should be acknowledged. First, the surrogate model is trained exclusively on simulation data and is therefore limited by the assumptions and fidelity of the underlying thermal model. While experimental validation was performed for a subset of conditions, broader experimental verification would further strengthen confidence in the digital twin. Second, the current regime classification relies solely on geometric criteria and does not explicitly account for fluid flow, vaporization, or spatter dynamics, which may influence melt pool stability under extreme conditions [252,277].

Future work will therefore focus on integrating hybrid simulation–experimental datasets and in-situ monitoring data to further improve physical representativeness. Furthermore, the digital twin framework can be extended to part-scale predictions, including porosity formation, surface roughness and residual stress development. Additionally, integration with in-situ sensing modalities such as melt pool imaging or pyrometry would enable closed-loop control and continuous model updating. These extensions would further enhance the applicability of the proposed framework for real-world additive manufacturing environments.

4.4 Conclusion

In this study, an offline physics-guided digital twin framework was developed for predicting and optimizing melt pool behavior in PBF-LB of NiTi. A high-fidelity thermal finite element model was first established and calibrated using single-track experimental measurements and temperature-dependent thermophysical properties obtained via the CALPHAD method. The calibrated thermal model demonstrated strong agreement with experimental observations, achieving prediction accuracies exceeding 90% for melt pool width and depth.

Leveraging the validated thermal model, an extensive dataset comprising melt pool width, depth, and length was generated over a broad range of process parameters. This dataset was subsequently employed to train a multi-output Random Forest surrogate model capable of rapidly predicting melt pool geometrical features with high computational efficiency. The surrogate demonstrated excellent predictive performance, achieving coefficients of determination (R^2) greater than 0.95 for all melt pool descriptors, along with low mean absolute error (MAE) and root mean square errors (RMSE) relative to the thermal model outputs.

To ensure physical interpretability and manufacturability, physics-based geometric criteria were embedded into the framework to classify melt pool regimes, including lack of fusion, keyholing, balling, and stable conduction. By integrating these criteria with surrogate predictions, the physics-guided digital twin functions as a decision engine that identifies process parameter combinations conducive to stable conduction-mode melting. A graphical user interface was developed to facilitate intuitive interaction with the digital twin and to support informed process parameter selection.

While the current implementation is focused on micro-scale melt pool predictions, the proposed framework is inherently extensible. Future work will target expansion to meso-scale, micro-scale and part-scale predictions, including porosity formation, surface roughness, residual stress development, microstructure, phase fractions and resulting functional properties, thereby enhancing its relevance for component-level performance assessment. Furthermore, integration of the offline digital twin with in-situ sensing and manufacturing hardware would enable closed-loop process control, paving the way toward adaptive and intelligent additive manufacturing systems. Additional experimental validation over the extended parameter space will further assess the robustness and generalizability of both the thermal and surrogate models. Overall, this work demonstrates that coupling high-fidelity thermal modeling with data-driven surrogates and physics-based decision logic provides a powerful and scalable approach for melt pool prediction, regime identification, and process optimization in PBF-LB of NiTi.

Contribution towards the thesis: In this chapter, a calibrated thermal finite element model was developed to simulate melt pool behaviour under PBF-LB conditions. Temperature-dependent material properties were derived using the CALPHAD method, enabling improved representation of NiTi's thermophysical and phase-dependent behaviour, addressing a major limitation identified in the literature. The FE model was validated against experimental melt pool measurements and subsequently used to generate datasets for training multi-output surrogate models. These surrogate models form the core of a physics-informed digital twin framework, enabling rapid melt pool prediction and process parameter optimisation within physically constrained regimes. The results represented a substantial improvement over analytical models and demonstrated the importance of temperature-dependent material data. The successful integration of FE modelling, CALPHAD data, surrogate machine learning, and physics-based constraints represents a step-change in melt pool prediction and optimisation for NiTi, bridging the gap between accuracy and computational efficiency.

5. Chapter: Evaluating Residual Stress in Additively Manufactured Nitinol Shape Memory Alloy

---

Publication Status: Published

Sampreet Rangaswamy, Josiah Cherian Chekotu, Thomas Gillick, Cian Hughes, Jayne Nicholl, David Easton, Caner Şimşir, Dermot Brabazon, **Evaluating Residual Stress in Additively Manufactured Nitinol Shape Memory Alloy**, npj Advanced Manufacturing 2 (2025).

https://doi.org/10.1038/s44334-025-00027-y

Abstract

This study provides a comprehensive analysis of residual stress characteristics in nitinol parts fabricated via PBF-LB. Unlike previous works that primarily focus on qualitative assessments or single-measurement techniques, this research employs a multi-modal experimental approach, Electronic Speckle Pattern Interferometry-Hole Drilling (ESPI-HD) and X-ray Diffraction (XRD), to achieve a more precise and spatially resolved evaluation of residual stress distribution. Furthermore, the study establishes a direct correlation between residual stress evolution and in situ pyrometric melt pool temperature data, an aspect that has not been extensively explored in prior investigations. A key novel finding is the non-monotonic relationship between volumetric energy density (VED) and residual stress. In this work, laser power was kept constant, and VED was varied by adjusting scanning speed and hatch spacing. The results show that the average residual stress initially increases with decreasing scan speed and hatch spacing, plateaus at a critical threshold, and subsequently decreases. However, residual stress was also found to vary in the build direction, indicating the complex stress distributions and accommodation mechanisms within the material. Additionally, an inverse relationship was recorded between the thermal gradient and VED which challenges conventional assumptions about their relationship. These insights offer a new perspective on optimizing PBF-LB process parameters for enhanced structural performance and long-term reliability of additively manufactured nitinol.

5.1 Introduction

Residual stress (RS) can be evaluated through destructive (distortion-based), semi-destructive and non-destructive techniques (diffraction-based). The destructive measurements work on the basis of the strain–release principle. When an RS-free material is sectioned at a plane, the total summation of stresses normal to the plane should be zero at static equilibrium. If a nonzero strain value is measured normal to the plane, then this difference caused by disturbance of the mechanical equilibrium provides an indication of the RS. The measured strain can then be processed via an analytical or finite element (FE) model to estimate the actual stress values. Common destructive methods include the hole-drilling (HD) method, contour method, and micro-ring core milling analysis [278,279]. A recent modification has been introduced to the traditional hole-drilling method, known as the electronic speckle-pattern interferometry (ESPI)-hole drilling method. ESPI is an innovative, noncontact optical measurement technique designed for the precise measurement of small displacements across the entire field of view. It is a semi-destructive RS measurement technique that is utilized to measure the distribution and magnitude of RS near the surface of a component. It involves drilling a small hole at small increments on the surface of the component, which is illuminated by coherent laser light. The removal of material causes surface displacements and strains as a result of stress release, while the back calculation of these strains is used to determine the original RS at each increment. The method is based on image analysis of images created by the interference of the object beam and the reference beam, where the reference beam is phase shifted and an image is taken at each shift. The ESPI method is therefore more effective in determining the stress relaxations identified by the changes in the speckle pattern. By subtracting this modified speckle pattern from a reference pattern, correlation fringes are obtained, enabling accurate quantification of RS in a highly efficient and non-invasive manner [280,281].

Diffraction-based methods, such as X-ray diffraction (XRD) and neutron diffraction (ND), rely on two fundamental principles. The first is Bragg's law presented in **Eq. 5.1**, which relates the position of the diffracted peak (θ) to the lattice spacing (d_{hkl}) and the wavelength of the incident radiation (λ). This relationship allows the measurement of the lattice spacing, which can then be compared with the unstrained lattice parameters and ray constants to determine the existing lattice strain [282,283].

$$n\lambda = 2d_{hkl}\sin\theta \qquad \textbf{(Eq. 5.1)}$$

The second principle is based on Hooke's law, which relates strain to stress through the material's modulus of elasticity (E). In diffraction-based methods, this relationship is used to estimate stress values. The stress normal to the measured plane is assumed to be zero, allowing the lattice spacing (d) to be directly interpreted as the strain measurement. The relationship between the stress (σ_φ), Young's modulus (E), Poisson's ratio (ν), and slope (m) of d vs. $\sin^2\Psi$ (Ψ is the angle between the sample surface normal and the diffraction vector) is given by **Eq. 5.2** [284,285], where φ represents the orientation angle.

$$\sigma_\varphi = \left(\frac{E}{1+\nu}\right).m \qquad \textbf{(Eq. 5.2)}$$

The primary objective of this study was to investigate the influence of VED (controlled through variations in scanning speed and hatch spacing while keeping laser power constant) on the development of RS in NiTi samples fabricated via PBF-LB. RS measurements were conducted using two complementary techniques: X-ray diffraction (XRD) for surface-level stress distribution (up to 100 μm depth) and Electronic Speckle Pattern Interferometry-Hole Drilling (ESPI-HD) for stress analysis up to 250 μm in depth. Unlike previous studies that primarily focus on qualitative residual stress assessments or single-measurement methods, this work provides a depth-resolved, multi-modal analysis, offering a more comprehensive understanding of RS distribution in additively manufactured NiTi. Furthermore, the measured residual stresses were systematically correlated with in situ pyrometric infrared (IR) melt pool temperature data—an approach that had received limited attention in the literature to date.

5.2 Materials and Methods

5.2.1 Experimental Details

The NiTi powder used was composed of 50 at.% Ni and 50 at.% Ti. The samples were fabricated using Aconity MINI (GmbH) PBF-LB machine equipped with a Nd:YAG fiber laser system from IPG Photonics, which has a wavelength of 1070 nm and a maximum power capacity of 200 W. The build chamber was installed with a rubber-based recoater blade. The chamber was purged with argon gas (99.999%) to ensure a minimum oxygen content (<50 ppm) throughout the melting and solidification process. A powder supply factor of 1.8 (nearly twice the layer thickness) was used in the print process to ensure sufficient powder spread. To reduce spatter on fresh layers, the printing sequence started from the inert gas exit side of the build chamber.

Printing was performed using the laser parameter levels shown in **Table 5.1**, with a layer thickness of 40 μm and a spot size of 50 μm. The sample dimensions were 20×10×7.5 mm^3. The layer thickness was determined on the basis of the feedstock particle size distribution to ensure good powder spread and flowability on the build platform.

The laser power was kept constant, while the scanning speed was decreased in increments of 300 mm/s, and the hatch spacing was reduced by 15 μm steps to achieve increasing VED.

The samples were arranged on the substrate plate at an in-plane angle of 30° to reduce any impact load on the re-coater assembly and to allow more gradual gas flow/fume removal over the layers in the chamber during printing. A simple stripe scanning strategy was maintained with a rotation of 90° for each subsequent layer. This prevents any unwanted overheating around the corners of the sample. The build chamber ambient temperature during the process was 20 ± 1 °C.

Table 5.1 Parameter levels used and respective volumetric energy densities.

Sample	LP (W)	SS (mm/s)	HS (μm)	VED (J/mm^3)
S1	150	1200	70	44.64
S2	150	900	55	75.76
S3	150	600	40	156.25

5.2.1.1 Thermal data monitoring

The thermal data of the molten pool were captured using two pyrometers from KLEIBER Infrared GmbH, which were employed in the Aconity PBF-LB machine. These pyrometers detect the light emitted from the area where the laser interacts, which falls within the 1500–1700 nm wavelength range. The resulting infrared (IR) data are recorded in terms of voltage (mV) units and the corresponding coordinates on the build plate (x, y, z). In this study, we generated graphical representations to visualize the temperature variations across different sections of a sample. The rate at which the data were collected was 100000 samples per second. Approximately 6 million data points were collected for a single layer, each comprising both coordinates and temperature values in mV. To depict the thermal profile, the temperature readings were transformed into a normalized scale ranging from 0 to 1.

5.2.1.2 Experimental RS measurement

XRD measurements were performed using a 3-circle portable-type stress diffractometer in modified-χ mode. Considering the fluorescence of copper with nickel and chromium with

titanium, it was not possible to measure the stresses with those well-known X-ray sources. As alternatives, Mn–Kα and Ti–Kα radiation were used, and the best results were acquired using Ti–Kα radiation with an average wavelength of 0.2752 nm. Using this radiation, considering the diffraction peaks above $2\theta > 120°$, it was possible to perform the measurements using the {1 1 0} or {2 0 0} set of planes of the austenite phase. Although a higher diffraction angle is favored for the {2 0 0} set of planes, the peaks were quite broad (reaching 10°–15°) because of the small crystallite size and high dislocation density, which resulted in the extension of the detection range. Thus, the measurements were carried out on a (2 1 1) set of planes located at approximately 134°. The tube voltage was set to 30 kV, and the tube current was 7 mA. Before the measurements, the focal distance was calibrated using both commercially pure Ti (CP-Ti) and Ti-6Al-4V powders, which are certified by the diffractometer manufacturer. In both cases, the focal distance was adjusted so that the total error in the stress calculations was lower than ±10 MPa. **Figure 5.1** (a) shows the XRD measurement setup.

For ESPI-hole drilling measurements, the sample surface was spray painted to reduce reflections. A drilling operation was performed precisely at the center of the sample using a Ø0.79 mm 2 flute carbide TiAlNi-coated inverted end mill. The drilling process involved incremental steps of approximately 50 μm until a depth of 250 μm was reached. A feed rate of 0.025 mm/s and a spindle speed of 30x1000/min were selected as the drilling conditions, according to the recommendations of the operation manual. Simultaneously, a laser beam was employed to illuminate the sample, while a camera captured the distinctive speckle pattern generated by the surface roughness. This camera image captures the interference between the object beam and the reference beam. The reference beam underwent phase shifting, and an image was acquired for each phase shift, resulting in a total of four images to characterize the surface conditions before and after each drilling increment. These four images facilitated the computation of a phase angle for every pixel. This phase angle information was subsequently translated into surface displacement. **Figure 5.1** (b) shows the ESPI-hole drilling setup.

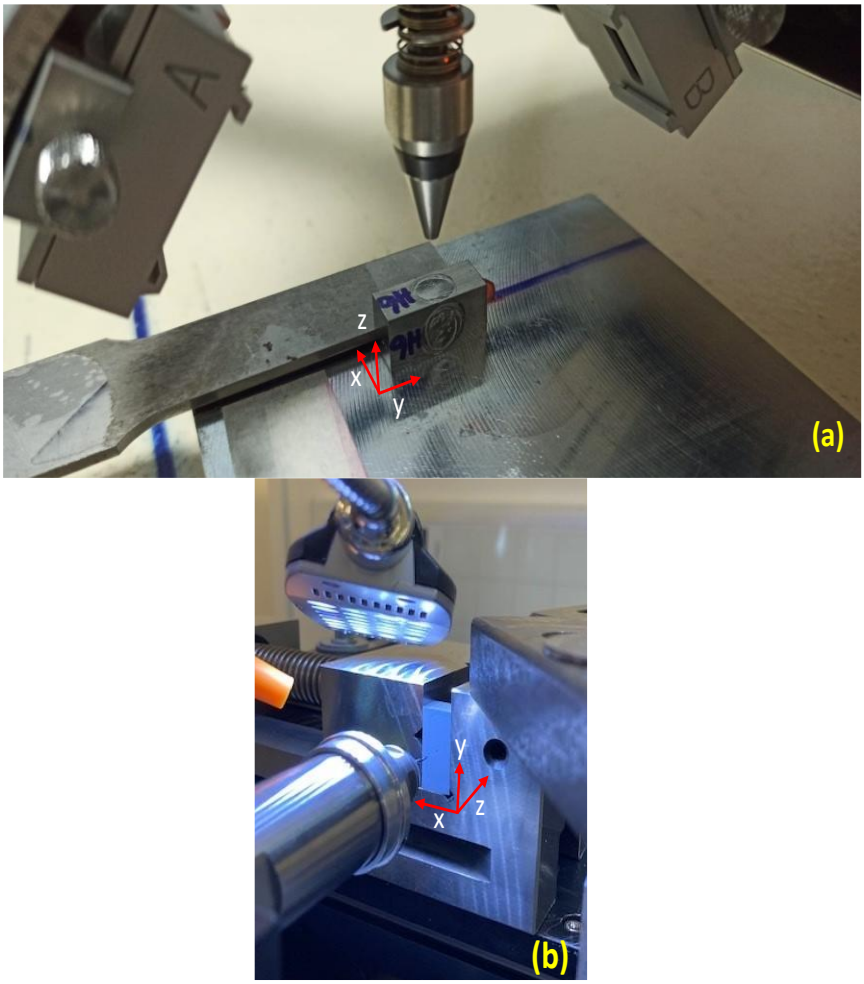


Figure 5.1 (a) XRD measurement setup and (b) ESPI-hole drilling measurement setup, with the three axes of the sample (x, y, z), where the z-axis represents the build direction.

5.3 Results and Discussion

5.3.1 RS analysis based on the XRD and ESPI-HD results

The XRD and ESPI-HD RS analyses were conducted on the XY plane of the samples (along the z-axis or build direction). In the XRD method, the residual strain (lattice spacing) in the samples was calculated as described earlier through the peak intensities, full width at half-maximum (FWHM) and shifts in the peaks observed. To convert the measured strains into stresses, **Eq. 5.2** was applied using material properties determined from previously conducted in-house experiments, where a Poisson's ratio of 0.3 and a Young's modulus of 28 GPa were measured. These values were further validated through published literature [286,287] to ensure consistency and accuracy. The first stress-measurement trials indicated the presence of a mild-medium texture on the basis of the intensities recorded for 5 positive and 5 negative χ-tilts, which is expected for PBF-LB parts. This resulted in a high relative uncertainty in the results.

To improve the results, the number of tilts was increased to 9 positive tilts and 9 negative tilts with a tilt (χ) oscillation of 2°. Moreover, for further improvement, the measurements were carried out on 3 different orientations (φ = 0°, 45°, 90°) with a rotation oscillation of ± 5°. The peak shifts were determined via the cross-correlation method after background removal and absorption correction. The individual stresses for each orientation were determined by fitting an ellipsoid model function to d-sin^{2}ψ plots. After this treatment, the relative measurement uncertainties were within 25%, which is considered acceptable for mild-medium textured samples. The XRD patterns of the samples are illustrated in **Figure 5.2**.

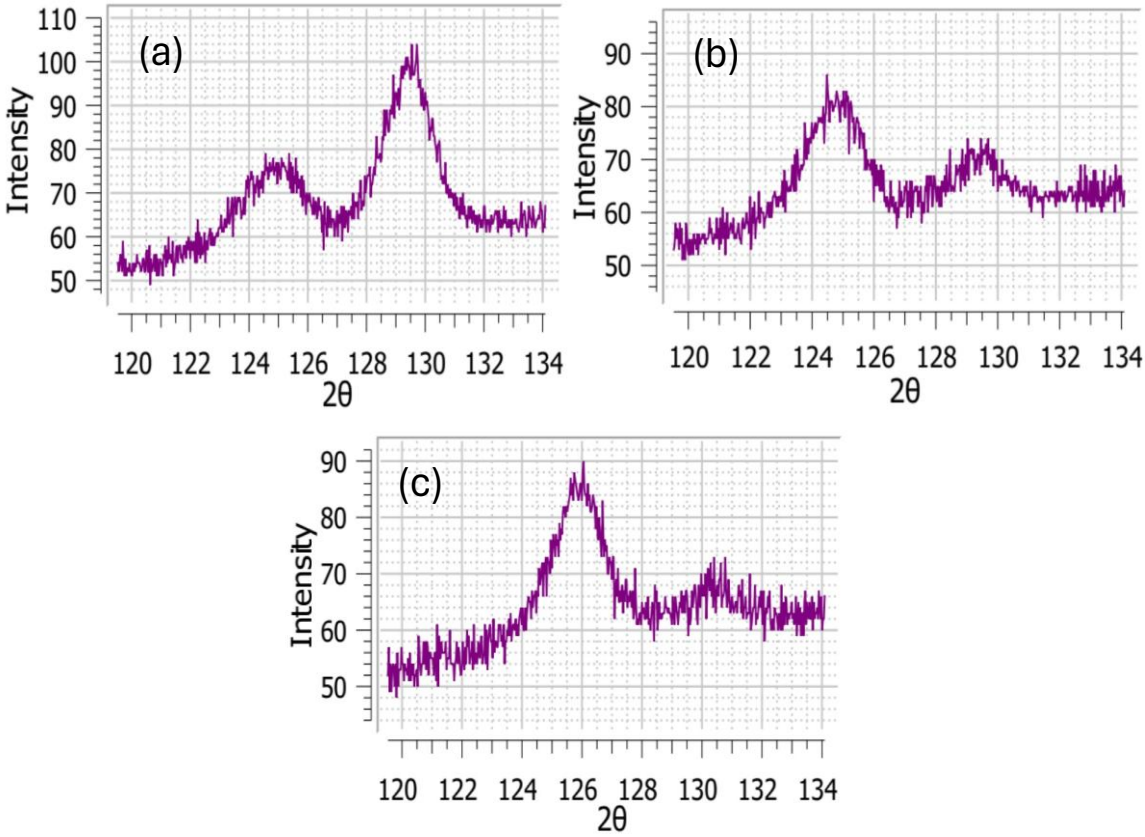


Figure 5.2 XRD patterns observed for samples (a) S1, (b) S2 and (c) S3.

The stress components are detailed in Table 1, where σ_xx and σ_yy represent normal stresses, τ_xy denotes shear stress, and σ_Max and σ_Min are principal stresses. To derive an average generalized stress value from the RS measurements, the von-Mises stress was calculated using the normal and shear stress components, as expressed in **Eq. 5.3**. The analysis revealed that the stresses exist in both the tensile and compressive regimes. Specifically, compressive stresses are predominant near the surface, whereas tensile stresses become more prevalent deeper within the material. Compressive stresses can be beneficial, as they increase the resistance of a material to crack initiation and improve its fatigue life. In contrast, tensile stresses may increase the susceptibility to crack propagation [288,289].

$$\sigma_{\text{von Mises}} = \sqrt{(\sigma_xx)^2 + (\sigma_yy)^2 - (\sigma_xx \times \sigma_yy) + 3(\tau_xy)^2} \quad \textbf{(Eq. 5.3)}$$

Table 5.2 Stress components in the XY plane for samples S1, S2, and S3.

Sample	Depth [µm]	Method	σ_xx [MPa]	σ_yy [MPa]	τ_xy [MPa]	σ_Max [MPa]	σ_Min [MPa]	Von-Mises [MPa]
S1 [Low VED]	<100	XRD	-11	-4	7	0.3	-15	15
	100	ESPI-HD	19	22	0.5	22	19	21
	150	ESPI-HD	4	8	-0.9	8	3	7
	200	ESPI-HD	11	8	-1	12	7	10
	250	ESPI-HD	15	4	10	21	-1	22
Average			7	7	3	12	2	13
S2 [Mid VED]	<100	XRD	0.4	-11	4	2	-13	14
	100	ESPI-HD	54	61	-5	64	51	58
	150	ESPI-HD	59	58	1	60	57	59
	200	ESPI-HD	36	8	2	36	8	33
	250	ESPI-HD	15	-4	-7	18	-6	22
Average			33	22	-1	36	19	37
S3 [High VED]	<100	XRD	0.7	7	-6	10	-2	12
	100	ESPI-HD	-9	-0.6	-3	0.6	-10	10
	150	ESPI-HD	35	25	-11	43	17	37
	200	ESPI-HD	35	35	-2	37	33	35
	250	ESPI-HD	33	20	-0.2	32	20	28
Average			19	17	-4	25	11	24

5.3.2 Effect of increasing VED by reduced scanning speed and hatch spacing on RS

Figure 5.3 (a) illustrates the relationship between the stress components and VED along with error bars calculated based on standard deviation of the stress values in **Table 5.2**. Our work focused on increasing the VED by decreasing the scanning speed and hatch spacing, while keeping the laser power constant. The data show that the RS behaviour varies significantly with depth and VED. When examining the stress trends at different depths, distinct variations emerge. For instance, at depths less than 100 µm, the von-Mises stress consistently decreases

with increasing VED. At deeper regions, specifically at 200 μm and 250 μm, a consistent increasing trend in von-Mises stress is observed with rising VED. This depth-dependent variation in RS highlights the need for a more nuanced interpretation of VED's effects across different regions of the sample. Upon analysing the averaged values of the stress components and von-Mises stress, it can be observed that, as VED increases, RS initially rises and then decreases. This trend suggests that at lower to intermediate VED levels, energy absorption within the material intensifies, likely causing localized heating that leads to uneven expansion and contraction, which in turn generates RS. Additionally, at these lower VED levels, rapid cooling rates can promote the formation of martensitic phases, further contributing to increased RS [290]. As VED continues to increase, the melt pool reaches higher temperatures and expands, resulting in a larger melt pool volume and reduced cooling rates. This mitigates the steep thermal gradients associated with high cooling and solidification rates, which are known to drive detrimental tensile RS. The elevated melt pool temperatures and slower cooling rates promote stress relaxation, as the material has more time to accommodate thermal strains during solidification. Consequently, the reduction in the RS at a higher VED is observed as the cooling rate decreases. Since scanning speed affects solidification rates, it is likely that both factors—higher thermal energy input and slower solidification—contribute to the stress relaxation observed at high VED. Materials exposed to high energy densities can adapt more effectively to thermal changes, leading to lower RS [291]. Furthermore, phase transformations, such as those from martensite to austenite at elevated temperatures, induce volume changes that aid in redistributing internal stresses, contributing to an overall reduction in RS levels [292,293]. Mugwagwa et al. [294] also reported that intermediate VED resulted in higher RS than both low and high VED in PBF-LB, similar to the findings of this study. These authors attributed the higher porosity in the low- and high-VED samples as the cause for lower RS. The porosity related to VED in PBF-LB can arise from two main causes. Excessively high VED can result in overheating, leading to keyhole porosity, whereas insufficient VED can cause underheating, leading to a lack of fusion porosity. However, in addition to VED, variations in scanning speed impact solidification dynamics, further influencing both RS and defect formation. Therefore, while VED remains a key parameter in RS development, differences in solidification rates resulting from varying scanning speeds must also be considered when interpreting the observed trends in the sample stress profile.

Figure 5.3 (b) shows the impact of increasing the VED on the FWHM of the diffraction peaks, as measured via XRD. A sharp increase in the FWHM is observed when the VED increases from low to intermediate levels, followed by a less significant increase from intermediate to

high levels. As indicated by the Scherrer equation, the FWHM is directly related to strain within the material and inversely related to crystallite size: larger FWHM values generally signify smaller crystallites, whereas smaller FWHM values are associated with larger grains and better crystalline quality [295]. With increasing VED, the elevated energy input promotes atomic mobility during solidification, lowers the cooling rate, and consequently leads to grain growth. According to the Hall-Petch relationship, a reduced grain size increases the material strength. However, the greater grain boundary area in smaller grains limits dislocation movement, which in turn increases internal stress levels [296,297]. In our study, the grain size reduction is more pronounced from low to intermediate VED and less so from intermediate to high VED, as evidenced by the changes in the FWHM. This trend aligns with the observed RS, where the intermediate VED results in the highest RS, which is likely due to the rapid decrease in the grain size at this level. In contrast, the reduction in RS at high VED may result from a less steep overall grain size reduction, potentially due to the formation of larger grains. Lin et al. [298] previously reported this unique grain size behaviour in NiTi processed via PBF-LB, noting that the grain size can vary nonlinearly with VED, increasing with increasing VED in some cases and decreasing in others. Additionally, elevated VED levels during PBF-LB of NiTi have been shown to increase melt pool temperatures, which can lead to Ni evaporation and the formation of fine martensitic grains and precipitates such as Ti_2Ni and Ni_4Ti_3 [299,300].

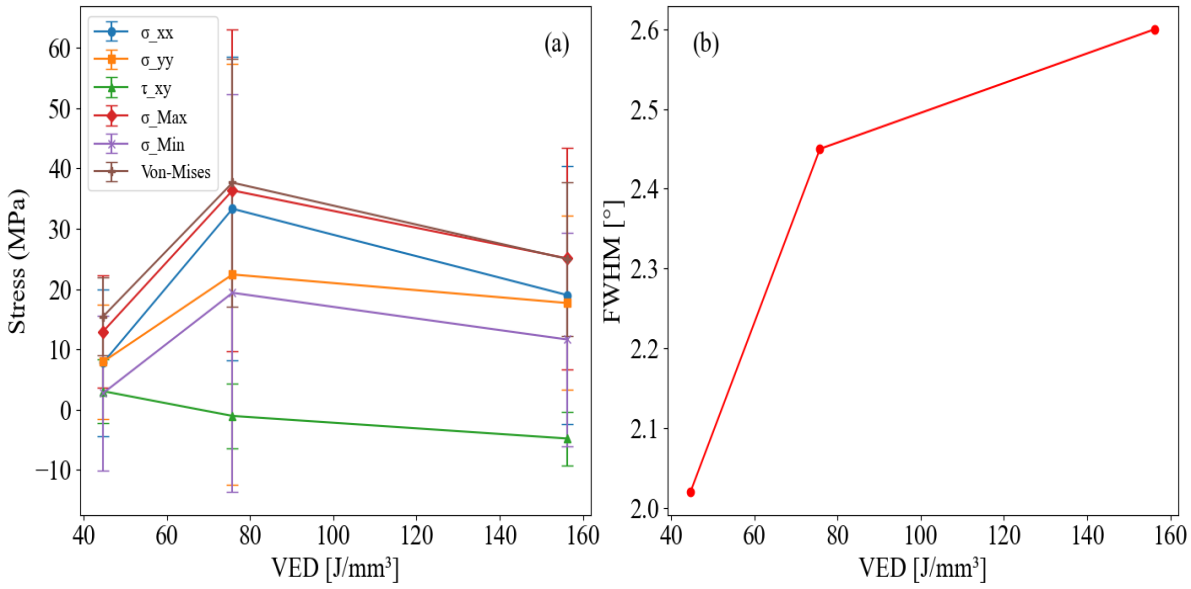


Figure 5.3 (a) Stress response to increasing VED, illustrating trends in normal stresses, shear stress, principal stresses and von-Mises stress, and (b) effect of increasing VED on the FWHM from XRD measurements.

5.3.3 Thermal data analysis for the correlation between the RS, VED and thermal gradient

The IR thermal data collected during the PBF-LB printing process were analysed across the XY plane for each sample, aligning with the RS measurements. The thermal profiles, which represent layer temperatures as a function of build height (z-axis), are presented in **Figure 5.4** (a). The recorded temperature can be seen to decrease with build height. This trend can be attributed to multiple factors. As more layers are deposited, the additional input energy results in a temperature rise locally. This heat conducts toward the substrate to raise the temperature toward the base of the sample. The substrate raises to a certain temperature threshold level before stabilizing. The upper layers experience more heat dissipation to their surrounding environment due to the convective gas flow [277,301]. These factors contribute to the observed temperature gradient with increasing build height. Another trend observed is the progressive temperature increase from samples S1 to S3 with increasing VED, indicating that higher VED levels lead to higher melt pool temperatures. The thermal gradient (TG) for each sample was calculated using **Eq. 5.4**, which assesses changes in the normalized temperature with respect to the build height:

$$\nabla T(z) = \left| \frac{\partial T_{norm}}{\partial z} \right| \qquad \textbf{(Eq. 5.4)}$$

The effect of VED (reduced scanning speed and hatch spacing) on the TG is illustrated in **Figure 5.4** (b), which shows a decrease in the TG with increasing VED. As VED increases, the larger melt pool volume and lower cooling rates promote a more uniform thermal distribution, leading to lower thermal gradients. **Figure 5.4** (c) shows the relationships between TG and the various stress components previously discussed along with error bars calculated based on standard deviation of the stress values in **Table 5.2**. Similar to the VED-RS trend, the average RS is highest at intermediate TG level. Owing to the inverse relationship between VED and TG, these trends mirror one another: a low TG corresponds to high VED, and vice versa. Initially, increasing TG increases RS due to disparities in thermal expansion and contraction. However, with further increases in TG, phase transformations (such as martensite-to-austenite) and increased plastic deformation contribute to reducing RS [302].

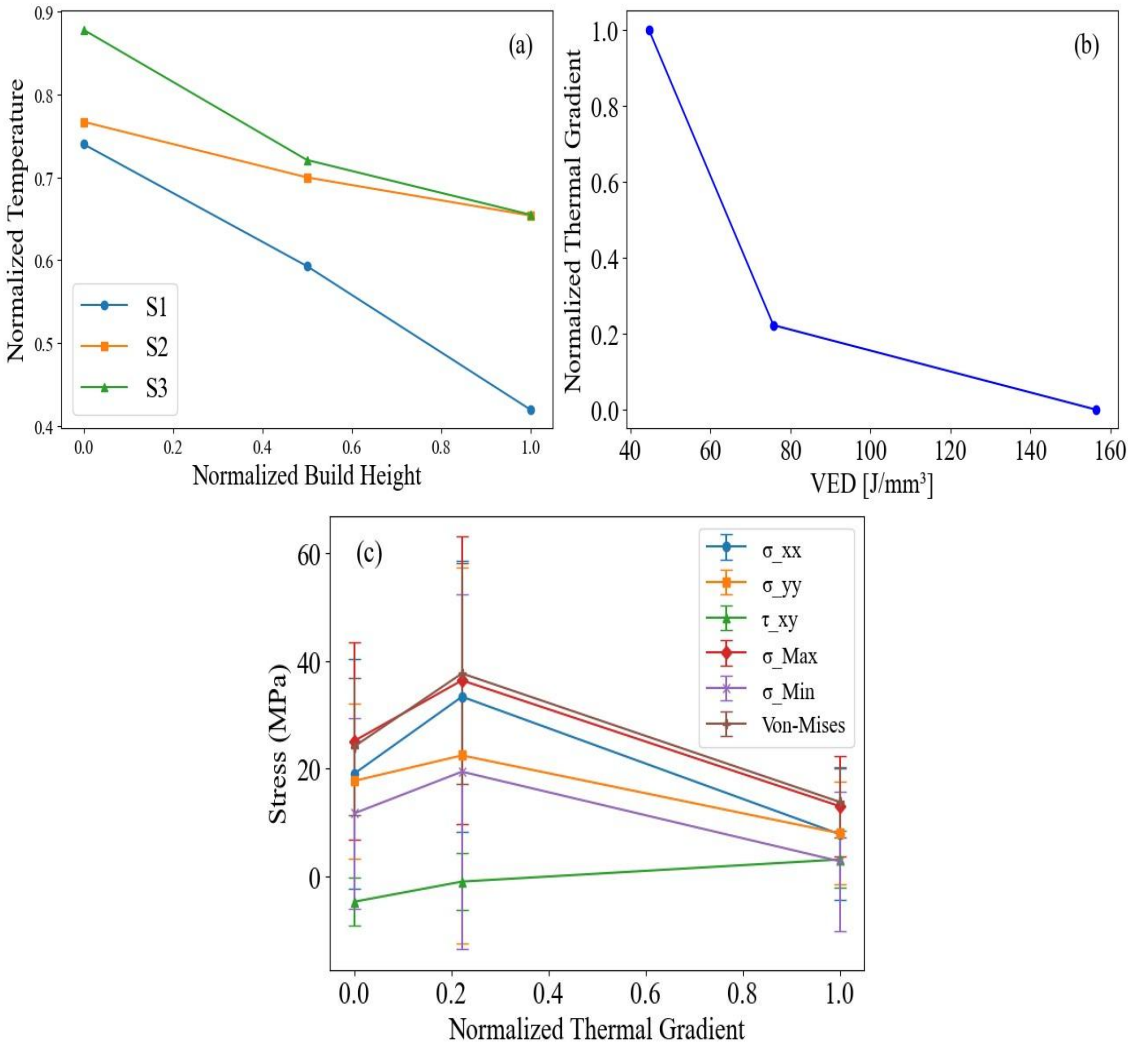


Figure 5.4 (a) Thermal profiles showing temperature variations with build height for samples S1, S2, and S3, (b) correlation between VED and the thermal gradient, and (c) correlation between the thermal gradient and residual stress components.

Xue et al. [122] investigated the effect of increasing VED in PBF-LB by reducing hatch spacing, similar to this study, and observed a reduction in RS, delamination, and cracking. Lin et al. [298] also reported that a higher VED, achieved by reducing the hatch distance, improved the thermal gradient, reduced the cooling rate, and lowered the RS, resulting in a favourable <001> texture in the PBF-LB of NiTi. However, as indicated by Monu et al. [115] , the relationship between VED and RS is not always straightforward. Their study showed that an increase in VED resulted in higher thermal gradients and increased RS in PBF-LB NiTi, underscoring the complex nature of RS evolution in this material. This discrepancy suggests that, while adjusting VED does influence RS, its effects are material- and process-dependent. Liu et al. [303] observed a consistent increase in RS in the PBF-LB of NiTi when they increased both laser power and scanning speed while keeping hatch spacing and VED constant. This

finding suggests that laser power plays a critical role in driving RS, highlighting the need for a more nuanced approach in optimizing process parameters. Furthermore, Li et al. [304] reported a trend similar to ours in their study on RS-induced cracking, where RS first increased with VED and then decreased with further increases in VED.

More broadly, the effect of VED on RS is highly material-dependent [305]. Additional studies examined this relationship in different materials, specifically steels, and presented trends between RS and VED for these materials [306,307]. Simson et al. [306] found that RS, that was measured on the top surface of austenitic 316L stainless steel samples, increased considerably between low to mid VED values and remained relatively constant at higher VED values. Narvan et al. [307] also examined the relationship between RS and VED on the top surface of H13 tool steel samples. This study found that compressive stresses existed on these surfaces and were observed to increase significantly from low to mid VED values and were then seen to decrease slightly moving to higher VED values. These contrasting results across different materials reinforce the need for continued research into how PBF-LB process parameters influence RS, including for NiTi specifically.

Our study's results, particularly the observed depth-dependent variation in RS, emphasize the need for further investigation into the interaction between scanning speed, hatch spacing, and laser power in determining RS. Moreover, the stochastic nature of the PBF-LB process and practical constraints on sample characterization limit the number of specimens we can measure. The time-intensive nature of stress measurement techniques, such as XRD and ESPI-HD, restricts the dataset size. Although the results in this study provide valuable insights into the role of VED in RS development, there is much more process window space that could be investigated to provide a more detailed understanding of the relationship between the parameters and RS. Further studies could also focus on varying laser power while keeping scanning speed constant. This would allow for more of an understanding of how power influences thermal gradients and RS, independent of other parameters. Additionally, VED can be calculated based on laser spot size instead of hatch spacing, providing a different perspective on how energy is distributed across the material during processing. Expanding experimental datasets and leveraging in situ monitoring techniques in these ways could help provide a more comprehensive understanding of the complex thermal-mechanical interactions governing residual stress evolution in PBF-LB components.

5.4 Conclusion

This study provides a comprehensive evaluation of residual stress in PBF-LB produced NiTi via the combined use of ESPI hole-drilling and XRD techniques. The results demonstrate that residual stress distributions are highly heterogeneous and vary significantly with build height and processing conditions, reflecting the complex thermal history inherent to PBF-LB process. A key finding is the non-linear relationship between VED and residual stress. Rather than exhibiting a monotonic trend, residual stress was observed to increase, plateau, and subsequently decrease with increasing energy input. This behaviour is closely linked to evolving thermal gradients during fabrication, highlighting that higher energy densities can, under certain conditions, reduce thermal gradients and mitigate stress accumulation. The study also confirms that process parameters such as scan speed and hatch spacing play a critical role in governing stress development. These parameters influence not only the magnitude of residual stress but also its spatial distribution, which has direct influence on structural integrity and functional performance.

Overall, the findings underscore the importance of employing multi-modal measurement techniques to accurately characterize residual stress in NiTi components. Future work should focus on integrating in-situ monitoring and predictive modelling to better control residual stress evolution, as well as exploring post-processing strategies to enhance the reliability and performance of NiTi structures manufactured through PBF-LB.

Contribution towards the thesis: The chapter establishes a direct experimental link between melt pool thermal history and residual stress formation. While earlier chapters focused on predicting melt pool behaviour and thermal conditions during PBF-LB processing of NiTi, this chapter extends the investigation to experimentally quantify how these thermal conditions translate into residual stress development. This enables identification of key trends, including the non-monotonic relationship between volumetric energy density and residual stress, which cannot be inferred from melt pool geometry alone.
By quantifying the relationship between process parameters, thermal gradients, and stress evolution, this chapter informs model assumptions, calibration, and boundary conditions. As such, it acts as a bridge between process-level melt pool understanding and predictive modelling of residual stress, strengthening the overall process–structure–property framework developed throughout the thesis.

6. Chapter: Residual Stress Estimation in Laser Powder Bed Fusion of Nitinol Shape Memory Alloy

---

Publication Status: Review Completed

Thomas Gillick, **Sampreet Rangaswamy**, Medad C.C. Monu, Hengfeng Gu, Dermot Brabazon, **Residual Stress Estimation in Laser Powder Bed Fusion of Nitinol Shape Memory Alloy**.

Abstract

Residual stress remains a critical challenge in Laser Beam Powder Bed Fusion (PBF-LB) manufacturing of metallic components, frequently leading to cracking, layer delamination, and distortion. This study presents a predictive framework for estimating residual stress in PBF-LB-fabricated NiTi cantilever beams by correlating beam deflection with processing parameters, thermal history, and phase evolution. Phase constitution was characterized using X-ray diffraction (XRD) along with Vickers microhardness measurements. In-situ infrared melt-pool pyrometry was used to capture process-induced thermal signatures. A CALPHAD-coupled thermo-mechanical finite element model (FEM) was developed to replicate experimental deflection measurements and estimate the corresponding von Mises residual stresses based on those deflections. The modelling strategy implemented an inverse estimation of the effective thermomechanical flow stresses responsible for the observed beam deflections. A trial-and-error process was utilised to determine approximate Young's modulus values that yielded deflection values which replicated those of experimental deflections. XRD phase analysis revealed that residual stress in NiTi is strongly influenced by phase evolution, with high retained austenite fractions and the evidence of Ni_4Ti_3 precipitates observed in samples exhibiting the largest deflections. Hardness measurements revealed an increase in hardness with increasing retained austenite content, reflecting the higher stiffness and indentation resistance of austenitic NiTi. This phase-dependent mechanical response may contribute indirectly to the observed variations in cantilever beam deflection. The proposed modelling approach provides a practical tool for estimating residual stress and distortion in PBF-LB NiTi cantilever beams and highlights the importance of integrated control of processing parameters, thermal history, and phase constitution to improve build quality.

6.1 Introduction

Numerous methods are used to measure and evaluate residual stresses in PBF-LB printed samples, encompassing destructive, semi-destructive, and non-destructive approaches. Non-destructive techniques include X-ray diffraction (XRD), neutron diffraction, synchrotron X-ray diffraction, and ultrasonic methods, while semi-destructive and destructive techniques commonly employed include hole-drilling and the contour method [308,309]. Although neutron and synchrotron diffraction offer highly accurate, full-depth residual stress measurements, their reliance on large-scale facilities, high energy consumption, and costly beam time restricts their routine use. More generally, direct residual stress measurements are often time-consuming and expensive.

As a result of these practical constraints, many studies assess residual stresses indirectly through their mechanical manifestations, most notably part distortion and deflection. Cantilever beam geometries are frequently employed in this context, as post-build deflection provides a measurable indicator of the underlying residual stress state and enables systematic evaluation of the influence of processing parameters and build conditions [310,311].

Compared with more extensively studied PBF-LB metals like 316L SS and Ti6Al4V, residual stress development in PBF-LB-fabricated NiTi has received comparatively limited attention. Consequently, existing NiTi-focused studies primarily employ accessible experimental techniques, including XRD, electronic pattern speckle interferometry (ESPI) hole-drilling and the contour method, supplemented by finite element modelling (FEM) to simulate residual stress evolution during processing [138,139]. More recently, empirical approaches, such as correlating residual stress with hardness measurements and thermal stress computation from *in-situ* melt pool thermal data have also been proposed as practical indirect indicators [115,312]. To better understand residual stress development in NiTi, a predictive framework is proposed which combines physically grounded modelling with experimental measurements and in situ process monitoring, particularly for PBF-LB-fabricated NiTi.

This work therefore presents a finite element thermo-mechanical model developed in Ansys Additive for estimating residual stress evolution during PBF-LB processing of NiTi cantilever beams. The thermal model was calibrated using the melt-pool dimensions measured from melt-pool single-track experiments. The model was coupled with temperature-dependent thermo-physical properties derived using the CALPHAD method implemented in Thermo-Calc, enabling a physically consistent description of thermal and phase-dependent material behaviour. The objective of modelling in this study is to develop a predictive framework for

estimating residual stresses that are present in NiTi cantilever beams, based on experimental cantilever beam deflections. A wide processing window is explored by varying the volumetric energy density (VED) to assess the sensitivity of residual stress formation to processing conditions.

A key novel contribution of this work lies in the combined analysis of residual stress effects through numerical modelling, experimental deflection measurements, and *in-situ* infrared (IR) melt pool thermal data, an integrated approach that has not been extensively reported for residual stress determination of NiTi parts produced from PBF-LB in the literature. In addition, phase analysis using X-ray diffraction (XRD) is performed to examine the influence of phase constitution on residual stress development. Vickers microhardness mapping is employed to complement XRD phase analysis by providing spatially resolved measurements of hardness across the sample surface, enabling assessment of local variations in mechanical response associated with phase distribution. By correlating melt pool thermal signatures with cantilever deflection, processing parameters, and phase composition, this study provides new insight into the coupled roles of thermal history and phase evolution in governing residual stress formation in PBF-LB-fabricated NiTi cantilever beams and demonstrates a pathway toward predictive residual stress assessment in NiTi.

6.2 Materials and Methods

6.2.1 Sample fabrication

NiTi cantilever beam samples were fabricated via PBF-LB and consisted of a fixed base, a deflecting beam, and supporting structures (**Figure 6.1**). Each sample measured 25 × 3 × 5 mm. The fixed portion, which remained attached to the build substrate, measured 3 × 3 × 5 mm. The beam portion, designed to deflect after printing, was 22 mm long, 3 mm wide, and 1 mm thick. It was printed on a set of outward-lofted support structures to avoid horizontal overhangs and ensure reliable fabrication. The feedstock powder contained 50.54 at% Ni and 49.46 at% Ti. All samples were produced using an AconityMINI (Aconity GmbH) PBF-LB system equipped with an IPG Photonics Nd:YAG fibre laser (λ = 1070 nm, maximum power 200 W). The build chamber was purged with 99.999% argon to maintain oxygen levels below 20 ppm. A powder supply factor of two was used, and all samples were printed on a NiTi substrate. To investigate the influence of processing conditions, a Box–Behnken design of experiment was implemented. Three key parameters (laser power, scanning speed, and hatch spacing) were varied at three levels (**Table 6.1**), yielding 17 experimental builds, including

five midpoint repetitions. Sample positions on the build plate were randomised to avoid positional bias. Constant parameters across all samples included a starting scan angle of 22.5°, a 67.5° rotation per layer, a 60 µm laser spot size, and a 60 µm layer thickness.

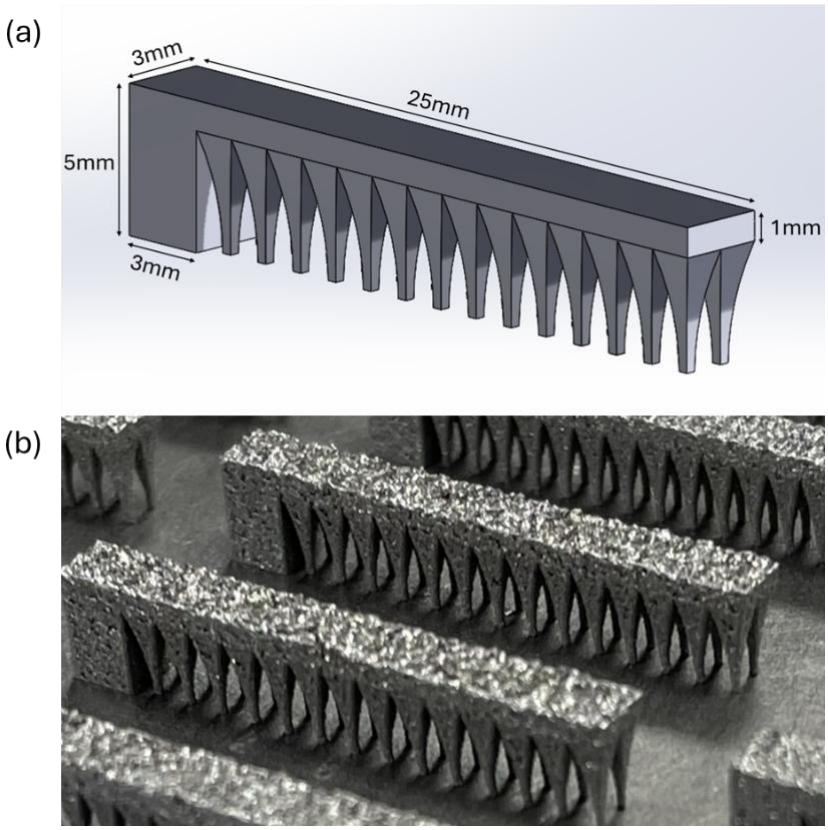


Figure 6.1 (a) Dimensions of the printed cantilever beam sample, (b) as-built samples attached to the build substrate.

Table 6.1 Box-Behnken design of experiment printing parameters.

DOE Samples:	Hatch Spacing (h) (µm)	Laser Power (P) (Watts)	Scanning Speed (V) (mm/s)	VED (J/mm³)
S1	60	120	1000	33.33
S2	120	120	1000	16.67
S3	60	180	1000	50.00
S4	120	180	1000	25.00
S5	60	150	800	52.08
S6	120	150	800	26.04
S7	60	150	1200	34.72
S8	120	150	1200	17.36

S9	90	120	800	27.78
S10	90	180	800	41.67
S11	90	120	1200	18.52
S12	90	180	1200	27.78
S13	90	150	1000	27.78
S14	90	150	1000	27.78
S15	90	150	1000	27.78
S16	90	150	1000	27.78
S17	90	150	1000	27.78

6.2.2 Infrared Melt-Pool Monitoring

In-situ infrared (IR) pyrometry data were collected during printing using a black-body calibrated KLIEBER Infrared (GmbH) pyrometer integrated into the AconityMINI system. The pyrometers captured melt-pool thermal signatures coincident with the laser scan by detecting radiation in the 1500–1700 nm wavelength range at a sampling rate of 100kHz. Data were recorded as thermal intensity with corresponding x and y coordinates for each measurement point, separated by print layer. After fabrication, the thermal data were exported and analysed using an in-house software platform, PyroVista. This software enables efficient processing of large in-situ IR datasets (>60 million data points), segmentation and visualisation of melt pool thermal signatures, extraction of layer-by-layer thermal descriptors, and application of integrated predictive models. These models combine advanced computational and physics-informed approaches to estimate critical material properties, such as density and hardness, at the layer level and across the entire build. To improve data quality, a thermal threshold was applied to remove the effect of laser "skywriting", eliminating signatures generated during laser movement between samples. The dataset was then filtered to include only the layers corresponding to the fabricated sample, enabling comprehensive layer-by-layer and full-height thermal evolution evaluation of the printed part.

6.2.3 Beam Deflection Measurements

Beam deflections were measured using a Keyence VHX-X1 3D digital microscope by recording the height difference between the free edge of the beam and the fixed base. A 3D surface profile was created by stitching together multiple images taken at small incremental

height variations. Support structures were progressively removed from the build substrate using side cutter snips, and beam deflection was recorded after each step. Two rows of supports were removed per measurement, allowing observation of deflection changes during the sequential removal of all fourteen support rows. This procedure yielded eight deflection measurements per sample, providing insight into how residual stresses were released as supports were removed.

6.2.4 X-ray Diffraction (XRD)

After the deflection measurements, samples were detached from the build substrate using a Lam Plan CUTLAM precision micro-cutter with a water-cooled system. Samples were cold-mounted in epoxy resin, then ground and polished using a Struers Tegramin-20 machine with silicon carbide papers from P80 to P1200. Thirteen samples were prepared for XRD analysis, representing the minimum number of samples required to satisfy all processing parameters of the Box-Behnken design of experiment. XRD was performed using a Bruker D8 Advance system with a Cu-Kα source. A locked coupled scan was conducted at room temperature over $2\theta = 35–80°$, with a step size of 0.02° and a scan speed of 1.6 s per step. Data were processed in Match! Analysis Software, with Kα2 radiation removed, background subtracted, and smoothing applied to isolate peaks. Phase identification was carried out using reference data from the Crystallography Open Database: martensitic NiTi (# 96-152-2311), austenitic NiTi (# 96-110-0133), Ni_4Ti_3 (# 96-210-0705, # 96-152-2817), Ni_3Ti_3O (# 96-154-1460), and $NiTi_2$ (# 96-231-0268)**.** Rietveld refinement using FullProf was used to quantify the percentage composition of each metallic phase present.

6.2.5 Vick Hardness Measurements

Vickers microhardness mapping was performed at ambient temperature using a Zwick/Roell DuraScan G5 semi-automatic testing system. Measurements were localized on the XY plane at the fixed base portion of the cantilever beam specimen. The area of the sample that was mapped for hardness was the cross-sectional area of the fixed support base portion of the sample. A measurement offset of 300μm was introduced from each edge to allow a complete area of 2.4mm×2.4mm to be mapped. A high-resolution 13×13 grid, comprising 169 discrete indentations, was implemented across the designated area. An indentation load of 0.2 kgf (HV0.2) was applied with a consistent spacing of 200 μm between indent centres. Spatial coordinates and corresponding hardness values (HV) were recorded for each point.

6.2.6 Modelling Details

A thermo-mechanical finite element model was developed using Ansys Additive Suite 2024R1 for predicting residual stress in PBF-LB of NiTi. NiTi was introduced to the software as a user-defined material. The thermal part of the model was tuned based on the melt pool dimensions of NiTi measured via in-house experiments. The temperature-dependent material properties of NiTi were determined using the CALPHAD approach implemented in Thermo-Calc 2025a with the TCTI6 database. This database is the most up-to-date titanium alloy database for shape memory alloys, as it includes both the B2 austenitic phase and the B19′ martensitic phase. These properties are given in **Table 6.2**.

For the initial calibration of the mechanical part of the model, the yield strength and elastic modulus were varied; 100, 200, and 300 MPa for yield strength, and 30, 40, and 50 GPa for elastic modulus, while all other parameters were kept constant **Table 6.3**. Finer calibration of the yield strength was carried out to accurately reflect the experimental beam deflection measurements. These variations reflect the fact that as-built NiTi exhibits significant property differences depending on the PBF-LB processing conditions, including scan strategy, laser power, and volumetric energy density, as well as local phase composition and microstructural evolution. By exploring a range of mechanical properties, the model is calibrated to capture the sensitivity of residual stress analysis to realistic variations in material behaviour, thereby improving the robustness and predictive capability of the simulations.

Table 6.2 CALPHAD temperature-dependent thermo-physical properties of NiTi.

Temperature (K)	Thermal Conductivity (W/m/K)	Thermal Diffusivity (m^2/s)	Heat Capacity (J/kg/K)	Heat Capacity (kg/m^3)
300	6.2	2.01e-6	479	6471
600	7.3	2.22e-6	514	6390
900	8.2	2.35e-6	552	6305
1200	9.5	2.58e-6	593	6215
1500	11.5	2.88e-6	654	6121

1800	22.4	4.83e-6	830	5595
2100	24.5	5.37e-6	838	5648
2400	26.4	5.91e-6	838	5344
2700	28.1	6.43e-6	838	5223
3000	29.6	6.92e-6	838	5104
3300	30.9	7.40e-6	838	4988

Table 6.3 Modelling parameters.

Attribute	**Value**
Voxel Size	0.25 mm
Voxel Sample Rate	5
Mesh Resolution Factor	5
Stress Model	J2 Plasticity
Thermal Expansion Coefficient	0.000011 K^{-1}
Yield Strength	100 MPa, 200 MPa, 300 MPa
Elastic Modulus	30 GPa, 40 GPa, 50 GPa
Poisson Ratio	0.33
Initial Temperature	298 K
Support Cutoff Method	Directional (-X)
Support Cutoff Steps	7

The governing equations of the thermal model are given in **Eq. 6.1** (Fourier thermal conduction equation), **Eq. 6.2 (**heat loss due to convection**)** and **Eq. 6.3** (Gaussian heat source).

$$\rho c \frac{\partial T}{\partial t} = \frac{\partial}{\partial x}\left(k \frac{\partial T}{\partial x}\right) + \frac{\partial}{\partial y}\left(k \frac{\partial T}{\partial y}\right) + \frac{\partial}{\partial z}\left(k \frac{\partial T}{\partial z}\right) + Q \qquad \textbf{(Eq. 6.1)}$$

where ρ is density, c is specific heat k thermal conductivity T is temperature, t is time, Q is heat source and x, y and z are directions.

$$Q_c = h(T - T_0) \quad \textbf{(Eq. 6.2)}$$

where Q_c is the heat loss due to convection, h is the coefficient of thermal convection, T is transient temperature and T_0 is the initial temperature.

$$Q = 2\frac{AP}{\pi w^2}\exp\frac{-2r^2}{w^2} \quad \textbf{(Eq. 6.3)}$$

where Q is the heat flux input, A is the absorptivity P is the laser power, w is the laser spot size and r is the position of the laser beam.

The mechanical model governing equations are given in **Eq. 6.4**, **Eq. 6.5** and **Eq. 6.6**.

$$\nabla\sigma + \rho b = 0 \quad \textbf{(Eq. 6.4)}$$

where σ is the stress tensor, b is the body force per unit volume.

$$\varepsilon_{total} = \varepsilon_{elastic} + \varepsilon_{plastic} + \varepsilon_{thermal} \quad \textbf{(Eq. 6.5)}$$

where ε is strain.

$$\varepsilon_{thermal} = \alpha\Delta T \quad \textbf{(Eq. 6.6)}$$

where α is the coefficient of thermal expansion.

In the thermal solver, every powder layer is deposited layer by layer similar to the experimental procedure, whereas in the mechanical solver, a lumped layer approach is utilized where one voxel layer contains several powder layers. In this work, a voxel size of 0.25 mm was selected as there would be four rows of elements representing the thickness of the beam sample. A voxel sample rate of 5 was selected so that each voxel would have 5x5x5 (125) samples. The mesh resolution factor determines the fidelity of the solution through mesh scaling for the thermal calculations. In our study, the default value of 5, recommended by Ansys, was used. It is also possible to set the support cutoff method and steps in the model. In this work, a directional (-X) cutoff method and 7 steps are used resembling the experimental methodology.

6.3 Results and Discussion

6.3.1 Thermal Response of NiTi Cantilever Samples during PBF-LB

The influence of PBF-LB processing parameters on melt-pool thermal behaviour was investigated using in-situ infrared (IR) pyrometry to characterise the thermal state of the NiTi cantilever samples during fabrication, when the parts remained fully constrained by the support structures and build substrate. The objective of this analysis is to establish the thermal history

that gives rise to the residual stress states subsequently manifested as cantilever deflection during post-build support removal.

Maximum and average sample temperatures were analysed as a function of volumetric energy density (VED) (**Figure 6.2** a-b), revealing strong positive correlations with R^2 values of 0.93 and 0.81, respectively. Layer-wise two-dimensional thermograms (**Figure 6.2** c) further illustrate this trend, with high-VED samples exhibiting more intense thermal signatures than low-VED samples. Although average melt-pool temperatures do not directly quantify thermal gradients, which are the primary drivers of thermally induced residual stresses, elevated temperatures under comparable constrained boundary conditions indicate increased local thermal input and prolonged thermal exposure during solidification. Such variations in thermal history influence the magnitude and spatial distribution of residual stresses that become locked into the component upon cooling under constraint. These residual stresses are not directly observable during the build, but are subsequently released and redistributed during post-build support removal, resulting in the cantilever deflections. Accordingly, the thermal data presented here should be interpreted as indicative of the stress-generating conditions during fabrication, rather than as a direct measure of deformation behaviour in the unconstrained state.

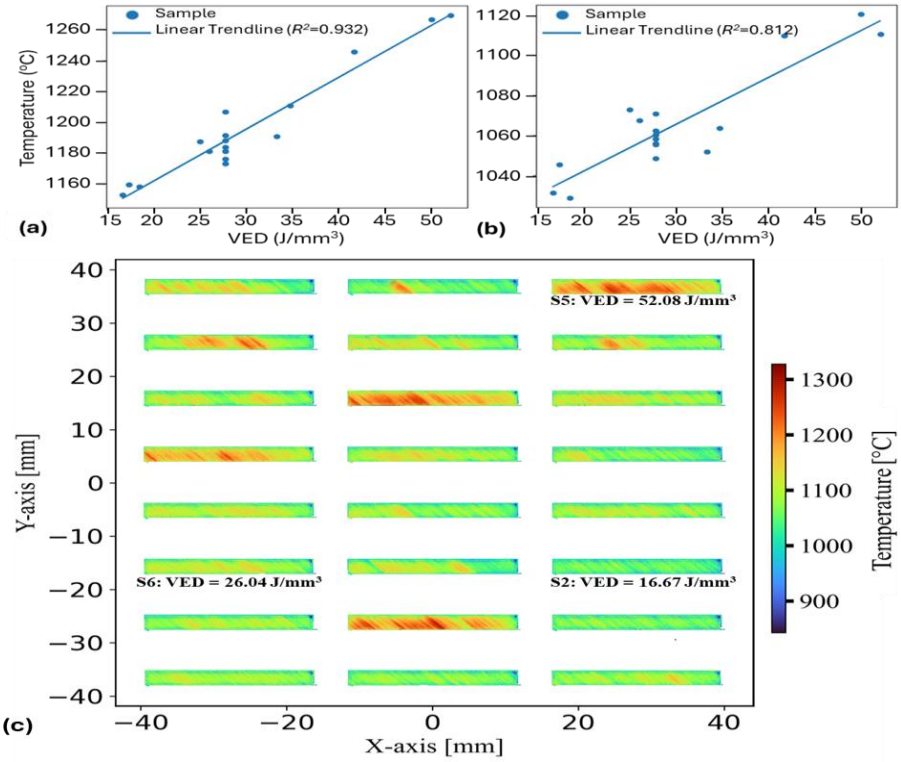


Figure 6.2 The variation of (a) maximum sample temperature and (b) average sample temperature with respect to increasing VED. (c) 2D Thermogram of melt pool thermal signatures of samples during printing of a single layer.

To quantitatively evaluate the influence of individual processing parameters on the constrained thermal response, DesignExpert software was used to perform an analysis of variance (ANOVA) on the average sample temperatures. A highly significant quadratic model was obtained ($p < 0.0001$), revealing strong interactions among laser power, hatch spacing, and scanning speed (**Figure 6.3** a-c). The coded regression equation indicates that laser power is the most influential parameter, followed by hatch spacing and scanning speed. Increasing hatch spacing reduces average sample temperature due to lower local energy input, whereas higher laser power increases temperature as expected (**Figure 6.3** a). Lower scanning speeds also produce higher temperatures owing to longer laser dwell times (**Figure 6.3** c). These results confirm how processing parameters govern the thermal conditions under constraint that ultimately drive residual stress accumulation in PBF-LB NiTi cantilever geometries.

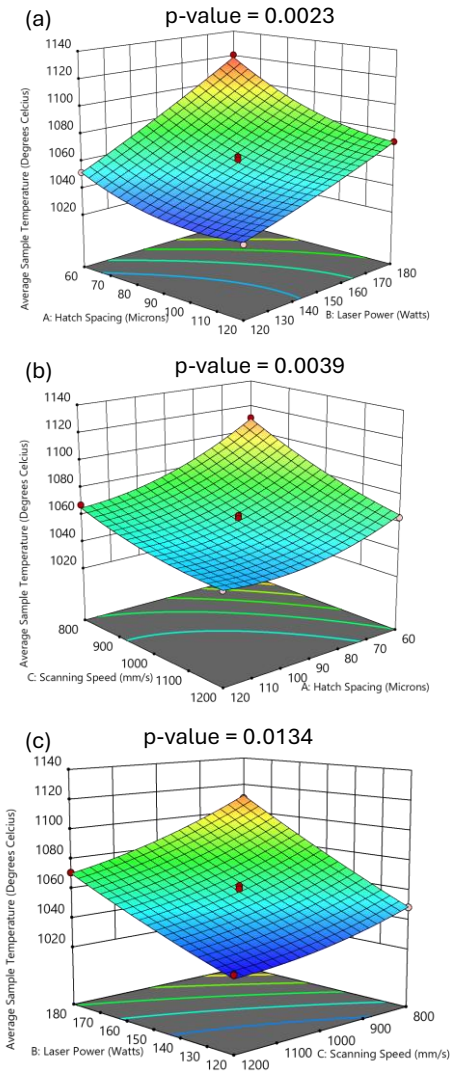


Figure 6.3 Surface response plots for the effect of DOE processing parameters on the average sample temperature.

6.3.2 Experimental Beam Deflection Analysis as an Indicator of Residual Stress

The magnitude of beam deflection, and the stage of support removal at which maximum deflection occurs, provide a qualitative proxy for the relative residual stress state in the printed beams. **Figure 6.4** illustrates the deflection of the beam samples during sequential support removal, together with the procedure used to measure the resulting deformation. **Figure 6.5** presents the maximum beam deflection for each sample and the corresponding number of support rows removed at the point of maximum deflection. A clear trend is observed, where specimens exhibiting larger maximum deflections generally reach their peak deflection earlier in the support-removal sequence. For example, Sample 12 exhibited the largest overall deflection (~0.94 mm) and reached its maximum after the removal of only six (6) rows of supports, indicating a comparatively high level of locked-in residual stress in the as-built condition. Conversely, specimens exhibiting smaller deflections or delayed peak responses reflect lower residual stress levels or a more gradual response to constraint removal.

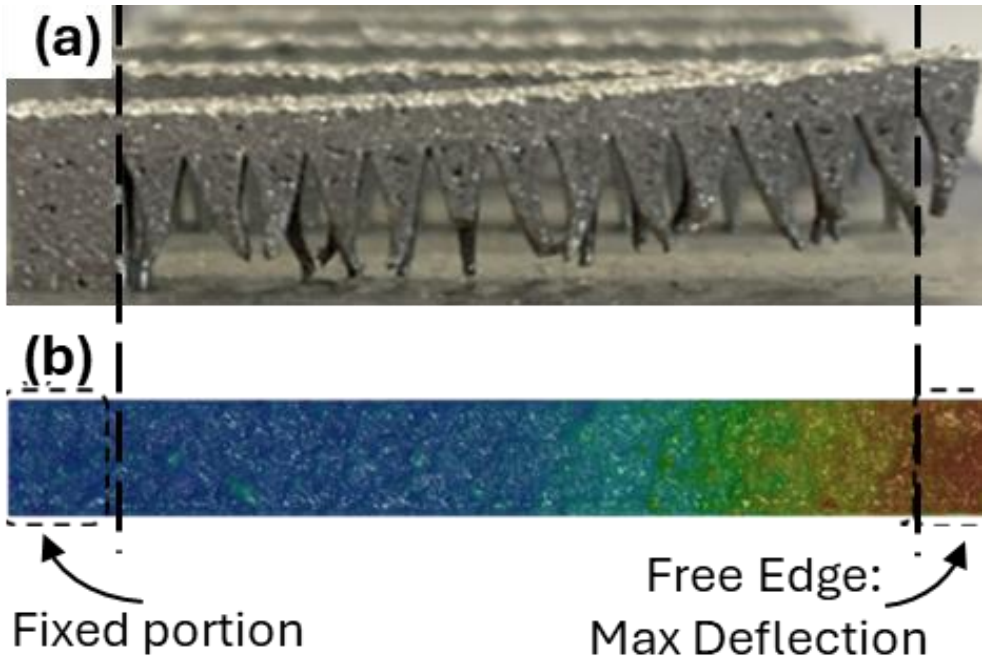


Figure 6.4 (a) As-built NiTi cantilever beam deflection following the separation of support structures from build substrate. (b) deflection profile of the top surface of a sample at the maximum beam deflection point, obtained from Keyence 3D microscope. The deflection was measured by measuring the height difference (build (z)-direction) between the fixed portion and the free edge of the beam. The red colouration indicates areas of high deflection, while the transition to blue indicates lower deflection.

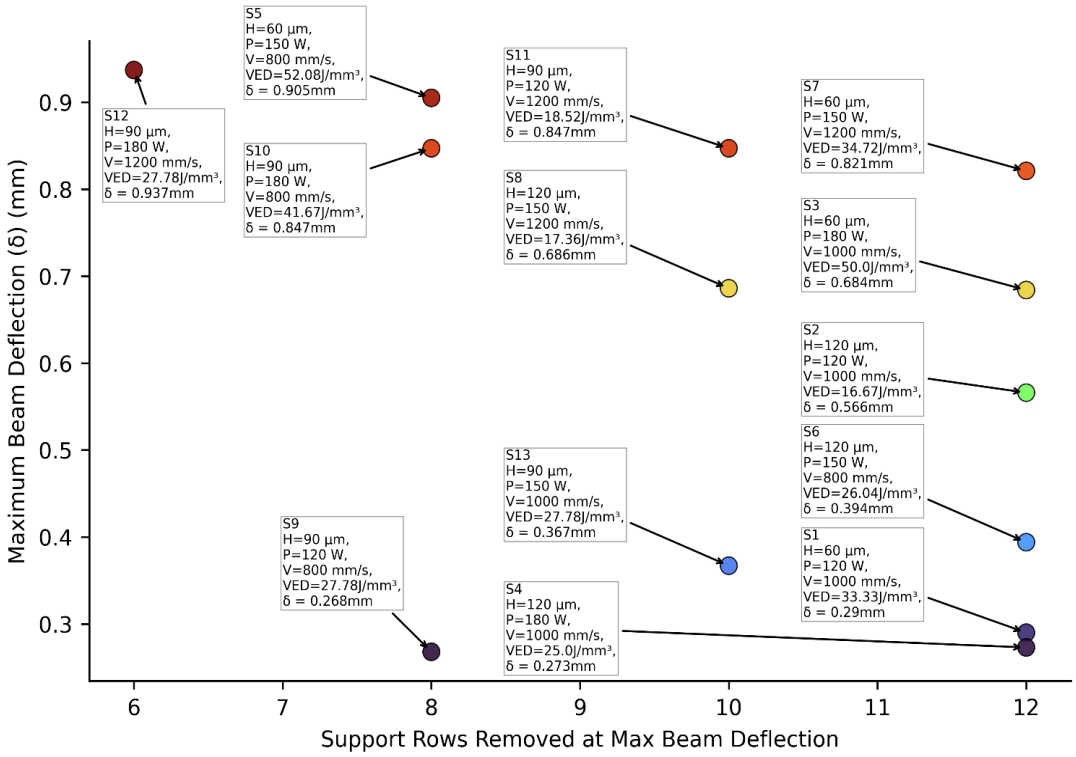


Figure 6.5 Maximum recorded deflection of each NiTi beam sample correlated with the corresponding number of support rows that are removed at the maximum deflection point.

The observed deflection behaviour can be explained mechanistically by the interaction between the through-thickness residual stress gradient within the beam and the progressive reduction in structural stiffness as support rows are removed. In the as-built condition, residual stress gradients, generated by cyclic thermal loading and constrained solidification during PBF-LB, are largely counterbalanced by the stiffness of the support structures and the build substrate. Sequential support removal reduces the effective boundary constraints and flexural stiffness, allowing the locked-in residual stress distribution to manifest as an effective bending moment and associated curvature. For specimens with higher residual stress gradients, this bending moment exceeds the remaining structural resistance at an earlier stage of support removal, leading to rapid curvature development and early peak deflection. In contrast, beams with lower residual stress gradients require a greater reduction in support stiffness before comparable bending moments are activated, resulting in delayed and smaller deflections. Accordingly, the magnitude and evolution of beam deflection during support removal reflect the combined influence of residual stress magnitude, it's through-thickness distribution, and the changing constraint stiffness, providing an indirect indicator of residual stress rather than a direct stress measurement [278,313].

Notably, several samples (Samples 5, 7, 10, and 11) exhibited deflection magnitudes comparable to Sample 12 (~0.82–0.91 mm) but reached these values only after removal of a larger number of support rows (8–12 rows). This behaviour suggests residual stress states of similar integrated magnitude but differing spatial distribution and interaction with structural stiffness. While Sample 12 undergoes rapid bending under relatively high remaining constraint (indicative of a steep through-thickness residual stress gradient), these other samples require further reduction in support stiffness before comparable curvature develops, consistent with lower stress gradients or more symmetric residual stress distributions. In contrast, Samples 4 and 9 exhibited the lowest maximum deflection (~0.27 mm), occurring after the removal of eight and twelve support rows, respectively. This response is indicative of a comparatively low residual stress gradient and reduced stored elastic strain energy in the as-built condition. Even after a substantial reduction in support stiffness, the internal residual stresses in both samples were insufficient to generate a significant bending moment, resulting in minimal curvature development. This behaviour further supports the interpretation that both the magnitude and timing of deflection are governed primarily by the residual stress gradient and its interaction with constraint stiffness, rather than by support removal alone.

6.3.3 Processing Parameter Influence on Beam Deflection

With the use of DesignExpert software, an ANOVA was carried out to quantify the influence of the PBF-LB processing parameters on the maximum deflection of the cantilever beam samples. A significant quadratic model was obtained from this analysis, with a respective p-value of 0.0494. The response curves, which present the respective effect of the PBF-LB processing parameters on the maximum cantilever beam deflection, are presented in **Figure 6.6 (**a-c). Scanning speed was observed to be the most influential parameter, and is evident in **Figure 6.6** (b) and **Figure 6.6** (c). Here, largest deflections can be seen to occur at scan speeds of 1200mm/s, with slightly smaller deflections also occurring at 800 mm/s. The smallest deflections can be seen to occur at intermediate speeds between these two values. The effect of laser power and hatch spacing is particularly evident in **Figure 6.6** (c), where an increase in laser power, and a decrease in hatch spacing can be seen to produce higher deflections in the printed cantilever beam samples.

Figure 6.7 examines the relationship between maximum beam deflection and volumetric energy density (VED). A distinct cluster of samples exhibiting relatively low deflection (<0.4 mm) is observed within a VED range of approximately 25–35 J/mm³ (highlighted by the dotted region in **Figure 6.7**). In contrast, larger deflections (>0.6 mm) are distributed across the full VED range investigated (16.67–52.08 J/mm³), indicating that, for NiTi processed by PBF-LB, the residual stress response is non-monotonic with respect to VED. These large deflections occur at both the highest (1200 mm/s) and lowest (800 mm/s) scanning speeds, as well as the full spectrum of laser power and hatch spacing. Specifically, four of the seven samples exhibiting large deflections were fabricated at a scanning speed of 1200 mm/s (Samples 7, 8, 11, and 12), while Samples 3, 5, and 10 produced at lower scanning speeds, also exhibited comparably high deflections. This dispersion demonstrates that neither VED nor the nominal parameters alone is sufficient to uniquely describe or predict the residual stress state in the NiTi cantilever samples. Instead, the observed behaviour reflects a more complex interaction among process parameters, including thermal gradients, melt pool dynamics, and local constraint conditions, rather than nominal energy input alone.

At lower scanning speeds and fixed laser power, increased VED is generally associated with larger and hotter melt pools, **Figure 6.2** (b), resulting in steeper thermal gradients and greater thermal contraction during solidification. Such conditions are commonly linked to elevated residual stress levels and, in some cases, microcracking if not mitigated through substrate preheating or scan strategy optimisation. However, our previous residual stress study using XRD and ESPI hole-drilling techniques [138] demonstrated that the average residual stress in PBF-LB equiatomic NiTi initially increased with decreasing scan speed (increasing VED), reached a plateau within a critical processing window, and subsequently decreased at higher VED values. This behaviour highlights a non-linear dependence on energy input rather than a simple monotonic relationship with scan speed, as observed in the current study (**Figure 6.7**). Comparable complexity has also been reported by Guo et al. [118], who observed no clear monotonic dependence of residual stress magnitude or anisotropy on scanning speed (400–1200 mm/s) in PBF-LB-processed NiTi. Their high-energy XRD measurements revealed anisotropic residual stresses, compressive along the build direction and tensile within the scan plane, suggesting that microstructural factors such as texture evolution, precipitation behaviour, and dislocation density play a significant role alongside thermal effects.

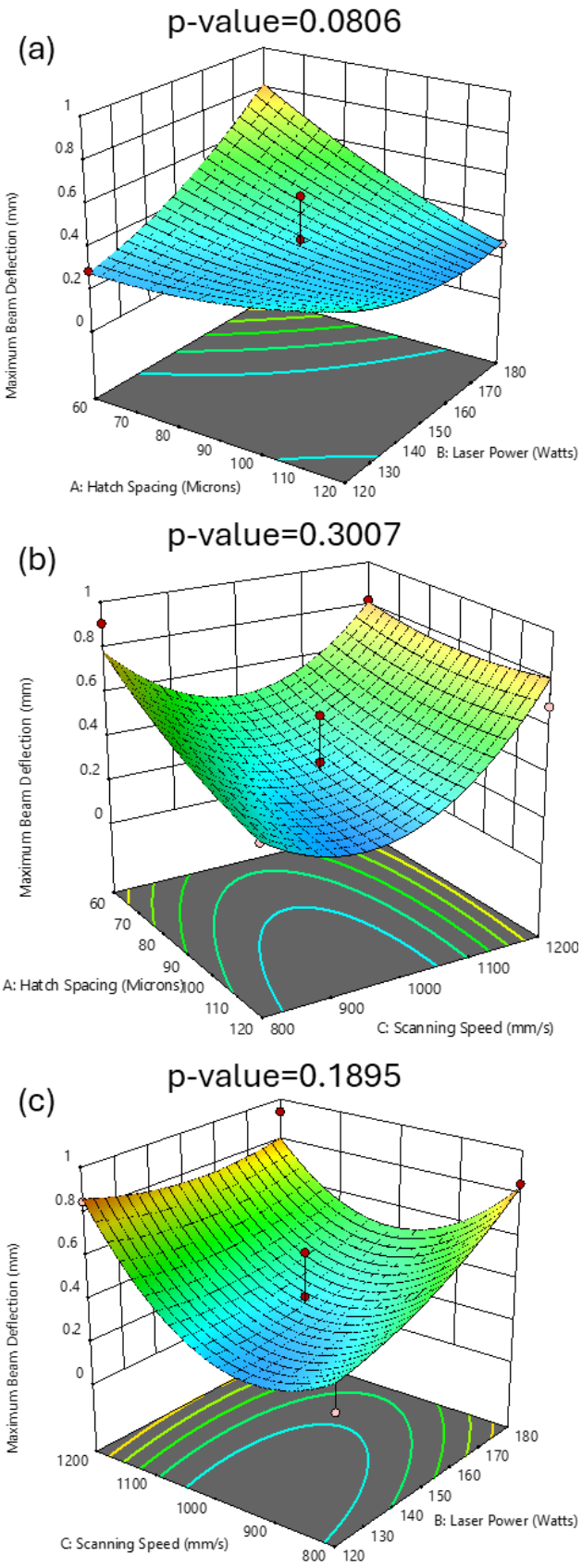


Figure 6.6 Surface response curves for the effect of DOE processing parameters on the maximum beam deflection.

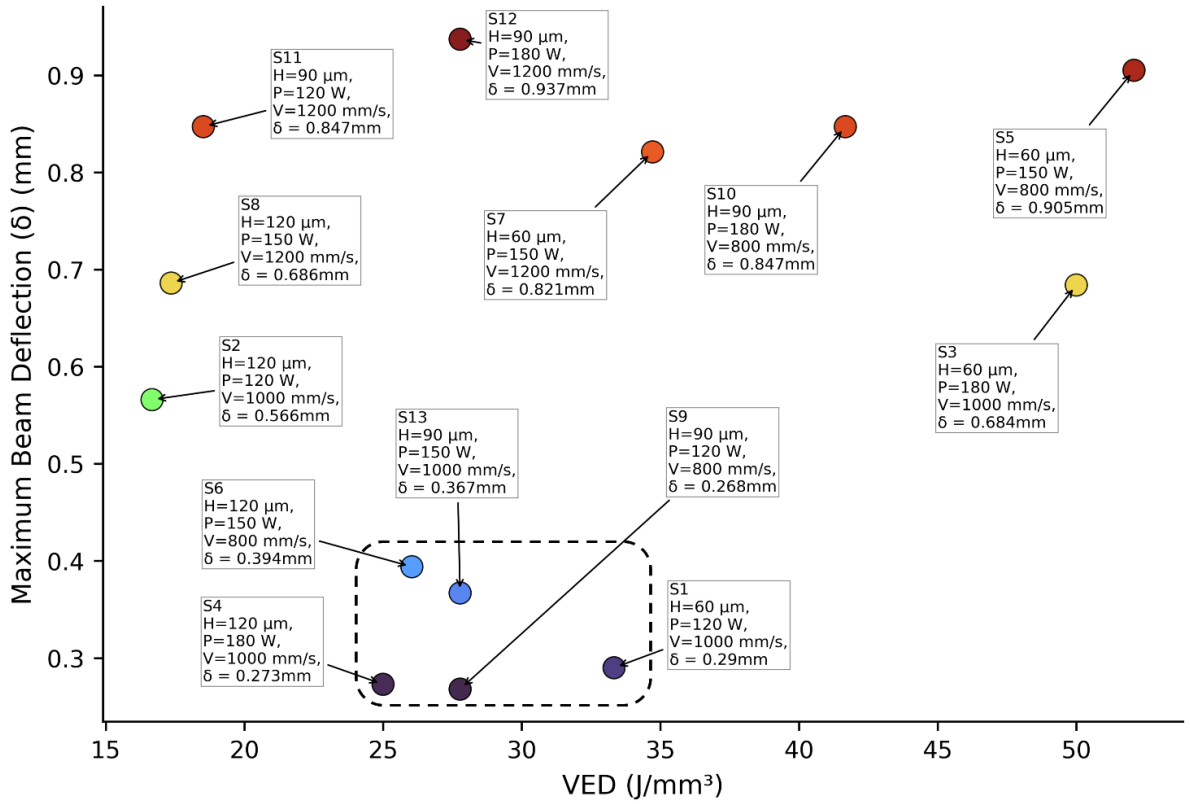


Figure 6.7 Maximum beam deflections with respect to VED. The processing parameters of each sample are shown in order of hatch spacing, laser power, scanning speed, as well as maximum sample deflection (δ).

Contextually, cantilever beam deflection, used here as an indirect indicator of residual stress state, has been reported to exhibit contrasting trends across different alloy systems processed by PBF-LB. Narvan et al. [307], for example, observed a general decrease in cantilever deflection with increasing volumetric energy density in H13 tool steel, which was attributed to reduced thermal gradients and more uniform heat distribution at higher energy inputs. In contrast, Yakout et.al. [310] reported increasing cantilever deflection with increasing VED in Ti-6Al-4V, particularly under conditions of higher laser power, lower scanning speed, and reduced hatch spacing, where steep thermal gradients and strong directional solidification were promoted. The divergence between these reported behaviours and the present NiTi results, where large deflections occur at both low and high VED, highlights the strong material dependence of residual stress evolution in PBF-LB processes. In NiTi, the coexistence of martensitic and austenitic phases, along with stress and temperature-induced phase transformations, introduces additional thermo-mechanical complexity beyond purely thermal

contraction effects, likely contributing to the observed non-linear and parameter-sensitive deflection behaviour.

Building on these observations, the unexpectedly high deflections observed under certain high scan speed conditions motivate further investigation into the underlying metallurgical mechanisms. Accordingly, XRD analysis was performed to examine phase constitution and its potential influence on residual stress accumulation, particularly in samples exhibiting anomalously high deflection behaviour.

6.3.4 Phase Constitution Influence on Beam Deflection

Results from the XRD scans of Samples 1-13 indicated a predominantly martensitic composition in all samples, with smaller quantities of austenitic NiTi, Ni_4Ti_3 precipitates, and oxides comprised of Ni_3Ti_3O also being identified. For example, in **Figure 6.8,** the five unique primary peaks for martensitic NiTi in Samples 2 and 5 are distinguishable from the graphs within the two-theta values of approximately 38 to 46 degrees. Evidence of $NiTi_2$ was found only in Sample 5, as shown in **Figure 6.8** (d). The martensitic NiTi phase concentration in the printed samples ranged from 56.6% - 82.5% as shown in **Figure 6.9** (a). Evidence of smaller concentrations of austenitic NiTi were found, with values ranging from 4.1% - 8.6% (**Figure 6.9** b). Ni_4Ti_3 precipitates were identified in ten samples (**Figure 6.9** c). The total precipitate fraction, which comprises the combination of Ni_4Ti_3, Ni_3Ti_3O, and $NiTi_2$, is summarized in **Figure 6.9** (d).

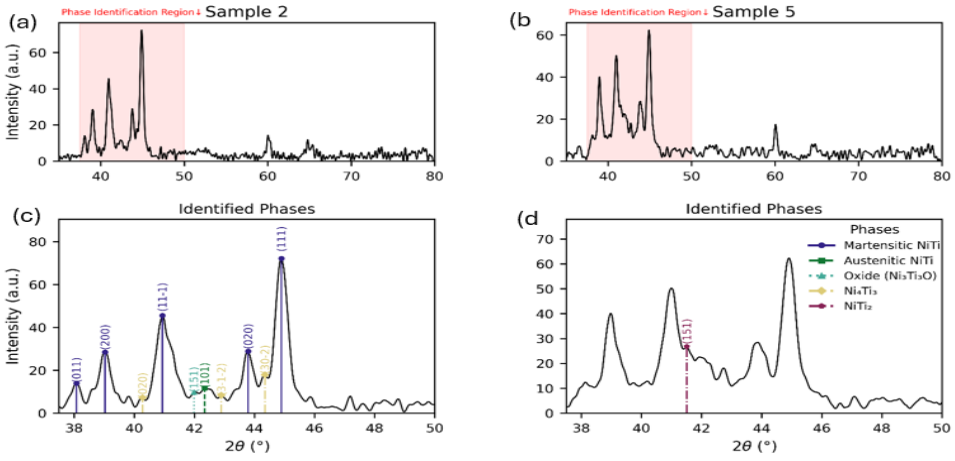


Figure 6.8 XRD pattern for sample 2 and sample 5 (highlighting $NiTi_2$). This includes data for the full two-theta range for (a) sample 2 and (b) sample 5, as well as a zoomed-in region of the region where the key phase peaks were identified in sample 2 (c) and sample 5 (d).

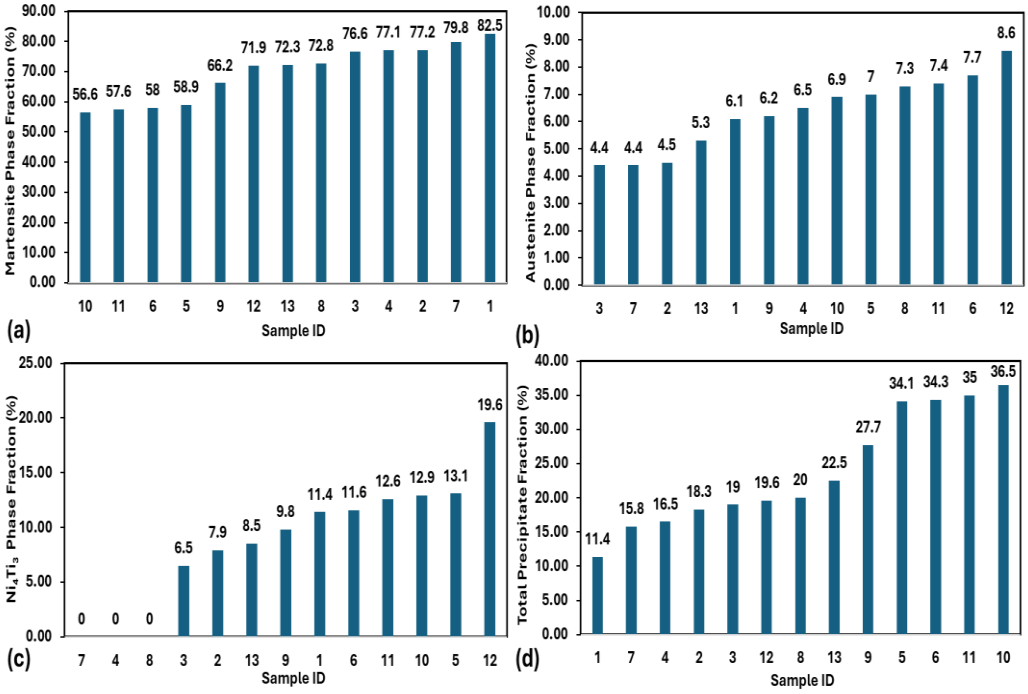


Figure 6.9 Percentage of identified phases in analysed samples. This includes (a) Martensitic NiTi, (b) Austenitic NiTi, (c) Ni_4Ti_3 precipitates, and (d) total precipitate formation, which is the total combined percentage of Ni_4Ti_3, Ni_3Ti_3O, and $NiTi_2$ (data shown in this figure is for Sample 5 only).

During PBF-LB, nickel evaporation can shift an equiatomic NiTi composition toward titanium-rich material, thereby promoting martensitic formation in the as-built state [314]. However, the rapid cooling following laser irradiation can also lead to austenite retention, as austenite may have insufficient time to fully transform into martensite during solidification, resulting in incomplete phase transformation [315]. These constrained thermal histories establish residual stress gradients that are subsequently released during post-build support removal, leading to the cantilever deflections**.**

A comparison between XRD-derived phase fractions, calculated via Rietveld refinement, and measured cantilever deflections indicates that austenite retention contributes to elevated residual stress states in the cantilever beam samples. As noted earlier, and shown in **Figure 6.7**, samples produced using the highest scanning speed (1200 mm/s) exhibited relatively large deflections. Correspondingly, these samples (Samples 8, 7, 11, and 12) showed both large deflections (ranked 6th, 5th, 3rd, and highest, respectively) and elevated austenite fractions (ranging from the third highest to the maximum; **Figure 6.10** a). A plausible explanation is that higher scanning speeds reduce the dwell time at peak melt-pool temperatures, thereby limiting

nickel evaporation and enhancing austenite retention. Because retained austenite is stiffer than martensite and cannot undergo stress-relieving phase transformation during cooling, its presence likely amplifies residual stress accumulation and, consequently, cantilever deflection [118].

Ni_4Ti_3 precipitates, detected in ten samples, may further promote R-phase formation and influence residual stress development. Notably, the four samples exhibiting the highest deflections also contained the highest Ni_4Ti_3 fractions, suggesting a contributory role of these precipitates in the observed deflection behaviour (**Figure 6.10** b). In contrast, $NiTi_2$ was detected only in Sample 5, which corresponded to the highest volumetric energy density (VED) in the design of experiments. Elevated VED increases nickel evaporation, leading to titanium enrichment and facilitating $NiTi_2$ formation, consistent with prior reports on PBF-LB-processed NiTi [315,316].

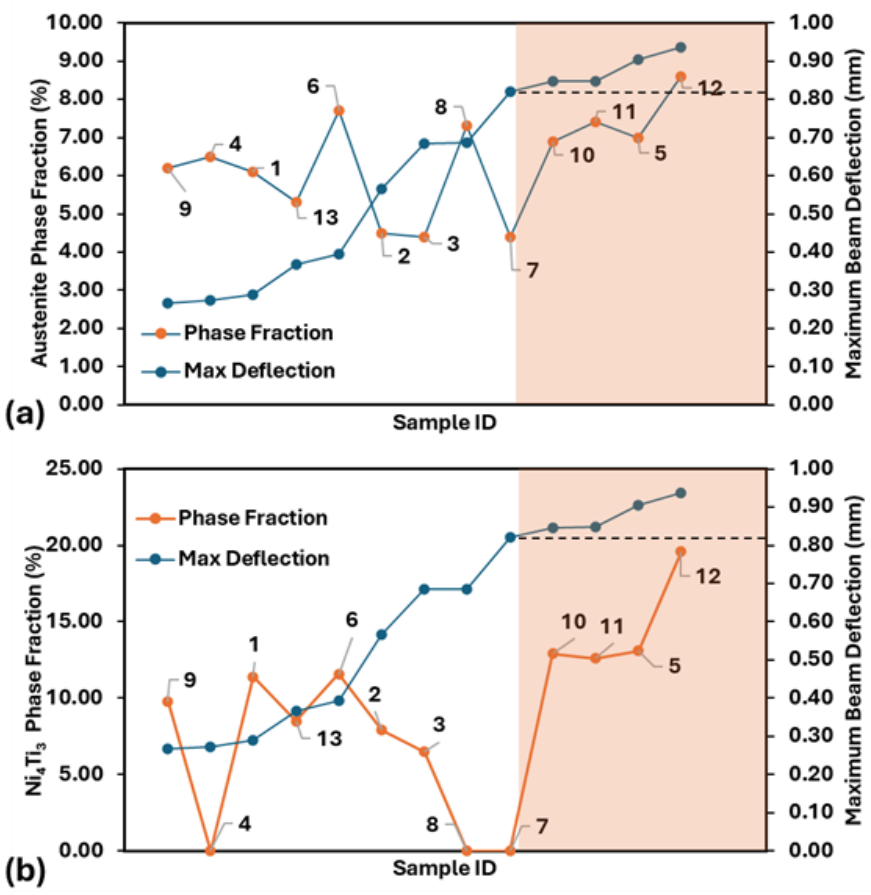


Figure 6.10 Influence of austenitic NiTi phase fraction (a) and Ni_4Ti_3 phase fraction (b) on maximum deflection in NiTi cantilever beams.

One thing to note is that no clear or systematic influence of phase constitution observed for samples exhibiting lower deflections (<0.8 mm) (**Figure 6.10** a-b). In these cases, the residual stress state levels appear insufficient for phase-related effects such as austenite stiffness or precipitate-induced transformation constraints, to dominate the mechanical response, suggesting that thermal stress magnitude and constraint conditions remain the primary governing factors. Overall, these results demonstrate that high residual stress and cantilever deflection are sensitive to both phase composition and precipitate content, but primarily once a critical stress threshold is exceeded. Austenite retention and Ni_4Ti_3 precipitation, both strongly influenced by processing parameters such as scan speed and energy input, contribute significantly to residual stress accumulation and deflection in high-distortion samples, whereas their influence is secondary in low-deflection regimes.

6.3.5 Vickers Hardness Analysis

Vickers hardness measurements were performed on Samples 3, 10, and 12, which were selected to represent low (4.4%), medium (6.9%), and high (8.6%) retained austenite phase fractions, respectively (see **Figure 6.9**). The primary objective of these measurements was to evaluate whether spatial variations in hardness could be used as a proxy for mapping retained austenite distribution across the printed samples.

The distribution of hardness are presented as colour maps in **Figure 6.11** (a-c). Sample 3 (**Figure 6.11** a) exhibits the lowest hardness distribution, with a mean value of 234 HV0.2. In contrast, Samples 10 and 12 (**Figure 6.11** b–c) show progressively higher hardness values, consistent with their increasing retained austenite content. Notably, Sample 10 displays localised regions of elevated hardness, particularly near the boundaries of the measurement, close to the sample edge. A similar spatial trend is observed in Sample 12, where the highest hardness values are concentrated in comparable regions.

To quantify the relationship between hardness and retained austenite content, the mean, median, and maximum hardness values for each sample were correlated with the corresponding phase fractions obtained via X-ray diffraction (XRD), as shown in **Figure 6.11** (d-f). A strong positive correlation is observed for both the mean ($R^2 = 0.892$) and median ($R^2 = 0.931$) hardness values. The strongest correlation is obtained when considering the maximum hardness values ($R^2 = 0.999$), suggesting that peak hardness measurements are particularly sensitive to elevated austenite content.

The observed increase in hardness with retained austenite content is consistent with the well-established mechanical contrast between martensitic and austenitic NiTi. Austenite is characterised by a higher elastic modulus and greater hardness, whereas martensite exhibits lower stiffness and is generally softer due to its twinned structure and deformation mechanisms (e.g., stress-induced detwinning and reorientation) [317,318]. Consequently, regions with higher retained austenite fractions are expected to exhibit elevated hardness values.

The strong correlations identified in **Figure 6.11** (d-f) support the use of hardness mapping as a complementary technique to XRD phase identification discussed earlier. In particular, the near-perfect correlation observed for maximum hardness values suggests that localised measurements are highly sensitive to microstructural heterogeneity, capturing regions where austenite is concentrated. This is especially relevant in PBF-LB NiTi, where steep thermal gradients and complex thermal histories can lead to significant spatial variation in phase distribution. Furthermore, the localisation of higher hardness values near sample edges (**Figure 6.11** b–c) may be indicative of edge-related thermal effects, such as enhanced cooling rates or altered melt pool dynamics, which can influence phase stability and transformation behaviour. Overall, these results demonstrate that high-resolution hardness mapping provides a practical method for assessing phase distribution in as-built PBF-LB NiTi. When used in conjunction with XRD, it offers enhanced spatial insight into mechanical property heterogeneity.

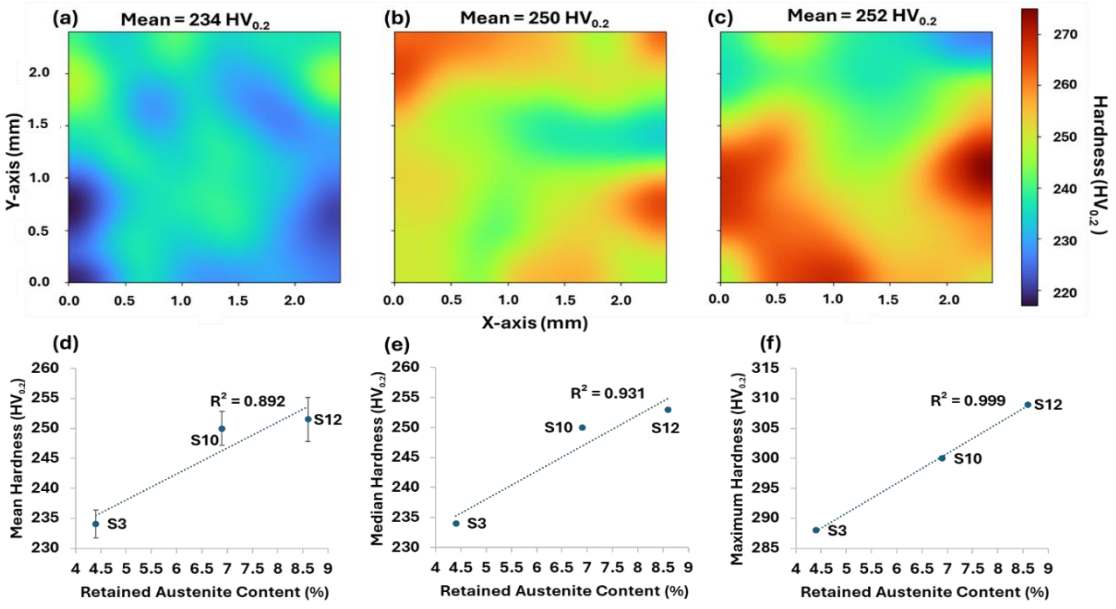


Figure 6.11 Hardness maps of 2.4mm × 2.4mm area of (a) Sample 3, (b) Sample 10, and (c) Sample 12. Relationship of (d) mean, (e) median, and (f) maximum hardness values with respect to increasing retained austenite content recorded from XRD. The error bars in (a) represent 95% confidence intervals.

6.3.6 Thermo-mechanical finite element modelling results

6.3.6.1 Model calibration strategy

The preceding sections established the thermal response inferred from in-situ infrared (IR) measurements, the experimental manifestation of residual stress in PBF-LB NiTi via cantilever beam deflection, and the underlying phase constitution of the printed material. While these analyses provide complementary insight into thermal history, elastic strain, and macroscopic distortion, they do not directly quantify the magnitude of residual stress retained within the printed components. To address this limitation, a calibrated thermomechanical finite element (FE) model was employed to translate experimentally measured cantilever deflections into corresponding estimates of residual stress trends.

The FE model was calibrated by reproducing the experimentally observed deflections arising from process-induced residual stresses. The constitutive description requires specification of both Young's modulus, E, and a stress-limiting parameter governing inelastic relaxation during cooling. Although this parameter is implemented as a yield strength in the Ansys Additive FE framework, the values identified in the present study do not represent a conventional uniaxial yield stress. Instead, they are interpreted as an effective thermomechanical flow stress which is associated with martensite detwinning of NiTi at room temperature. In this framework, the effective thermomechanical flow stress, $\sigma_{\text{flow}}^{\text{eff}}$, is defined as the stress limit at which further thermally induced strain is accommodated by inelastic mechanisms rather than additional elastic stress accumulation, such that the residual stress state satisfies **Eq. 6.8.**

$$\sigma_{\text{vM}}^{\text{res}} \geq \sigma_{\text{flow}}^{\text{eff}} \qquad \textbf{(Eq. 6.8)}$$

where $\sigma_{\text{vM}}^{\text{res}}$ is the retained von Mises residual stress following cooling. This effective flow stress implicitly captures martensitic detwinning, variant reorientation, and transformation-assisted plasticity activated under the cyclic thermal loading imposed by the PBF-LB process. Since neither E nor this effective flow stress can be directly measured under such conditions, a calibration strategy was required to identify physically meaningful values consistent with both the experimental deflection data and the independently measured phase constitution. The sensitivity of model predictions in PBF-LB NiTi to assumed properties has previously been highlighted by Rangaswamy et al. [170], underscoring the importance of appropriate parameter selection. Similar distortion-based identification strategies, in which effective elastoplastic parameters are adjusted to reproduce measured warpage/deflection, have been reported in thermo-mechanical simulations of powder-based additive processes [319].

As discussed earlier, all samples exhibit a predominantly martensitic phase constitution (>56%), which constrains the elastic modulus to a relatively narrow and well-established range for martensitic NiTi, typically 30–50 GPa [320,321]. Based on this constraint, an exploratory analysis was performed in which E was varied between 30, 40, and 50 GPa, while the model-predicted deflection was compared against the experimentally measured average maximum deflection across all samples (δ_{mean}= 0.61 mm), as shown in **Figure 6.12** (a). The results indicate that a Young's modulus of 50 GPa, combined with an effective thermomechanical flow stress of approximately 100 MPa, produces a estimated deflection (~0.67 mm) in closest agreement with the experimental mean.

On this basis, E was fixed at 50 GPa for all subsequent simulations, while $\sigma_{\text{flow}}^{\text{eff}}$ was treated as the primary fitting parameter governing the magnitude of residual stress retained through the cantilever thickness. For each sample, this flow stress was iteratively adjusted until the predicted steady-state deflection matched the experimentally measured value. This approach reflects the mechanics of residual-stress-driven bending, wherein elastic stiffness controls structural compliance, while the final residual stress state, and thus the bending moment, is limited by inelastic stress relaxation during cooling. The calibrated effective thermomechanical flow stresses estimated von Mises residual stresses, and resulting deflection errors are summarised in **Table 6.4**.

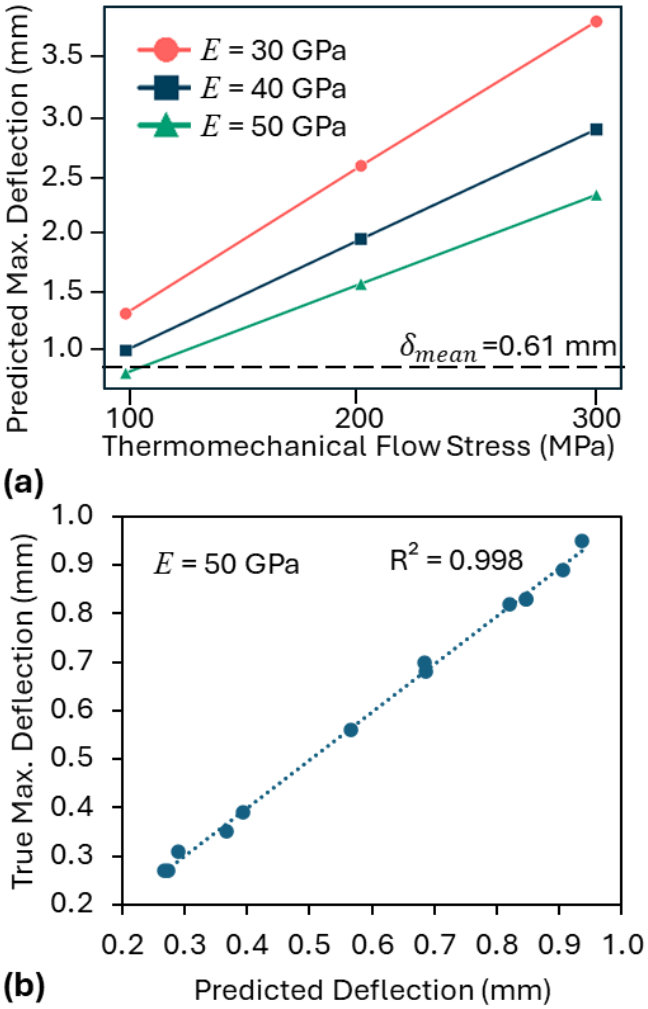


Figure 6.12 Model calibration results: (a) effect of varying Young's modulus between 30 and 50 GPa on predicted deflection and required effective thermomechanical flow stress, $\sigma_{\text{flow}}^{\text{eff}}$, relative to the experimentally measured average maximum deflection, δ_{mean}=0.61 mm; and (b) comparison of true versus predicted deflection for all samples at the calibrated Young's modulus of 50 GPa.

6.3.6.2 Model performance and residual stress interpretation

Figure 6.12 (b) compares experimental and predicted deflections, yielding a coefficient of determination (R^2) of 0.998. Across all thirteen samples, the deflection error remains within ±6%, with the majority of samples (11 out of 13) exhibiting errors below ±2% (**Table 6.4**). This close agreement demonstrates that the adopted modelling framework captures the dominant physics governing cantilever bending, despite the absence of explicit phase-transformation modelling.

Importantly, the calibrated model accurately reproduces both low-deflection samples (<0.4 mm), where limited residual stress is retained, and high-deflection samples (>0.8 mm for Samples 7, 10, 11, 5, and 12), where substantial curvature develops (**Table 6.4**). This behaviour indicates that the observed variation in deflection is not driven by changes in elastic compliance, but rather by differences in the magnitude of residual stress locked into the structure during cooling. **Figure 6.13** (a-b) shows the simulated beam deflection following the incremental support removal process, and the corresponding residual stress distribution within the printed sample. As is seen in **Figure 6.13** (a), a similar deflection profile is observed in the model compared to the experimental deflection depicted in **Figure 6.4**.

Table 6.4 Model calibration results from fixed Young's modulus the and varying flow stress.

Sample ID	Experimental Deflection (mm)	Model Deflection (mm)	Deflection Error (%)	Model von Mises Stress (MPa)	Effective Thermomechanical Flow Stress (MPa)
9	0.268	0.27	0.86	38	35
4	0.273	0.27	-1.18	37	35
1	0.290	0.31	6.47	44	40
13	0.367	0.35	-4.90	49	45
6	0.394	0.39	-1.02	54	50
2	0.566	0.56	-1.11	80	75
3	0.684	0.7	2.26	98	90
8	0.686	0.68	-0.87	95	90
7	0.821	0.82	-0.10	114	105
10	0.847	0.83	-1.99	113	105
11	0.847	0.83	-2.08	113	105
5	0.905	0.89	-1.70	125	115
12	0.937	0.95	1.38	130	120

Note: This **Table 6.4** is sorted by 'Experimental Deflection' from smallest to largest deflection value.

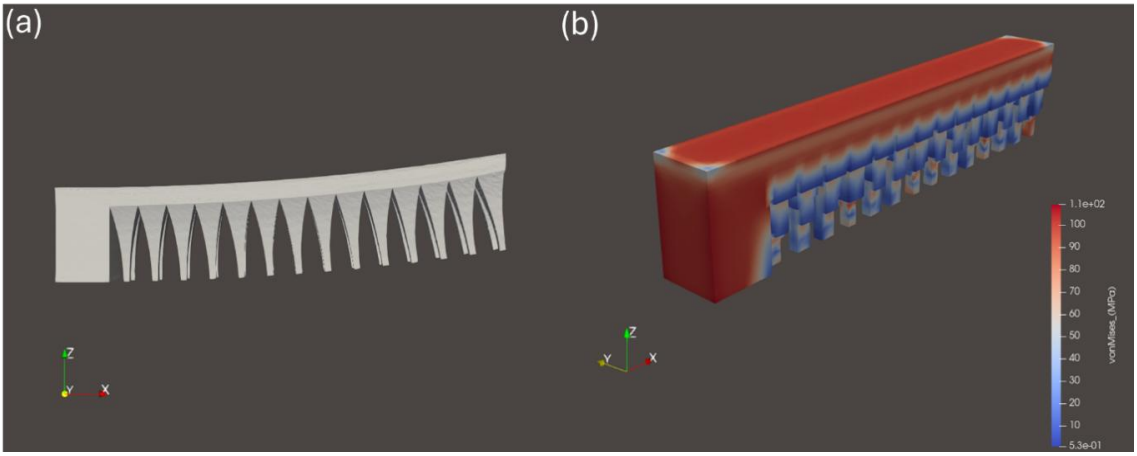


Figure 6.13 (a) Model-deflection following support structure removal and (b) model-predicted stress distribution within beam sample.

6.3.6.3 Identifiability of elastic versus inelastic parameters

Although comparable agreement with experimental deflection can be achieved by fixing the $\sigma_{\text{flow}}^{\text{eff}}$ and varying Young's modulus (**Table 6.5**), this alternative calibration strategy yields non-physical elastic moduli ranging from 40 to 150 GPa, together with nearly constant residual stress magnitudes across all samples (~105–108 MPa). Such behaviour indicates that deflection variation is artificially accommodated through stiffness modulation rather than through physically meaningful inelastic stress relaxation mechanisms.

As a result, Young's modulus cannot be reliably identified from residual-stress-induced beam bending, whereas the $\sigma_{\text{flow}}^{\text{eff}}$ remains a well-posed and physically interpretable parameter. This finding confirms that cantilever deflection in PBF-LB NiTi is governed primarily by residual stress saturation rather than by variations in elastic stiffness.

Table 6.5 Model calibration results from fixed flow stress and varying Young's modulus.

Sample ID	Experimental Deflection (mm)	Model Deflection (mm)	Deflection Error (%)	Model von Mises Stress (MPa)	Effective Thermomechanical Flow Stress (MPa)
9	0.268	0.26	-2.95	108	150
4	0.273	0.27	-1.18	107	145
1	0.290	0.28	-3.55	109	135
13	0.367	0.36	-1.99	108	110
6	0.394	0.39	-1.02	107	100

2	0.566	0.57	0.67	105	65
3	0.684	0.7	2.26	108	55
8	0.686	0.69	0.59	106	55
7	0.821	0.78	-5.24	109	50
10	0.847	0.87	2.70	108	45
11	0.847	0.87	2.61	108	45
5	0.905	0.86	-5.25	108	45
12	0.937	0.99	5.36	108	40

Note: This **Table 6.5** is sorted by 'Experimental Deflection' from smallest to largest deflection value.

6.3.6.4 Residual stress saturation and effective thermomechanical flow stress, σ_{flow}^{eff}

A key outcome of the simulations is the strong correspondence between the model-estimated von Mises residual stress and the imposed effective thermomechanical flow stress, σ_{flow}^{eff}. For all samples, the retained residual stress magnitude closely approaches the specified flow stress limit, typically within 5–10% (**Table 6.4**), demonstrating that residual stress accumulation during cooling is capped by inelastic deformation rather than continued elastic loading. As a result, the final beam curvature is governed by the magnitude of the through-thickness residual stress gradient, which is directly controlled by σ_{flow}^{eff} (**Eq. 6.8**). Samples with higher fitted flow stresses retain larger residual stress gradients and therefore exhibit greater bending moments and cantilever deflections. This behaviour is consistent with classical residual-stress-limited bending mechanics, in which curvature scales with the stress distribution rather than elastic stiffness. A clear monotonic relationship is observed between experimental deflection and the extracted effective thermomechanical flow stress. Low-deflection samples (<0.4 mm) correspond to σ_{flow}^{eff}values of 35–50 MPa, whereas samples exhibiting large deflections (>0.8 mm) require values of 105–120 MPa to reproduce the measured curvature.

As noted earlier, these values should not be interpreted as intrinsic room-temperature uniaxial yield strengths. Instead, they represent effective thermomechanical flow stresses governing residual stress retention under the complex thermal histories of the PBF-LB process of NiTi. In predominantly martensitic NiTi, this flow stress is physically associated with the onset of martensitic variant reorientation (detwinning), stress-assisted transformation mechanisms, and high-temperature inelastic accommodation. Under the multiaxial stress states and repeated thermal cycling inherent to layer-wise fabrication, these mechanisms activate at substantially

lower stress levels than classical dislocation-mediated yielding (often represented as yield strength). In its martensitic state, NiTi is exceptionally "soft" regarding its initial departure from linearity. Literature values for the start of the martensite detwinning plateau typically range from 50 to 150 MPa [322]. The $\sigma_{\text{flow}}^{\text{eff}}$ range of 35–120 MPa sits perfectly at the lower end of this physical phenomenon.

6.3.6.5 Role of phase constitution

The extracted trends are consistent with independent observations that increased retained austenite and higher Ni_4Ti_3 precipitate fractions correlate with larger cantilever deflections (**Figure 6.10** a-b). Austenite-rich material is expected to sustain higher residual stresses due to its reduced capacity for stress accommodation via martensitic reorientation, while Ni_4Ti_3 precipitates introduce internal stress fields that modify twin boundary mobility and transformation-assisted relaxation. As a result, samples with higher retained austenite and precipitate content can support larger residual stress gradients, leading to increased curvature.
Crucially, the success of the model without varying Young's modulus demonstrates that phase constitution influences deflection primarily through its impact on inelastic stress-limiting behaviour rather than through changes in elastic stiffness. This reinforces the interpretation that residual stress saturation, governed by an effective thermomechanical flow stress, is the dominant control parameter for beam bending in additively manufactured NiTi cantilevers.

6.3.6.6 Implications for residual stress estimation

By matching experimentally measured deflections through flow-stress-controlled thermomechanical simulations, the present approach provides a physically consistent means of estimating residual stress magnitudes in PBF-LB NiTi components. The predicted von Mises stresses obtained from the calibrated models therefore represent reasonable estimates of the residual stress state within the cantilevers.
This inverse identification framework enables residual stress to be inferred from simple deflection measurements, offering a practical alternative to direct residual stress measurement techniques, which are often challenging to apply to small, additively manufactured components.

6.3.6.7 Effect of VED and other processing parameters

Figure 6.14 presents the correlation matrix relating process parameters, experimental deflection measurements, and model beam deflection predictions. Among the process parameters, scanning speed exhibits the strongest influence on experimental deflection (0.35),

suggesting that thermal gradients and cooling rates play a more dominant role than absolute energy input (0.3). However, VED has a moderate positive correlation (0.56) on the model von Mises stress. Hatch spacing displays a strong negative correlation with the model von-Mises stress (-0.82), highlighting its role in controlling thermal overlap and heat accumulation in the model.

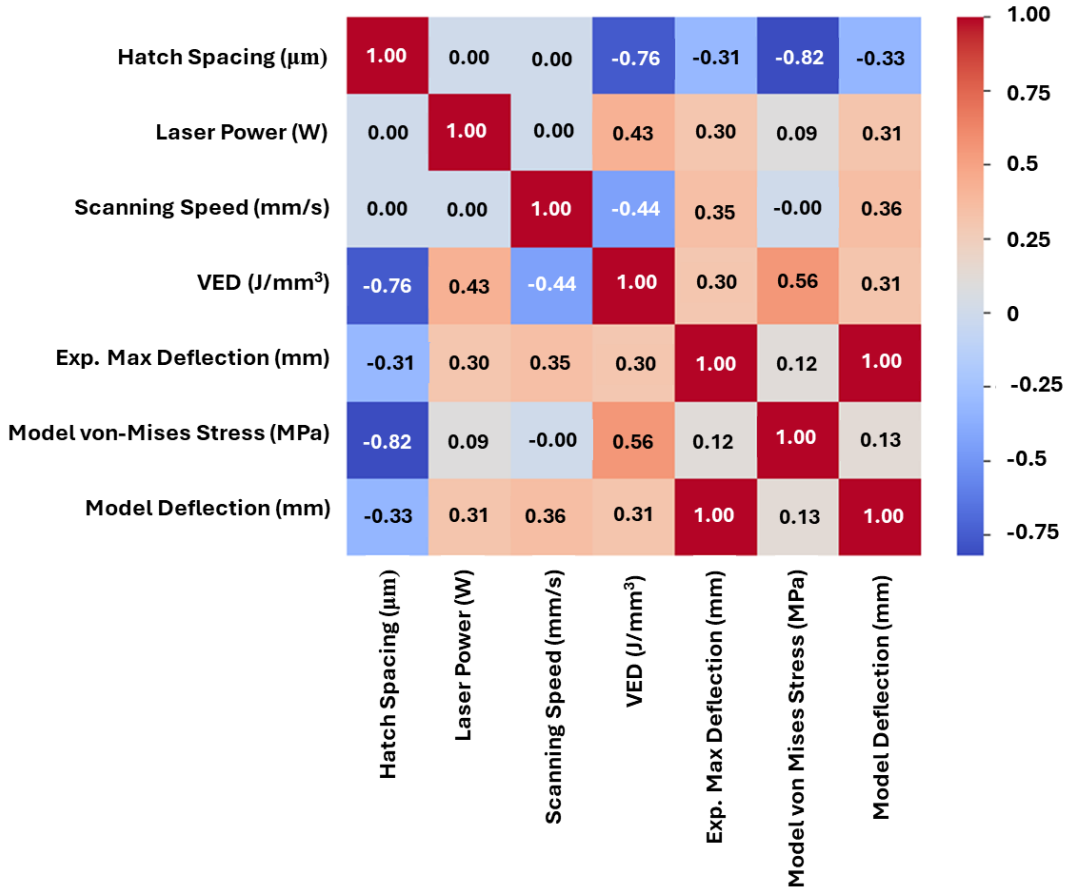


Figure 6.14 Correlation heatmap showing relation between various entities of the model and experiments.

6.4 Conclusion

In this study, a novel framework was developed which analysed residual stresses in NiTi cantilever beam samples that were additively manufactured via PBF-LB. A broad range of influential factors, which aid in the development of residual stresses, were investigated, which comprised of both experimental and computational methods. Using in-situ IR data, the complex thermal conditions experienced during the PBF-LB printing process were analysed to provide an indication of the residual stress state in the NiTi cantilever samples in their constrained, as-built condition. This also revealed a linear increase in average sample temperature with respect

to increasing VED. Among the processing parameters investigated, scanning speed was identified as the most influential factor governing beam deflection, with large deflections observed at both low and high scan speeds and reduced deflection at intermediate values. Additionally, an increase in laser power, and a decrease in hatch spacing, were both seen to increase maximum beam deflection values.

Phase analysis using X-ray diffraction indicated that high scanning speeds promote increased retained austenite content. The presence of retained austenite together with Ni_4Ti_3 precipitates suggests incomplete austenite-to-martensite transformation during rapid solidification, which limits strain accommodation and contributes to elevated residual stresses. This interpretation is supported by the observation that samples exhibiting higher fractions of both phases also displayed larger maximum deflections. For future study, it would be of interest to further examine the influence of secondary phases and precipitates on the residual stresses in additively manufactured NiTi samples.

The hardness mapping results provided an additional insight into the observed relationship between retained austenite content and cantilever beam deflection. Samples with higher austenite fractions exhibited increased Vickers hardness, indicating locally higher stiffness. This could potentially indicate that these regions may contribute to greater macroscopic deflection upon stress release, consistent with the higher beam deflections that were observed experimentally. For future study, it would be of interest to further examine in further detail the influence of secondary phases and precipitates on the residual stresses in additively manufactured NiTi samples.

A thermo-mechanical finite element model was developed to estimate residual stress and deflection in PBF-LB-processed NiTi, demonstrating its capability to capture both deflection and stress evolution during fabrication. In the absence of well-defined mechanical properties for the as-printed material, a trial-and-error calibration approach was adopted, through which an elastic modulus of 50 GPa, and a range of effective thermal mechanical flow stress ($\sigma_{\text{flow}}^{\text{eff}}$) values were identified as providing the closest agreement with experimental deflection measurements. Using this calibrated parameter set, the calculated von Mises residual stresses in the printed samples were found to lie within the range of 35–120 MPa.

This study establishes a physically consistent framework linking process parameters, thermal history, phase evolution, and residual stress development in PBF-LB NiTi. The proposed

modelling approach provides a practical pathway for inverse estimation of effective material properties and offers valuable insight into distortion control in NiTi additive manufacturing. Future work will extend the model to predict individual residual stress components and will integrate machine learning techniques with the thermo-mechanical framework to enable rapid and accurate stress prediction. Experimental validation using established residual stress measurement techniques such as hole-drilling, the contour method, and neutron diffraction will further strengthen the robustness and applicability of the proposed approach.

Contribution towards the thesis: This chapter builds directly upon the experimental insights established in Chapter 5 by developing a predictive thermo-mechanical modelling framework for residual stress and distortion in PBF-LB fabricated NiTi. The use of cantilever beam deflection as a measurable indicator of residual stress provides a practical link between experimental observations and model calibration, enabling inverse estimation of effective material properties for additively manufactured NiTi. Furthermore, the incorporation of in-situ thermal data and phase characterization ensures that the model reflects the underlying physical mechanisms identified in earlier chapters, particularly the role of thermal history and phase transformation behaviour in stress accumulation. This chapter represents the transition from experimental understanding to predictive capability within the thesis. It consolidates the process–thermal–stress relationships established in Chapters 3–5 into a unified modelling framework, enabling estimation of residual stress and distortion under varying processing conditions. As such, it provides a foundation for future development of rapid prediction tools and closed-loop process control strategies for PBF-LB NiTi, completing the progression from melt pool physics to component-level performance prediction.

7. Chapter: Conclusion and Future Work

This thesis has addressed the critical challenge of improving the predictability and control of Laser Powder Bed Fusion (PBF-LB) processing of nickel–titanium (NiTi) shape memory alloys. Given the strong sensitivity of NiTi to thermal history, composition, and phase transformation behaviour, achieving reliable process–structure–property relationships remains a significant barrier to industrial adoption. Through a combination of experimental investigation, physics-based modelling, and data-driven approaches, this work has developed an integrated framework linking melt pool behaviour, thermal history, and residual stress evolution.

The literature review (**Chapter 2**) established that while both physics-based and data-driven models are widely used in additive manufacturing, neither approach alone is sufficient for NiTi. The review highlighted the importance of accurately predicting local thermal history and composition to control phase transformation behaviour and functional performance. It also identified physics-informed machine learning and digital twin frameworks as promising pathways for bridging the gap between accuracy and computational efficiency.

Building on this foundation, **Chapter 3** provided a systematic evaluation of analytical melt pool models for NiTi. Taking results from this work and comparing with the literature for different alloys, it is shown that model performance is strongly dependent on both the alloy system as well as the process parameter regime. While the Eagar–Tsai model accurately predicted melt pool width and the Gladush–Smurov model provided reasonable depth predictions, no single model was sufficient to capture all melt pool characteristics. This highlighted the limitations of simplified analytical approaches and motivated the development of more advanced modelling strategies, including both finite element and data-driven machine learning methods, as presented in the next chapter.

Chapter 4 addressed these limitations through the development of a physics-informed digital twin framework. A high-fidelity thermal finite element model, incorporating CALPHAD-derived temperature-dependent material properties, achieved strong agreement with experimental melt pool measurements. The integration of this model with a machine learning surrogate enabled rapid and accurate prediction of melt pool geometry across a wide parameter space. By embedding physics-based stability criteria, the framework was extended into a decision-making tool capable of identifying stable processing regimes. This represents a significant advancement in melt pool prediction and process optimisation for NiTi.

Chapter 5 extended the investigation from melt pool behaviour to residual stress formation through detailed experimental characterization. Using a multi-modal approach combining ESPI-HD and XRD, this chapter provided spatially resolved residual stress measurements and established a direct link between melt pool thermal history and stress development. A key finding was the identification of a non-monotonic relationship between volumetric energy density (VED) and residual stress, challenging conventional assumptions that higher energy input always increases stress. This demonstrated that residual stress evolution is governed by complex interactions between process parameters and thermal gradients.

Finally, **Chapter 6** translated these experimental insights into a predictive modelling framework. A CALPHAD-coupled thermo-mechanical finite element model was developed to estimate residual stress and distortion in PBF-LB fabricated NiTi. The model was calibrated using cantilever beam deflection measurements and validated against experimental observations. Importantly, the work demonstrated that residual stress development is governed by thermal gradients and phase evolution, including the extent of retained austenite and Ni_4Ti_3 precipitates. This chapter represents the culmination of the thesis by integrating process parameters, thermal history, phase transformation, and mechanical response into a unified predictive framework.

Overall, this thesis makes several key contributions to the field:

- Demonstrates the limitations of analytical melt pool models for NiTi and highlights the need for material-specific modelling approaches
- Develops a physics-informed digital twin framework combining finite element modelling and machine learning for rapid melt pool prediction and optimisation
- Establishes a direct experimental link between melt pool thermal history and residual stress development
- Identifies a non-monotonic relationship between energy input and residual stress, challenging existing assumptions
- Develops a predictive thermo-mechanical modelling framework incorporating phase evolution effects for residual stress estimation

Collectively, these contributions advance the understanding of process–thermal–structure relationships in PBF-LB NiTi and provide practical tools for improving process control and component reliability. Future work should focus on extending the modelling frameworks developed in this thesis toward fully integrated multi-scale and multi-physics approaches. This includes coupling thermal, microstructural, phase transformation, and mechanical models

within a unified framework. Such integration is particularly important for NiTi, where functional properties are highly sensitive to local thermal history and composition.

The digital twin framework developed in this work currently focuses on melt pool-scale predictions. Extending this framework to part-scale analysis could enable prediction of porosity distribution, microstructure, phase volume fraction and composition, surface roughness, and residual stress fields across full components. This will enhance its applicability for industrial process optimisation and component qualification.

While machine learning was successfully applied to melt pool prediction, its integration into residual stress modelling remains an important area for future research. Hybrid approaches combining thermo-mechanical modelling with data-driven methods could significantly reduce computational cost while maintaining predictive accuracy.

A major limitation identified throughout this work is the lack of reliable temperature-dependent thermophysical and mechanical property data for additively manufactured NiTi. Future research should focus on systematic experimental characterization of these properties across the relevant temperature ranges to improve model fidelity.

The integration of predictive models with in-situ monitoring systems represents a key step toward intelligent additive manufacturing. Future work should explore the use of real-time thermal data, combined with digital twin frameworks, to enable closed-loop process control. This would allow dynamic adjustment of process parameters to mitigate defects and ensure consistent part quality. Further investigation is required into the relationship between process parameters, phase evolution, and functional properties such as transformation temperatures and superelastic response. Incorporating phase transformation modelling into predictive frameworks would provide a more complete understanding of NiTi behaviour in PBF-LB. Expanding the experimental dataset through additional residual stress measurement techniques, such as neutron diffraction and the contour method, would provide deeper insight into stress distributions and improve validation of predictive models. Larger datasets would also enable more robust statistical analysis of process–stress relationships.

This thesis demonstrates that achieving reliable additive manufacturing of NiTi requires an integrated understanding of melt pool physics, thermal history, phase transformation behaviour, and residual stress development. The methodologies and insights developed here contribute not only to the advancement of NiTi additive manufacturing but also to the broader field of metal additive manufacturing, where similar challenges exist in linking process conditions to material performance.

References

[1] C.Y. Yap, C.K. Chua, Z.L. Dong, Z.H. Liu, D.Q. Zhang, L.E. Loh, S.L. Sing, Review of selective laser melting: Materials and applications, Appl. Phys. Rev. 2 (2015) 041101. https://doi.org/10.1063/1.4935926.

[2] S.L. Sing, W.Y. Yeong, Laser powder bed fusion for metal additive manufacturing: perspectives on recent developments, Virtual Phys. Prototyp. 15 (2020) 359–370. https://doi.org/10.1080/17452759.2020.1779999.

[3] I. V. Shishkovsky, I.A. Yadroitsev, I.Yu. Smurov, Manufacturing three-dimensional nickel titanium articles using layer-by-layer laser-melting technology, Technical Physics Letters 39 (2013) 1081–1084. https://doi.org/10.1134/S1063785013120250.

[4] P. Jamshidi, C. Panwisawas, E. Langi, S.C. Cox, J. Feng, L. Zhao, M.M. Attallah, Development, characterisation, and modelling of processability of nitinol stents using laser powder bed fusion, J. Alloys Compd. 909 (2022) 164681. https://doi.org/10.1016/j.jallcom.2022.164681.

[5] W.J. Buehler, R.C. Wiley, The Properties of TiNi and Associated Phases, 1961. https://doi.org/https://apps.dtic.mil/sti/tr/pdf/AD0266607.pdf.

[6] K. Otsuka, X. Ren, Physical metallurgy of Ti-Ni-based shape memory alloys, Prog. Mater. Sci. 50 (2005) 511–678. https://doi.org/10.1016/j.pmatsci.2004.10.001.

[7] J.A. Shaw, C.B. Churchill, M.A. Iadicola, Tips and tricks for characterizing shape memory alloy wire: Part 1-differential scanning calorimetry and basic phenomena, Exp. Tech. 32 (2008) 55–62. https://doi.org/10.1111/j.1747-1567.2008.00410.x.

[8] N. Hertlein, S. Deshpande, V. Venugopal, M. Kumar, S. Anand, Prediction of selective laser melting part quality using hybrid Bayesian network, Addit. Manuf. 32 (2020) 101089. https://doi.org/10.1016/j.addma.2020.101089.

[9] U. Scipioni Bertoli, A.J. Wolfer, M.J. Matthews, J.P.R. Delplanque, J.M. Schoenung, On the limitations of Volumetric Energy Density as a design parameter for Selective Laser Melting, Mater. Des. 113 (2017) 331–340. https://doi.org/10.1016/j.matdes.2016.10.037.

[10] C. Wei, L. Li, Recent progress and scientific challenges in multi-material additive manufacturing via laser-based powder bed fusion, Virtual Phys. Prototyp. 16 (2021) 347–371. https://doi.org/10.1080/17452759.2021.1928520.

[11] P. Wang, Y. Yang, N.S. Moghaddam, Process modeling in laser powder bed fusion towards defect detection and quality control via machine learning: The state-of-the-art and research challenges, J. Manuf. Process. 73 (2022) 961–984. https://doi.org/10.1016/j.jmapro.2021.11.037.

[12] S.R. Narasimharaju, W. Zeng, T.L. See, Z. Zhu, P. Scott, X. Jiang, S. Lou, A comprehensive review on laser powder bed fusion of steels: Processing, microstructure, defects and control methods, mechanical properties, current challenges and future trends, J. Manuf. Process. 75 (2022) 375–414. https://doi.org/10.1016/j.jmapro.2021.12.033.

[13] J.C. Chekotu, R. Groarke, K. O'Toole, D. Brabazon, Advances in Selective Laser Melting of Nitinol Shape Memory Alloy Part Production, Materials 12 (2019) 809. https://doi.org/10.3390/ma12050809.

[14] M. Elahinia, N. Shayesteh Moghaddam, M. Taheri Andani, A. Amerinatanzi, B.A. Bimber, R.F. Hamilton, Fabrication of NiTi through additive manufacturing: A review, Prog. Mater. Sci. 83 (2016) 630–663. https://doi.org/10.1016/j.pmatsci.2016.08.001.

[15] A.K. Agrawal, B. Rankouhi, D.J. Thoma, Predictive process mapping for laser powder bed fusion: A review of existing analytical solutions, Curr. Opin. Solid State Mater. Sci. 26 (2022). https://doi.org/10.1016/j.cossms.2022.101024.

[16] J. Liu, B. Jalalahmadi, Y.B. Guo, M.P. Sealy, N. Bolander, A review of computational modeling in powder-based additive manufacturing for metallic part qualification, Rapid Prototyp. J. 24 (2018) 1245–1264. https://doi.org/10.1108/RPJ-04-2017-0058.
[17] T. Gatsos, K.A. Elsayed, Y. Zhai, D.A. Lados, Review on Computational Modeling of Process–Microstructure–Property Relationships in Metal Additive Manufacturing, JOM 72 (2020) 403–419. https://doi.org/10.1007/s11837-019-03913-x.
[18] Z. Zhang, C.K. Sahu, S.K. Singh, R. Rai, Z. Yang, Y. Lu, Machine learning based prediction of melt pool morphology in a laser-based powder bed fusion additive manufacturing process, Int. J. Prod. Res. 62 (2024) 1803–1817. https://doi.org/10.1080/00207543.2023.2201860.
[19] P. Akbari, F. Ogoke, N.-Y. Kao, K. Meidani, C.-Y. Yeh, W. Lee, A. Barati Farimani, MeltpoolNet: Melt pool characteristic prediction in Metal Additive Manufacturing using machine learning, Addit. Manuf. 55 (2022) 102817. https://doi.org/10.1016/j.addma.2022.102817.
[20] M. Tian, H. Mu, T. Liu, M. Li, D. Ding, J. Zhao, Physics-informed machine learning-based real-time long-horizon temperature fields prediction in metallic additive manufacturing, Communications Engineering 4 (2025) 168. https://doi.org/10.1038/s44172-025-00501-7.
[21] V. Karkaria, A. Goeckner, R. Zha, J. Chen, J. Zhang, Q. Zhu, J. Cao, R.X. Gao, W. Chen, Towards a digital twin framework in additive manufacturing: Machine learning and bayesian optimization for time series process optimization, J. Manuf. Syst. 75 (2024) 322–332. https://doi.org/10.1016/j.jmsy.2024.04.023.
[22] B.D. Bevans, A. Carrington, A. Riensche, A. Tenequer, C. Barrett, H. (Scott) Halliday, R. Srinivasan, K.D. Cole, P. Rao, Digital twins for rapid in-situ qualification of part quality in laser powder bed fusion additive manufacturing, Addit. Manuf. 93 (2024) 104415. https://doi.org/10.1016/j.addma.2024.104415.
[23] A.W. Malik, M.A. Mahmood, F. Liou, Digital twin–driven optimization of laser powder bed fusion processes: a focus on lack-of-fusion defects, Rapid Prototyp. J. 30 (2024) 1977–1988. https://doi.org/10.1108/RPJ-02-2024-0091.
[24] R. Yavari, A. Riensche, E. Tekerek, L. Jacquemetton, H. Halliday, M. Vandever, A. Tenequer, V. Perumal, A. Kontsos, Z. Smoqi, K. Cole, P. Rao, Digitally twinned additive manufacturing: Detecting flaws in laser powder bed fusion by combining thermal simulations with in-situ meltpool sensor data, Mater. Des. 211 (2021) 110167. https://doi.org/10.1016/j.matdes.2021.110167.
[25] R. Alfattani, M.M. Hotami, Digital twin–driven multiscale modelling for real-time defect prediction in metal additive manufacturing, Sci. Rep. (2026). https://doi.org/10.1038/s41598-026-58348-7.
[26] X. Peng, Z. Chen, A. Zhang, X. Chen, Y. Zhang, Digital twin temperature field prediction of laser powder bed fusion through proper orthogonal decomposition with radial basis function, Mater. Today Commun. 38 (2024) 107883. https://doi.org/10.1016/j.mtcomm.2023.107883.
[27] X. Peng, R. Jiang, Z. Yuan, A. Zhang, Z. Chen, D. Wang, X. Chen, Y. Zhang, A sensor-integrated digital twin framework for molten pool monitoring of laser powder bed fusion, Comput. Ind. 171 (2025) 104332. https://doi.org/10.1016/j.compind.2025.104332.
[28] S.Y. Yang, G.S. Dui, Temperature analysis of one-dimensional NiTi shape memory alloys under different loading rates and boundary conditions, Int. J. Solids Struct. 50 (2013) 3254–3265. https://doi.org/10.1016/j.ijsolstr.2013.05.026.

[29] R. Srivastava, S.H. Alsamhi, N. Murray, D. Devine, Shape Memory Alloy-Based Wearables: A Review, and Conceptual Frameworks on HCI and HRI in Industry 4.0, Sensors 22 (2022) 6802. https://doi.org/10.3390/s22186802.
[30] M. Speirs, X. Wang, S. Van Baelen, A. Ahadi, S. Dadbakhsh, J.-P. Kruth, J. Van Humbeeck, On the Transformation Behavior of NiTi Shape-Memory Alloy Produced by SLM, Shape Memory and Superelasticity 2 (2016) 310–316. https://doi.org/10.1007/s40830-016-0083-y.
[31] J. Frenzel, E.P. George, A. Dlouhy, Ch. Somsen, M.F.-X. Wagner, G. Eggeler, Influence of Ni on martensitic phase transformations in NiTi shape memory alloys, Acta Mater. 58 (2010) 3444–3458. https://doi.org/10.1016/j.actamat.2010.02.019.
[32] S.M. Russell, Nitinol Melting and Fabrication, SMST -2000 Conference Proceedings 9 (2000).
[33] S. Xi, Y. Su, Phase Field Study of the Microstructural Dynamic Evolution and Mechanical Response of NiTi Shape Memory Alloy under Mechanical Loading, Materials 14 (2021) 183. https://doi.org/10.3390/ma14010183.
[34] J. Burow, E. Prokofiev, C. Somsen, J. Frenzel, R. Valiev, G.F. Eggeler, Martensitic Transformations and Functional Stability in Ultra-Fine Grained NiTi Shape Memory Alloys, Materials Science Forum 584–586 (2008) 852–857. https://doi.org/10.4028/www.scientific.net/MSF.584-586.852.
[35] C.A. Canbay, O. Karaduman, N. Ünlü, İ. Özkul, Study on Basic Characteristics of CuAlBe Shape Memory Alloy, Brazilian Journal of Physics 51 (2021) 13–18. https://doi.org/10.1007/s13538-020-00823-1.
[36] M. Zarinejad, Y. Liu, Y. Tong, Transformation temperature changes due to second phase precipitation in NiTi-based shape memory alloys, Intermetallics (Barking). 17 (2009) 914–919. https://doi.org/10.1016/j.intermet.2009.03.022.
[37] Z.Z. Wei, X. Ma, X.P. Zhang, Defect Structure and Martensitic Transformation Crystallography in Ni₂MnGa Alloy, Materials Science Forum 687 (2011) 463–466. https://doi.org/10.4028/www.scientific.net/MSF.687.463.
[38] C. Peng, X. Wang, Y. Huo, Characteristics of stress-induced transformation and microstructure evolution in Cu-based SMA, Acta Mechanica Solida Sinica 21 (2008) 1–8. https://doi.org/10.1007/s10338-008-0801-x.
[39] V.S. Nair, R. Nachimuthu, The role of NiTi shape memory alloys in quality of life improvement through medical advancements: A comprehensive review, Proc. Inst. Mech. Eng. H 236 (2022) 923–950. https://doi.org/10.1177/09544119221093460.
[40] B. He, X. Dong, R. Nie, Y. Wang, S. Ao, G. Wang, Comprehensive shape memory alloys constitutive models for engineering application, Mater. Des. 225 (2023) 111563. https://doi.org/10.1016/j.matdes.2022.111563.
[41] C. Yang, S. Abanteriba, A. Becker, A review of shape memory alloy based filtration devices, AIP Adv. 10 (2020). https://doi.org/10.1063/1.5133981.
[42] J.J. Bundy, J.F.B. Chick, R.N. Srinivasa, K.J. Cooper, J.J. Gemmete, V. Wadhwa, J.M. Moriarty, Retrieval of Bard Simon Nitinol inferior vena cava filters: Approaches, technical successes, complications, and clinical outcomes, Phlebology: The Journal of Venous Disease 36 (2021) 555–561. https://doi.org/10.1177/0268355520925986.
[43] S.S. Jousheghan, A.Y. Chari, F.Y. Chari, Computational modeling of cardiovascular stent struts configuration and influences on NiTi stent shape memory behavior, in: 8th International Conference on Mechanical Engineering, Industries & Aerospace, 2025.
[44] F. Hoseini, A. Bellelli, L. Mizzi, F. Pecoraro, A. Spaggiari, Self-expanding Nitinol stents for endovascular peripheral applications: A review, Mater. Today Commun. 41 (2024) 111042. https://doi.org/10.1016/j.mtcomm.2024.111042.

[45] N. Cruden, Wilson, Advances in coronary stent technology: current expectations and new developments, Research Reports in Clinical Cardiology (2013) 85. https://doi.org/10.2147/RRCC.S34408.
[46] O. Subasi, S. Torabnia, I. Lazoglu, In silico analysis of Superelastic Nitinol staples for trans-sternal closure, J. Mech. Behav. Biomed. Mater. 107 (2020) 103770. https://doi.org/10.1016/j.jmbbm.2020.103770.
[47] K. Tsikopoulos, K. Sidiropoulos, D. Kitridis, C. Loizou, A. Felstead, Continuous Compression Implants in Foot and Ankle Surgery: Tips and Tricks, J. Clin. Med. 14 (2025) 3507. https://doi.org/10.3390/jcm14103507.
[48] A. Sleiman, C. Bejcek, A. Nestler, N. Revelt, S. Thuppal, A. Mills, M. Gardner, The history of orthopaedic use of nitinol compression staples, Injury 54 (2023) 111036. https://doi.org/10.1016/j.injury.2023.111036.
[49] D. Safranski, K. Dupont, K. Gall, Pseudoelastic NiTiNOL in Orthopaedic Applications, Shape Memory and Superelasticity 6 (2020) 332–341. https://doi.org/10.1007/s40830-020-00294-y.
[50] N.B. Morgan, Medical shape memory alloy applications—the market and its products, Materials Science and Engineering: A 378 (2004) 16–23. https://doi.org/10.1016/j.msea.2003.10.326.
[51] B. Le, K. McVary, K. McKenna, A. Colombo, A Novel Thermal-activated Shape Memory Penile Prosthesis: Comparative Mechanical Testing, Urology 99 (2017) 136–141. https://doi.org/10.1016/j.urology.2016.09.007.
[52] A. Wadood, Brief Overview on Nitinol as Biomaterial, Advances in Materials Science and Engineering 2016 (2016) 1–9. https://doi.org/10.1155/2016/4173138.
[53] J.-C. Yu, M.-H. Zhang, L. Yu, L.-P. Zhai, X. Song, F.-D. Dong, Y. Qiu, Experiment of a novel four-spherical intrauterine contraceptive device with nickel-titanium, Clinical Journal of Obstetrics and Gynecology 3 (2020) 142–144. https://doi.org/10.29328/journal.cjog.1001068.
[54] R. Chaudhari, J.J. Vora, D.M. Parikh, A Review on Applications of Nitinol Shape Memory Alloy, in: 2021: pp. 123–132. https://doi.org/10.1007/978-981-33-4176-0_10.
[55] T. Luchetti, A. Zanella, M. Biasiotto, A. Saccagno, Electrically Actuated Antiglare Rear-View Mirror Based on a Shape Memory Alloy Actuator, J. Mater. Eng. Perform. 18 (2009) 717–724. https://doi.org/10.1007/s11665-009-9487-6.
[56] A. Chellangi, S. Santhanam, G.S. Reddy, Design of aircraft morphing wing using shape memory alloy as an actuator, in: PROCEEDINGS OF GLOBAL CONFERENCE ON AERONAUTICAL, AEROSPACE AND MECHANICAL SCIENCES, AIP Conference Proceedings, Bangalore, India, 2025: p. 070001. https://doi.org/10.1063/5.0263964.
[57] D.J. Hartl, D.C. Lagoudas, Aerospace applications of shape memory alloys, Proc. Inst. Mech. Eng. G J. Aerosp. Eng. 221 (2007) 535–552. https://doi.org/10.1243/09544100JAERO211.
[58] G. Costanza, M.E. Tata, Shape Memory Alloys for Aerospace, Recent Developments, and New Applications: A Short Review, Materials 13 (2020) 1856. https://doi.org/10.3390/ma13081856.
[59] H. Ossmer, F. Wendler, M. Gueltig, F. Lambrecht, S. Miyazaki, M. Kohl, Energy-efficient miniature-scale heat pumping based on shape memory alloys, Smart Mater. Struct. 25 (2016) 085037. https://doi.org/10.1088/0964-1726/25/8/085037.
[60] L. Mañosa, A. Planes, Materials with Giant Mechanocaloric Effects: Cooling by Strength, Advanced Materials 29 (2017) 1603607. https://doi.org/https://doi.org/10.1002/adma.201603607.

[61] C. Zuo, L. Zheng, S. Yang, B. Li, H. Zhang, The current research status and development of elastocaloric refrigeration based on NiTi alloys, Next Materials 5 (2024). https://doi.org/10.1016/j.nxmate.2024.100270.
[62] J. Tušek, A. Žerovnik, M. Čebron, M. Brojan, B. Žužek, K. Engelbrecht, A. Cadelli, Elastocaloric effect vs fatigue life: Exploring the durability limits of Ni-Ti plates under pre-strain conditions for elastocaloric cooling, Acta Mater. 150 (2018) 295–307. https://doi.org/10.1016/j.actamat.2018.03.032.
[63] M.J. Mahtabi, N. Shamsaei, M.R. Mitchell, Fatigue of Nitinol: The state-of-the-art and ongoing challenges, J. Mech. Behav. Biomed. Mater. 50 (2015) 228–254. https://doi.org/10.1016/j.jmbbm.2015.06.010.
[64] F. Kordizadeh, K. Safaei, S. Mohajerani, M. Elahinia, Investigation of the elastocaloric effect in laser powder bed fusion NiTi porous structures, Additive Manufacturing Letters 6 (2023) 100131. https://doi.org/10.1016/j.addlet.2023.100131.
[65] A. Nyabadza, K. Tamil, M.C.C. Monu, É. McCarthy, L.A. Khan, C. Muilwijk, K. O'Toole, L. Fitzsimons, D. Brabazon, Effect of geometry on the coefficient of performance of Ni–Ti elastocaloric parts manufactured via powder bed fusion, Journal of Materials Research and Technology 30 (2024) 6082–6091. https://doi.org/10.1016/j.jmrt.2024.04.243.
[66] Y. Cao, X. Zhou, D. Cong, H. Zheng, Y. Cao, Z. Nie, Z. Chen, S. Li, N. Xu, Z. Gao, W. Cai, Y. Wang, Large tunable elastocaloric effect in additively manufactured Ni–Ti shape memory alloys, Acta Mater. 194 (2020) 178–189. https://doi.org/10.1016/j.actamat.2020.04.007.
[67] J. Zhan, Y. Li, Z. Guo, R. Ma, S. Wang, X. Yang, A. Jarlöv, H. Cao, F. Lin, Y. Xu, K. Li, Y.-W. Zhang, K. Zhou, A 4D-printed NiTi alloy with encoded microstructures evades the cooling capacity–energy efficiency trade-off in elastocaloric refrigeration, Materials Science and Engineering: R: Reports 169 (2026) 101191. https://doi.org/10.1016/j.mser.2026.101191.
[68] J. Zhan, K. Li, R. Ma, L. Zhu, J. Fang, H. Cao, D.Z. Zhang, L.E. Murr, Achieving fine tailoring of elastocaloric properties of laser powder bed-fused NiTi alloy via laser beam manipulation, Int. J. Mach. Tools Manuf. 202 (2024) 104210. https://doi.org/10.1016/j.ijmachtools.2024.104210.
[69] T. Merzouki, A. Duval, T. Ben Zineb, Finite Element analysis of a shape memory alloy actuator for a micropump, Simul. Model. Pract. Theory 27 (2012) 112–126. https://doi.org/10.1016/j.simpat.2012.05.006.
[70] S. Ahmad, A.W. Hashmi, F. Iqbal, S. Rab, Y. Tian, Exploring the potential of 3D printing for shape memory alloys: a critical review, Meas. Sci. Technol. 35 (2024) 122001. https://doi.org/10.1088/1361-6501/ad7525.
[71] J.M. Doyle, J.C. Chekotu, D. Brabazon, A comprehensive review of NiTiCu alloys for actuator applications, Smart Mater. Struct. 34 (2025) 103003. https://doi.org/10.1088/1361-665X/ae1174.
[72] R. Bogue, Shape-memory materials: a review of technology and applications, Assembly Automation 29 (2009) 214–219. https://doi.org/10.1108/01445150910972895.
[73] J. Mohd Jani, M. Leary, A. Subic, M.A. Gibson, A review of shape memory alloy research, applications and opportunities, Materials & Design (1980-2015) 56 (2014) 1078–1113. https://doi.org/10.1016/j.matdes.2013.11.084.
[74] M. Carl, J. Smith, B. Van Doren, M. Young, Effect of Ni-Content on the Transformation Temperatures in NiTi-20 at. % Zr High Temperature Shape Memory Alloys, Metals (Basel). 7 (2017) 511. https://doi.org/10.3390/met7110511.

[75] M. Mehrpouya, M. Elahinia, Introduction to additive manufacturing of shape memory materials, in: Additive Manufacturing of Shape Memory Materials, Elsevier, 2025: pp. 1–13. https://doi.org/10.1016/B978-0-443-29594-2.00012-2.
[76] S.W. Robertson, M. Launey, O. Shelley, I. Ong, L. Vien, K. Senthilnathan, P. Saffari, S. Schlegel, A.R. Pelton, A statistical approach to understand the role of inclusions on the fatigue resistance of superelastic Nitinol wire and tubing, J. Mech. Behav. Biomed. Mater. 51 (2015) 119–131. https://doi.org/10.1016/j.jmbbm.2015.07.003.
[77] M.H. Wu, Fabrication of Nitinol Materials and Components, Materials Science Forum 394–395 (2002) 285–292. https://doi.org/10.4028/www.scientific.net/MSF.394-395.285.
[78] P. Freitas Rodrigues, J.P. Oliveira, Functional performance of shape memory alloys, in: Additive Manufacturing of Shape Memory Materials, Elsevier, 2025: pp. 15–51. https://doi.org/10.1016/B978-0-443-29594-2.00010-9.
[79] T.C. Dzogbewu, D.J. de Beer, Additive manufacturing of NiTi shape memory alloy and its industrial applications, Heliyon 10 (2024). https://doi.org/10.1016/j.heliyon.2023.e23369.
[80] N. Nayan, Govind, C.N. Saikrishna, K.V. Ramaiah, S.K. Bhaumik, K.S. Nair, M.C. Mittal, Vacuum induction melting of NiTi shape memory alloys in graphite crucible, Materials Science and Engineering: A 465 (2007) 44–48. https://doi.org/10.1016/j.msea.2007.04.039.
[81] K. Kubášová, V. Drátovská, M. Losertová, P. Salvetr, M. Kopelent, F. Kořínek, V. Havlas, J. Džugan, M. Daniel, A Review on Additive Manufacturing Methods for NiTi Shape Memory Alloy Production, Materials 17 (2024). https://doi.org/10.3390/ma17061248.
[82] M.H. Elahinia, M. Hashemi, M. Tabesh, S.B. Bhaduri, Manufacturing and processing of NiTi implants: A review, Prog. Mater. Sci. 57 (2012) 911–946. https://doi.org/10.1016/j.pmatsci.2011.11.001.
[83] S. Parvizi, S.M. Hashemi, F. Asgarinia, M. Nematollahi, M. Elahinia, Effective parameters on the final properties of NiTi-based alloys manufactured by powder metallurgy methods: A review, Prog. Mater. Sci. 117 (2021) 100739. https://doi.org/10.1016/j.pmatsci.2020.100739.
[84] M. Bram, A. Ahmad-Khanlou, A. Heckmann, B. Fuchs, H.P. Buchkremer, D. Stöver, Powder metallurgical fabrication processes for NiTi shape memory alloy parts, Materials Science and Engineering: A 337 (2002) 254–263. https://doi.org/10.1016/S0921-5093(02)00028-X.
[85] K. Weinert, V. Petzoldt, Machining of NiTi based shape memory alloys, Materials Science and Engineering: A 378 (2004) 180–184. https://doi.org/10.1016/j.msea.2003.10.344.
[86] X. Wang, Z. Pu, J. Van Humbeeck, Application of 3D-printed shape memory alloys, in: Additive Manufacturing of Shape Memory Materials, Elsevier, 2025: pp. 405–447. https://doi.org/10.1016/B978-0-443-29594-2.00004-3.
[87] W.E. Frazier, Metal Additive Manufacturing: A Review, J. Mater. Eng. Perform. 23 (2014) 1917–1928. https://doi.org/10.1007/s11665-014-0958-z.
[88] J. Walker, M.T. Andani, C. Haberland, M. Elahinia, Additive Manufacturing of Nitinol Shape Memory Alloys to Overcome Challenges in Conventional Nitinol Fabrication, in: Volume 2A: Advanced Manufacturing, American Society of Mechanical Engineers, 2014. https://doi.org/10.1115/IMECE2014-40432.
[89] S. Vanaei, M. Mehrpouya, M. Elahinia, L-PBF additive manufacturing of shape memory alloys, in: Additive Manufacturing of Shape Memory Materials, Elsevier, 2025: pp. 229–276. https://doi.org/10.1016/B978-0-443-29594-2.00003-1.

[90] G. Shi, L. Li, Z. Yu, R. Liu, P. Sha, Z. Xu, Y. Guo, R. Xi, J. Liu, R. Xin, L. Chen, X. Wang, Z. Zhang, The interaction effect of process parameters on the phase transformation behavior and tensile properties in additive manufacturing of Ni-rich NiTi alloy, J. Manuf. Process. 77 (2022) 539–550. https://doi.org/10.1016/j.jmapro.2022.03.027.
[91] O. Abdulhameed, A. Al-Ahmari, W. Ameen, S.H. Mian, Additive manufacturing: Challenges, trends, and applications, Advances in Mechanical Engineering 11 (2019) 168781401882288. https://doi.org/10.1177/1687814018822880.
[92] T. DebRoy, H.L. Wei, J.S. Zuback, T. Mukherjee, J.W. Elmer, J.O. Milewski, A.M. Beese, A. Wilson-Heid, A. De, W. Zhang, Additive manufacturing of metallic components – Process, structure and properties, Prog. Mater. Sci. 92 (2018) 112–224. https://doi.org/10.1016/j.pmatsci.2017.10.001.
[93] R. Weber, E. Tosoratti, A.B. Spierings, K. Wegener, Functional graded NiTi manufactured with powder bed fusion, Progress in Additive Manufacturing 9 (2024) 2313–2326. https://doi.org/10.1007/s40964-024-00584-2.
[94] C. Haberland, M. Elahinia, J.M. Walker, H. Meier, J. Frenzel, On the development of high quality NiTi shape memory and pseudoelastic parts by additive manufacturing, Smart Mater. Struct. 23 (2014) 104002. https://doi.org/10.1088/0964-1726/23/10/104002.
[95] B. Song, X. Zhao, S. Li, C. Han, Q. Wei, S. Wen, J. Liu, Y. Shi, Differences in microstructure and properties between selective laser melting and traditional manufacturing for fabrication of metal parts: A review, Frontiers of Mechanical Engineering 10 (2015) 111–125. https://doi.org/10.1007/s11465-015-0341-2.
[96] R. Li, J. Liu, Y. Shi, L. Wang, W. Jiang, Balling behavior of stainless steel and nickel powder during selective laser melting process, The International Journal of Advanced Manufacturing Technology 59 (2012) 1025–1035. https://doi.org/10.1007/s00170-011-3566-1.
[97] J. Wang, D. He, X. Wu, W. Shao, X. Guo, Z. Zhou, Z. Tan, Heat transfer mode shift for regulating microstructure of NiTi alloys in laser powder bed fusion, 362 (2024). https://doi.org/10.1016/j.matlet.2024.136182.
[98] L. Xue, K.C. Atli, S. Picak, C. Zhang, B. Zhang, A. Elwany, R. Arroyave, I. Karaman, Controlling martensitic transformation characteristics in defect-free NiTi shape memory alloys fabricated using laser powder bed fusion and a process optimization framework, Acta Mater. 215 (2021) 117017. https://doi.org/10.1016/j.actamat.2021.117017.
[99] D. Bourke, M.C.C. Monu, P. Healy, A. Sloane, I.U. Ahad, D. Brabazon, Effect of build distribution and particle properties on the physical characteristics of laser powder bed fusion of in situ alloyed nitinol, Engineering Science in Additive Manufacturing 1 (2025) 025340020. https://doi.org/10.36922/ESAM025340020.
[100] B. Fosse, Détection in-situ par thermographie infrarouge de défauts de fabrication par Laser-Powder Bed Fusion (L-PBF) en vue d'un contrôle procédé en boucle fermée : applications aux alliages de TA6V et 15-5PH, (n.d.).
[101] W.E. King, H.D. Barth, V.M. Castillo, G.F. Gallegos, J.W. Gibbs, D.E. Hahn, C. Kamath, A.M. Rubenchik, Observation of keyhole-mode laser melting in laser powder-bed fusion additive manufacturing, J. Mater. Process. Technol. 214 (2014) 2915–2925. https://doi.org/10.1016/j.jmatprotec.2014.06.005.
[102] P. Yadav, O. Rigo, C. Arvieu, E. Le Guen, E. Lacoste, In Situ Monitoring Systems of The SLM Process: On the Need to Develop Machine Learning Models for Data Processing, Crystals (Basel). 10 (2020) 524. https://doi.org/10.3390/cryst10060524.
[103] J.N. Zhu, E. Borisov, X. Liang, E. Farber, M.J.M. Hermans, V.A. Popovich, Predictive analytical modelling and experimental validation of processing maps in additive

manufacturing of nitinol alloys, Addit. Manuf. 38 (2021). https://doi.org/10.1016/j.addma.2020.101802.
[104] S. Pramod, D. Kesavan, Melting modes of laser powder bed fusion (L-PBF) processed IN718 alloy: Prediction and experimental analysis, Advances in Industrial and Manufacturing Engineering 6 (2023) 100106. https://doi.org/10.1016/j.aime.2022.100106.
[105] Y. Yang, Y. Huang, W. Wu, One-step shaping of NiTi biomaterial by selective laser melting, in: S. Deng, A. Matsunawa, X. Zhu (Eds.), S. Deng, A. Matsunawa, X. Zhu (Eds.), 2007: p. 68250C. https://doi.org/10.1117/12.757753.
[106] A.A. Martin, N.P. Calta, S.A. Khairallah, J. Wang, P.J. Depond, A.Y. Fong, V. Thampy, G.M. Guss, A.M. Kiss, K.H. Stone, C.J. Tassone, J. Nelson Weker, M.F. Toney, T. van Buuren, M.J. Matthews, Dynamics of pore formation during laser powder bed fusion additive manufacturing, Nat. Commun. 10 (2019) 1987. https://doi.org/10.1038/s41467-019-10009-2.
[107] W.M. Tucho, V.H. Lysne, H. Austbø, A. Sjolyst-Kverneland, V. Hansen, Investigation of effects of process parameters on microstructure and hardness of SLM manufactured SS316L, J. Alloys Compd. 740 (2018) 910–925. https://doi.org/10.1016/j.jallcom.2018.01.098.
[108] I. Yadroitsev, A. Gusarov, I. Yadroitsava, I. Smurov, Single track formation in selective laser melting of metal powders, J. Mater. Process. Technol. 210 (2010) 1624–1631. https://doi.org/10.1016/j.jmatprotec.2010.05.010.
[109] B. Song, S.J. Dong, H.L. Liao, C. Coddet, Morphology evolution mechanism of single tracks of FeAl intermetallics in selective laser melting, Materials Research Innovations 16 (2012) 321–325. https://doi.org/10.1179/1433075X11Y.0000000045.
[110] E. Yasa, J. Deckers, J. Kruth, The investigation of the influence of laser re-melting on density, surface quality and microstructure of selective laser melting parts, Rapid Prototyp. J. 17 (2011) 312–327. https://doi.org/10.1108/13552541111156450.
[111] D.T. Papageorgiou, On the breakup of viscous liquid threads, Physics of Fluids 7 (1995) 1529–1544. https://doi.org/10.1063/1.868540.
[112] J. Yang, L.M. Schlenger, M.H. Nasab, S. Van Petegem, F. Marone, R.E. Logé, C. Leinenbach, Experimental quantification of inward Marangoni convection and its impact on keyhole threshold in laser powder bed fusion of stainless steel, Addit. Manuf. 84 (2024) 104092. https://doi.org/10.1016/j.addma.2024.104092.
[113] R. Morgan, C.J. Sutcliffe, W. O'Neill, Density analysis of direct metal laser re-melted 316L stainless steel cubic primitives, J. Mater. Sci. 39 (2004) 1195–1205. https://doi.org/10.1023/B:JMSC.0000013875.62536.fa.
[114] S. Das, Physical Aspects of Process Control in Selective Laser Sintering of Metals, Adv. Eng. Mater. 5 (2003) 701–711. https://doi.org/10.1002/adem.200310099.
[115] M.C.C. Monu, E.J. Ekoi, C. Hughes, S. Kumar S., D. Brabazon, Resultant physical properties of as-built nitinol processed at specific volumetric energy densities and correlation with in-situ melt pool temperatures, Journal of Materials Research and Technology 21 (2022) 2757–2777. https://doi.org/10.1016/j.jmrt.2022.10.073.
[116] J.M. Walker, C. Haberland, M. Taheri Andani, H.E. Karaca, D. Dean, M. Elahinia, Process development and characterization of additively manufactured nickel–titanium shape memory parts, J. Intell. Mater. Syst. Struct. 27 (2016) 2653–2660. https://doi.org/10.1177/1045389X16635848.
[117] N. Agarwal, M.C.C. Monu, K. Tamil Selvam, M.A. Obeidi, D. Brabazon, Study of the effects of laser power and scanning speed on the microstructural morphologies and physical properties of L-PBF produced Ni52.39Ti47.61, Journal of Materials Research and Technology 27 (2023) 8334–8343. https://doi.org/10.1016/j.jmrt.2023.11.146.

[118] W. Guo, B. Feng, Y. Yang, Y. Ren, Y. Liu, H. Yang, Q. Yang, L. Cui, X. Tong, S. Hao, Effect of laser scanning speed on the microstructure, phase transformation and mechanical property of NiTi alloys fabricated by LPBF, Mater. Des. 215 (2022) 110460. https://doi.org/10.1016/j.matdes.2022.110460.
[119] C. Wang, X.P. Tan, Z. Du, S. Chandra, Z. Sun, C.W.J. Lim, S.B. Tor, C.S. Lim, C.H. Wong, Additive manufacturing of NiTi shape memory alloys using pre-mixed powders, J. Mater. Process. Technol. 271 (2019) 152–161. https://doi.org/10.1016/j.jmatprotec.2019.03.025.
[120] S. Miyazaki, Y. Kohiyama, K. Otsuka, T.W. Duerig, Effects of Several Factors on the Ductility of the Ti-Ni Alloy, in: Martensitic Transformations, Trans Tech Publications Ltd, 1990: pp. 765–770. https://doi.org/10.4028/www.scientific.net/MSF.56-58.765.
[121] K. Li, R. Ma, J. Zhan, J. Wu, J. Fang, S. Wang, Q. Yang, N. Gong, L.E. Murr, H. Cao, Insight into the cracking mechanism of super-elastic NiTi alloy fabricated by laser powder bed fusion, Virtual Phys. Prototyp. 19 (2024). https://doi.org/10.1080/17452759.2024.2368654.
[122] L. Xue, K.C. Atli, C. Zhang, N. Hite, A. Srivastava, A.C. Leff, A.A. Wilson, D.J. Sharar, A. Elwany, R. Arroyave, I. Karaman, Laser Powder Bed Fusion of Defect-Free NiTi Shape Memory Alloy Parts with Superior Tensile Superelasticity, Acta Mater. 229 (2022) 117781. https://doi.org/10.1016/j.actamat.2022.117781.
[123] M. Jaskari, A. Hamada, T. Allam, K. Dzieciol, S. Ghosh, R. Schwaiger, P. Karjalainen, A. Järvenpää, Effects of volumetric energy density on defect structure and fatigue behaviour of powder bed fusion manufactured 316L stainless steel, Materials Science and Engineering: A 925 (2025) 147868. https://doi.org/10.1016/j.msea.2025.147868.
[124] H.T. Tan, E. Lopez, A. Selbmann, D. Karl, L. Stepien, F. Brueckner, Parameter analysis to correlate density with surface roughness and productivity in Powder Bed Fusion – Laser Beam (PBF-LB) of AlSi10Mg, Procedia CIRP 124 (2024) 157–162. https://doi.org/10.1016/j.procir.2024.08.090.
[125] C. Smith, G. Hommer, M. Keeler, J. Gockel, K. Findley, C. Brice, A. Clarke, J. Klemm-Toole, Assessing Volumetric Energy Density as a Predictor of Defects in Laser Powder Bed Fusion 316L Stainless Steel, Jom 77 (2025) 737–748. https://doi.org/10.1007/s11837-024-06946-z.
[126] M. Nematollahi, G.P. Toker, K. Safaei, A. Hinojos, S.E. Saghaian, O. Benafan, M.J. Mills, H. Karaca, M. Elahinia, Laser Powder Bed Fusion of NiTiHf High-Temperature Shape Memory Alloy: Effect of Process Parameters on the Thermomechanical Behavior, Metals (Basel). 10 (2020) 1522. https://doi.org/10.3390/met10111522.
[127] S. Gur, G.N. Frantziskonis, K. Muralidharan, Atomistic simulation of shape memory effect (SME) and superelasticity (SE) in nano-porous NiTi shape memory alloy (SMA), Comput. Mater. Sci. 152 (2018) 28–37. https://doi.org/10.1016/j.commatsci.2018.05.031.
[128] I.H. Abidi, F.A. Khalid, Sintering and Morphology of Porous Structure in NiTi Shape Memory Alloys for Biomedical Applications, Adv. Mat. Res. 570 (2012) 87–95. https://doi.org/10.4028/www.scientific.net/AMR.570.87.
[129] X. Yang, S. Wang, H. Pan, C. Zhang, J. Chen, X. Zhang, L. Gao, Microstructure Transformation in Laser Additive Manufactured NiTi Alloy with Quasi-In-Situ Compression, Micromachines (Basel). 13 (2022) 1642. https://doi.org/10.3390/mi13101642.
[130] S. Rangaswamy, T. Gillick, M.C.C. Monu, I.U. Ahad, D. Brabazon, Estimation of Residual Stress in Additive-Manufactured NiTi Alloy through Beam Mechanics and Finite Element Analysis, in: 2024: pp. 9–10. https://doi.org/10.31399/asm.cp.smst2024p0009.

[131] J.L. Bartlett, X. Li, An overview of residual stresses in metal powder bed fusion, Addit. Manuf. 27 (2019) 131–149. https://doi.org/10.1016/j.addma.2019.02.020.
[132] C. Garrido, S. Perosanz, A. Elliott, M. Simoes, D. Barba, On the effect of the processing parameters in microstructure and thermomechanical properties of LPBF NiTi shape memory alloys, Journal of Materials Research and Technology 33 (2024) 2414–2429. https://doi.org/10.1016/j.jmrt.2024.09.155.
[133] H.Z. Lu, L.H. Liu, X. Luo, H.W. Ma, W.S. Cai, R. Lupoi, S. Yin, C. Yang, Formation mechanism of heterogeneous microstructures and shape memory effect in NiTi shape memory alloy fabricated via laser powder bed fusion, Mater. Des. 232 (2023) 112107. https://doi.org/10.1016/j.matdes.2023.112107.
[134] Y. Lu, S. Wu, Y. Gan, T. Huang, C. Yang, L. Junjie, J. Lin, Study on the microstructure, mechanical property and residual stress of SLM Inconel-718 alloy manufactured by differing island scanning strategy, Opt. Laser Technol. 75 (2015) 197–206. https://doi.org/10.1016/j.optlastec.2015.07.009.
[135] M. Kaess, M. Werz, S. Weihe, Residual Stress Formation Mechanisms in Laser Powder Bed Fusion—A Numerical Evaluation, Materials 16 (2023). https://doi.org/10.3390/ma16062321.
[136] Fraunhofer ILT, Flying High with VCSEL Heating, (2018).
[137] S. Chen, H. Gao, Y. Zhang, Q. Wu, Z. Gao, X. Zhou, Review on residual stresses in metal additive manufacturing: formation mechanisms, parameter dependencies, prediction and control approaches, Journal of Materials Research and Technology 17 (2022) 2950–2974. https://doi.org/10.1016/j.jmrt.2022.02.054.
[138] S. Rangaswamy, J.C. Chekotu, T. Gillick, C. Hughes, J. Nicholl, D. Easton, C. Şimşir, D. Brabazon, Evaluating residual stress in additively manufactured nitinol shape memory alloy, Npj Advanced Manufacturing 2 (2025) 16. https://doi.org/10.1038/s44334-025-00027-y.
[139] B. Ma, J. Li, D. Chen, K. Pan, D. Li, Y. Zhang, Influence of residual stress on the superelasticity of Ni-Ti alloys prepared by laser powder bed fusion, Materials Science and Engineering: A 941 (2025) 148608. https://doi.org/10.1016/j.msea.2025.148608.
[140] M. Mohri, C. Leinenbach, Alloy design for 3D-printed shape memory alloys, in: Additive Manufacturing of Shape Memory Materials, Elsevier, 2025: pp. 85–118. https://doi.org/10.1016/B978-0-443-29594-2.00001-8.
[141] M. Pérez-Cerrato, I. Fraile, J.F. Gómez-Cortés, E. Urionabarrenetxea, I. Ruiz-Larrea, I. González, M.L. Nó, N. Burgos, J.M. San Juan, Designing for Shape Memory in Additive Manufacturing of Cu–Al–Ni Shape Memory Alloy Processed by Laser Powder Bed Fusion, Materials 15 (2022) 6284. https://doi.org/10.3390/ma15186284.
[142] M. Alimardani, E. Toyserkani, J.P. Huissoon, C.P. Paul, On the delamination and crack formation in a thin wall fabricated using laser solid freeform fabrication process: An experimental–numerical investigation, Opt. Lasers Eng. 47 (2009) 1160–1168. https://doi.org/10.1016/j.optlaseng.2009.06.010.
[143] S. Dadbakhsh, M. Speirs, J. Van Humbeeck, J.-P. Kruth, Laser additive manufacturing of bulk and porous shape-memory NiTi alloys: From processes to potential biomedical applications, MRS Bull. 41 (2016) 765–774. https://doi.org/10.1557/mrs.2016.209.
[144] H.Z. Lu, H.W. Ma, W.S. Cai, X. Luo, S.G. Qu, J. Wang, R. Lupoi, S. Yin, C. Yang, Altered phase transformation behaviors and enhanced bending shape memory property of NiTi shape memory alloy via selective laser melting, J. Mater. Process. Technol. 303 (2022) 117546. https://doi.org/10.1016/j.jmatprotec.2022.117546.
[145] M.C.C. Monu, Y. Afkham, J.C. Chekotu, E.J. Ekoi, H. Gu, C. Teng, J. Ginn, J. Gaughran, D. Brabazon, Bi-directional Scan Pattern Effects on Residual Stresses and

Distortion in As-built Nitinol Parts: A Trend Analysis Simulation Study, Integr. Mater. Manuf. Innov. 12 (2023) 52–69. https://doi.org/10.1007/s40192-023-00292-9.
[146] A. Nespoli, A.M. Grande, N. Bennato, D. Rigamonti, P. Bettini, E. Villa, G. Sala, F. Passaretti, Towards an understanding of the functional properties of NiTi produced by powder bed fusion, Progress in Additive Manufacturing 6 (2021) 321–337. https://doi.org/10.1007/s40964-020-00155-1.
[147] H. Jiang, W. Li, R. Xi, J. Luo, H. Wei, Z. Zhang, G. Zhao, J. Van Humbeeck, R. Tao, X. Wang, Tailoring the transformation behavior and functionalities of NiTi alloy achieved by L-PBF in-situ alloying using NiTi and Ni powder mixture, Rare Metals 44 (2025) 5793–5810. https://doi.org/10.1007/s12598-025-03288-w.
[148] N. Bouchareb, M. Fellah, N. Hezil, A. Guesmi, L. Khezami, A Review of Nitinol Shape Memory Alloys for Biomedical Applications: Advancements and Biocompatibility, JOM 78 (2026) 140–167. https://doi.org/10.1007/s11837-025-07932-9.
[149] C.A. Biffi, J.N. Lemke, P. Bassani, J. Fiocchi, C. Bregoli, A. Tuissi, Characterization and postprocessing of additively manufactured shape memory alloys, in: Additive Manufacturing of Shape Memory Materials, Elsevier, 2025: pp. 315–360. https://doi.org/10.1016/B978-0-443-29594-2.00006-7.
[150] J.C. Snyder, K.A. Thole, Understanding Laser Powder Bed Fusion Surface Roughness, J. Manuf. Sci. Eng. 142 (2020). https://doi.org/10.1115/1.4046504.
[151] M.C. Sow, T. De Terris, O. Castelnau, Z. Hamouche, F. Coste, R. Fabbro, P. Peyre, Influence of beam diameter on Laser Powder Bed Fusion (L-PBF) process, Addit. Manuf. 36 (2020) 101532. https://doi.org/10.1016/j.addma.2020.101532.
[152] P. Bayati, K. Safaei, M. Nematollahi, A. Jahadakbar, A. Yadollahi, M. Mahtabi, M. Elahinia, Toward understanding the effect of remelting on the additively manufactured NiTi, The International Journal of Advanced Manufacturing Technology 112 (2021) 347–360. https://doi.org/10.1007/s00170-020-06378-4.
[153] Z. Xiong, P. Zhang, C. Tan, D. Dong, W. Ma, K. Yu, Selective Laser Melting and Remelting of Pure Tungsten, Adv. Eng. Mater. 22 (2020). https://doi.org/10.1002/adem.201901352.
[154] G. Mani, D. Porter, K. Grove, S. Collins, A. Ornberg, R. Shulfer, Surface finishing of <scp>N</scp> itinol for implantable medical devices: A review, J. Biomed. Mater. Res. B Appl. Biomater. 110 (2022) 2763–2778. https://doi.org/10.1002/jbm.b.35112.
[155] N.I. de A. Lopes, L.Á. de O. Silva, L. de A. Santos, V.T.L. Buono, Surface Characterization of NiTi Superelastic and Shape Memory Alloys After Electrolytic Polishing, Materials Research 20 (2017) 572–579. https://doi.org/10.1590/1980-5373-mr-2016-0933.
[156] J. Yang, C. Gong, A. Li, G. Wang, L. Yang, W. Huang, P. Wang, Research on NiTi shape memory alloy electrolyte based on optimization of corrosion performance, Phys. Scr. 100 (2025) 045955. https://doi.org/10.1088/1402-4896/adbfd1.
[157] S. V. Chernyshikhin, D. V. Panov, T. Van Tuan, D.Yu. Ozherelkov, V.A. Sheremetyev, I. V. Shishkovsky, Laser Polishing of Nickel-Titanium Shape Memory Alloy Produced via Laser Powder Bed Fusion, Metals and Materials International 29 (2023) 3024–3038. https://doi.org/10.1007/s12540-023-01432-8.
[158] W. Zhang, Z. Li, C. Xu, M. Chai, P. Dong, Surface characteristics of NiTi cardiovascular stents by selective laser melting and electrochemical polishing, The International Journal of Advanced Manufacturing Technology 130 (2024) 623–634. https://doi.org/10.1007/s00170-023-12734-x.
[159] S.A. Shabalovskaya, J. Anderegg, F. Laab, P.A. Thiel, G. Rondelli, Surface conditions of Nitinol wires, tubing, and as-cast alloys. The effect of chemical etching, aging in

boiling water, and heat treatment, J. Biomed. Mater. Res. B Appl. Biomater. 65B (2003) 193–203. https://doi.org/10.1002/jbm.b.10001.
[160] S. Shabalovskaya, G. Rondelli, J. Anderegg, J.P. Xiong, M. Wu, Comparative corrosion performance of black oxide, sandblasted, and fine-drawn nitinol wires in potentiodynamic and potentiostatic tests: Effects of chemical etching and electropolishing, J. Biomed. Mater. Res. B Appl. Biomater. 69B (2004) 223–231. https://doi.org/10.1002/jbm.b.30006.
[161] N.D. Dejene, H.G. Lemu, Current Status and Challenges of Powder Bed Fusion-Based Metal Additive Manufacturing: Literature Review, Metals (Basel). 13 (2023) 424. https://doi.org/10.3390/met13020424.
[162] H. Dabbaghi, M. Nematollahi, K.S. Baghbaderani, P. Bayatimalayeri, M. Elahinia, High-temperature oxidation kinetics of additively manufactured NiTiHf, ASME 2020 15th International Manufacturing Science and Engineering Conference, MSEC 2020 1 (2020) 1–5. https://doi.org/10.1115/MSEC2020-8449.
[163] A. Mahmud, Z. Wu, J. Zhang, Y. Liu, H. Yang, Surface oxidation of NiTi and its effects on thermal and mechanical properties, Intermetallics (Barking). 103 (2018) 52–62. https://doi.org/10.1016/j.intermet.2018.09.013.
[164] S. Saedi, A.S. Turabi, M.T. Andani, N.S. Moghaddam, M. Elahinia, H.E. Karaca, Texture, aging, and superelasticity of selective laser melting fabricated Ni-rich NiTi alloys, Materials Science and Engineering: A 686 (2017) 1–10. https://doi.org/10.1016/j.msea.2017.01.008.
[165] F. Tian, G. Li, L. Li, Z. Wang, S. Yan, X. Li, Advance in solid-state purification technology for metals, J. Alloys Compd. 592 (2014) 176–184. https://doi.org/10.1016/j.jallcom.2013.12.260.
[166] K. Dietrich, J. Diller, S. Dubiez-Le Goff, D. Bauer, P. Forêt, G. Witt, The influence of oxygen on the chemical composition and mechanical properties of Ti-6Al-4V during laser powder bed fusion (L-PBF), Addit. Manuf. 32 (2020) 100980. https://doi.org/10.1016/j.addma.2019.100980.
[167] J.M. Oh, B.K. Lee, C.Y. Suh, J.W. Lim, Removal of metallic impurities from Ti binary alloy scraps using hydrogen plasma arc melting, J. Alloys Compd. 574 (2013) 1–5. https://doi.org/10.1016/j.jallcom.2013.04.041.
[168] N. Emminghaus, R. Bernhard, J. Hermsdorf, L. Overmeyer, S. Kaierle, Laser-based powder bed fusion of Ti-6Al-4V structures with different surface-area-to-volume ratios in oxygen-reduced and oxygen-free environment, Tagungsband 5. Niedersächsisches Symposium Materialtechnik: 23. Bis 24. Februar 2023 12 (2023). https://doi.org/10.21268/20230711-12.
[169] E. Brizes, E. Young-Dohe, J. Milner, Bending Performance of Tungsten Printed via Laser Powder Bed Fusion With Ceramic Dispersion Modified Powder Feedstock, NASA/TM-20240012642 (2024).
[170] S. Rangaswamy, D. Bourke, M.C.C. Monu, P. Healy, H. Gu, I.U. Ahad, D. Brabazon, Investigating Melt Pool Dimensions in Laser Powder Bed Fusion of Nitinol: An Analytical Approach, Adv. Eng. Mater. 26 (2024). https://doi.org/10.1002/adem.202401636.
[171] M. Afrasiabi, H. Hosseinzadeh, E. Tosoratti, R. Weber, Modeling of 3D-printed shape memory alloys, in: Additive Manufacturing of Shape Memory Materials, Elsevier, 2025: pp. 361–404. https://doi.org/10.1016/B978-0-443-29594-2.00005-5.
[172] T. Moges, G. Ameta, P. Witherell, A Review of Model Inaccuracy and Parameter Uncertainty in Laser Powder Bed Fusion Models and Simulations, J. Manuf. Sci. Eng. 141 (2019). https://doi.org/10.1115/1.4042789.

[173] F. Xu, F. Xiong, M.-J. Li, Y. Lian, Three-Dimensional Numerical Simulation of Grain Growth during Selective Laser Melting of 316L Stainless Steel, Materials 15 (2022) 6800. https://doi.org/10.3390/ma15196800.
[174] D. Palmeri, G. Pollara, R. Licari, F. Micari, Finite Element Method in L-PBF of Ti-6Al-4V: Influence of Laser Power and Scan Speed on Residual Stress and Part Distortion, Metals (Basel). 13 (2023) 1907. https://doi.org/10.3390/met13111907.
[175] S. Chen, Y. Xu, Y. Jiao, A hybrid finite-element and cellular-automaton framework for modeling 3D microstructure of Ti–6Al–4V alloy during solid–solid phase transformation in additive manufacturing, Model. Simul. Mat. Sci. Eng. 26 (2018) 045011. https://doi.org/10.1088/1361-651X/aabcad.
[176] C. Li, Y. Pan, Y. Shi, W. Wang, Optimization of process prediction models for hot-wire laser metal deposition using transfer learning strategies based on simulation datasets, Welding in the World 69 (2025) 1193–1205. https://doi.org/10.1007/s40194-024-01921-3.
[177] Z. Alomar, F. Concli, A Review of the Selective Laser Melting Lattice Structures and Their Numerical Models, Adv. Eng. Mater. 22 (2020). https://doi.org/10.1002/adem.202000611.
[178] I. Baturynska, K. Martinsen, Prediction of geometry deviations in additive manufactured parts: comparison of linear regression with machine learning algorithms, J. Intell. Manuf. 32 (2021) 179–200. https://doi.org/10.1007/s10845-020-01567-0.
[179] A. Al Amin, Y. Li, Y. Lu, X. Xie, Z. Gan, S. Mojumder, G.J. Wagner, W.K. Liu, Physics guided heat source for quantitative prediction of IN718 laser additive manufacturing processes, NPJ Comput. Mater. 10 (2024) 37. https://doi.org/10.1038/s41524-024-01198-6.
[180] E. Wycisk, A. Solbach, S. Siddique, D. Herzog, F. Walther, C. Emmelmann, Effects of Defects in Laser Additive Manufactured Ti-6Al-4V on Fatigue Properties, Phys. Procedia 56 (2014) 371–378. https://doi.org/10.1016/j.phpro.2014.08.120.
[181] X. Xing, X. Duan, X. Sun, H. Gong, L. Wang, F. Jiang, Modification of Residual Stresses in Laser Additive Manufactured AlSi10Mg Specimens Using an Ultrasonic Peening Technique, Materials 12 (2019) 455. https://doi.org/10.3390/ma12030455.
[182] A. Farrag, Y. Yang, N. Cao, D. Won, Y. Jin, Physics-Informed Machine Learning for metal additive manufacturing, Progress in Additive Manufacturing 10 (2025) 171–185. https://doi.org/10.1007/s40964-024-00612-1.
[183] F. Jiang, M. Xia, Y. Hu, Physics-Informed Machine Learning for Accurate Prediction of Temperature and Melt Pool Dimension in Metal Additive Manufacturing, 3D Print. Addit. Manuf. 11 (2024) e1679–e1689. https://doi.org/10.1089/3dp.2022.0363.
[184] S. Yang, S. Peng, J. Guo, F. Wang, A Review on Physics-Informed Machine Learning for Monitoring Metal Additive Manufacturing Process, Advanced Manufacturing 1 (2024) 1–2. https://doi.org/10.55092/am20240008.
[185] S. Liao, T. Xue, J. Jeong, S. Webster, K. Ehmann, J. Cao, Hybrid thermal modeling of additive manufacturing processes using physics-informed neural networks for temperature prediction and parameter identification, Comput. Mech. 72 (2023) 499–512. https://doi.org/10.1007/s00466-022-02257-9.
[186] N. Hassine, S. Chatti, M. Ben Slama, L. Kolsi, Sensitivity of Melt Pool Dimensions and Keyhole to Laser Beam Diameter, Annals of Dunarea de Jos University of Galati Fascicle XII Welding Equipment and Technology 32 (2021) 30–36. https://doi.org/10.35219/awet.2021.04.
[187] H. Hosseinzadeh, M. Nematollahi, K. Safaei, H. Abedi, P. Bayati, R. Javan, B. Poorganji, L. Yuan, M. Elahinia, A Numerical Approach to Model Microstructure Evolution for NiTi Shape Memory Alloy in Laser Powder Bed Fusion Additive

Manufacturing, Integr. Mater. Manuf. Innov. 11 (2022). https://doi.org/10.1007/s40192-022-00252-9.
[188] E. Vaghefi, S. Hosseini, B. Prorok, E. Mirkoohi, Geometrically-informed predictive modeling of melt pool depth in laser powder bed fusion using deep MLP-CNN and metadata integration, J. Manuf. Process. 119 (2024) 952–963. https://doi.org/10.1016/j.jmapro.2024.03.098.
[189] N. Hassinie, S. Chatti, L. Kolsi, Sensitivity of Melt Pool Size and Porosity Appearing to Base Plate Preheating in Laser Powder Bed Fusion Process, Annals of Dunarea de Jos University of Galati. Fascicle XII, Welding Equipment and Technology 33 (2022) 112–116. https://doi.org/10.35219/awet.2022.11.
[190] D. Rosenthal, The Theory of Moving Sources of Heat and Its Application to Metal Treatments, J. Fluids Eng. 68 (1946) 849–865. https://doi.org/10.1115/1.4018624.
[191] T.V. Eagar, N.-S. Tsai, Temperature Fields Produced by Traveling Distributed Heat Sources, n.d.
[192] P. Scheel, Towards Fast and Reliable Heat Transfer Models for Laser Powder Bed Fusion, (2023).
[193] T.W. Eagar, N.-S. Tsai, Use of a Gaussian heat distribution in dimensionless form indicates final weld pool shape can be predicted accurately for many welds and materials, Weld. Res. Suppl (1983).
[194] M. Khorasani, A. Ghasemi, M. Leary, W. O'Neil, I. Gibson, L. Cordova, B. Rolfe, Numerical and analytical investigation on meltpool temperature of laser-based powder bed fusion of IN718, Int. J. Heat Mass Transf. 177 (2021) 121477. https://doi.org/10.1016/j.ijheatmasstransfer.2021.121477.
[195] M. Kusano, M. Watanabe, Heat Source Model Development for Thermal Analysis of Laser Powder Bed Fusion Using Bayesian Optimization and Machine Learning, Integr. Mater. Manuf. Innov. 13 (2024). https://doi.org/10.1007/s40192-023-00334-2.
[196] C.S. Wu, H.G. Wang, Y.M. Zhang, A new heat source model for keyhole plasma arc welding in FEM analysis of the temperature profile, Welding Journal (Miami, Fla) 85 (2006).
[197] L. Ladani, J. Romano, W. Brindley, S. Burlatsky, Effective liquid conductivity for improved simulation of thermal transport in laser beam melting powder bed technology, Addit. Manuf. 14 (2017) 13–23. https://doi.org/10.1016/j.addma.2016.12.004.
[198] W. Zhou, X. Wang, J. Hu, X. Zhu, Melting process and mechanics on laser sintering of single layer polyamide 6 powder, The International Journal of Advanced Manufacturing Technology 69 (2013) 901–908. https://doi.org/10.1007/s00170-013-5113-8.
[199] M. Bayat, S. Mohanty, J.H. Hattel, A systematic investigation of the effects of process parameters on heat and fluid flow and metallurgical conditions during laser-based powder bed fusion of Ti6Al4V alloy, Int. J. Heat Mass Transf. 139 (2019) 213–230. https://doi.org/10.1016/j.ijheatmasstransfer.2019.05.017.
[200] S. V. Chernyshikhin, D.G. Firsov, I. V. Shishkovsky, Selective Laser Melting of Pre-Alloyed NiTi Powder: Single-Track Study and FE Modeling with Heat Source Calibration, Materials 14 (2021) 7486. https://doi.org/10.3390/ma14237486.
[201] H. Tupac-Yupanqui, A. Armani, Additive Manufacturing of Functional Inconel 718 Parts from Recycled Materials, J. Mater. Eng. Perform. 30 (2021) 1177–1187. https://doi.org/10.1007/s11665-020-05402-8.
[202] J.-N. Zhu, E. Borisov, X. Liang, R. Huizenga, A. Popovich, V. Bliznuk, R. Petrov, M. Hermans, V. Popovich, Controlling microstructure evolution and phase transformation behavior in additive manufacturing of nitinol shape memory alloys by tuning hatch distance, J. Mater. Sci. 57 (2022) 6066–6084. https://doi.org/10.1007/s10853-022-07007-z.

[203] J. Yin, H. Zhu, L. Ke, P. Hu, C. He, H. Zhang, X. Zeng, A finite element model of thermal evolution in laser micro sintering, International Journal of Advanced Manufacturing Technology 83 (2016) 1847–1859. https://doi.org/10.1007/s00170-015-7609-x.
[204] A. Zakirov, S. Belousov, M. Bogdanova, B. Korneev, A. Stepanov, A. Perepelkina, V. Levchenko, A. Meshkov, B. Potapkin, Predictive modeling of laser and electron beam powder bed fusion additive manufacturing of metals at the mesoscale, Addit. Manuf. 35 (2020) 101236. https://doi.org/10.1016/j.addma.2020.101236.
[205] J. Goldak, A. Chakravarti, M. Bibby, A new finite element model for welding heat sources, Metallurgical Transactions B 15 (1984) 299–305. https://doi.org/10.1007/BF02667333.
[206] S. Kollmannsberger, M. Carraturo, A. Reali, F. Auricchio, Accurate Prediction of Melt Pool Shapes in Laser Powder Bed Fusion by the Non-Linear Temperature Equation Including Phase Changes: Model validity: isotropic versus anisotropic conductivity to capture AM Benchmark Test AMB2018-02, Integr. Mater. Manuf. Innov. 8 (2019) 167–177. https://doi.org/10.1007/s40192-019-00132-9.
[207] C. Li, M.F. Gouge, E.R. Denlinger, J.E. Irwin, P. Michaleris, Estimation of part-to-powder heat losses as surface convection in laser powder bed fusion, Addit. Manuf. 26 (2019). https://doi.org/10.1016/j.addma.2019.02.006.
[208] C. Bayraktar, E. Demir, A thermomechanical finite element model and its comparison to inherent strain method for powder-bed fusion process, Addit. Manuf. 54 (2022). https://doi.org/10.1016/j.addma.2022.102708.
[209] G.G. Gladush, I. Smurov, Physics of Laser Materials Processing, Springer Berlin Heidelberg, Berlin, Heidelberg, 2011. https://doi.org/10.1007/978-3-642-19831-1.
[210] D. Sarkar, A. Kapil, A. Sharma, Advances in computational modeling for laser powder bed fusion additive manufacturing: A comprehensive review of finite element techniques and strategies, Addit. Manuf. 85 (2024) 104157. https://doi.org/10.1016/j.addma.2024.104157.
[211] N. Hang, Z. Wang, M. Liu, A novel data-driven dimensional analysis framework for predicting melt pool morphology and porosity evolution in powder bed fusion, J. Mater. Process. Technol. 315 (2023). https://doi.org/10.1016/j.jmatprotec.2023.117929.
[212] L. Meng, B. McWilliams, W. Jarosinski, H.Y. Park, Y.G. Jung, J. Lee, J. Zhang, Machine Learning in Additive Manufacturing: A Review, JOM 72 (2020). https://doi.org/10.1007/s11837-020-04155-y.
[213] Q. Fang, G. Xiong, M. Zhao, T.S. Tamir, Z. Shen, C.-B. Yan, F.-Y. Wang, Probabilistic Data-Driven Modeling of a Melt Pool in Laser Powder Bed Fusion Additive Manufacturing, IEEE Transactions on Automation Science and Engineering 22 (2025) 4908–4925. https://doi.org/10.1109/TASE.2024.3412431.
[214] P. Mercelis, J. Kruth, Residual stresses in selective laser sintering and selective laser melting, Rapid Prototyp. J. 12 (2006) 254–265. https://doi.org/10.1108/13552540610707013.
[215] W.E. King, A.T. Anderson, R.M. Ferencz, N.E. Hodge, C. Kamath, S.A. Khairallah, A.M. Rubenchik, Laser powder bed fusion additive manufacturing of metals; physics, computational, and materials challenges, Appl. Phys. Rev. 2 (2015) 041304. https://doi.org/10.1063/1.4937809.
[216] L.Y. Bahar, R.B. Hetnarski, STATE SPACE AFPROACH TO THERMOELASTICITY, Journal of Thermal Stresses 1 (1978) 135–145. https://doi.org/10.1080/01495737808926936.
[217] Z. Xiao, Y. Qi, C. Chen, X. Nie, J. Wang, H. Zhu, Analytical model of predicting residual stress-process parameter relationship for laser powder bed fusion of Ti6Al4V,

Journal of Materials Research and Technology 35 (2025) 6372–6382. https://doi.org/10.1016/j.jmrt.2025.03.001.
[218] E. Mirkoohi, H.-C. Tran, Y.-L. Lo, Y.-C. Chang, H.-Y. Lin, S.Y. Liang, Analytical Modeling of Residual Stress in Laser Powder Bed Fusion Considering Part's Boundary Condition, Crystals (Basel). 10 (2020) 337. https://doi.org/10.3390/cryst10040337.
[219] W. Woo, D.-K. Kim, Ed.J. Kingston, V. Luzin, F. Salvemini, M.R. Hill, Effect of interlayers and scanning strategies on through-thickness residual stress distributions in additive manufactured ferritic-austenitic steel structure, Materials Science and Engineering: A 744 (2019) 618–629. https://doi.org/10.1016/j.msea.2018.12.078.
[220] S. Liu, A. Kouadri-Henni, A. Gavrus, DP600 dual phase steel thermo-elasto-plastic constitutive model considering strain rate and temperature influence on FEM residual stress analysis of laser welding, J. Manuf. Process. 35 (2018) 407–419. https://doi.org/10.1016/j.jmapro.2018.07.006.
[221] L. Li, Y. Zhang, X. Cui, Z. Said, S. Sharma, M. Liu, T. Gao, Z. Zhou, X. Wang, C. Li, Mechanical behavior and modeling of grinding force: A comparative analysis, J. Manuf. Process. 102 (2023) 921–954. https://doi.org/10.1016/j.jmapro.2023.07.074.
[222] C. Körner, M. Markl, J.A. Koepf, Modeling and Simulation of Microstructure Evolution for Additive Manufacturing of Metals: A Critical Review, Metallurgical and Materials Transactions A 51 (2020) 4970–4983. https://doi.org/10.1007/s11661-020-05946-3.
[223] R. Tavakoli, D. Tourret, Phase-field study of polycrystalline growth and texture selection during melt pool solidification, IOP Conf. Ser. Mater. Sci. Eng. 1281 (2023) 012011. https://doi.org/10.1088/1757-899X/1281/1/012011.
[224] C. Chen, Q. Xia, H. Zhou, J. Zhao, Y. Qin, G. Xiao, Study of the microstructure evolution of alloy structural steel and inhomogeneity effect of the microscale pulsed currents during current-assisted plane strain compressions by modeling a novel cellular automata method, Mater. Charact. 212 (2024) 113983. https://doi.org/10.1016/j.matchar.2024.113983.
[225] M. Bernacki, H. Resk, T. Coupez, R.E. Logé, Finite element model of primary recrystallization in polycrystalline aggregates using a level set framework, Model. Simul. Mat. Sci. Eng. 17 (2009) 064006. https://doi.org/10.1088/0965-0393/17/6/064006.
[226] H. Yang, C. Wu, H. Li, X. Fan, Review on cellular automata simulations of microstructure evolution during metal forming process: Grain coarsening, recrystallization and phase transformation, Sci. China Technol. Sci. 54 (2011) 2107–2118. https://doi.org/10.1007/s11431-011-4464-3.
[227] S. Cummins, P.W. Cleary, G. Delaney, A. Phua, M. Sinnott, D. Gunasegaram, C. Davies, A coupled dem/sph computational model to simulate microstructure evolution in ti-6al-4v laser powder bed fusion processes, Metals (Basel). 11 (2021). https://doi.org/10.3390/met11060858.
[228] O. Zinovieva, A. Zinoviev, O. Gokcekaya, Y. Tang, Large-scale microstructure modelling of an additively manufactured part using cellular automata, IOP Conf. Ser. Mater. Sci. Eng. 1310 (2024) 012005. https://doi.org/10.1088/1757-899X/1310/1/012005.
[229] A. Qadeer, S.S. Akhtar, A.A. Abubakar, A.F.M. Arif, S. Mekid, K.S. Al-Athel, Accelerating Microstructure and Melt Pool Prediction in Laser Powder Bed Fusion Processes Using Data Driven Neural Network, in: Volume 2: Advanced Manufacturing, American Society of Mechanical Engineers, 2024. https://doi.org/10.1115/IMECE2024-145983.
[230] M. Parsazadeh, D. Wu, S. Sharma, S.S. Joshi, M. V. Pantawane, N. Dahotre, A new data-driven framework for prediction of molten pool evolution and lack of fusion defects

in multi-track multi-layer laser powder bed fusion processes, International Journal of Advanced Manufacturing Technology 124 (2023). https://doi.org/10.1007/s00170-022-10550-3.
[231] J. Zhao, Z. Yang, Q. Chen, C. Zhang, J. Zhao, G. Zhang, F. Dong, S. Liu, Real-time detection of powder bed defects in laser powder bed fusion using deep learning on 3D point clouds, Virtual Phys. Prototyp. 20 (2025). https://doi.org/10.1080/17452759.2024.2449171.
[232] M. Mehrpouya, A. Gisario, A. Rahimzadeh, M. Nematollahi, K.S. Baghbaderani, M. Elahinia, A prediction model for finding the optimal laser parameters in additive manufacturing of NiTi shape memory alloy, International Journal of Advanced Manufacturing Technology 105 (2019). https://doi.org/10.1007/s00170-019-04596-z.
[233] B.Y. Benchabane, Y. Belkacemi, M. el A. Belouchrani, H. Kebir, Thermomechanical modelling of residual stresses and distortion in laser powder bed fusion: Assessment of the effect of build plate preheating on the behaviour of Inconel 718, Opt. Laser Technol. 181 (2025) 111641. https://doi.org/10.1016/j.optlastec.2024.111641.
[234] Z.-D. Zhang, O. Ibhadode, S.I. Shahabad, X.-Y. Zhai, D.-Y. Yu, T. Gao, J.-H. Zhu, W.-H. Zhang, High-resolution inherent strain method using actual layer thickness in laser powder bed fusion additive manufacturing with experimental validations, Journal of Materials Research and Technology 30 (2024) 6576–6595. https://doi.org/10.1016/j.jmrt.2024.05.047.
[235] L.-X. Lu, H. Jiang, Q. Bian, W. Shao, L. Li, Y.-W. Zhang, B. Liang, Y. Shi, L. Zhen, Integrated modelling and simulation of NiTi alloy by powder bed fusion: Single track study, Mater. Des. 227 (2023) 111755. https://doi.org/10.1016/j.matdes.2023.111755.
[236] A.M. Rubenchik, W.E. King, S.S. Wu, Scaling laws for the additive manufacturing, J. Mater. Process. Technol. 257 (2018) 234–243. https://doi.org/10.1016/j.jmatprotec.2018.02.034.
[237] P. Promoppatum, S.-C. Yao, P.C. Pistorius, A.D. Rollett, A Comprehensive Comparison of the Analytical and Numerical Prediction of the Thermal History and Solidification Microstructure of Inconel 718 Products Made by Laser Powder-Bed Fusion, Engineering 3 (2017) 685–694. https://doi.org/10.1016/J.ENG.2017.05.023.
[238] H. Hekmatjou, Z. Zeng, J. Shen, J.P. Oliveira, H. Naffakh-Moosavy, A Comparative Study of Analytical Rosenthal, Finite Element, and Experimental Approaches in Laser Welding of AA5456 Alloy, Metals (Basel). 10 (2020) 436. https://doi.org/10.3390/met10040436.
[239] M. Tang, P.C. Pistorius, J.L. Beuth, Prediction of lack-of-fusion porosity for powder bed fusion, Addit. Manuf. 14 (2017) 39–48. https://doi.org/10.1016/j.addma.2016.12.001.
[240] S. Mondal, D. Gwynn, A. Ray, A. Basak, Investigation of Melt Pool Geometry Control in Additive Manufacturing Using Hybrid Modeling, Metals (Basel). 10 (2020) 683. https://doi.org/10.3390/met10050683.
[241] P. Honarmandi, R. Seede, L. Xue, D. Shoukr, P. Morcos, B. Zhang, C. Zhang, A. Elwany, I. Karaman, R. Arroyave, A rigorous test and improvement of the Eagar-Tsai model for melt pool characteristics in laser powder bed fusion additive manufacturing, Addit. Manuf. 47 (2021) 102300. https://doi.org/10.1016/j.addma.2021.102300.
[242] Y. He, M. Zhong, N. Jones, J. Beuth, B. Webler, The Columnar-to-Equiaxed Transition in Melt Pools During Laser Powder Bed Fusion of M2 Steel, Metallurgical and Materials Transactions A 52 (2021) 4206–4221. https://doi.org/10.1007/s11661-021-06380-9.
[243] M. Ranaiefar, P. Honarmandi, L. Xue, C. Zhang, A. Elwany, I. Karaman, E.J. Schwalbach, R. Arroyave, A differential evaporation model to predict chemistry change

of additively manufactured metals, Mater. Des. 213 (2022) 110328. https://doi.org/10.1016/j.matdes.2021.110328.
[244] S. Sheikh, B. Vela, V. Attari, X. Huang, P. Morcos, J. Hanagan, C. Acemi, I. Karaman, A. Elwany, R. Arroyave´, Exploring chemistry and additive manufacturing design spaces: a perspective on computationally-guided design of printable alloys, Mater. Res. Lett. 12 (2024) 235–263. https://doi.org/10.1080/21663831.2024.2316204.
[245] J. Walker, M. Elahinia, C. Haberland, An Investigation of Process Parameters on Selective Laser Melting of Nitinol, in: Volume 1: Development and Characterization of Multifunctional Materials; Modeling, Simulation and Control of Adaptive Systems; Integrated System Design and Implementation, American Society of Mechanical Engineers, 2013. https://doi.org/10.1115/SMASIS2013-3074.
[246] M.A. Obeidi, Achieving high quality nitinol parts with minimised input thermal energy by optimised pulse wave laser powder bed fusion process, Results in Materials 14 (2022) 100279. https://doi.org/10.1016/j.rinma.2022.100279.
[247] E.M. Sequeda Leon, S. Singamneni, T. Guraya, Z.W. Chen, Effect of laser power in laser powder bed fusion on Ni content and structure of Nitinol, Mater. Today Proc. (2023). https://doi.org/10.1016/j.matpr.2023.05.678.
[248] D. Bourke, K.T. Selvam, M.A. Obeidi, I.U. Ahad, D. Brabazon, Effect of powder and process parameters on in-situ alloying of nitinol during laser powder bed fusion, Journal of Materials Research and Technology 30 (2024) 7988–7997. https://doi.org/10.1016/j.jmrt.2024.05.178.
[249] I. Yadroitsev, P. Krakhmalev, I. Yadroitsava, S. Johansson, I. Smurov, Energy input effect on morphology and microstructure of selective laser melting single track from metallic powder, J. Mater. Process. Technol. 213 (2013) 606–613. https://doi.org/10.1016/j.jmatprotec.2012.11.014.
[250] I. McCue, C. Peitsch, T. Montalbano, A. Lennon, J. Sopcisak, M.M. Trexler, S. Storck, Scalable laser powder bed fusion processing of nitinol shape memory alloy, MRS Commun. 9 (2019) 1214–1220. https://doi.org/10.1557/mrc.2019.134.
[251] R.P. PARIDA, V. SENTHILKUMAR, Analytical Analysis and Experimental Validation of the Effects of Process Parameters on Meltpool Size During the Selective Laser Melting (SLM) of Inconel 718., Lasers in Engineering (Old City Publishing) 49 (2021) 85–105. https://search.ebscohost.com/login.aspx?direct=true&db=a9h&AN=151579336&site=eds-live.
[252] L.E. Criales, Y.M. Arısoy, B. Lane, S. Moylan, A. Donmez, T. Özel, Laser powder bed fusion of nickel alloy 625: Experimental investigations of effects of process parameters on melt pool size and shape with spatter analysis, Int. J. Mach. Tools Manuf. 121 (2017) 22–36. https://doi.org/10.1016/j.ijmachtools.2017.03.004.
[253] J. Metelkova, Y. Kinds, K. Kempen, C. de Formanoir, A. Witvrouw, B. Van Hooreweder, On the influence of laser defocusing in Selective Laser Melting of 316L, Addit. Manuf. 23 (2018) 161–169. https://doi.org/10.1016/j.addma.2018.08.006.
[254] B. Lane, J. Heigel, R. Ricker, I. Zhirnov, V. Khromschenko, J. Weaver, T. Phan, M. Stoudt, S. Mekhontsev, L. Levine, Measurements of Melt Pool Geometry and Cooling Rates of Individual Laser Traces on IN625 Bare Plates, Integr. Mater. Manuf. Innov. 9 (2020) 16–30. https://doi.org/10.1007/s40192-020-00169-1.
[255] Z.R. Francis, The Effects of Laser and Electron Beam Spot Size in Additive Manufacturing Processes, Carnegie Mellon University, 2017.
[256] J. Harbig, D.L. Wenzler, S. Baehr, M.K. Kick, H. Merschroth, A. Wimmer, M. Weigold, M.F. Zaeh, Methodology to Determine Melt Pool Anomalies in Powder Bed Fusion of

Metals Using a Laser Beam by Means of Process Monitoring and Sensor Data Fusion, Materials 15 (2022) 1265. https://doi.org/10.3390/ma15031265.
[257] T. Yue, Z. Zou, S. Zhang, H. Liu, Q. Chen, W. Wen, Y. Zang, Effects of volumetric energy density on melting modes, printability, microstructures, and mechanical properties of laser powder bed fusion (L-PBF) printed pure nickel, Materials Science and Engineering: A 909 (2024) 146871. https://doi.org/10.1016/j.msea.2024.146871.
[258] M. Afrasiabi, D. Keller, C. Lüthi, M. Bambach, K. Wegener, Effect of Process Parameters on Melt Pool Geometry in Laser Powder Bed Fusion of Metals: A Numerical Investigation, Procedia CIRP 113 (2022) 378–384. https://doi.org/10.1016/j.procir.2022.09.187.
[259] L. Johnson, M. Mahmoudi, B. Zhang, R. Seede, X. Huang, J.T. Maier, H.J. Maier, I. Karaman, A. Elwany, R. Arróyave, Assessing printability maps in additive manufacturing of metal alloys, Acta Mater. 176 (2019) 199–210. https://doi.org/10.1016/j.actamat.2019.07.005.
[260] T.R. Watkins, K.A. Unocic, A. Peralta, M. Megahed, J.R. Bunn, C.M. Fancher, C.R. D'Elia, M.R. Hill, J.F. Neumann, Residual stresses and microstructure within Allvac 718Plus laser powder bed fusion bars, Addit. Manuf. 47 (2021) 102334. https://doi.org/10.1016/j.addma.2021.102334.
[261] H. Xiao, X. Liu, W. Xiao, J. Yang, C. Li, Y. Li, L. Song, Influence of molten-pool cooling rate on solidification structure and mechanical property of laser additive manufactured Inconel 718, Journal of Materials Research and Technology 19 (2022) 4404–4416. https://doi.org/10.1016/j.jmrt.2022.06.162.
[262] J. Wang, R. Zhu, Y. Liu, L. Zhang, Understanding melt pool characteristics in laser powder bed fusion: An overview of single- and multi-track melt pools for process optimization, Advanced Powder Materials 2 (2023) 100137. https://doi.org/10.1016/j.apmate.2023.100137.
[263] S. Afazov, A. Roberts, L. Wright, P. Jadhav, A. Holloway, H. Basoalto, K. Milne, N. Brierley, Metal powder bed fusion process chains: an overview of modelling techniques, Progress in Additive Manufacturing 7 (2022) 289–314. https://doi.org/10.1007/s40964-021-00230-1.
[264] Y. Wang, X. Ji, S.Y. Liang, Analytical modeling of temperature distribution in laser powder bed fusion with different scan strategies, Opt. Laser Technol. 157 (2023) 108708. https://doi.org/10.1016/j.optlastec.2022.108708.
[265] X. Li, N. Polydorides, Time-efficient surrogate models of thermal modeling in laser powder bed fusion, Addit. Manuf. 59 (2022) 103122. https://doi.org/10.1016/j.addma.2022.103122.
[266] U. Kizhakkinan, P.L.T. Duong, R. Laskowski, G. Vastola, D.W. Rosen, N. Raghavan, Development of a surrogate model for high-fidelity laser powder-bed fusion using tensor train and gaussian process regression, J. Intell. Manuf. 34 (2023) 369–385. https://doi.org/10.1007/s10845-022-02038-4.
[267] J. Grose, A. Liao, C.S. Foong, M. Cullinan, Data-Efficient Surrogate Model for Rapid Prediction of Temperature Evolution in a Microscale Selective Laser Sintering System, J. Micro Nanomanuf. 11 (2023). https://doi.org/10.1115/1.4064106.
[268] S. Rangaswamy, C. Rubio, M.C.C. Monu, M.N. Doğu, D. Brabazon, Review of the laser powder bed fusion of nitinol: Defect formation and prediction, Mater. Today Adv. 30 (2026) 100771. https://doi.org/10.1016/j.mtadv.2026.100771.
[269] Y. Du, T. Mukherjee, T. DebRoy, Physics-informed machine learning and mechanistic modeling of additive manufacturing to reduce defects, Appl. Mater. Today 24 (2021) 101123. https://doi.org/10.1016/j.apmt.2021.101123.

[270] M.S. Rahman, N.S. Sattar, R.U. Ahmed, J. Ciaccio, U.K. Chakravarty, A Machine Learning Framework for Melt-Pool Geometry Prediction and Process Parameter Optimization in the Laser Powder-Bed Fusion Process, J. Eng. Mater. Technol. 146 (2024). https://doi.org/10.1115/1.4065687.
[271] M. Mahmoudi, G. Tapia, B. Franco, J. Ma, R. Arroyave, I. Karaman, A. Elwany, On the printability and transformation behavior of nickel-titanium shape memory alloys fabricated using laser powder-bed fusion additive manufacturing, J. Manuf. Process. 35 (2018) 672–680. https://doi.org/10.1016/j.jmapro.2018.08.037.
[272] C. Teng, H. Gong, A. Szabo, J.J.S. Dilip, K. Ashby, S. Zhang, N. Patil, D. Pal, B. Stucker, Simulating Melt Pool Shape and Lack of Fusion Porosity for Selective Laser Melting of Cobalt Chromium Components, J. Manuf. Sci. Eng. 139 (2017). https://doi.org/10.1115/1.4034137.
[273] S.A. Khairallah, A.T. Anderson, A. Rubenchik, W.E. King, Laser powder-bed fusion additive manufacturing: Physics of complex melt flow and formation mechanisms of pores, spatter, and denudation zones, Acta Mater. 108 (2016) 36–45. https://doi.org/10.1016/j.actamat.2016.02.014.
[274] L. Thijs, F. Verhaeghe, T. Craeghs, J. Van Humbeeck, J.-P. Kruth, A study of the microstructural evolution during selective laser melting of Ti–6Al–4V, Acta Mater. 58 (2010) 3303–3312. https://doi.org/10.1016/j.actamat.2010.02.004.
[275] M.J. Matthews, G. Guss, S.A. Khairallah, A.M. Rubenchik, P.J. Depond, W.E. King, Denudation of metal powder layers in laser powder bed fusion processes, Acta Mater. 114 (2016) 33–42. https://doi.org/10.1016/j.actamat.2016.05.017.
[276] M.M. Rosli, A. Rachini, M.K. Mahmood, Data-Driven Melt Pool Monitoring and Defect Prediction in LPBF of Ti-6Al-4V Alloy, Babylonian Journal of Mechanical Engineering 2025 (2025) 51–67. https://doi.org/10.58496/BJME/2025/004.
[277] Y.S. Lee, W. Zhang, Modeling of heat transfer, fluid flow and solidification microstructure of nickel-base superalloy fabricated by laser powder bed fusion, Addit. Manuf. 12 (2016) 178–188. https://doi.org/10.1016/j.addma.2016.05.003.
[278] M. Salem, S. Le Roux, A. Hor, G. Dour, A new insight on the analysis of residual stresses related distortions in selective laser melting of Ti-6Al-4V using the improved bridge curvature method, Addit. Manuf. 36 (2020) 101586. https://doi.org/10.1016/j.addma.2020.101586.
[279] J. GUO, H. FU, B. PAN, R. KANG, Recent progress of residual stress measurement methods: A review, Chinese Journal of Aeronautics 34 (2021) 54–78. https://doi.org/10.1016/j.cja.2019.10.010.
[280] A.E. Díaz-Mendoza, G. Capilla-González, I. Martínez-Ramírez, M.E. Gutiérrez-Rivera, D. Díaz-Infante, I. Ruíz-López, Experimental and numerical analysis of the residual stress distribution in a three-point bending test of a TRIP sheet by using ESPI, Journal of the Brazilian Society of Mechanical Sciences and Engineering 42 (2020) 544. https://doi.org/10.1007/s40430-020-02640-8.
[281] X. Li, J. Liu, H. Wu, K. Miao, H. Wu, R. Li, C. Liu, W. Fang, G. Fan, Research progress of residual stress measurement methods, Heliyon 10 (2024) e28348. https://doi.org/10.1016/j.heliyon.2024.e28348.
[282] S. Ao, C. Li, Y. Huang, Z. Luo, Determination of residual stress in resistance spot-welded joint by a novel X-ray diffraction, Measurement 161 (2020) 107892. https://doi.org/10.1016/j.measurement.2020.107892.
[283] S. Marola, S. Bosia, A. Veltro, G. Fiore, D. Manfredi, M. Lombardi, G. Amato, M. Baricco, L. Battezzati, Residual stresses in additively manufactured AlSi10Mg: Raman spectroscopy and X-ray diffraction analysis, Mater. Des. 202 (2021) 109550. https://doi.org/10.1016/j.matdes.2021.109550.

[284] S. CHEN, B. SHEN, J. ZHANG, L. WANG, F. SUN, Evaluation on residual stresses of silicon-doped CVD diamond films using X-ray diffraction and Raman spectroscopy, Transactions of Nonferrous Metals Society of China 22 (2012) 3021–3026. https://doi.org/10.1016/S1003-6326(11)61565-3.
[285] Q. Luo, A modified X-ray diffraction method to measure residual normal and shear stresses of machined surfaces, The International Journal of Advanced Manufacturing Technology 119 (2022) 3595–3606. https://doi.org/10.1007/s00170-021-08645-4.
[286] O. Muwafaq Mohmmed Ali, R. Hamid Mohammed Al-Kalali, E. Mohamed Mahdi Mubarak, Vibrational Analysis of Composite Beam Embedded with Nitinol Shape Memory Alloy Wires, International Journal of Engineering & Technology 7 (2018) 143. https://doi.org/10.14419/ijet.v7i3.4.16763.
[287] C.G. McKenna, T.J. Vaughan, A finite element investigation on design parameters of bare and polymer-covered self-expanding wire braided stents, J. Mech. Behav. Biomed. Mater. 115 (2021) 104305. https://doi.org/10.1016/j.jmbbm.2020.104305.
[288] M. Braun, T. Chen, J. Shen, H. Fassmer, B. Klusemann, S. Sheikhi, S. Ehlers, E. Müller, A. Sarmast, J. Schubnell, Fatigue crack initiation and propagation in plain and notched PBF-LB/M, WAAM, and wrought 316L stainless steel specimens, Mater. Des. 244 (2024) 113122. https://doi.org/10.1016/j.matdes.2024.113122.
[289] M. Fan, C. Chen, H. Xuan, H. Qin, M. Qu, S. Shi, Z. Bi, W. Hong, Effect of Residual Stress Induced by Different Cooling Methods in Heat Treatment on the Fatigue Crack Propagation Behaviour of GH4169 Disc, Materials 15 (2022) 5228. https://doi.org/10.3390/ma15155228.
[290] S. Moritz, T. Schwanekamp, M. Reuber, J. Lentz, J. Boes, S. Weber, Impact of in Situ Heat Treatment Effects during Laser-Based Powder Bed Fusion of 1.3343 High-Speed Steel with Preheating Temperatures up to 700 °C, Steel Res. Int. 94 (2023). https://doi.org/10.1002/srin.202200775.
[291] D.N. Luu, W. Zhou, S.M.L. Nai, Mitigation of liquation cracking in selective laser melted Inconel 718 through optimization of layer thickness and laser energy density, J. Mater. Process. Technol. 299 (2022) 117374. https://doi.org/10.1016/j.jmatprotec.2021.117374.
[292] V. Praveen Kumar, A. Vinoth Jebaraj, Microscale investigations on additively manufactured Inconel 718: influence of volumetric energy density on microstructure, texture evolution, defects control and residual stress, Applied Physics A 129 (2023) 370. https://doi.org/10.1007/s00339-023-06642-w.
[293] D.N. Croft, Effects of heat treatment, in: Heat Treatment of Welded Steel Structures, Elsevier, 1996: pp. 21–47. https://doi.org/10.1533/9781845698812.21.
[294] L. Mugwagwa, I. Yadroitsev, S. Matope, Effect of Process Parameters on Residual Stresses, Distortions, and Porosity in Selective Laser Melting of Maraging Steel 300, Metals (Basel). 9 (2019) 1042. https://doi.org/10.3390/met9101042.
[295] A. Sharif, N. Farid, R.K. Vijayaraghavan, P.J. McNally, G.M. O'Connor, Femtosecond Laser Assisted Crystallization of Gold Thin Films, Nanomaterials 11 (2021) 1186. https://doi.org/10.3390/nano11051186.
[296] S. Zhang, Y. Lei, Z. Chen, P. Wei, W. Liu, S. Yao, B. Lu, Effect of Laser Energy Density on the Microstructure and Texture Evolution of Hastelloy-X Alloy Fabricated by Laser Powder Bed Fusion, Materials 14 (2021) 4305. https://doi.org/10.3390/ma14154305.
[297] V.P. Kumar, A.V. Jebaraj, Attainment of favorable microstructure for residual stress reduction through high-temperature heat treatment on additive manufactured inconel 718 alloy, The International Journal of Advanced Manufacturing Technology 121 (2022) 4455–4472. https://doi.org/10.1007/s00170-022-09640-z.

[298] Z. Lin, Y. Zhou, S. Zuo, X. Cai, K. Feng, K. Wang, H. Wei, F. Xiao, X. Jin, Controlling the crystal texture and microstructure of NiTi alloy by adjusting the thermal gradient of laser powder bed melting, Materials Science and Engineering: A 912 (2024) 146970. https://doi.org/10.1016/j.msea.2024.146970.
[299] J.C. Chekotu, S. Kumar S, G. Degli-Alessandrini, M.Z. Mughal, R. Goodall, D. Kinahan, D. Brabazon, Formation of β-Ti phase during L-PBF processing of martensitic NiTi, Mater. Today Commun. 36 (2023) 106668. https://doi.org/10.1016/j.mtcomm.2023.106668.
[300] M.A. Obeidi, M. Monu, C. Hughes, D. Bourke, M.N. Dogu, J. Francis, M. Zhang, I.U. Ahad, D. Brabazon, Laser beam powder bed fusion of nitinol shape memory alloy (SMA), Journal of Materials Research and Technology 14 (2021) 2554–2570. https://doi.org/10.1016/j.jmrt.2021.07.126.
[301] F. Trevisan, F. Calignano, A. Aversa, G. Marchese, M. Lombardi, S. Biamino, D. Ugues, D. Manfredi, Additive manufacturing of titanium alloys in the biomedical field: processes, properties and applications, J. Appl. Biomater. Funct. Mater. 16 (2018) 57–67. https://doi.org/10.5301/jabfm.5000371.
[302] N. Ahmed, I. Barsoum, R.K. Abu Al-Rub, Numerical Investigation on the Effect of Residual Stresses on the Effective Mechanical Properties of 3D-Printed TPMS Lattices, Metals (Basel). 12 (2022) 1344. https://doi.org/10.3390/met12081344.
[303] M. Liu, L. Hu, X. Kang, Y. Zhang, X. Liu, L. Xu, Y. Han, Deformation mechanism of defect-free Ni50Ti50 alloys via laser powder bed fusion, J. Mater. Sci. Technol. 225 (2025) 111–124. https://doi.org/10.1016/j.jmst.2024.10.051.
[304] S. Li, H. Hassanin, M.M. Attallah, N.J.E. Adkins, K. Essa, The development of TiNi-based negative Poisson's ratio structure using selective laser melting, Acta Mater. 105 (2016) 75–83. https://doi.org/10.1016/j.actamat.2015.12.017.
[305] A.L. Vyatskikh, X. Wang, J. Haley, B. Zheng, L. Valdevit, E.J. Lavernia, J.M. Schoenung, Residual stress mitigation in directed energy deposition, Materials Science and Engineering: A 871 (2023) 144845. https://doi.org/10.1016/j.msea.2023.144845.
[306] T. Simson, A. Emmel, A. Dwars, J. Böhm, Residual stress measurements on AISI 316L samples manufactured by selective laser melting, Addit. Manuf. 17 (2017) 183–189. https://doi.org/10.1016/j.addma.2017.07.007.
[307] M. Narvan, A. Ghasemi, E. Fereiduni, S. Kendrish, M. Elbestawi, Part deflection and residual stresses in laser powder bed fusion of H13 tool steel, Mater. Des. 204 (2021) 109659. https://doi.org/10.1016/j.matdes.2021.109659.
[308] L. Mugwagwa, I. Yadroitsava, N.W. Makoana, I. Yadroitsev, Residual stress in laser powder bed fusion, in: Fundamentals of Laser Powder Bed Fusion of Metals, Elsevier, 2021: pp. 245–276. https://doi.org/10.1016/B978-0-12-824090-8.00014-7.
[309] B. Vrancken, V. Cain, R. Knutsen, J. Van Humbeeck, Residual stress via the contour method in compact tension specimens produced via selective laser melting, Scr. Mater. 87 (2014) 29–32. https://doi.org/10.1016/j.scriptamat.2014.05.016.
[310] M. Yakout, M.A. Elbestawi, S.C. Veldhuis, A study of the relationship between thermal expansion and residual stresses in selective laser melting of Ti-6Al-4V, J. Manuf. Process. 52 (2020) 181–192. https://doi.org/10.1016/j.jmapro.2020.01.039.
[311] B. Kavas, L. Witte, E.C. Balta, M.R. Tucker, M. Afrasiabi, M. Bambach, Physics-aware feedforward dwell time adjustment for mitigating distortion in additively manufactured cantilevers, Progress in Additive Manufacturing 10 (2025) 10961–10977. https://doi.org/10.1007/s40964-025-01270-7.
[312] N.T. Andani, S. Mohajerani, A. Behvar, K. Safaei, A. Celebi, M. Elahinia, Exploring the Impact of Scan Strategies on the Superelastic Behavior of NiTi Alloys Fabricated by

Laser Powder Bed Fusion, Shape Memory and Superelasticity 12 (2026) 46–62. https://doi.org/10.1007/s40830-025-00572-7.
[313] I. Hatos, Improvement of the cantilever test geometry deflection measurement method to assess residual stresses in laser powder bed fusion, Production Engineering Archives 31 (2025) 474–480. https://doi.org/10.30657/pea.2025.31.44.
[314] J.C. Chekotu, R. Goodall, D. Kinahan, D. Brabazon, Control of Ni-Ti phase structure, solid-state transformation temperatures and enthalpies via control of L-PBF process parameters, Mater. Des. 218 (2022) 110715. https://doi.org/10.1016/j.matdes.2022.110715.
[315] M.C.C. Monu, S. Kumar S., D. Brabazon, Heat treatment of NiTi alloys: Influence of volumetric energy density on ageing parameters and the resulting physical properties, Journal of Materials Research and Technology 26 (2023) 9532–9555. https://doi.org/10.1016/j.jmrt.2023.09.251.
[316] C. Tan, S. Li, K. Essa, P. Jamshidi, K. Zhou, W. Ma, M.M. Attallah, Laser Powder Bed Fusion of Ti-rich TiNi lattice structures: Process optimisation, geometrical integrity, and phase transformations, Int. J. Mach. Tools Manuf. 141 (2019) 19–29. https://doi.org/10.1016/j.ijmachtools.2019.04.002.
[317] S. Wei, J. Zhang, L. Zhang, Y. Zhang, B. Song, X. Wang, J. Fan, Q. Liu, Y. Shi, Laser powder bed fusion additive manufacturing of NiTi shape memory alloys: a review, International Journal of Extreme Manufacturing 5 (2023) 032001. https://doi.org/10.1088/2631-7990/acc7d9.
[318] J.C. Chekotu, G. Degli-Alessandrini, M.Z. Mughal, S. Chatterjee, R. Goodall, D. Kinahan, D. Brabazon, Control of mechanical and shape memory characteristics in martensitic NiTi by setting L-PBF parameters and build orientation, Journal of Materials Research and Technology 25 (2023) 6407–6431. https://doi.org/10.1016/j.jmrt.2023.07.092.
[319] Y. Yang, S. Bharech, N. Finger, X. Zhou, J. Schröder, B.-X. Xu, Elasto-plastic residual stress analysis of selective laser sintered porous materials based on 3D-multilayer thermo-structural phase-field simulations, NPJ Comput. Mater. 10 (2024) 117. https://doi.org/10.1038/s41524-024-01296-5.
[320] Z. Yan, J.-N. Zhu, E. Borisov, T. Riemslag, S.P. Scott, M. Hermans, J. Jovanova, V. Popovich, Superelastic response and damping behavior of additively manufactured Nitinol architectured materials, Addit. Manuf. 68 (2023) 103505. https://doi.org/10.1016/j.addma.2023.103505.
[321] S. Qiu, B. Clausen, S.A. Padula, R.D. Noebe, R. Vaidyanathan, On elastic moduli and elastic anisotropy in polycrystalline martensitic NiTi, Acta Mater. 59 (2011) 5055–5066. https://doi.org/10.1016/j.actamat.2011.04.018.
[322] H. Sehitoglu, I. Karaman, X. Zhang, A. Viswanath, Y. Chumlyakov, H.J. Maier, Strain–temperature behavior of NiTiCu shape memory single crystals, Acta Mater. 49 (2001) 3621–3634. https://doi.org/10.1016/S1359-6454(01)00192-6.

Declaration of Authorship for PhD by Publication

Section 1: Candidate's Details	
Candidate's Name	Sampreet Rangaswamy
DCU Student Number	22269710
School	School of Mechanical and Manufacturing Engineering
Principal Supervisor	Prof. Dermot Brabazon
Title of PhD by Publication Thesis	Multiscale, Multiphysics, and Data-Driven Modelling of the Laser Powder Bed Fusion Processing of Nitinol Shape Memory Alloy
Section 2: Paper Details	
Title of co-authored paper included in the thesis under examination	Review of the Laser Powder Bed Fusion of Nitinol: Defect Formation and Prediction
List of authors as in order given on accepted/published version	Sampreet Rangaswamy, Camille Rubio, Merve Nur Doğu, Medad C.C. Monu, Dermot Brabazon
Publication Details (e.g. Year of Publication, Journal Name, Issue Number, Page Numbers, Place of Publication, DOI, ISSN, URL etc.)	2026, Materials Today Advances https://doi.org/10.1016/j.mtadv.2026.100771
Publication Status (e.g. Published, Accepted)	Published
Provide a brief statement here on the disciplinary ranking of this publication and the peer-review process involved (e.g. how many reviewers, single blinded or other, initial decision, revision timeline etc and any other details that speak to the rigour of the peer review process)	3 reviewers, single blinded, minor revision, 2 months.
This paper (Chapter 2) is one of 5 co-authored papers to be submitted as part of the PhD by publication thesis submitted for examination.	
Section 3: Candidate's Contribution to the Paper	
Provide details below of the **nature** and **extent of your contribution** to the paper (include both your intellectual and practical contributions) and your overall contribution in **percentage terms**. Note that these categories can be customised according to disciplinary norms Briefly outline your contribution to the **conception** of the work described in this paper: I conceptualised the idea of writing the review article along with Prof. Dermot Brabazon.	

Briefly outline your contribution to the **literature review** in this paper:
I conducted most of the literature review with the help of other co-authors.

Briefly outline your contribution to the **methodological design**:
I designed the methodology described in the paper.

Briefly outline your contribution to **data collection**:
I collected most of the data from the required for the review paper.

Briefly outline your contribution to **data analysis**:
Most of the analysis of the collected data was performed by me by using different tools and coding.

Briefly outline your contribution to the **synthesis and summary of findings**:
I summarised and synthesised the reviewed literature to systematically present it in the paper.

Finally, outline your contribution to the **writing** and **revision** of the paper:
I contributed significantly to the writing and revision of the review paper along with the support from the co-authors.

Section 4: Signature and Validation

I confirm that the following statements are true:

(a) the information I have provided in this form is correct
(b) this paper is based on research undertaken during my candidature at DCU

Signature of PhD Candidate: ____Sampreet Rangaswamy____ **Date:**_01/08/2026_

I confirm that the information provided by the candidate is correct:

Signature of Principal Supervisor: Dermot Brabazon **Date:** _01/08/2026_

In some cases, it may be appropriate for verification to be given by both the principal supervisor **and** the lead/corresponding author of the work (where the lead/corresponding author of the work is not the candidate or the principal supervisor):

Signature of Lead/Corresponding Author Sampreet Rangaswamy **Date:** _01/08/2026_

Nature of Current Post/Responsibilities: _____PhD Researcher_____
Home institution: ___Dublin City University___

Section 1: Candidate's Details	
Candidate's Name	Sampreet Rangaswamy
DCU Student Number	22269710
School	School of Mechanical and Manufacturing Engineering
Principal Supervisor	Prof. Dermot Brabazon
Title of PhD by Publication Thesis	Multiscale, Multiphysics, and Data-Driven Modelling of the Laser Powder Bed Fusion Processing of Nitinol Shape Memory Alloy
Section 2: Paper Details	
Title of co-authored paper included in the thesis under examination	Investigating Melt Pool Dimensions in Laser Powder Bed Fusion of Nitinol: An Analytical Approach
List of authors as in order given on accepted/published version	Sampreet Rangaswamy, Declan Bourke, Medad C. C. Monu, Paul Healy, Hengfeng Gu, Inam Ul Ahad, and Dermot Brabazon
Publication Details (e.g. Year of Publication, Journal Name, Issue Number, Page Numbers, Place of Publication, DOI, ISSN, URL etc.)	2024, Advanced Engineering Materials 26 https://doi.org/10.1002/adem.202401636
Publication Status (e.g. Published, Accepted)	Published
Provide a brief statement here on the disciplinary ranking of this publication and the peer-review process involved (e.g. how many reviewers, single blinded or other, initial decision, revision timeline etc and any other details that speak to the rigour of the peer review process)	3 reviewers, single blinded, major revision, 3 months.

This paper (Chapter 3) is one of 5 co-authored papers to be submitted as part of the PhD by publication thesis submitted for examination.

Section 3: Candidate's Contribution to the Paper

Provide details below of the **nature** and **extent of your contribution** to the paper (include both your intellectual and practical contributions) and your overall contribution in **percentage terms**. Note that these categories can be customised according to disciplinary norms

Briefly outline your contribution to the **conception** of the work described in this paper:
I conceptualised the idea of using the analytical models suggested by the industrial partner along with Prof. Dermot Brabazon.

Briefly outline your contribution to the **literature review** in this paper:
I reviewed the literature and decided on the models to be used in the research.

Briefly outline your contribution to the **methodological design**:
I designed the methodology presented in the paper.

Briefly outline your contribution to **data collection**:
I collected the required data with the help of co-authors of the paper.

Briefly outline your contribution to **data analysis**:
I performed majority of the data analysis for the research.

Briefly outline your contribution to the **synthesis and summary of findings**:
I synthesised and summarised the data and presented properly in the paper.

Finally, outline your contribution to the **writing** and **revision** of the paper:
I contributed significantly to the writing and revision of the manuscript before submission and after peer-review.

Section 4: Signature and Validation

I confirm that the following statements are true:

(a) the information I have provided in this form is correct
(b) this paper is based on research undertaken during my candidature at DCU

Signature of PhD Candidate: ____Sampreet Rangaswamy____ **Date:**_01/08/2026_

I confirm that the information provided by the candidate is correct:

Signature of Principal Supervisor: Dermot Brabazon **Date:** _01/08/2026_

In some cases, it may be appropriate for verification to be given by both the principal supervisor **and** the lead/corresponding author of the work (where the lead/corresponding author of the work is not the candidate or the principal supervisor):

Signature of Lead/Corresponding Author Sampreet Rangaswamy **Date:** _01/08/2026_

Nature of Current Post/Responsibilities: _____PhD Researcher_____
Home institution: ___Dublin City University___

Section 1: Candidate's Details	
Candidate's Name	Sampreet Rangaswamy
DCU Student Number	22269710
School	School of Mechanical and Manufacturing Engineering
Principal Supervisor	Prof. Dermot Brabazon
Title of PhD by Publication Thesis	Multiscale, Multiphysics, and Data-Driven Modelling of the Laser Powder Bed Fusion Processing of Nitinol Shape Memory Alloy
Section 2: Paper Details	
Title of co-authored paper included in the thesis under examination	Physics-Guided Digital Twin Framework for Melt Pool Prediction and Stability in Laser Powder Bed Fusion of Nitinol.
List of authors as in order given on accepted/published version	Sampreet Rangaswamy, Merve Nur Doğu, Camille Rubio, Hengfeng Gu, Abdul Khader Khan, Chong Teng, Inam Ul Ahad, Dermot Brabazon
Publication Details (e.g. Year of Publication, Journal Name, Issue Number, Page Numbers, Place of Publication, DOI, ISSN, URL etc.)	2026, Materials
Publication Status (e.g. Published, Accepted)	Review Completed
Provide a brief statement here on the disciplinary ranking of this publication and the peer-review process involved (e.g. how many reviewers, single blinded or other, initial decision, revision timeline etc and any other details that speak to the rigour of the peer review process)	2 reviewers, single blinded, major revision, 1 month.

This paper (Chapter 4) is one of 5 co-authored papers to be submitted as part of the PhD by publication thesis submitted for examination.

Section 3: Candidate's Contribution to the Paper

Provide details below of the **nature** and **extent of your contribution** to the paper (include both your intellectual and practical contributions) and your overall contribution in **percentage terms**. Note that these categories can be customised according to disciplinary norms

Briefly outline your contribution to the **conception** of the work described in this paper:
I conceptualised the development of the digital twin for NiTi proposed in the paperx along with Prof. Dermot Brabazon.

Briefly outline your contribution to the **literature review** in this paper:
I conducted the literature review required for the research.

Briefly outline your contribution to the **methodological design**:
I performed and designed the experimental, modelling, simulation and machine learning methodologies.

Briefly outline your contribution to **data collection**:
I collected most of the experimental and modelling data necessary for the digital twin.

Briefly outline your contribution to **data analysis**:
I analysed the collected data using software tools and coding.

Briefly outline your contribution to the **synthesis and summary of findings**:
I summarised the findings appropriately for a wide audience.

Finally, outline your contribution to the **writing** and **revision** of the paper:
I wrote and revised majority of the manuscript.

Section 4: Signature and Validation

I confirm that the following statements are true:

(a) the information I have provided in this form is correct
(b) this paper is based on research undertaken during my candidature at DCU

Signature of PhD Candidate: ____Sampreet Rangaswamy____ **Date:**_01/08/2026_

I confirm that the information provided by the candidate is correct:

Signature of Principal Supervisor: Dermot Brabazon **Date:** _01/08/2026_

In some cases, it may be appropriate for verification to be given by both the principal supervisor **and** the lead/corresponding author of the work (where the lead/corresponding author of the work is not the candidate or the principal supervisor):

Signature of Lead/Corresponding Author Sampreet Rangaswamy **Date:** _01/08/2026_

Nature of Current Post/Responsibilities: _____PhD Researcher_____
Home institution: ___Dublin City University___

Section 1: Candidate's Details	
Candidate's Name	Sampreet Rangaswamy
DCU Student Number	22269710
School	School of Mechanical and Manufacturing Engineering
Principal Supervisor	Prof. Dermot Brabazon
Title of PhD by Publication Thesis	Multiscale, Multiphysics, and Data-Driven Modelling of the Laser Powder Bed Fusion Processing of Nitinol Shape Memory Alloy
Section 2: Paper Details	
Title of co-authored paper included in the thesis under examination	Evaluating Residual Stress in Additively Manufactured Nitinol Shape Memory Alloy
List of authors as in order given on accepted/published version	Sampreet Rangaswamy, Josiah Cherian Chekotu, Thomas Gillick, Cian Hughes, Jayne Nicholl, David Easton, Caner Şimşir, Dermot Brabazon
Publication Details (e.g. Year of Publication, Journal Name, Issue Number, Page Numbers, Place of Publication, DOI, ISSN, URL etc.)	2025, npj Advanced Manufacturing 2 https://doi.org/10.1038/s44334-025-00027-y
Publication Status (e.g. Published, Accepted)	Published
Provide a brief statement here on the disciplinary ranking of this publication and the peer-review process involved (e.g. how many reviewers, single blinded or other, initial decision, revision timeline etc and any other details that speak to the rigour of the peer review process)	3 reviewers, single blinded, major revision, 4 months.

This paper (Chapter 5) is one of 5 co-authored papers to be submitted as part of the PhD by publication thesis submitted for examination.

Section 3: Candidate's Contribution to the Paper

Provide details below of the **nature** and **extent of your contribution** to the paper (include both your intellectual and practical contributions) and your overall contribution in **percentage terms**. Note that these categories can be customised according to disciplinary norms

Briefly outline your contribution to the **conception** of the work described in this paper:
The conceptualisation of the experimental measurement of residual stress was done by Prof. Dermot Brabazon, Dr. Josiah Cherian Chekotu and myself.

Briefly outline your contribution to the **literature review** in this paper:
I conducted major part of the literature review for the paper.

Briefly outline your contribution to the **methodological design**:
The experimental methodology was performed by the collaborators abroad.

Briefly outline your contribution to **data collection**:
I collected the data required for the research.

Briefly outline your contribution to **data analysis**:
I analysed the collected data to obtain insightful results.

Briefly outline your contribution to the **synthesis and summary of findings**:
I synthesised and summarized the findings in a meaningful manner necessary for the paper.

Finally, outline your contribution to the **writing** and **revision** of the paper:
I wrote and revised the manuscript before and after peer-review.

Section 4: Signature and Validation

I confirm that the following statements are true:

(a) the information I have provided in this form is correct
(b) this paper is based on research undertaken during my candidature at DCU

Signature of PhD Candidate: ____Sampreet Rangaswamy____ **Date:**_01/08/2026_

I confirm that the information provided by the candidate is correct:

Signature of Principal Supervisor: Dermot Brabzon **Date:** _01/08/2026_

In some cases, it may be appropriate for verification to be given by both the principal supervisor **and** the lead/corresponding author of the work (where the lead/corresponding author of the work is not the candidate or the principal supervisor):

Signature of Lead/Corresponding Author Sampreet Rangaswamy **Date:** _01/08/2026_

Nature of Current Post/Responsibilities: _____PhD Researcher_____
Home institution: ___Dublin City University___

Section 1: Candidate's Details	
Candidate's Name	Sampreet Rangaswamy
DCU Student Number	22269710
School	School of Mechanical and Manufacturing Engineering
Principal Supervisor	Prof. Dermot Brabazon
Title of PhD by Publication Thesis	Multiscale, Multiphysics, and Data-Driven Modelling of the Laser Powder Bed Fusion Processing of Nitinol Shape Memory Alloy
Section 2: Paper Details	
Title of co-authored paper included in the thesis under examination	Residual Stress Estimation in Laser Powder Bed Fusion of Nickel-Titanium Shape Memory Alloy Cantilever Beams
List of authors as in order given on accepted/published version	Thomas Gillick, Sampreet Rangaswamy, Medad C.C. Monu, Hengfeng Gu, Dermot Brabazon
Publication Details (e.g. Year of Publication, Journal Name, Issue Number, Page Numbers, Place of Publication, DOI, ISSN, URL etc.)	2026, Journal of Materials Research and Technology
Publication Status (e.g. Published, Accepted)	Review Completed
Provide a brief statement here on the disciplinary ranking of this publication and the peer-review process involved (e.g. how many reviewers, single blinded or other, initial decision, revision timeline etc and any other details that speak to the rigour of the peer review process)	2 reviewers, single blinded, major revision, 2 months.
This paper (Chapter 6) is one of 5 co-authored papers to be submitted as part of the PhD by publication thesis submitted for examination.	
Section 3: Candidate's Contribution to the Paper	
Provide details below of the **nature** and **extent of your contribution** to the paper (include both your intellectual and practical contributions) and your overall contribution in **percentage terms**. Note that these categories can be customised according to disciplinary norms Briefly outline your contribution to the **conception** of the work described in this paper: I conceptualised the residual stress prediction research along with Prof. Dermot Brabazon. Briefly outline your contribution to the **literature review** in this paper:	

I conducted the significant part of the literature review required for the research.

Briefly outline your contribution to the **methodological design**:
I performed the modelling and simulation described in the paper.

Briefly outline your contribution to **data collection**:
I collected one half of the data presented, along with Thomas Gillick.

Briefly outline your contribution to **data analysis**:
7I contribute to most of the experimental and modelling data analysis required for the research.

Briefly outline your contribution to the **synthesis and summary of findings**:
I synthesised and summarized the findings from the modelling part of work.

Finally, outline your contribution to the **writing** and **revision** of the paper:
I wrote and revised the manuscript both for the initial submission as well as post peer review.

Section 4: Signature and Validation

I confirm that the following statements are true:

(a) the information I have provided in this form is correct
(b) this paper is based on research undertaken during my candidature at DCU

Signature of PhD Candidate: ____Sampreet Rangaswamy____ **Date:**_01/08/2026_

I confirm that the information provided by the candidate is correct:

Signature of Principal Supervisor: Dermot Brabazon **Date:** _01/08/2026_

In some cases, it may be appropriate for verification to be given by both the principal supervisor **and** the lead/corresponding author of the work (where the lead/corresponding author of the work is not the candidate or the principal supervisor):

Signature of Lead/Corresponding Author Sampreet Rangaswamy **Date:** _01/08/2026_

Nature of Current Post/Responsibilities: _____PhD Researcher_____
Home institution: ___Dublin City University___